Biocompatible Neural Electrodes and Polymeric Interface Studies

Yuanmin Zhang

Jesus College

University of Oxford

Supervisors: Prof. Sonia Contera and Prof. Richard Compton

A thesis submitted for the degree of

Doctor of Philosophy

Trinity Term 2024

Abstract

Over the last two decades, biomaterials have gained significant attention due to their versatility and practicality in biomedical applications. Polymers such as polydimethylsiloxane (PDMS) and poly(3,4-ethylenedioxythiophene) (PEDOT) have been extensively utilized, driving advancements in fields such as tissue engineering, drug delivery, and neural implants. This thesis investigates biocompatible materials for neural electrodes and the interactions at polymeric interfaces. The studies presented follow a general logic: it begins by understanding the basics of materials, advances to exploring their properties and functionalities, and concludes with in vivo studies.

Chapter 1 includes an overview of fundamental principles in neuroscience, electrochemistry, and mechanics, followed by an introduction to experimental tools such as cyclic voltammetry (CV), chronoamperometry, and atomic force microscopy (AFM) (**Chapter 2**). These foundational chapters provide the basis for the methodologies employed in subsequent material characterizations.

Chapter 3 investigates the mechanical properties of PDMS over time using AFM, revealing surface changes under different conditions. These findings emphasize the importance of monitoring interface properties for long-term applications. **Chapters 4 and 5** focus on PEDOT with different dopants (PSS^- and Cl^-), detailing the optimization of coating techniques using electropolymerization. Surface morphology analysis via AFM and electrochemical studies were conducted to ensure the production of stable, isolated coatings suitable for neural electrodes.

Building on these characterizations, **Chapter 6** describes in vitro experiments to study ionic motion at the polymer-solution interface using a biopotentiostat setup mimicking neural activity. **Chapter 7** advances to in vivo studies by implanting PEDOT-coated tetrodes into a

mouse brain, demonstrating the device biocompatibility and evaluating its neural recording performance.

Overall, the thesis establishes a solid understanding of biomaterials PDMS and PEDOT, revealing insights into polymer surface alterations, ionic response dynamics, and coating optimization for neural electrodes. Together, these results can be instrumental in the further development of neural recording devices.

Acknowledgement

I would like to express my deepest gratitude to my supervisors, Prof. Sonia Contera and Prof. Richard Compton. I first met Prof. Sonia during my third-year undergraduate lab work involving AFM, which was one of the key occasions that initiated my consideration of pursuing a DPhil in biophysics. Conversations with Prof. Sonia have always been inspiring, not only in the context of research but also in terms of her life philosophy. I feel equally fortunate to meet Prof. Richard Compton during my first year of DPhil. I am sincerely thankful that he welcomed me into his group after being introduced by Dr. Yuqi, allowing me to use the lab equipment and guiding me through electrochemical analysis. Both of my supervisors are highly dedicated to research and work while remaining approachable and genuinely caring about their students. I deeply appreciate the support, guidance, and encouragement I have received from both of them. I could not have completed my DPhil so smoothly without their invaluable help.

I would like to extend my gratitude to the members of both Contera's and Compton's group. I would like to thank Dr. Casey Adam and Dr. Yuqi Chen for introducing me to the lab, training me on the use of AFM and Autolab, and guiding me through the learning and interpretation of experimental results. I am also grateful to Dr. Minjun Yang, Dr. Huanxin Li, and Dr. Haotian Chen for their patience in answering my questions about unfamiliar equipment and Python code. A special thanks to Henrik Rehnstrom for collaborating with me in the cell culture lab to resolve various challenges. Additionally, I would like to express my appreciation to all the master, summer, and visiting students in the lab. It has been a wonderful experience working with you, and I have learned a lot through our project discussions.

I would also like to express my gratitude to the members of Dupret's group in the Oxford Nuffield Department of Clinical Neurosciences. I am especially thankful to Prof. David Dupret for answering my questions and supporting my neuron electrode project. My thanks also go to

Dr. Katja Hartwich for training and assisting me with device design and fabrication, and to Dr. Vitor Lopes dos Santos for his clear explanations of the signal processing.

Furthermore, I would like to thank everyone who has helped me in the lab. My thanks go to Sanna Piippo-Henderson for helping me with everything unfamiliar in the physics department, and to Dr. Kalin Dragnevski for training me on the use of the SEM in the LIMA lab in the engineering department. I am also grateful to Dr. Raquel Martínez González for her valuable suggestions on using microscopes and for introducing me to the biochemistry department's lab.

In addition, I would like to express my warm thanks to my friends Yiheng Yang, Shenyu Zhu, Yawen Hu, Houke Chen, and Jialu Liu for our weekend game nights and dinners together. A special thanks to Jinghan Wang—it was wonderful to have you around during my first year of DPhil in the UK, and the Christmas we spent together. It has been a great experience meeting you all and being friends with each of you.

Lastly, my deepest thanks go to my mother and father for their support in my studies and all the decisions I have made. I also want to thank all my family members for the vacations and dinners we enjoyed together. Thank you for looking after me and supporting my growth.

Looking back on my journey, I remember first stepping into Oxford at the age of fifteen, just after graduating from secondary school, and taking a summer trip with my parents. At that time, I could never have imagined that I would pursue both an undergraduate and a doctoral degree here. So, in the end, I want to express my gratitude to Oxford and Jesus College for having me for these many years. It has been a wonderful journey, and I have truly enjoyed my studies and research here.

Statement of Originality

I declare that the work presented in the thesis is my own. Any contributions made by collaborators are explicitly stated and acknowledged in the main text. Main contributions made by collaborators to this thesis are as follows:

— The in vivo experiments were carried out by Prof David Dupret (Oxford Nuffield Department of Clinical Neurosciences) and members of his group. Dr. Katja Hartwich trained me in tetrode fabrication and helped in implant device fabrication. Dr. Vitor Lopes dos Santos and Dr. Tabitha Broadbelt helped in collecting and analyzing data for in vivo experiments.

— Dr. Casey Adam trained me using AFM, and Dr. Yuqi Chen trained me to use CV to conduct experiments.

Chapter 3 of the thesis has been published in the *Journal of Mechanical Behavior of Biomedical Materials*. Chapter 4 of the thesis has been published in *ACS Applied Polymer Material*s. Chapters 5~7 have been published in *ACS Applied Materials and Interfaces*. All of the contents and experiments in the papers were done by myself, except the in vivo experiment (so the main procedures are included in the Appendix instead of the thesis main text), with no integration of other people's work. The work has also been presented at the following conference:

— Yuanmin Zhang, Yuqi Chen, Sonia Contera, Richard Compton. *Electrochemical and Nanostructural Characterization of Poly(3,4-ethylenedioxythiophene): Poly(styrenesulfonate) Films as Coatings for Neural Electrodes.* RMS AFM & SPM Meeting 2024 (poster presentation, Durham, 2024)

Glossary

Roman Symbols

Symbol	Meaning	Unit
	(Neuroscience and Electrochemistry Part)	
A	Area	m^2
$[A^Z]$	Bulk concentration of species A^Z	mol cm^{-3}
a_j	Activity of species j	
C_d	Capacitance per unit area	F m^{-2}
C_j	Concentration of species j	mol cm^{-3}
D	Diffusion coefficient	cm^2 s^{-1}
D_j	Diffusion coefficient of species j	cm^2 s^{-1}
d	Diffusion layer thickness	cm
I	Electrical current	A
I_p	Peak current	A
I_c , I_{ox} , I_{red}	Capacitive, oxidation, reduction current	A
J	Heterogeneous reaction flux	mol cm^{-2} s^{-1}
$J_j(x)$	Flux of species j	mol cm^{-2} s^{-1}
$[j]$	Concentration of species j	mol dm^{-3}
E	Applied potential at the electrode	V
E^0	Standard electrode potential	V

E_f^0	Formal potential	V
E_{mid}	Mid-point potential	V
ΔE_{pp}	Peak to peak separation	V
F	Faraday constant	C mol^{-1}
k^0	Standard electrochemical rate constant	cm s^{-1}
k_c, k_a	Rate constant for cathodic/anodic reactions	Unitless
m_T	Mass transport coefficient	cm s^{-1}
M	Molar mass	g mol^{-1}
N	Collection Efficiency	Unitless
N_A	Avogadro constant	mol^{-1}
n	Number of electrons transferred	Unitless
P_j	Permeability of species j	m s^{-1}
p_s	Smoothing parameter	Unitless
Q	Electric charge	C
R	Universal gas constant	J K^{-1} mol^{-1}
R_{bulk}	Bulk solution resistance	Ω
T	Absolute temperature	K
t	Time	s
$wvscore$	Waveform score	Unitless
w_i	Mean waveform of species i	Unitless

z	Charge of the species	C
z_j	Ionic charge of species j	C
P	Permeability	cm s^{-1}
V_{eq}	Equilibrium potential	V
V_{in} , V_{out}	Intracellular, extracellular potential	V
V_m	Membrane potential	V
$V_{measured}$	Measured potential difference	V
V_r	Resting membrane potential	V

(Mechanics Part)

a	Contact radius	m
E	Young's modulus	Pa
E_{eff} , E_t , E_s	Effective, indenter, surface Young's modulus	Pa
F	Force	N
f_c	Resonance frequency	Hz
k	Stiffness, spring constant	N m^{-1}
k_c	Cantilever stiffness	N m^{-1}
$InVOLS$	Inverse optical lever sensitivity	m V^{-1}
Q	Quality factor	Unitless
R	Radius	m
w	Energy of adhesion	J m^{-2}

z	Cantilever deflection	m
Z_p	Piezo displacement	m
Z_{cp}	Contact point position	m

Greek Symbols

Symbol	Meaning	Unit
	(Neuroscience and Electrochemistry Part)	
α, β	Transfer coefficient	Unitless
γ_j	Activity coefficient of species j	Unitless
Λ	Matsuda-Ayabe parameter	Unitless
μ_j	Chemical potential of species j	J mol^{-1}
μ_j^0	Standard chemical potential of species j	J mol^{-1}
$\bar{\mu}_j$	Electrochemical potential	J mol^{-1}
v	Scan rate	Vs^{-1}
$v_{flow}(x)$	Local fluid velocity	cm s^{-1}
ρ	Density	g cm^{-3}
σ_{ave}	Average charge density	C cm^{-2}
τ	Response time	s
ϕ	Electrical potential	V

	(Mechanics Part)	
δ	Indentation depth	m
ϵ	Strain	Unitless
η	Viscosity	Pa s
v	Poisson's ratio	Unitless
σ	Stress	Pa
τ	Relaxation time	s

Abbreviation

Abbreviation	Full name
ACSF	Artificial cerebrospinal fluid
ADP	Adenosine diphosphate
AFM	Atomic force microscopy
AP	Action potential
ATP	Adenosine triphosphate
CE	Counter electrode
CNT	Carbon nanotube
CP	Conductive polymer
CV	Cyclic voltammetry
DI	Deionized water

ECF	Extracellular Fluid
EDX	Energy dispersive X-ray
GMM-N	General Maxwell Model with N arms
HFV	Heavy Formvar
ICF	Intracellular Fluid
JKR	Johnson-Kendall-Robertson
KV	Kelvin-Voigt
MW	Maxwell
OCP	Open circuit potential
P	Inorganic phosphate
PANI	Polyanilines
PBS	Phosphate buffered saline
PDMS	Polydimethylsiloxane
PEDOT	Poly(3,4-ethylenedioxythiophene)
PPY	Poly(pyrrole)
PSS	Polystyrene sulfonate
Pt	Platinum
PTE	Photothermal excitation
RE	Reference electrode
RMS	Root-mean-square

SCE	Saturated calomel electrode
SEM	Scanning electrode microscope
SLS	Standard linear solid
SS	Stainless steel
W	Tungsten
WE	Working electrode

Contents

Chapter 1

Introduction

A neural electrode is an implantable device used to record neural electrical activity extracellularly. Neural electrodes are used for establishing functional links between neurophysiological phenomena in specific brain areas and processes such as memory [1], sleep, brain oscillations and how they relate to the complex behaviours of animals [2], and neurological disorders like epilepsy [3], Parkinson's [4], Alzheimer's diseases [5].

The aim of this project is to develop a biocompatible neural recording electrode and to study associated interfacial processes. This requires a comprehensive understanding of electrode design, and working principles, together with material properties to achieve the project goals. Therefore, this chapter introduces some fundamental theories of neuroscience, electrochemistry, and mechanics. It begins by explaining the origin of neural signals and how these signals are captured by electrodes. This is not a purely brain electrophysiology problem, on the one hand, at the electrode surface, there are usually ion motions and electron transfer; how these species migrate from distant bulk to the electrode also requires consideration. Hence, electrochemistry is required to explain how the electrode measures electrical signals. On the other hand, since a rigid electrode is implanted within soft tissues, complex mechanical contributions to the process are also likely to be important, both for the electrical measurement itself, and for the response of the living tissue surrounding the electrode. Thus, mechanical properties such as elasticity and viscoelasticity are investigated to understand the 'mechanical mismatch' at the interface between materials. Collectively, these topics lay a foundation that helps in understanding the experiments and analyses conducted in subsequent chapters.

1.1 Introduction to Neural Electrode

This section explains the origin of one of the dominant neural signals captured during extracellular recording, the action potential (AP). Then the shape of the recorded signals due to charge movement is explained.

1.1.1 Origin of Neural Signal – Action Potential

Nerve cells, or neurons, are the signaling units of the nervous system [6]. A typical neuron, illustrated in **Figure 1.1**, comprises four morphologically distinct regions: the cell body (also known as the soma), dendrites, an axon, and presynaptic terminals [6, 7]. The cell body, or soma, contains a nucleus and radiates multiple protrusions. Typically, the protrusions include one long axon, which conducts signals away from the soma to distant targets, and several shorter, branched dendrites, acting as antennae to increase the surface area for receiving signals from axons of other neurons [6, 7]. At the distant end of the axon, it often divides into numerous branches, enabling the transmission of messages to multiple target cells simultaneously [6, 7]. Despite the varying significance of the signals conveyed by different neuronal classes, the form of the signal remains consistent – a change in the electrical potential across the neuron membrane [6, 7].

In an excitable membrane, such as that of a nerve or muscle fiber, an influx of current exceeding a certain threshold can lead to membrane depolarization, which may trigger a regenerative change in potential known as an action potential (AP) (Figure 1.2) [6]. The AP can be described as a rapid sequence of changes in voltage across the membrane or membrane potential. The membrane potential (V_m) is defined by the equation:

$$V_m = V_{in} - V_{out} \tag{1.1}$$

where V_{in} and V_{out} represent the intracellular and extracellular potentials, respectively. The membrane potential at rest is known as the resting membrane potential V_r [6].

At the rest state of a neuron, the concentration of cations between the intracellular and extracellular space differs from one side of the membrane to the other [6, 8, 9], as detailed in Table 1.1 and Table 1.2. This separation of charges is maintained by the lipid bilayer of the membrane (Figure 1.3), which impedes ion diffusion. Consequently, the concentration difference establishes a chemical gradient, while the separation of charges results in an electrical gradient, together constituting an electrochemical gradient across the membrane [6, 8, 9]. Equilibrium for a specific ion is reached when the potential difference produced across the membrane balances the opposing force due to the concentration gradient. Such equilibrium potentials can be described by the Nernst equation [6, 8, 9]:

$$V_{Eq}^{[X]} = \frac{RT}{zF} \ln \frac{[\mathrm{X}]_{out}}{[X]_{in}} \tag{1.2}$$

where $V_{Eq}^{[X]}$ is the equilibrium potential of the ion [X], R is the universal gas constant, T is the absolute temperature (unit: K), z is the charge on the ion X which passes through the membrane (e.g. For X = K^+, z = +1; for X = Cl^-, z = -1), and F is the Faraday constant [6, 8, 9]. However, the membrane potential V_m is not equal directly to the ionic equilibrium potential $V_{Eq}^{[X]}$. The resting membrane potential varies among different nerve cells, where the variation depends on two factors: the unequal distribution of ions, particularly Na^+ and K^+ ions (maintained by Na^+—K^+ ion pump), and the selective permeability due to the presence of ion channels in the membrane (Figure 1.3) [6]. The dependence of membrane potential on ionic permeability and concentration can be quantified by the Goldman equation [6]:

$$V_m = \frac{RT}{zF} ln \frac{\sum_i P_i [X_i]_{out}}{\sum_i P_i [X_i]_{in}} \tag{1.3}$$

where $[X_i]$ represents the ionic species, and P_i represents their corresponding permeability.

As shown in Figure 1.3, ion channels are embedded within the membrane, functioning as gates that regulate the transmembrane movement of ions. For example, voltage-gated Na^+

channels selectively permit the passage of Na^+ ions, with their opening and closing governed by the membrane potential. Ion pumps, also depicted in Figure 1.3, are embedded in the membrane and utilize energy in the form of Adenosine triphosphate (ATP) to operate. ATP is a nucleotide that serves as a 'molecular unit of currency' of energy to drive a variety of processes and chemical reactions in cells [7]. Through the hydrolysis of ATP into Adenosine diphosphate (ADP) and inorganic phosphate (denoted as P), ion pumps acquire the necessary energy to actively transport ions against their concentration gradient, such as extruding Na^+ ions from the intracellular space to the outside as illustrated in Figure 1.3, thereby maintaining an uneven ion distribution.

After understanding the basic mechanisms of ion movement across the cell membrane, the next stage is to explain the generation and characteristics of the action potential (AP). As mentioned previously, an AP is a transient change in membrane potential driven by the movement of ions into and out of the cell. The ionic basis of the AP has been extensively studied using the giant axon of the squid (Table 1.1). This research revealed that the AP arises primarily from the interplay of two currents: voltage-gated Na^+ and K^+ currents, which respectively produce the rising and falling phases of the AP [8].

Figure 1.2 presents a general shape of an AP. When the level of excitation exceeds the activation threshold, the Na^+ ion channels are activated and opened (Figure 1.2, Stage ①), resulting in a rapid influx of Na^+ ions from the extracellular space into the cell, driven by the concentration gradient. If the stimulus is insufficient, depolarization does not occur, leading to minor fluctuations that represent failed initiation events. Because the Na^+ channels activate more rapidly than the K^+ channels, a brief spike in depolarization is observed, reaching a maximum (Figure 1.2, Stage ②). Subsequently, the Na^+ channels spontaneously inactivate, while the strong depolarization triggers the opening of K^+ channels, leading to the outflow of K^+ ions in alignment with their concentration gradient. Consequently, repolarization takes place

(Figure 1.2, Stage ③), gradually lowering the membrane potential and taking it towards the equilibrium potential of K^+, $V_{Eq}^{[K^+]}$ (Table 1.1) [8]. Because K^+ channels close slowly, the membrane potential may transiently undershoot the resting potential, a phenomenon referred to as hyperpolarization (Figure 1.2, Stage ④) [8]. Following an AP, there is a refractory period (Figure 1.2, Stage ④) during which some Na^+ channels remain inactivated, and K^+ channels have not yet closed. After this, the resting membrane potential is recovered and ready for the next stimulus to trigger a new AP. Throughout the process, the Na^+— K^+ ion pump always works to re-establish the initial electrochemical equilibrium [8].

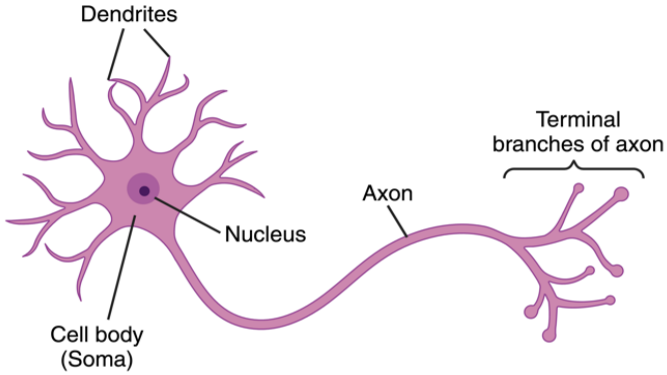

Figure 1.1: Structure of a typical neuron. Most neurons consist of a cell body, dendrites, an axon, and axonal terminal branches. The cell body, also known as soma, contains a nucleus. The cell body and dendrites act as input elements of the neuron, receiving signals from other neurons; branched dendrites expand the surface area for signal reception. The axon serves as the transmitting element of the neuron. Terminal branches of the axon transmit signals to the other cells [6, 7]. The picture was created using Biorender.

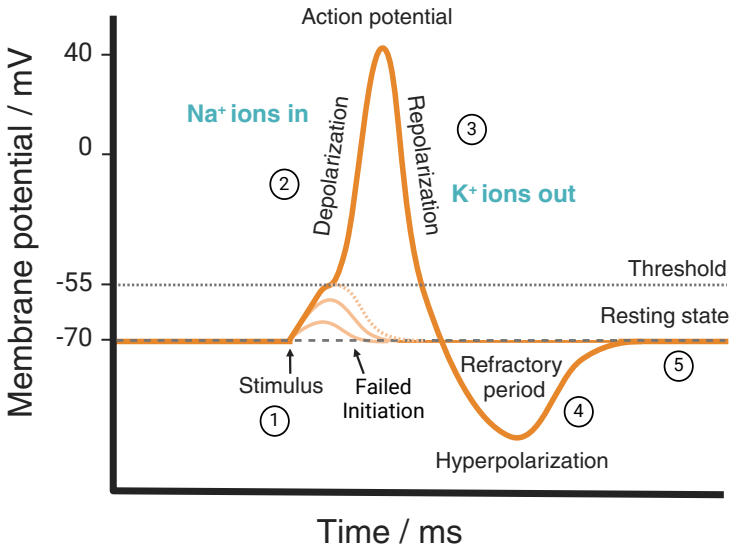

Figure 1.2: The general shape of an action potential (AP) [8]. The shape of AP is mainly the interplay of Na^+ and K^+ currents, which causes depolarization and repolarization, respectively. The picture was created using Biorender.

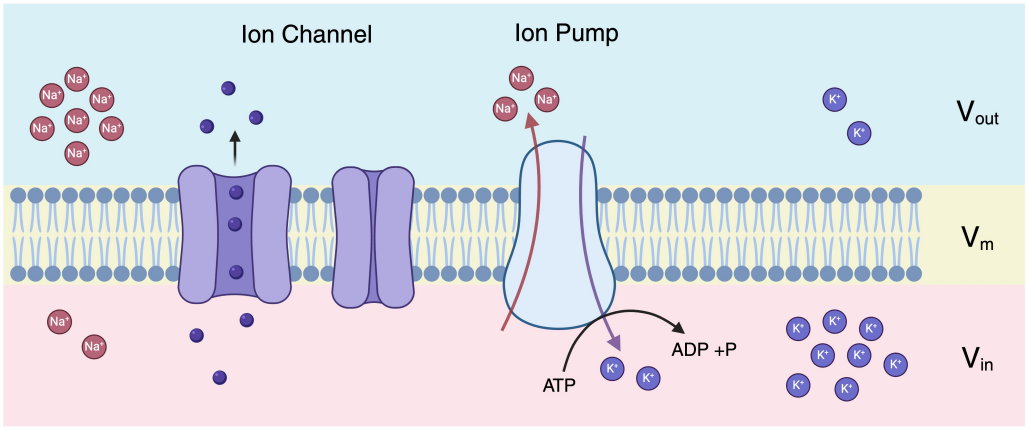

Figure 1.3: An illustration of the environment across the neural membrane [6, 9]. Na^+ ions have a much larger concentration in the extracellular space, whereas K^+ is more concentrated inside. Across the membrane, there are ion channels, either open (left one) or closed (right one), allowing the passage for a specific type of ions, and an ion pump that transports 3 Na^+ out and brings in 2 K^+ ions each time it consumes one ATP. V_{in}, V_{out}, and V_m are the intracellular, extracellular, and membrane potentials. The picture was created using *Biorender*.

Table 1.1: Major ion concentrations on either side of an at-rest neuronal membrane from a giant axon of the squid. A^- represents organic anions, which primarily are amino acids and proteins inside the cell [6]. ECF: Extracellular fluid. ICF: Intracellular fluid. The equilibrium potential for each ionic species is calculated using equation (1.2).

Ion	ECF Concentration /mM	ICF Concentration /mM	Equilibrium Potential /mV
Na^+	440	50	+55
K^+	20	400	-75
Cl^-	560	52	-60
A^-	/	385	/

1.1.2 Principle of Extracellular Recording

In general, there are two primary methods for performing single-unit neural recordings: intracellular and extracellular recordings. These methods differ in the positioning of the recording electrodes. For instance, the detailed shape of the AP was initially measured by Hodgkin and Huxley using intracellular techniques [10], where one recording electrode penetrates the interior of the cell membrane, and another was placed in the extracellular environment to serve as a reference. However, extracellular recording is more commonly employed to record neural activity during in vivo experiments. In this method, the working electrode is positioned near neurons but without direct contact, which simplifies the procedure compared to intracellular measurement by eliminating the need for the electrode to be precisely placed on a specific neuron.

To understand the extracellular recording, a volume conduction theory is assumed, where the axon acts as a conductor immersed in an electrolyte and that the medium between the source and the recording site exhibits low and uniform resistance [11].

Once an AP is initiated at any point on the membrane, the resulting local depolarization spreads passively along the axon. This passive spread causes successive adjacent membrane

regions to reach the threshold needed to generate subsequent APs, and hence, the AP can propagate along the axon [6] (Figure 1.4). As depicted in Figure 1.4, the point of greatest depolarization is called the 'sink', while the neighboring areas serve as the 'source' for the current flowing into the sink, where the current is conventionally defined as the cation flow. The difference in membrane potential drives a local ionic current from the source to the sink outside the membrane. Consequently, the AP or 'spike' recorded by an extra-cellular micro-electrode is the result of ion currents flowing in the extracellular space surrounding an active neuron [11].

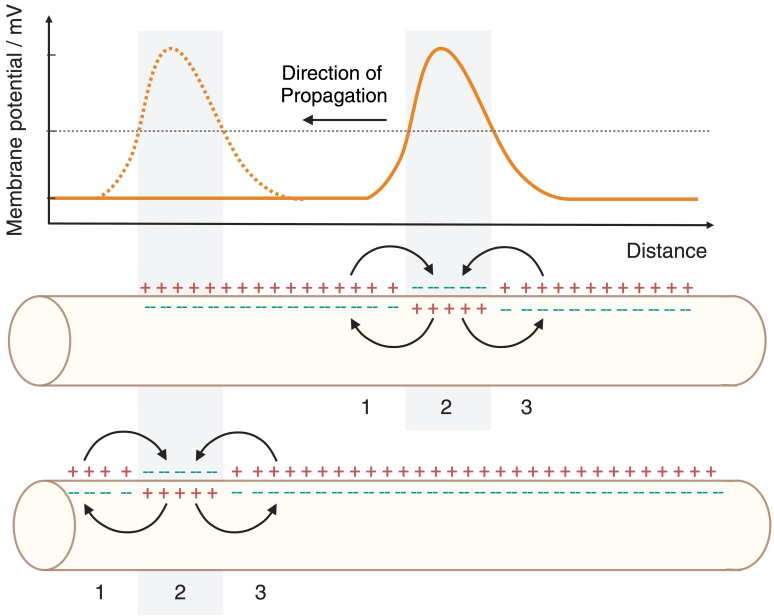

Figure 1.4: Plot of membrane potential along an axon reflects the propagation of action potential [6]. The arrow indicates the direction of current flow (cation movement) from adjacent regions into the depolarized region. Regions 1 and 3 are the 'sources,' and region 2 is the 'sink'.

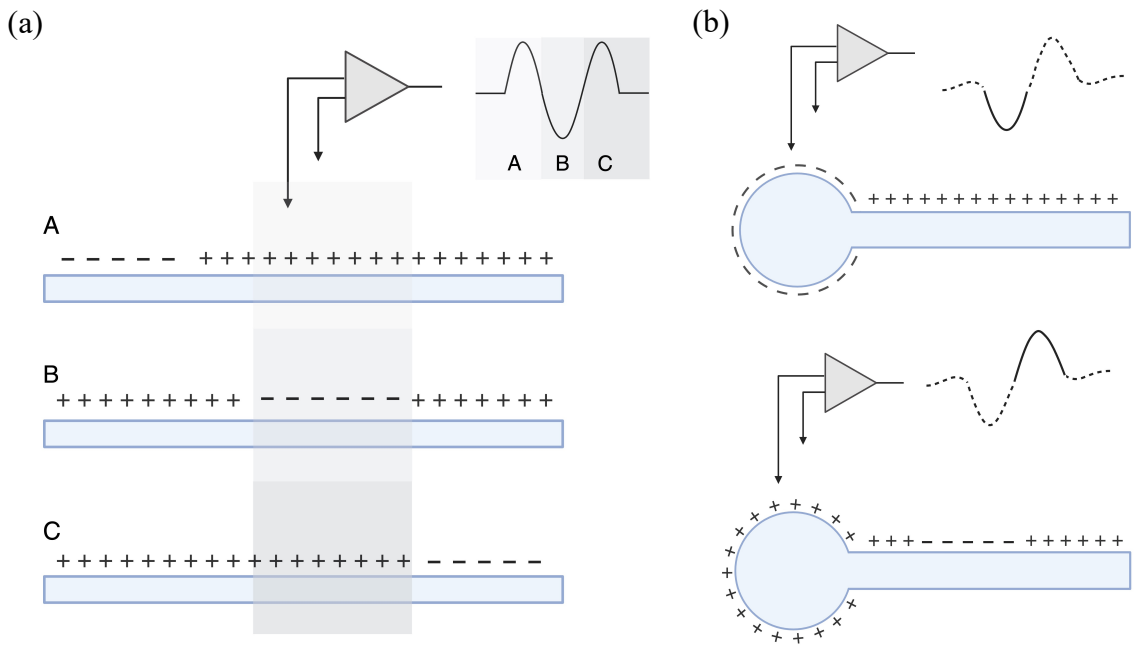

Figure 1.5: Model of neuron to predict and explain the shape of the waveform recorded. **(a)** A triphasic waveform can be recorded from an isolated axon as the action potential (AP) approaches, passes, and recedes from the recording site. **(b)** A biphasic waveform can be recorded from a cell body (soma) or the initial segment of an axon where the AP is initiated and then propagates.

To further understand the recording signal, consider an electrode placed near a neuron, either along the long axon (Figure 1.5(a)) or near the soma of a neuron (Figure 1.5(b)). The electrode setup in Figure 1.5 includes one recording site (the long probe), one reference electrode (the short probe), and one amplifier (indicated by the triangle symbol).

When the neuron is at rest, the membrane potential is uniform across the entire cell, resulting in no current flow. However, once depolarization occurs at any point and approaches the recording site (Figure 1.5 (a)-A), current in the adjacent area flows toward the activated region. In this case (Figure 1.5 (a)-A), the recording site is positioned above the 'source' area, from which the current moves away from the electrode, registering as a positive signal. Conversely, when the AP reaches the regions beneath the electrode (Figure 1.5 (a)-B), the

electrode is then above a ‘sink’. Thus, currents from the surrounding regions converge toward the electrode, resulting in a negative recorded signal. As the AP recedes, the direction of the current flow reverses again (Figure 1.5 (a)-C). Collectively, these three stages in Figure 1.5 (a) generate a triphasic waveform in the recorded signal.

Moreover, there could be a situation where the electrode is positioned near the soma of a cell or the initial segment of an axon, which is the origin point of the signal. In this case, as depicted in Figure 1.5(b), a biphasic signal is recorded. Initially, the electrode captures a negative signal as depolarization happens, which then reverses as the AP propagates away from the soma.

Overall, this simplified neuron model provides a clear understanding of the recorded signals. The theoretical constructs of triphasic and biphasic waveforms have been experimentally confirmed by several previous studies [12, 13]. However, in reality, neuron morphology and the resulting recorded signals are often more complex than this simple model suggests. Several factors influence the shape of the recorded signal, such as cell morphology, the distribution of active conductance on the somatic and dendritic membranes, the state of cell excitability, and the electrode's position relative to the cell body [11, 14]. Conversely, this complexity is advantageous as it allows for the differentiation of signals from various neurons, thereby facilitating the processes of spike separation and sorting. Individual neurons represent the structural and functional units of the nervous system, and their spatially and temporally resolved activities are crucial for understanding the working mechanism of a brain [15-17].

In this thesis, a specific type of electrode called a tetrode, which is formed by twisting four microwires together (Figure 1.6), is used for extracellular recording. As described in **Chapter 6** in vitro experiments were conducted using PBS, which has an ionic constitution similar to that of ECF (Table 1.2). Descriptions of the electrode and the experimental procedures are included in the introductory sections of the relevant following chapters.

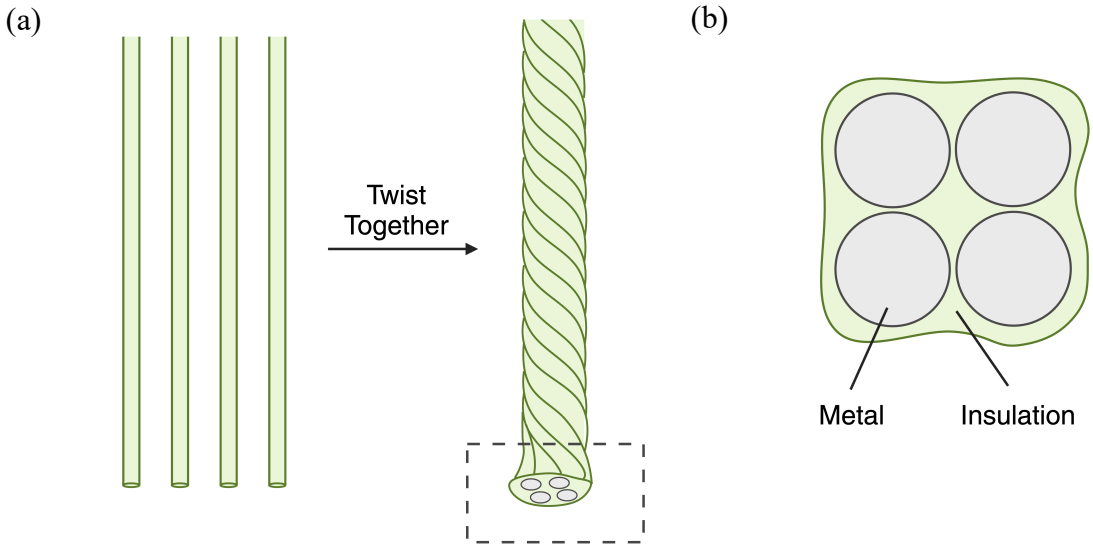

Figure 1.6: (a, b) Planar and cross-sectional view of a tetrode. Four insulated metal wires are twisted together to form a tetrode, where the green sections represent insulation, and the grey areas are the exposed metal discs. The boxed region of the tetrode tip is shown in (b). It needs to be noted that the four metal discs on a tetrode are separated by the insulation.

Table 1.2: Extracellular fluid (ECF) content [18], intracellular fluid (ICF) for a typical mammalian cell [19, 20], and 0.01M phosphate buffered saline (PBS) [18] ion content.

Ion	ECF concentration / mM	ICF concentration / mM	0.01M PBS / mM
Na^+	147	12	153
K^+	2.90	140	4.20
Ca^{2+}	1.14	10^{-4}	/
Mg^{2+}	1.10	3.5	/
Cl^-	113	2.5-50	140
HCO_3^-	23.3	10	/
PO_4^{3-}	0.358	60	9.57

1.2 Introduction to Electrochemical Processes at the Interface

This section examines the processes occurring at the electrode-solution interface. First, it discusses the electrochemical aspects to understand the nature of the current flowing at an electrode. Second, electrode kinetics and equilibria are introduced to quantify different processes.

1.2.1 Faradaic and Non-Faradaic Processes

In general, when a current passes through an electrode, there are two possible processes: Faradaic and non-Faradaic [21, 22]. During an electrochemical experiment, both processes can coexist. The distinction is that Faradaic current results from electron transfer at the electrode/solution interface, while non-Faradaic current results from the movement of ions around the electrode [21, 22]. During extracellular neural recording, the non-Faradaic current is the dominant current. However, when electropolymerization is used to deposit polymers via oxidation or reduction, the increase of current collected at the working electrode is due to Faradaic processes. Both types of processes are important to understand neural electrodes and coating materials. They are discussed separately in the following sections.

1.2.1.1 Faradaic Processes

A Faradaic process involves a redox reaction and the transfer of electrons across the metal/solution interface, producing a current called a Faradaic current [21, 22]. To understand how the electron transfer occurs at the interface, consider a one-electron transfer reaction in an aqueous solution with a redox couple A^Z and B^{Z-1} (Figure 1.7(a, b)):

$$A^z(aq) + e^-(m) \underset{k_a}{\overset{k_c}{\rightleftharpoons}} B^{z-1}(aq) \tag{1.4}$$

where k_c and k_a represent the rate of reaction at the cathode and anode, *(aq)* indicates that the ion is in the aqueous phase, and *(m)* means the electron is in the metal electrode. The metal

electrode has a continuous conduction band with the energy level filled up to the Fermi level. However, the energy levels associated with A^Z and B^{Z-1} in the solution phase are discrete and related to their unfilled molecular orbital. If the Fermi level naturally exceeds the vacant orbital energy level in the ion, it is then energetically favourable for electrons to leave the Fermi level to join the unoccupied molecular orbital of A^Z, resulting in the formation of B^{Z-1} (Figure 1.7(a, b)). As the electron transfer proceeds, positive charge gradually accumulates on the electrode, lowering the Fermi level [21]. Simultaneously, negative charges developed in the solution phase elevate the energy levels of the solution species (Figure 1.7(b)) [21]. When the energy levels in the electrode and the solution match, electron transfer occurs in both directions (Figure 1.7(b)) [21]. When the rate of transfer is equal in both directions ($k_c = k_a$), dynamic equilibrium is established, resulting in no further net charge [21].

The dynamic equilibrium concept is useful for understanding the mechanism of a saturated calomel electrode (SCE) or other type of reference electrode as discussed in a later section. However, in many cases, the unoccupied orbital energy level of a molecule or ion is not ideally positioned for spontaneous electron transfer, such as species *X* (in solution) shown in Figure 1.7(c, d). To drive a redox reaction, the Fermi level can be shifted through the application of an external potential [22]. Hence, at a certain potential, the electrons of ions in solution will find it energetically more favourable to transfer to a lower energy state on the electrode, i.e., oxidation happens (Figure 1.7(c)), or vice versa causing a reduction (Figure 1.7(d)). This generates a current flow between the solution and the electrode. As the number of electrons cross the electrode/solution interface is related stoichiometrically to the extent of the chemical reaction, the current can reflect the amount of reactant consumed or product generated. The relationship between the charge and amount of product formation is described by Faraday's law [22]:

$$Q = nFN \tag{1.5}$$

where Q (unit: C) is the total amount of charge transferred at the electrode/solution interface, n is the number of electrons transferred during the redox reaction (e.g. $A + ne^- \rightarrow B$), F is the Faraday constant (= 9.65×10^4 C mol^{-1}), and N (unit: mol) is the amount of product formed or reactant consumed [22].

It is important to note that the electron transfer process between the electrode and the reactant at the electrode-solution interface involves quantum mechanical tunnelling. For this tunnelling phenomenon to occur, the reactants must be located within approximately 10 to 20 Å of the electrode [21]. At this proximity, the electron wavefunctions of reactants and the electrode can overlap, enabling electrons to transfer from one site to another [21]. Beyond this distance, the rate of tunnelling becomes negligible. Consequently, it is the local concentrations of redox species in close proximity to the electrode surface that influence the measured current rather than species in the distant bulk solution.

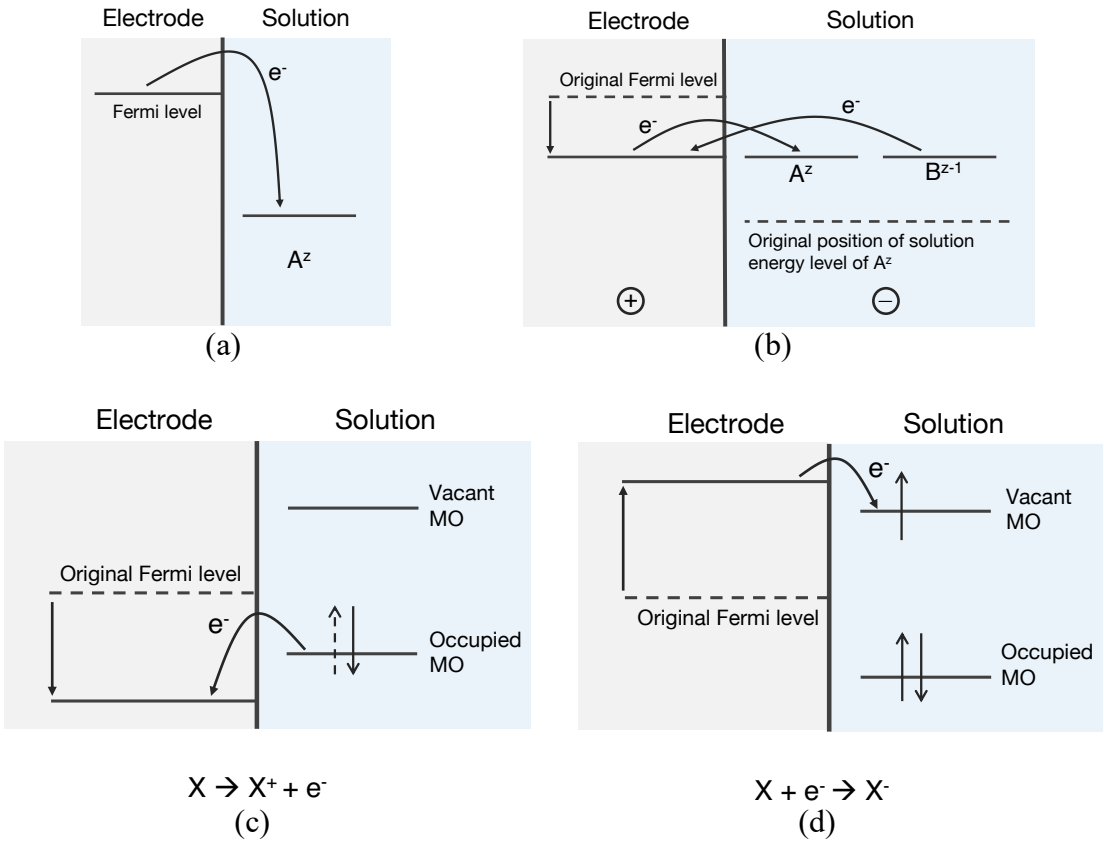

Figure 1.7: (a, b) Illustration of energy level changes between the redox pairs (A^z and B^{z-1}) and the Fermi energy level change for an equilibrating redox couple. **(c, d)** Redox reactions of species X (in solution) are driven by external potential, which shifts the Fermi level up or down. MO: molecular orbital. [21, 22]

1.2.1.2 Non-Faradaic Processes

A non-Faradaic process does not involve any transfer of electrons. Instead, its current flow is generated due to the repulsion and attraction of ionic species towards and away from the electrode.

The electrical double layer is the basis of the non-Faradaic process. As shown in Figure 1.8(a), when a charged electrode, for instance, one with a positive charge, is introduced into a solution, it attracts adjacent anions to its surface, resulting in a higher concentration of anions than cations in the layer immediately surrounding the electrode. From Figure 1.8(a), the innermost layer, known as the Stern layer, comprises solvent molecules and ions that form through desolvation as a result of the applied potential [22]. The next layer corresponds to the Inner Helmholtz Plane (IHP), which is the electrical center of the specifically adsorbed ions [22]. Specific adsorption denotes a substantial chemical interaction between these ions and the electrode surface. Moving further from the electrode, the subsequent layer is the Outer Helmholtz Plane (OHP), inhabited by solvated ions that are not specifically adsorbed [22]. These ions in the OHP strongly interact with the charged electrode through long-range electrostatic forces [22]. Beyond the OHP is the diffuse layer, which extends into the bulk solution, containing non-specifically adsorbed solvated anions and cations [22]. Overall, these layers exist to balance the charges on the electrode, and the separation of two layers of different charges at the electrode/solution interface functions analogously to an electrical capacitor [22] (Figure 1.8(b)).

During electrochemical processes, current-potential curves obtained from a redox system can be influenced by non-Faradaic current due to the charging of the double layer. This current is also known as charging current or capacitive current (I_c) and can be quantified as follows [22]:

$$I_c = \frac{dQ}{dt} = C_d A \frac{dE}{dt} = C_d A v \tag{1.6}$$

where Q (unit: C) is the charge, t (unit: s) is time, C_d (unit: F m^{-2}) is the capacitance per unit area of the double layer, A (unit: m^2) is the electroactive layer area, E (unit: V) is the applied

potential on the electrode, and v is the scan rate (unit: V s^{-1}), defined as the rate of change of potential applied. As the potential applied to the electrode becomes more positive, the increased potential leads to a higher current flow, driven by the movement of local ionic species and the reorientation of dipole molecules within the solvent. According to equation (1.6), an increased rate of change in potential, which corresponds to a larger scan rate, will result in a linear relationship between the measured current and the scan rate if the process is purely capacitive (i.e., only involves I_c). This linear relationship is useful in determining whether a redox reaction is occurring, particularly when assessing our polymer-coated electrodes for the recording process in subsequent chapters.

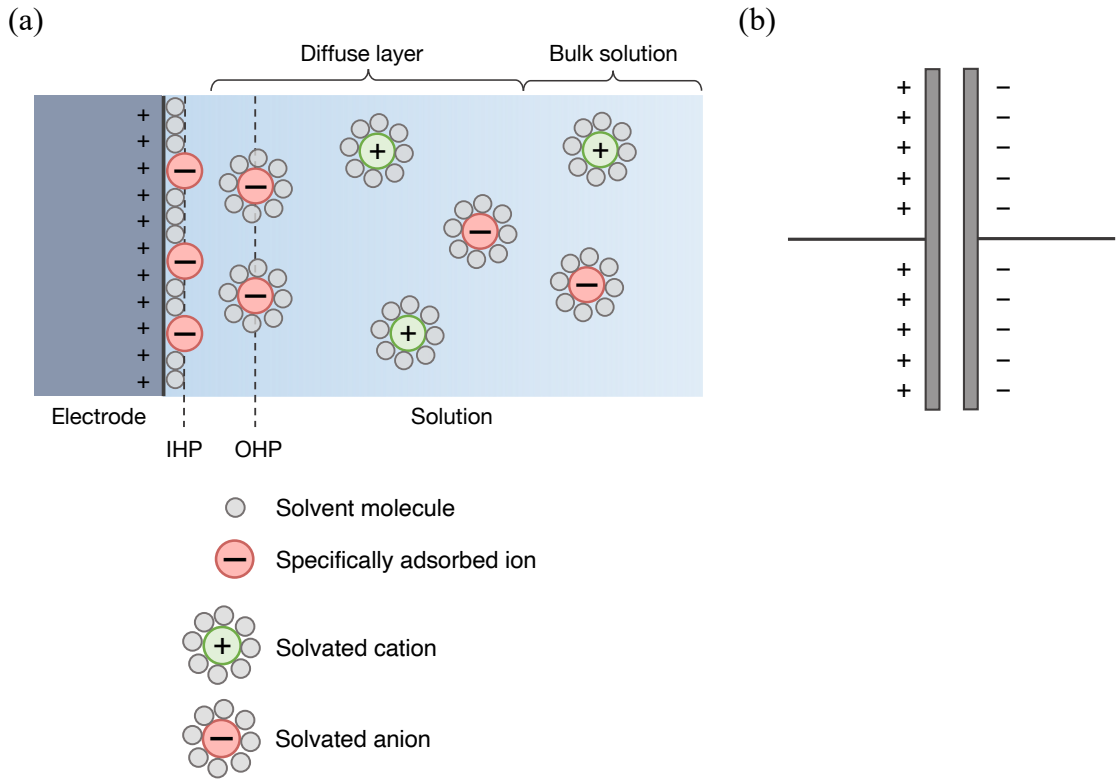

Figure 1.8: (a) Illustration of a double layer at the electrode surface. **(b)** Analogue of the electrode/solution interface as a capacitor. IHP: Inner Helmholtz Plane. OHP: Outer Helmholtz Plane [22].

1.2.2 Electrochemical Equilibrium and Electrode Kinetics

Faradaic processes (Figure 1.7(a, b)) involving fast electron transfers can achieve local dynamic equilibrium at the electrode surface. Otherwise, they require the application of an external potential to drive the redox reactions (Figure 1.7(c, d)). Nevertheless, the equilibrium of the system and transfer of electrons are complex. To further understand these processes, this section discusses electrochemical equilibrium and electrode kinetics.

1.2.2.1 Electrochemical Equilibrium

To account for both the chemical and electrical energies of species (*j*) involved in redox reactions, the electrochemical potential ($\bar{\mu}_j$) is considered. Following the example reaction between A^z and B^{z-1} in equation (1.4), by balancing the forward and backward reaction electrochemical potential at equilibrium ($\bar{\mu}_{A^z} + \bar{\mu}_{e^-}$ and $\bar{\mu}_{B^{z-1}}$), the system can be described by the Nernst equation: (See Appendix A.1 for detailed explanation and derivation.)

$$E = E_0 + \frac{RT}{F} ln \frac{a_{A^z}}{a_{B^{z-1}}} \tag{1.7}$$

where E_0 is the standard potential, a_j represents the activity of species *j*.

$$a_j = \gamma_j C_j \tag{1.8}$$

γ_j is the activity coefficient and C_j is the concentration of species *j*. The activity is introduced as to consider the interaction between the reactants, the solvent, and the ions in a non-ideal solution. By expanding out a_j using equation (*1.8*), the Nernst equation can be further rearranged to:

$$E = E_f^0 + \frac{RT}{F} ln \frac{[A^z]}{[B^{z-1}]} \tag{1.9}$$

$$E_f^0 = E_0 + \frac{RT}{F} ln \frac{\gamma_{A^z}}{\gamma_{B^{z-1}}} \tag{1.10}$$

E_f^0 represents the formal potential. Comparing to the standard potential (E_0), E_f^0 accounts for the actual conditions in a solution, such as the pH, ionic strength, and presence of other complexing species, which can affect the electrochemical behavior of the reactants involved.

1.2.2.2 Electrode Kinetics

In the previous section (1.2.2.1), the Nernst equation was introduced. It describes the relationship between the potential and the concentration of redox couples, but it only applies to systems in dynamic equilibrium. Additionally, the Nernst equation does not provide details on the mechanisms preceding equilibrium or how equilibrium is maintained. Therefore, this section introduces electrode kinetics to quantitatively describe the evolution of chemical changes to achieve and maintain the dynamic equilibrium state.

Consider again the A^z/B^{z-1} redox couple in equation (1.4). Electron transfer at the working electrode leads to the formation of current (I):

$$I = nFA_{WE}J \tag{1.11}$$

where *n* is the number of electrons transferred (a single electron transfer will be considered in the following section, so n=1), *F* is the Faradaic constant, A_{WE} is the area of the working electrode (unit: cm^2), and *J* is the flux at the interface (unit: mol cm^{-2} s^{-1}) defined as

$$J = k_c[A^z]_0 - k_a[B^{z-1}]_0 \tag{1.12}$$

$[A^z]_0$ and $[B^{z-1}]_0$ represents the concentrations of each species at the electrode surface. The electron transfer rates for the cathodic and anodic reactions, k_c and k_a, are described by:

$$k_c = k^0 e^{-\frac{\alpha F}{RT}\eta} \tag{1.13}$$

$$k_a = k^0 e^{\frac{\beta F}{RT}\eta} \tag{1.14}$$

α and β are the electron transfer coefficient ($\alpha + \beta = 1$), k^0 is the standard electron transfer rate, η is the overpotential, defined as the difference between the applied potential to the formal potential of the redox couple:

$$\eta = E - E_f^0 \tag{1.15}$$

The inclusion of overpotential illustrates the dependency of the current generated on the applied potential. Substituting equations ((1.12) ~(1.15)) into (1.11) gives the Butler-Volmer equation:

$$I = FA_{WE}k^0([A^z]_0 e^{-\frac{\alpha F}{RT}\eta} - [B^{z-1}]_0 e^{\frac{\beta F}{RT}\eta}) \tag{1.16}$$

Different extreme cases of the equation (1.16) are considered as follows:

(1) If the electron transfer rate is very fast ($k^0 >> 0$), then $I/k^0$is very small and can be approximated to 0, causing equation (1.16) to collapse to Nernst equation (equation (1.9)).

(2) If the oxidation in the reaction process is significantly faster than the reduction ($\eta >> 0$), the reduction term becomes negligible and the oxidation current can be represented as in equation (1.17).

(3) Conversely, if reduction is much faster ($\eta << 0$), then a reduction current can be obtained as in equation (1.18).

$$I_{ox} = FA_{WE}k^0[B^{z-1}]_0 e^{\frac{\beta F}{RT}\eta} \tag{1.17}$$

$$I_{red} = FA_{WE}k^0 [A^z]_0 e^{-\frac{\alpha F}{RT}\eta} \tag{1.18}$$

Plots of $ln|I_{ox}|$ or $ln|I_{red}|$ with potential E or η produces Tafel plots. Tafel plots can be used to assess the nature of the reaction, and information, notably the transfer coefficients α and β can be obtained from the gradient of the graphs.

1.2.3 Mass Transport

For a reaction to occur at the electrode, in addition to electron transfer, it is also necessary to consider the movement of the reaction species from the distant bulk to the layer of solution adjacent to the electrode surface. Mass transport refers to the movement of reaction species in the bulk solution towards and away from the electrode surface. This process occurs through various mechanisms, as described by the following one-dimensional (1D) Nernst-Planck equation:

$$\text{(1D)} \qquad J_j(x) = -D_j \frac{\partial C_j}{\partial x} + C_j v_{flow}(x) - \frac{z_j F}{RT} D_j C_j \frac{\partial \phi}{\partial x} \qquad (1.19)$$

The three terms from left to right represent the diffusional flux (due to a concentration gradient), the convection flux, and the migration flux (due to the electric field). J_j is the flux of species j (units: mol cm^{-2} s^{-1}), D_j is the diffusion coefficient of that species (units: cm^{-2} s^{-1}), C_j is the concentration (units: mol cm^{-3}), v_{flow} is the local flow velocity (units: cm s^{-1}), z_j is the ionic charge of species j. In this project, diffusion transport is the dominant mechanism, with the effects of the other two mechanisms being significantly less compared to diffusion. Therefore, in the following section, diffusion will be discussed and explained in more detail.

1.2.3.1 Diffusion

Consider an electrode is placed in a solution containing an electro-active species. If an appropriate potential is applied, a reaction occurs, consuming the materials near the electrode. This consumption creates a concentration gradient, as illustrated in **Figure 1.9**, and forms a diffusion layer. The concentration gradient drives the diffusion of the active species toward the electrode surface, enabling the reaction to proceed. The diffusion flux, J, and the concentration gradient are governed by Fick's First Law [21]:

$$\text{(1D)} \qquad J(x) = -D \frac{\partial C}{\partial x} \qquad (1.20)$$

The negative sign indicates that the species flow from a region of high concentration to a region of low concentration.

To further illustrate this concept, consider molecules at an arbitrary point in a solution, confined within a box of size $2\delta x$ (**Figure 1.10**) [21]. Inside each half of the box, molecules have an equal probability of moving either left or right. It takes an average time of δt for molecules to travel a distance of δx. So the flux of molecules travel in one direction is $\frac{C_j \delta x}{2\delta t}$ and the net flux can be calculated as

$$J = \frac{(C_1 - C_2)\delta x}{2\delta t} \tag{1.21}$$

As the concentration gradient can be approximated as:

$$\frac{C_1 - C_2}{\delta x} \sim -\frac{\partial C}{\partial x} \tag{1.22}$$

substituting this approximation (equation (1.22)) into the expression for net flux (equation (1.21)) yields:

$$J = -\frac{(\delta x)^2}{2\delta t}\frac{\partial C}{\partial x} \tag{1.23}$$

Comparison between equation (1.23) and Fick's First Law (equation (1.20)) suggests

$$D = \frac{(\delta x)^2}{2\delta t} \tag{1.24}$$

$$\sqrt{< x^2 >} = \sqrt{2Dt} \tag{1.25}$$

Rearrangement of equation (1.24) leads to equation (1.25) which describes the average root mean square distance, in 1D, that a particle can diffuse given its diffusion coefficient D over a time t.

As particles are constantly moving, the concentration of different species at any point is also continually changing. The rate of change of concentration at point *x* is described by Fick's Second Law

(1D)
$$\frac{\partial C}{\partial t} = D\frac{\partial^2 C}{\partial x^2} \tag{1.26}$$

At an electrode surface ($x = 0$), before a potential is applied, no reactions happen and hence no change of concentration occurs. When the potential is applied at $t = 0$, a reduction or oxidation reaction is initiated, causing a gradual depletion of materials near the electrode surface over time. Using the boundary conditions assuming all reactants which reach the electrode are electrolyzed, equation (1.26) can be solved to obtain the Cottrell equation[21] (see Appendix A.2 for derivation):

$$I = \frac{nFA_{WE}\sqrt{D}C^*}{\sqrt{\pi t}} \tag{1.27}$$

C^* represents the bulk solution concentration. The Cottrell equation demonstrates that the oxidation or reduction current generated from a potential step will gradually decay, inversely proportional to the square root of time. This decay is due to the depletion of materials near the electrode, as illustrated by the concentration profile in **Figure 1.9**. The zone of depletion is known as the diffusion layer [21], where reactants must diffuse through to reach the electrode. As time progresses, the depletion continues, leading to a thicker diffusion layer and consequently reducing both the rate of diffusion and the current generated.

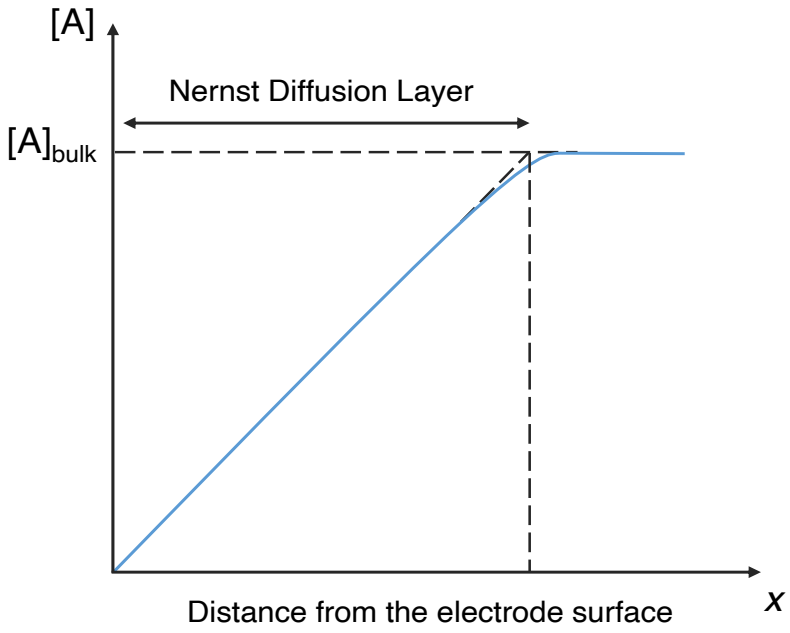

Figure 1.9: Development of concentration gradient and diffusion layer.

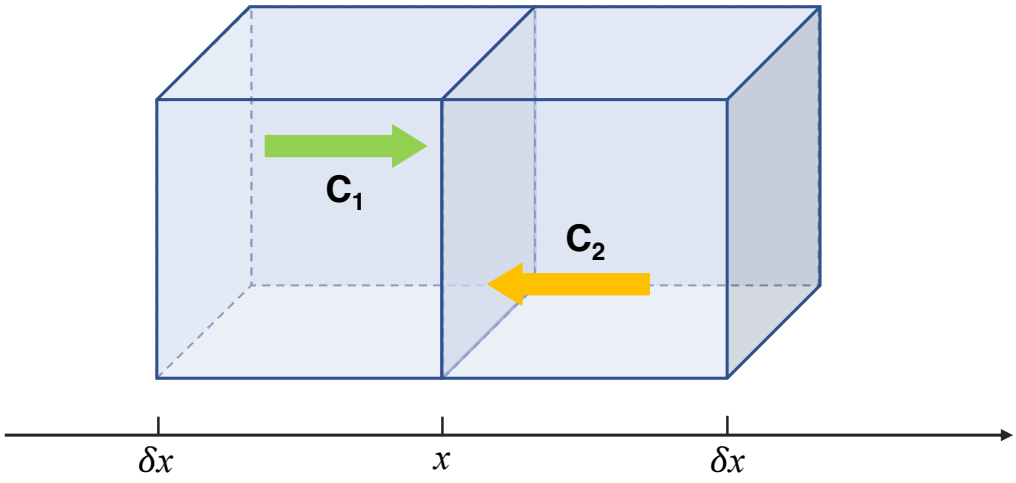

Figure 1.10: The molecular basis of Fick's First Law (1D case).

1.3 Introduction to Mechanics

As discussed in previous sections, understanding the electrochemical processes at interfaces is crucial for comprehending the working principles of neural electrodes. However, in practical applications other than electric signals and ionic flow, adjacent tissues and cells also engage in interactions with electrode surfaces. One of the causes of electrode failure is the immune response induced by mismatches in mechanical properties. Consequently, a thorough understanding of force responses, particularly at the micro and nanoscale, which simulate cellular interactions, is important. This section will begin by explaining fundamental mechanical properties of materials (elasticity, viscosity, and viscoelasticity), and subsequently present methodologies for quantifying these properties using rigorous mathematical models.

1.3.1 Elasticity, Viscosity, and Viscoelasticity

1.3.1.1 Elasticity and Viscosity

To quantify different material deformation upon the application of external forces, stress (σ) and strain (ϵ) are used. Stress is defined as the force acting per unit area (equation (1.28)) [23]. Strain is the ratio of the material displacement due to deformation to its original dimension (equation (1.29)) [23].

Stress $$\sigma = \frac{F}{A} \tag{1.28}$$

Strain $$\epsilon = \frac{\Delta x}{x} \; or \; = \frac{\Delta y}{x} \tag{1.29}$$

For the strain in equation (1.29), $\Delta x \; or \; \Delta y$ depends on the direction of the material displacement (**Figure 1.11**) [23].

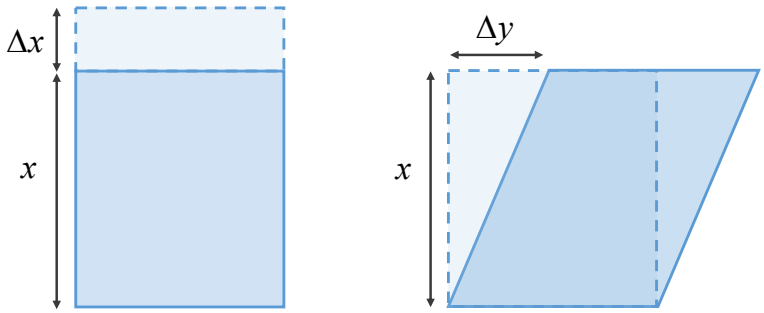

Figure 1.11 Deformation of material.

The relationship between stress and strain varies depending on the material properties. An ideal elastic material responds instantaneously to an applied stimulus and returns to its original shape upon removal of the force, obeying Hooke's law:

$$F = k\Delta x \tag{1.30}$$

where k (unit: N m^{-1}) is the proportionality constant known as the spring constant.

In contrast, an ideal viscous material continues to deform even in the absence of a stimulus. For a Newtonian viscous material, the response to an applied force is described by:

$$F = \eta A\dot{\epsilon} \tag{1.31}$$

where η is the viscosity (unit: Pa s), $\dot{\epsilon} = \frac{v}{x}$ is the velocity gradient (unit: s^{-1}), v represents the horizontal flow velocity, and x represents the vertical direction thickness of the material. Combining the force equations (1.30), (1.31) with stress equation (1.28) obtains:

Elastic
$$\sigma = \frac{F}{A} = \frac{k\Delta x}{A} = \frac{kx}{A}\frac{\Delta x}{x} = E\epsilon \tag{1.32}$$

Viscous
$$\sigma = \frac{F}{A} = \eta\dot{\epsilon} \tag{1.33}$$

where E is defined as Young's modulus or elastic modulus (unit: Pa) of a material when the force acts perpendicularly to the surface. Physically, E and η can be thought of as energy densities in the material. E (unit: Pa = J m^{-3}) can be considered as the potential energy density

that resists the material shape change, while η (unit: Pa s = J m^{-3} s) is the kinetic energy density dissipated by the material per deformation rate.

It should be noted that the above equations (1.30)~(1.33) assume a linear stress/strain relationship (i.e. constant, *k, E,* η over time and throughout the material). These equations can be extended into non-linear forms, which typically occur when a large force causes significant deformation [23, 24]. However, for small deformations, the linear stress/strain relationships are generally valid, and this range of deformation where a response from a material can be described by linear models is referred to as the linear regime of the material [23, 24]. For biomedical applications, interactions with tissues and cells usually fall within this regime, where the interactive forces are small enough to maintain a linear relationship [23]. Therefore, in this thesis, only the linear models will be discussed, and nonlinear models will not be considered.

1.3.1.2 Viscoelasticity

For most materials, they behaviours cannot be strictly classified as purely elastic or viscous. Instead, they exhibit characteristics of both, classifying them as viscoelastic [23, 24]. A viscoelastic material both stores and dissipates energy, responding to external stimuli with a characteristic time delay defined by the ratio of the material's viscosity to its elasticity [23, 24]:

$$\tau = \frac{E}{\eta} \tag{1.34}$$

1.3.1.3 Origin of Viscoelasticity in Polymer

Polymer networks are usually viscoelastic. As with the progression in biomedical research, a wide range of biocompatible polymers have been put into applications. In this thesis, two popular polymers, poly(3,4-ethylenedioxythiophene) (PEDOT) and polydimethylsiloxane (PDMS), have been systematically studied. Therefore, it is worth mentioning here about the origin of viscoelasticity in a polymeric network.

Under steady-state conditions, where no external forces disturb the polymers, the polymer matrices adopt a statistically favored configuration with their coiled and entangled polymer chains [24].

When a mechanical stimulus is applied, the movement of polymers and other constituents (e.g., water, ions if in solution) within the matrices causes the chains to slide past each other, thereby altering their coiling and entanglements [24]. Once the stimulus is removed, the network returns to its original configuration [24]. The movement of the chains require time, and the delay between the application of the stimulus and the point at which the networks stabilize in a new equilibrium state characterize the behavior of viscoelastic materials [23, 24]. As for an ideally elastic material, such delay is zero due to its instantaneous response, whereas the delay is infinite for a viscous one as the material continues to relax.

A polymer can exhibit multiple time responses, attributing to varying conformations, the composition of the polymer, or responses from other materials (e.g. water molecules or different polymers) within the network [23, 24]. Generally, if the polymer chains in the network have strong interactions (e.g. due to crosslinks) with each other, the polymer will be more elastic because these strong interactions impede the sliding motion of the chains. Consequently, such materials demonstrate greater resistance to deformation, as reflected in their high Young's modulus (E) and faster response. Conversely, in networks with weak interactions, polymer chains can slide relative to each other more freely, which facilitates the transfer of kinetic energy to smaller molecules nearby in the polymer matrices (e.g. water and ions), thereby dissipating energy. This weakly interacted network generally leads to a small E value and slow response time.

Experiments typically do not directly measure interactions within polymers. Instead, by measuring energy storage, dissipation, and response time, they infer information about the mechanical properties of the material. Different experimental methods will be introduced in the following sections.

1.3.2 Contact Indentation for Quantifying Elasticity

The contact indentation experiment is one of the methods for quantifying a material's elasticity. Generally, this involves indenting a material with an indenter and recording the force applied and the displacement of the indenter. The indenter may vary in size from macroscopic to microscopic and can have different shapes, such as flat or circular. In this thesis, all mechanical-related experiments were conducted using atomic force microscopy (AFM) equipped with a micrometer-scale circular indenter, which is discussed later in Section 2.

The recorded data will be plotted into a graph of force vs displacement or force vs indentation. Representative force-indentation curves are illustrated in Figure 1.12, where the orange line represents the force curve when the tip is approaching the surface, and the blue line represents the force when the tip is retracting from the surface. These two curves will be referred to as loading (orange line) and retraction (blue line) curves, respectively, in the following sections.

Two well-known models for determining material elasticity are the Hertz and Johnson-Kendall-Robertson (JKR) models. The Hertz model assumes non-adhesive contact (Figure 1.12(a)), while the JKR model is used for adhesive materials (Figure 1.12(b)) [25].

1.3.2.1 Hertz Model

The Hertz model is one of the most fundamental models for understanding an indenter/surface interaction. The Hertz model relates the normal force (F) and the indentation (δ) for a spherical indenter contacting and deforming a flat uniform surface with negligible adhesion [25]:

$$F = gE_{eff}\delta^{\alpha} \tag{1.35}$$

$$\delta = Z_p - Z_{cp} - z_c \tag{1.36}$$

$$\frac{1}{E_{eff}} = \frac{1-v_I^2}{E_t} + \frac{1-v_S^2}{E_s} \tag{1.37}$$

When uses an AFM, the indentation can be calculated using equation (1.36), where Z_p represents piezo displacement, Z_{cp} denotes the contact point position (that is, Z_{cp} is when the tip first touches the sample surface), and z_c denotes cantilever deflection (detail of these factors are discussed in Section 2.3). g and α are factors depend on the geometry of the indenter. For a spherical indenter [25-27], $g = 4\sqrt{R}/3$, $\alpha = 3/2$, where R is the indenter radius. E and v correspond to Young's modulus and Poisson ratio, respectively, with subscripts t and s distinguishing between the indenter (t) and the surface (s) [27]. E_{eff} is the effective Young's modulus obtained from indentation curve fitting using equation (1.37). Normally $E_t \gg E_s$ to ensure that the sample deforms more than the cantilever (the 'indenter' used by AFM, detail is discussed in Section 2.3). With this condition, equation (1.37) can be approximated and the sample's Young's modulus can be calculated as below [27]:

$$E_s = E_{eff}(1-v_s)^2 \tag{1.38}$$

In the case of small indentation depths, and assuming the sample is an incompressible material, the value of v_s can be taken as 0.5 [25].

However, the Hertz model is limited because adhesive forces that could influence contact geometry are not considered by the model. Hence, for adhesive samples, applying the Hertz model without accounting for adhesion could result in an erroneous calculation of E_s.

1.3.2.2 JKR Model

The JKR model is an alternative to the Hertz model that accounts for adhesive indenter/sample interactions [25].

For JKR model fits, two specific points, P_0 and P_1, are identified on the indenter retraction curve (Figure 1.12 (b)): P_1 is where the force $F_0 = 0$, and P_1 is where the indentation δ_1=0 [28]. According to the JKR theory [28, 29] :

$$a^3 = \frac{R}{K}\left[F + 3\pi R\omega + \sqrt{6\pi F\omega + (3\pi R\omega)^2}\right] \tag{1.39}$$

$$\delta = \frac{a^2}{R}\left[1 - \frac{2}{3}\left(\frac{a_0}{a}\right)^{\frac{3}{2}}\right] \tag{1.40}$$

$$R = \frac{R_t R_s}{R_t + R_s} \tag{1.41}$$

$$K = \frac{4}{3\pi(k_t + k_s)} \tag{1.42}$$

a is the contact radius, δ is the indentation depth, F is the applied force, and ω is the interfacial energy. k and R represent the spring constant and radius respectively, and the subscript 't' and 's' denote tip and indenting surface.

At P_0, where $F_0 = 0\ N$, $a = a_0$ and $\delta = \delta_0$, so by substituting into equation (1.39) and (1.40):

$$a^3 = a_0^3 = \frac{R}{K}[0 + 3\pi R\omega + 3\pi R\omega] = \frac{6\pi R^2\omega}{K} \tag{1.43}$$

$$\delta = \delta_0 = \frac{a_0^2}{R}\left[1 - \frac{2}{3}\right] = \frac{a_0^2}{3R} \tag{1.44}$$

At P_1, where $F = F_1$, $a = a_1$ and $\delta_1 = 0$, so by substituting into equation (1.40):

$$\delta_2 = 0 = \frac{a_1^2}{R}\left[1 - \frac{2}{3}\left(\frac{a_0}{a_1}\right)^{\frac{3}{2}}\right] \tag{1.45}$$

Rearrange and solve to obtain:

$$a_1^3 = \frac{4}{9}a_0^3 \tag{1.46}$$

Equate equation (1.39) and (1.46) at P_1:

$$a_1^3 = \frac{4}{9}a_0^3 = \frac{R}{K}\left[F_1 + 3\pi R\omega + \sqrt{6\pi F_1\omega + (3\pi R\omega)^2}\right] \tag{1.47}$$

To simplify the above equation, rearrange equation (1.43) to obtain:

$$3\pi R\omega = \frac{a_0^3 K}{2R} \tag{1.48}$$

Substitute equation (1.48) into (1.47) and then rearrange to have:

$$\left(\frac{R}{K}F_1 - \frac{10}{9}a_0^3\right)\left(\frac{R}{K}F_1 + \frac{2}{9}a_0^3\right) = 0 \tag{1.49}$$

Because F_1 is an attractive force where its value is defined to be negative, $F_1 = -|F_1|$. Substitute in $\delta_0 = a_0^3/3R$ and solve equation (1.49):

$$K = \frac{|F_1|}{2}\left(\frac{3}{R\delta_0^3}\right)^{\frac{1}{2}} \tag{1.50}$$

When indenting materials, especially when using AFM, the cantilever is usually selected to have a larger Young's modulus than the material to ensure that surface deformation is more relative to the cantilever bending $E_s \ll E_t$. Therefore, combining equation (1.42) and (1.50), the elastic modulus of the surface E_s can be solved as shown below:

$$E = \frac{3(1-\nu^2)K}{4} \tag{1.51}$$

$$E = \frac{3(1-\nu^2)\,F_1}{8}\sqrt{\frac{3}{R\delta_0^3}} \tag{1.52}$$

Overall, comparing to the Hertz model, which fits a continuous section of the loading curve using equation (1.35), the JKR approach identifies two critical points for analysis on retraction curve (equation (1.52)), avoiding the need for continuous fitting and thereby reducing errors due to sample adhesion. In addition, unlike the Hertz model, the JKR model does not fit the loading curve, thereby reducing fit errors due to irregularities caused by adhesive forces while the sample is indented. Hence it provides a better choice of fitting model when dealing with adhesive surfaces.

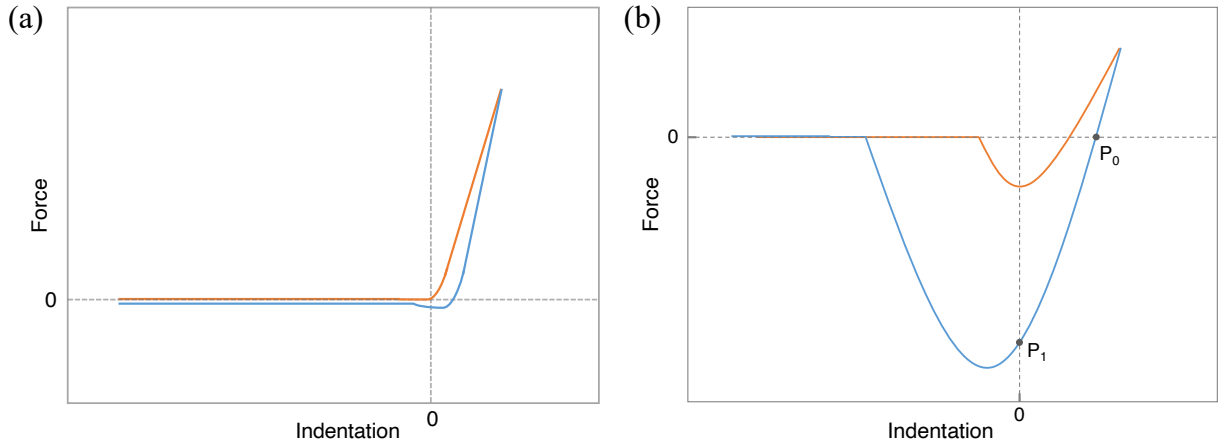

Figure 1.12: Illustrations of a force-indentation curve on **(a)** non-adhesive and **(b)** adhesive surface. P_0 is where force equals zero, and P_1 is where indentation equals 0. The orange line represents the force on the indentor as it approaches the sample surface (loading curve). The blue line represents the force where the indentor retracted from the sample surface (retraction curve).

1.3.3 Relaxation Experiment for Quantifying Viscoelasticity

While the Hertz and JKR models quantify sample elasticity in a contact experiment, a relaxation experiment can be used to quantify sample viscoelasticity. In a relaxation experiment, the indenter dwells in the sample for a specific duration. During this period, the strain (ϵ) is held constant, while changes in stress (σ) are recorded. The mechanical model of viscoelasticity can be represented by connecting elastic (springs) and viscous elements (dampers) (Figure 1.13) [23, 30]. For a purely elastic or viscous material, its stress can be expressed by equations (1.32) and(1.33) as deduced before. However, real materials typically exhibit a combination of both properties. The simplest model of linear viscoelasticity is the Standard Linear Solid (SLS), which can be extended to the general Maxwell Model (GMM) or reduced to the Kelvin-Voigt (KV) or Maxwell model (MW) under different conditions (Figure 1.13) [27].

Despite the variety of combinations possible for the elastic and viscous elements, all configurations can be categorized into two types: parallel and series. For components connected in parallel, the displacement for each segment is identical, while for those in series, the force exerted on each component remains consistent. Hence,

In parallel $$\sigma = \sum_{i=1}^{N} \sigma_i \ , \ \epsilon = \epsilon_i \tag{1.53}$$

In series $$\epsilon = \sum_{i=1}^{N} \epsilon_i \ , \ \sigma = \sigma_i \tag{1.54}$$

Starting from SLS (Figure 1.13(a)), apply equation (1.53) and (1.54) to have:

LHS component: $$\sigma_L = E_c \tag{1.55}$$

RHS component: $$\sigma_R = E_r \epsilon_1 = \eta \dot{\epsilon_2} \tag{1.56}$$

The LHS and RHS components represent the components on two arms in Figure 1.13 (a), respectively, and ϵ_1 and ϵ_2 denote the extension on the spring and damper, respectively, on the right-hand side. Because they are in parallel,

$$\sigma = \sigma_L + \sigma_R \tag{1.57}$$

$$\epsilon = \epsilon_R = \epsilon_L = \epsilon_1 + \epsilon_2 \tag{1.58}$$

Substitute equation (1.55), (1.56), and (1.58) into equation (1.57) and differentiate both side with respect to time *t*:

$$\dot{\sigma} = E_c\dot{\epsilon} + E_r\dot{\epsilon_1} \tag{1.59}$$

$$\dot{\sigma} = E_c\dot{\epsilon} + E_r(\dot{\epsilon} - \dot{\epsilon_2}) \tag{1.60}$$

$$\dot{\sigma} = E_c\dot{\epsilon} + E_r\dot{\epsilon} - E_r\,\frac{\sigma - E_c\epsilon}{\eta} \tag{1.61}$$

Rearrange to obtain:

$$\dot{\sigma}(t) + \frac{E_r}{\eta}\,\sigma(t) = (E_c + E_r)\,\dot{\epsilon}(t) + \frac{E_cE_r}{\eta}\,\epsilon(t) \tag{1.62}$$

For a relaxation experiment, the indenter is held at a constant indentation depth while measuring the response of a force. Hence, equation (1.62) can be simplified and solved by substituting $\epsilon = \epsilon_0, \dot{\epsilon} = 0$:

$$\dot{\sigma}(t) = -(\sigma(t) - E_c\epsilon_0)\frac{E_r}{\eta} \tag{1.63}$$

Integrate both sides and obtain:

$$\sigma(t) = (\sigma_i - E_c\epsilon_0)e^{-\frac{E_r}{\eta}t} + E_c\epsilon_0 \tag{1.64}$$

$(\sigma_i - E_c\epsilon_0)$ produces a constant, so the entire term can be absorbed into just one constant term, denoted as σ_0. In addition, $\tau_r = \eta \backslash E_r$ represents the relaxation time. Equation (1.64) can be rewritten as the following:

SLS
$$\sigma(t) = \sigma_0 e^{-\frac{t}{\tau_r}} + E_c\epsilon_0 \tag{1.65}$$

Consider limiting cases for SLS, $\sigma(t)$ can be deduced for the other models illustrated in Figure 1.13:

$MWM(E_c \to 0)$:
$$\sigma(t) = \sigma_0 e^{-\frac{t}{\tau_r}} \tag{1.66}$$

$\mathrm{KVM}(\mathrm{E_r} \to \infty)$: $$\sigma(t) = E_c \epsilon_0 \tag{1.67}$$

$GMM - N$: $$\sigma(t) = E_c \epsilon_0 + \sum_{i=1}^{N} \sigma_{0i}\, e^{-\frac{t}{\tau_r}} \tag{1.68}$$

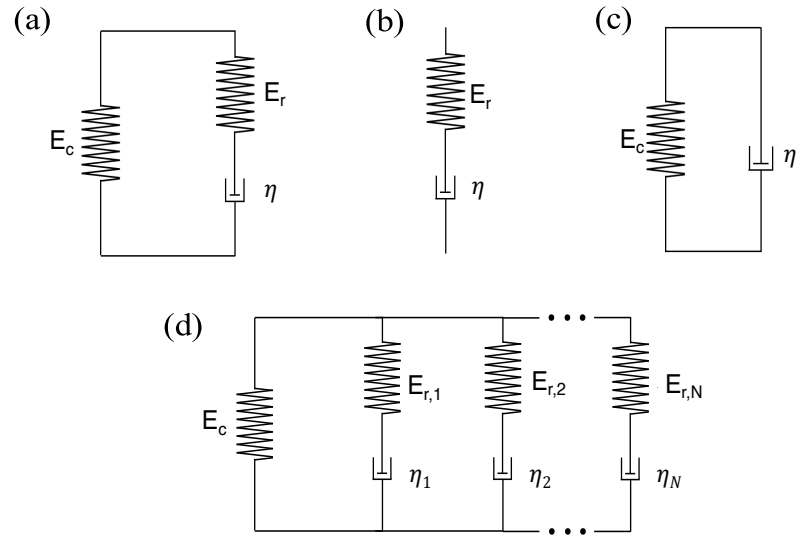

Figure 1.13: Equivalent circuit representation of models of linear viscoelasticity. *E* is the elastic modulus of the spring component. η represents the viscosity coefficient of the damper. **(a)** Standard Linear Solid (SLS). **(b)** Maxwell Model (MWM), limiting case of SLS ($E_c \to 0$). **(c)** Kelvin-Voigt model (KVM), limiting case of SLS ($E_r \to \infty$). **(d)** General Maxwell model (GMM) with a total of N arms (GMM-N)

1.4 Summary

In summary, Chapter 1 has introduced fundamental theories and principles across multiple disciplines. **Section 1.1** outlines the basics of neural electrodes, from the origins of neural spikes and what is recorded at the electrode, to current developments in neural electrode types. As signal propagation and detections constitute a series of electrochemical events, **Section 1.2** focuses and discusses in detail the fundamental principles of electrochemistry, including Faradaic and non-Faradaic processes, equilibrium, electrode kinetics, and mass transport from bulk solution to the surface. However, there is not only ionic interaction at the interface, cells will also physically interact with materials in the surroundings as well. Therefore, **Section 1.3** explores mechanical properties to understand the elastic and viscoelastic nature of polymeric materials, presenting corresponding mathematical models to quantify these properties.

The need for improved biocompatibility of neural electrodes and interface studies arises from previous in vivo experiment reports indicating a reduction in signal over time [15]. Signal reduction could be due to the mechanical mismatch between the hard electrode probe and the soft brain tissue or chemical instability of the electrode material. These factors together often trigger an immune response, which could result in the formation of an encapsulating glial scar that isolates the electrode from the neurons [15], leading to signal loss. The purpose of a thorough introduction in Chapter 1 is to provide a comprehensive understanding that improving neural electrodes is not merely a biomedical challenge but an interdisciplinary one. In this project, I will begin with the characterization of materials, focusing on two popular biocompatible polymers, PDMS and PEDOT, which have been extensively used in biosensor applications. The details of these polymers are discussed and explained in the introductory section of the relevant chapters.

PDMS is selected for its tunable mechanical properties, making it ideal for studying elasticity and response times at the micro- and nanoscale using AFM (Figure 1.14(a)). It will

be observed in both aqueous environments and air to monitor its evolution of interface properties (elasticity, response time) over time.

PEDOT is known for its electrical conductivity and will be thoroughly assessed using AFM and cyclic voltammetry (CV), then applied as a coating on neural electrodes (Figure 1.14(b)). Despite the longstanding use of tetrodes, there has been limited research on tetrode coating due to the challenges on coating small, densely packed microelectrodes without causing polymer overgrowth and cross-connections. Hence, this thesis will detail systematic pre-development procedures for PEDOT on tetrode, including coating and testing methods. Following the development of a modified tetrode, the electrochemical processes at the interface during recordings with and without the polymer will be compared and investigated.

Last, a pilot vivo experiment (Figure 1.14(c)) using the developed polymer-coated tetrodes were conducted to assess their biocompatibility and the signals recorded with coated electrodes.

Overall, this research, viewed holistically, contributes to a better understanding of material and method development, providing a solid foundation that addresses gaps in previous studies and offers insights for future research.

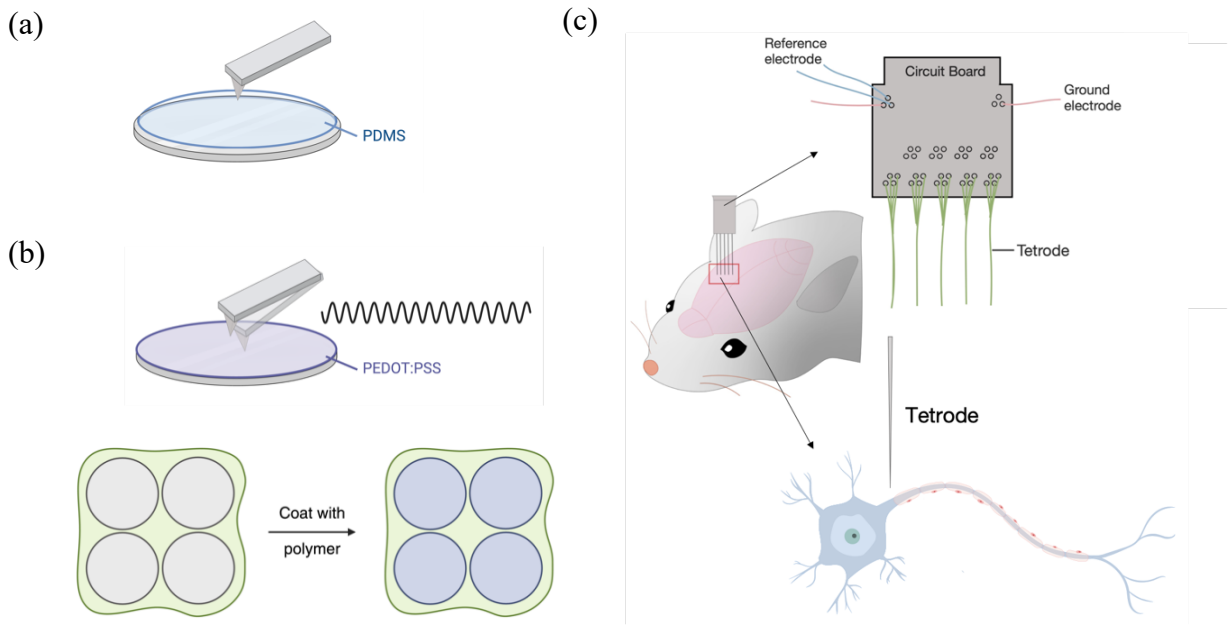

Figure 1.14: (a) AFM indentation on a PDMS sample. **(b)** AFM tapping mode to image PEDOT polymer surface. After characterization, the PEDOT coating will be applied onto a tetrode. **(c)** Illustrative scheme of in vivo recording.

References

(1) Dupret, D.; O'Neill, J.; Pleydell-Bouverie, B.; Csicsvari, J. The reorganization and reactivation of hippocampal maps predict spatial memory performance. *Nat Neurosci* **2010**, *13* (8), 995-1002.

(2) Eliades, S. J.; Wang, X. Chronic multi-electrode neural recording in free-roaming monkeys. *Journal of Neuroscience Methods* **2008**, *172* (2), 201-214.

(3) Chari, A.; Thornton, R. C.; Tisdall, M. M.; Scott, R. C. Microelectrode recordings in human epilepsy: a case for clinical translation. *Brain Commun* **2020**, *2* (2), fcaa082.

(4) Mcintyre, C. C.; Thakor, N. V. Uncovering the mechanisms of deep brain stimulation for Parkinson's disease through functional imaging, neural recording, and neural modeling. *Critical Reviews™ in Biomedical Engineering* **2002**, *30* (4-6).

(5) Chang, C. H.; Lane, H. Y.; Lin, C. H. Brain Stimulation in Alzheimer's Disease. *Front Psychiatry* **2018**, *9*, 201.

(6) Kandel, E. R.; Schwartz, J. H.; Jessell, T. M.; Siegelbaum, S. A.; Hudspeth, A. *Principles of neural science*; McGraw-Hill, 2013.

(7) Alberts, B. *Molecular biology of the cell*; Garland Science, 2002.

(8) Ashcroft, F. M. *Ion Channels and Disease*; Academic Press, 2000.

(9) Phillips, R. *Physical biology of the cell*; Garland Science, 2013.

(10) Hodgkin, A. L.; Huxley, A. F. Action Potentials Recorded from Inside a Nerve Fibre. *Nature* **1939**, *144* (3651), 710-711.

(11) Israel, Z.; Burchiel, K. *Microelectrode recording in movement disorder surgery*; Thieme, 2004.

(12) Gur, M.; Beylin, A.; Snodderly, D. M. Physiological properties of macaque V1 neurons are correlated with extracellular spike amplitude, duration, and polarity. *J Neurophysiol* **1999**, *82* (3), 1451-1464.

(13) Henze, D. A.; Borhegyi, Z.; Csicsvari, J.; Mamiya, A.; Harris, K. D.; Buzsáki, G. Intracellular features predicted by extracellular recordings in the hippocampus in vivo. *J Neurophysiol* **2000**, *84* (1), 390-400.

(14) Rutkove, S. B. Introduction to Volume Conduction. In *The Clinical Neurophysiology Primer*, Blum, A. S., Rutkove, S. B. Eds.; Humana Press, 2007; pp 43-53.

(15) Hong, G.; Lieber, C. M. Novel electrode technologies for neural recordings. *Nature Reviews Neuroscience* **2019**, *20* (6), 330-345.

(16) Yuste, R. From the neuron doctrine to neural networks. *Nature Reviews Neuroscience* **2015**, *16* (8), 487-497.

(17) Harris, K. D.; Quiroga, R. Q.; Freeman, J.; Smith, S. L. Improving data quality in neuronal population recordings. *Nature Neuroscience* **2016**, *19* (9), 1165-1174. DOI: 10.1038/nn.4365.
(18) Boehler, C.; Carli, S.; Fadiga, L.; Stieglitz, T.; Asplund, M. Tutorial: guidelines for standardized performance tests for electrodes intended for neural interfaces and bioelectronics. *Nat Protoc* **2020**, *15* (11).
(19) Ashcroft, F. M.; ScienceDirect. *Ion channels and disease : channelopathies*; Academic Press, 1999.
(20) Pieprzycki, A.; Krol, D. General Concept of the EMG Controlled Bionic Hand. *Science Technology and Innovation* **2020**, *8*, 26-34.
(21) Compton, R. G.; Banks, C. E. *Understanding voltammetry, 3rd Edition*; World Scientific, 2018.
(22) Bard, A. J.; Faulkner, L. R. *Electrochemical methods : fundamentals and applications*; John Wiley & Sons, 2001.
(23) Doi, M. *Soft matter physics*; Oxford University Press, 2013.
(24) Popov, V. L.; He√ü, M.; Willert, E. *Handbook of Contact Mechanics: Exact Solutions of Axisymmetric Contact Problems*; Springer Berlin Heidelberg, 2019.
(25) Butt, H.-J.; Cappella, B.; Kappl, M. Force measurements with the atomic force microscope: Technique, interpretation and applications. *Surface Science Reports* **2005**, *59* (1), 1-152.
(26) Efremov, Y. M.; Okajima, T.; Raman, A. Measuring viscoelasticity of soft biological samples using atomic force microscopy. *Soft Matter* **2020**, *16* (1), 64-81, 10.1039/C9SM01020C.
(27) Popov, V. L.; Heß, M.; Willert, E. *Handbook of contact mechanics: exact solutions of axisymmetric contact problems*; Springer Nature, 2019.
(28) Sun, Y.; Akhremitchev, B.; Walker, G. C. Using the Adhesive Interaction between Atomic Force Microscopy Tips and Polymer Surfaces to Measure the Elastic Modulus of Compliant Samples. *Langmuir* **2004**, *20* (14), 5837-5845.
(29) Johnson, K. L.; Kendall, K.; Roberts, A. D.; Tabor, D. Surface energy and the contact of elastic solids. *Proceedings of the Royal Society of London. A. Mathematical and Physical Sciences* **1971**, *324* (1558), 301-313.
(30) Ferry, J. D. *Viscoelastic properties of polymers*; Wiley, 1980.

Chapter 2

Materials and Experimental Methods

This chapter will introduce the main materials and techniques applied in this thesis for polymer characterization and electrode interface studies. The electrochemical methods are detailed and Section 2.2, and methods related to AFM are introduced in Section 2.3. Specific descriptions of each experiment are included in the 'Materials and Methods' section of each later chapters (Chapter 3~7).

2.1 Chemicals and Reagents

This thesis focuses on investigating two popular biocompatible polymers: poly(3,4-ethylenedioxythiophene) (PEDOT) and polydimethylsiloxane (PDMS). Chemical reagents are listed below in Table 2.1. Deionized water with a resistivity of 18.2 MΩ·cm at 298 K (Millipore, Millipak Express 20, Watford, UK) was utilized for preparing all solutions.

Table 2.1 : Lists of chemicals used in the thesis.

Chemical	Formula	Note	Supplier
3,4-Ethylenedioxythiophene	EDOT	Purity = 97%	Sigma-Aldrich
poly(sodium 4-styrenesulfonate)	NaPSS	Mw = 70,000	Sigma-Aldrich
phosphate-buffered saline	PBS	/	Sigma-Aldrich
hexaammineruthenium(III) chloride	$Ru(NH_3)_6Cl_3$	Purity = 98%	Sigma-Aldrich
Potassium chloride	KCl	Purity = 99%	ThermoFisher Scientific
sodium chloride	NaCl	Purity > 99.5%	Scientific Laboratory Supplies
polydimethylsiloxane (curing agents and base)	PDMS	/	Sylgard® 184 Dow-Corning Corporation

2.2 Electrochemical Methods

This section introduces the different electrochemical methods required to interpret and analyze the various processes mentioned in Section 1.2. It begins with the basic electrochemical cell setup and progresses to cyclic voltammetry (CV), chronoamperometry and bipotentiostat. These setups and techniques were employed throughout the project and are essential for understanding the experimental results and subsequent analysis.

2.2.1 Electrochemical Cell

During electrochemical studies, a three-electrode setup is commonly used, which comprises a working electrode (WE), a reference electrode (RE), and a counter electrode (CE). These electrodes are connected to, and controlled by a potentiostat, as shown in Figure 2.1. The WE is the primary electrode of interest and is the site where the main redox reactions under study occur. The RE provides a stable potential against which the potential difference with the WE is measured. The working principle of the RE is introduced in Section 2.2.1.1. Since the potential at the RE is fixed, any changes can be attributed to reactions occurring at the WE. The CE facilitates the passage of current and completes the circuit (Figure 2.1). Moreover, the presence of the CE prevents current from flowing to the RE, which could alter the predefined potential through chemical changes or cause a potential drop between the RE and WE due to the electrical resistance of the bulk solution (R_{bulk}, equation (2.4) and Figure 2.2(b)). Therefore, with the inclusion of the CE, a constant potential at the RE is maintained allowing controlled changes in potential to be applied to the WE.

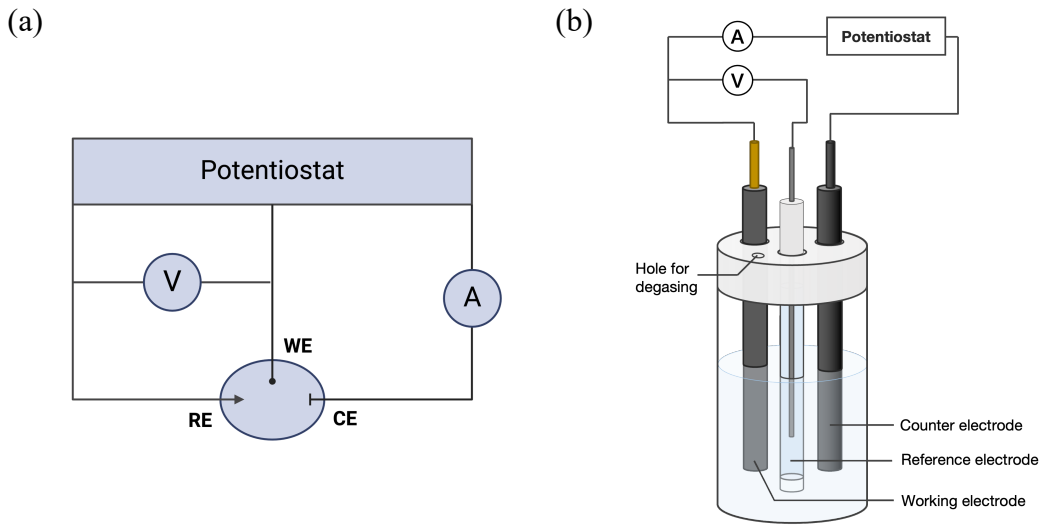

Figure 2.1: (a) Schematic circuit of a three-electrode electrochemical cell. **(b)** Illustration of a commonly used three-electrode electrochemical cell setup and its connections to the circuit.

2.2.1.1 Reference Electrodes

In this thesis, the main reference electrode utilized was the Saturated Calomel Electrode (SCE). An SCE electrode, as shown in Figure 2.2(a), consists of a column of liquid mercury (Hg) with insoluble di-mercury (I) (Hg_2Cl_2, known as 'calomel') at the bottom of the column [1]. Both Hg and Hg_2Cl_2 are in contact with a saturated potassium chloride solution (KCl), establishing a dynamic equilibrium:

$$\frac{1}{2}Hg_2Cl_2(s) + e^-(m) \rightleftharpoons Hg(l) + Cl^-(aq) \tag{2.1}$$

As a consequence of the equilibrium, the rate of electron release and uptake by the electrode are balanced, resulting in no net electron flow. While there is no net flow of electrons at equilibrium, the movement of charges leading to the formation of equilibrium will make one phase to have a relatively more positive potential and the other phase to be more negative, reflecting charge separation across the interface [1]. This charge separation is the origin of a

potential difference between the metal and the solution, also known as the electrode potential. The electrode potential remains stable at equilibrium because, despite the dynamic transfer of charges, the overall charge distribution across the interface does not change.

For an SCE, this constant potential difference between the metal and the solution is maintained by the dynamic equilibrium of the reaction shown in equation (2.1), where this electrode potential can be calculated using the Nernst equation[1] (Detailed derivations are included in Appendix A.1):

$$E = \phi_M - \phi_S = \frac{\Delta\mu^0}{F} - \frac{RT}{F} ln[Cl^-] \tag{2.2}$$

$$\Delta\mu^0 = \frac{1}{2}\mu^0_{Hg_2Cl_2} + \mu_{e^-} - \mu^0_{Hg} - \mu^0_{Cl^-} \tag{2.3}$$

$\phi_M - \phi_S$ represents the electrical potential difference between the metal (*M*) and the solution (*S*), $\Delta\mu^0$ is the standard electrochemical potential difference from the reaction, *F* is the Faraday constant, *R* is the universal gas constant, *T* is the temperature (unit: K), and [Cl^-] is the chloride ion concentration. [Cl^-] remains constant as fixed by the solubility of KCl, thereby keeping the potential difference $\phi_M - \phi_S$ constant. Hence, the stable and predictable potential of SCE makes it a useful reference electrode in electrochemical measurements. A schematic of measuring electrode potential against a RE is shown in Figure 2.2(b) [1]. The measured potential difference ($V_{measured}$) can be calculated as the following:

$$V_{measured} = (\phi_M - \phi_S)_{Pt\ Wire} + IR_{bulk} - (\phi_M - \phi_S)_{SCE} \tag{2.4}$$

It should be noted that a porous frit at the bottom of an SCE (Figure 2.2(a)) is necessary to allow conduction between the internal KCl and the external solution, completing the electrical circuit between the WE and the RE in Figure 2.2(b). When a voltmeter is used to measure the potential difference (Figure 2.2(b)), a small current (*I*) needs to be applied, and the bulk solution can be considered as a resistor with resistance R_{bulk}, leading to a potential drop during

conduction in the solution with a value of IR_{bulk}. However, because the current is very small and is usually negligible, the measured potential difference can be approximated to:

$$V_{measured} = (\phi_M - \phi_S)_{Pt\ Wire} - (\phi_M - \phi_S)_{SCE} \quad (2.5)$$

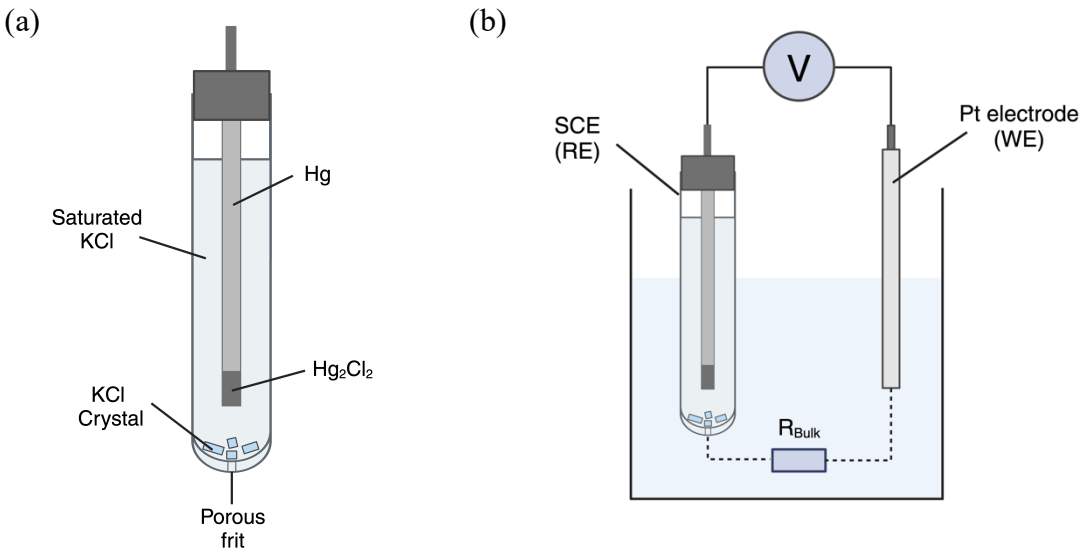

Figure 2.2: (a) Illustration of a Saturated Calomel Electrode (SCE) [1]. (b) Example of how a potential difference is measured between a WE and RE.

2.2.2 Cyclic Voltammetry

Cyclic voltammetry (CV) is a commonly used and powerful tool in electrochemical analysis, employed to characterize the analyte of interest at the chosen working electrode. The working principle, as shown in Figure 2.3, involves applying a triangular potential to the WE [1]. The process starts at an initial potential, E_1, and sweeps linearly to a maximum potential E_2, at a constant scan rate v (unit: Vs^{-1}) [1]:

$$v = \frac{\partial E}{\partial t} = gradient. \tag{2.6}$$

The current flowing through the WE is recorded and plotted against the applied potential, resulting in a graph known as a voltammogram. Typically, E_1 is chosen such that no redox reaction occurs and, hence, negligible current flows at the start. E_2 is the point at which the scan direction is reversed, and its value is chosen so that the potential interval from E_2 to E_1 encompasses the oxidation or reduction reaction of the analyte under investigation.

As the potential is swept, Faradaic and non-Faradaic processes occur, resulting in the current passed at the WE. Consequently, the observed voltammogram can be influenced by (1) the rates of electron transfer at the WE and (2) mass transport.

For factor (1), the electron transfer rate, as introduced in Section 1.2.2.2, is related to the standard electrochemical rate constant (k^0) and the formal potential of the redox couple. For factor (2), mass transport, as discussed in Section 1.2.3, mainly corresponds to the diffusional movement of the reaction species in the bulk solution to and from the electrode surface. Therefore, it can be significantly affected by the diffusion coefficient (D), the voltage scan rate (v), and the shape and size of the WE.

In this thesis, both macro and microdisk electrodes have been utilized, each displaying distinct diffusion patterns as illustrated in Figure 2.4. For macroelectrodes (size on the scale of mm or cm), a linear diffusion pattern is present. Due to their much larger disk size compared to

the thickness of the diffusion layer ($r_e >> d$), a planar diffusion layer forms (Figure 2.4(a)). The rapid depletion of reactants, faster than their replenishment by diffusion, results in the characteristic peak shape of the cyclic voltammogram (Figure 2.5). In contrast, microelectrodes (size on the scale of μm) exhibit convergent diffusion due to their smaller size relative to the diffusion layer ($r_e << d$). Over time, the shape of the diffusion layer approaches a hemispherical form (Figure 2.4(b)), and this three-dimensional diffusion is much more efficient than the one-dimensional flux at a macroelectrode. Consequently, if the scan rate is sufficiently slow, electron transfer and mass transport can achieve a steady-state current with two flat tails at the ends (Figure 2.6), unlike the peak shape observed with macroelectrodes (Figure 2.5).

The voltammograms for macro and micro electrodes will be discussed separately and in more detail in the following sections.

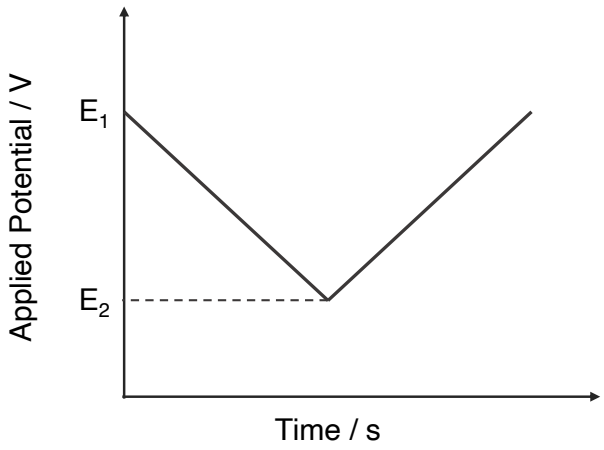

Figure 2.3: The potential-time graph of a cyclic voltammogram for a reduction

.

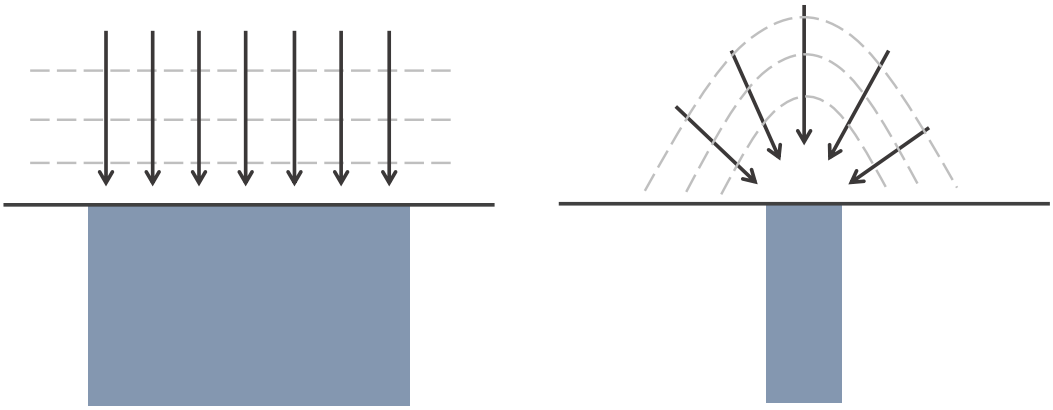

Figure 2.4: Diffusion pattern at **(a)** macrodisk electrode and **(b)** microdisk electrode. Arrows: indicate the direction of diffusion of species. Dashed lines: represent the diffusion layers.

2.2.2.1 Cyclic Voltammetry at Macroelectrodes

In general, the shape of a CV scan is interpreted through consideration of the competition between the rate of electron transfer and that of mass transport. For a macroelectrode, an example of a CV scan is presented in Figure 2.5(a), and the concentration profiles at different times during the scan are shown in Figure 2.5(b-i). The scan initiates at E_1, chosen where no Faradaic reactions occur, resulting in no initial current and no change in the concentration of reactant $[A^z]$ near the electrode. As the potential sweeps towards the reduction potential, a reduction reaction is initiated. Current is generated, and $[A^z]$ is gradually consumed (Figure 2.5(c~d)). As the scan proceeds, the current then reaches a peak when the electron transfer rate equals the mass transport rate (Figure 2.5(e)). However, as the potential continues, the current begins to decrease because the diffusion of the reactant from the distant bulk solution cannot keep up with its consumption at the surface (Figure 2.5(f)). When the scan is reversed, due to the previous formation of enough $[B^{z-1}]$ at the vicinity of the electrode, oxidation reactions can

happen when the potential is at an appropriate value (Figure 2.5(g)). The current then peaks (Figure 2.5(h)) and subsequently drops (Figure 2.5(i)) for the same reasons as in the reduction scan, due to the competition between electron transfer and diffusion rates.

In an electrochemically reversible system concentrations near the electrode surface are predicted by the Nernst Equation. Conversely, in an electrochemically irreversible system, the rate of electron transfer is smaller than the rate of mass transport, giving a current following the Bulter-Volmer equation (equation (1.16)), which is related to the reaction rate (k) and concentration of the reactant (e.g. $[A^z]$).

For a one-electron transfer process at a macroelectrode, the reversibility of the reaction can be quantified by analyzing several factors in voltammograms (Detailed explanation of irreversibility due to mass transport and electrode kinetics is included in the Appendix A.3):

(1) Peak-to-peak separation (ΔE_{pp})

Peak-to-peak separation (ΔE_{pp}) is the difference between the cathodic and anodic peak potentials. For an irreversible reaction, ΔE_{pp} depends on the scan rate and enlarges as the scan rate increases. The more irreversible the reaction, the greater the ΔE_{pp}. In contrast, for a reversible system, ΔE_{pp} remains a value of ca. 57mV at 298K, and it is independent of the scan rate.

(2) Mid-point potential (E_{mid})

The mid-point potential (E_{mid}) is defined as the average of the forward and backward peaks and can be expressed as follows:

(Reversible) $$E_{mid} = E_f^0 + \frac{RT}{2F} ln \frac{D_B}{D_A} \quad (2.7)$$

(Irreversible) $$E_{mid} = E_f^0 + \frac{RT}{F} ln \frac{D_B}{D_A} \quad (2.8)$$

For an irreversible reaction, equation (2.8) assumes $\alpha = \beta = 1/2$. D_A and D_B are the diffusion coefficients of species A and B, respectively. $E_{mid} = E_f^0$ if the diffusion coefficients are equal, regardless of the reversibility of the processes.

(3) Peak current (I_p)

Peak currents (I_p) are described by the Randles-Sevcik equations. For a one electron transfer, diffusionally controlled reduction process at a macroelectrode, I_p for reversible and irreversible reactions is expressed as:

(Reversible) $$I_p = -0.446FA_{WE}[A]_{bulk}\sqrt{\frac{F\upsilon D}{RT}} \quad (2.9)$$

(Irreversible) $$I_p = -0.496\sqrt{\alpha}FA_{WE}[A]_{bulk}\sqrt{\frac{F\upsilon D}{RT}} \quad (2.10)$$

Note that if specific adsorption of the reactant and product occurs on the electrode surface during the reaction, the peak current will be directly proportional to the scan rate υ instead of $\upsilon^{1/2}$ as shown above (equations (2.9)(2.10)).

(a)

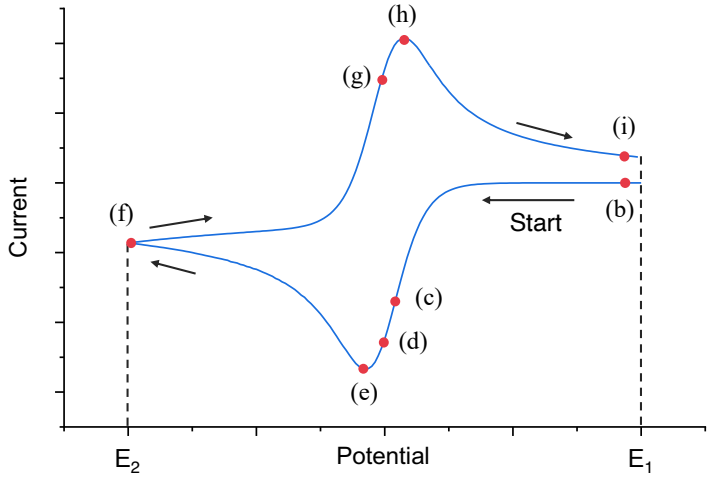
(h)
(g)
(i)
(f)
(b)
Start
(c)
(d)
(e)
Current
E2
Potential
E1

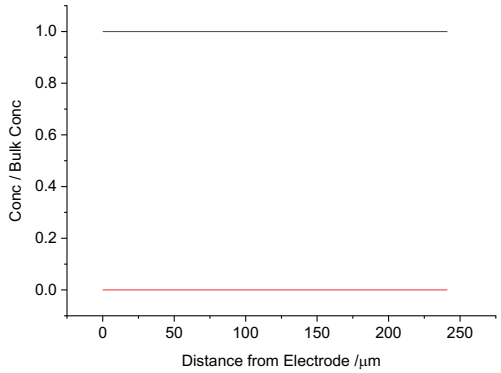
Conc / Bulk Conc
Distance from Electrode /μm

(b)

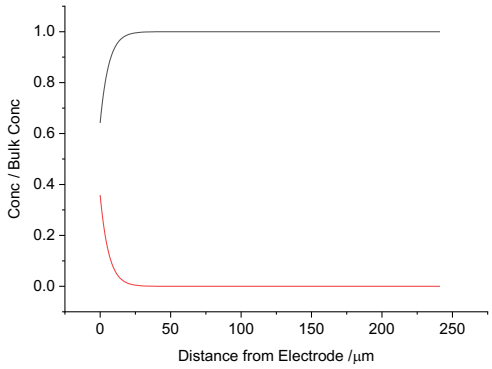
Conc / Bulk Conc
Distance from Electrode /μm

(c)

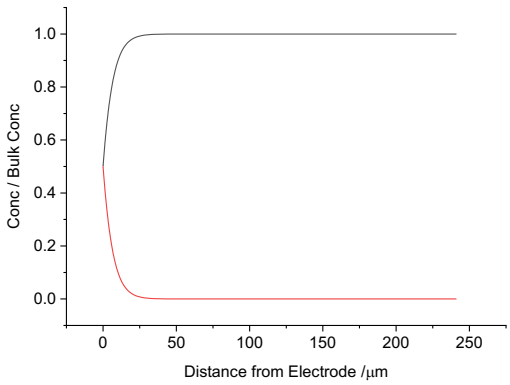
Conc / Bulk Conc
Distance from Electrode /μm

(d)

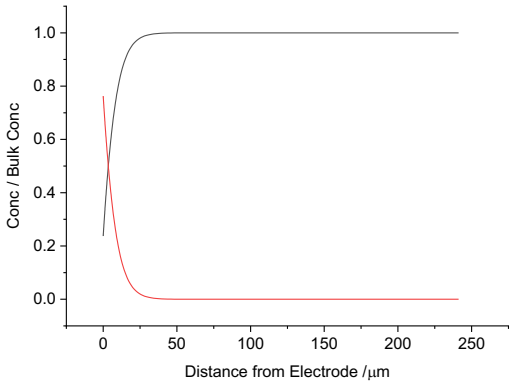
Conc / Bulk Conc
Distance from Electrode /μm

(e)

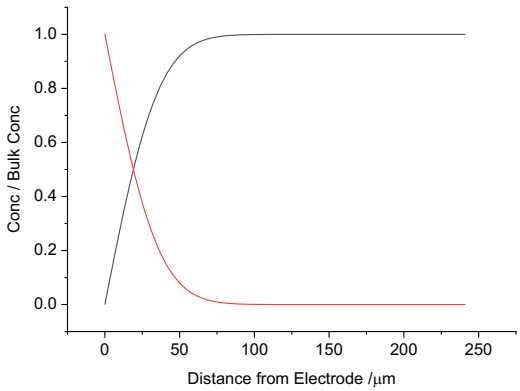
Conc / Bulk Conc
Distance from Electrode /μm

(f)

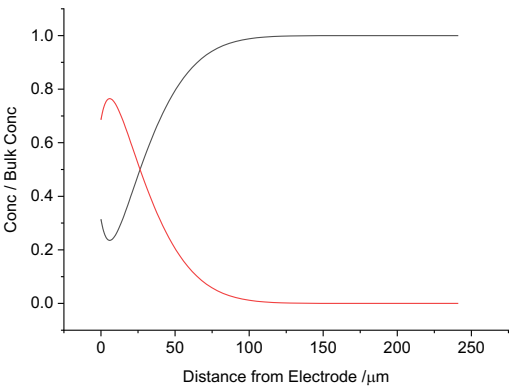
Conc / Bulk Conc
Distance from Electrode /μm

(g)

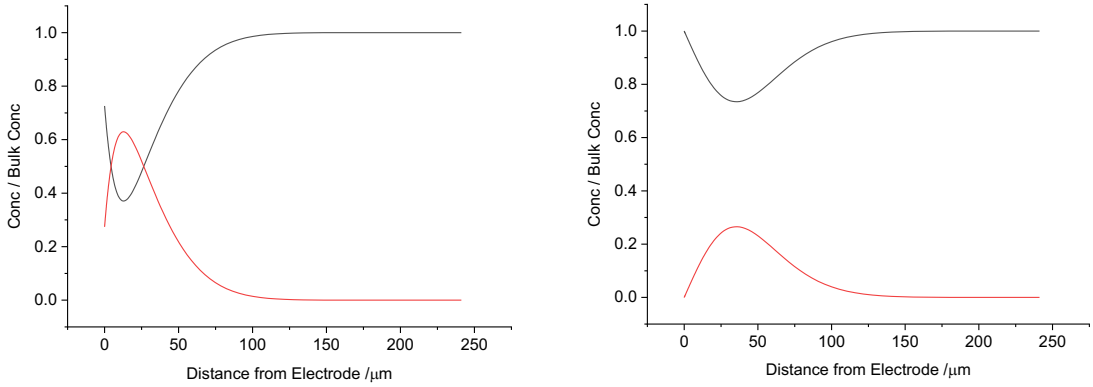

(h) (i)

Figure 2.5: (a) Voltammogram of a macroelectrode. Redox reactions ($A^z + e^- \rightleftharpoons B^{z-1}$) happen as the potential sweeps from E_1 to E_2 and reverses back to E_1. **(b~i)** The concentration profile of different positions of the CV scan. The red lines represent the concentration profile of $[A]/[A]_{bulk}$, and the black lines represent the concentration profile of $[B]/[B]_{bulk}$. Graphs are generated using *FreeSim*[2].

2.2.2.2 Cyclic Voltammetry at Microelectrodes

At a microelectrode, the observed voltammetry also reflects competition between the reaction and the diffusive supply of reactant. However, if the scan rate is slow, a steady-state current instead of a peak is observed. As shown in Figure 2.6, the peak diminishes as the scan rate decreases. The disappearance of the peak suggests a steady-state between the electron transfer rate and the mass transport rate. This phenomenon occurs because convergent diffusion at a microelectrode is more efficient than planar diffusion at a macroelectrode, allowing enough reactants to reach the electrode surface to sustain a reaction.

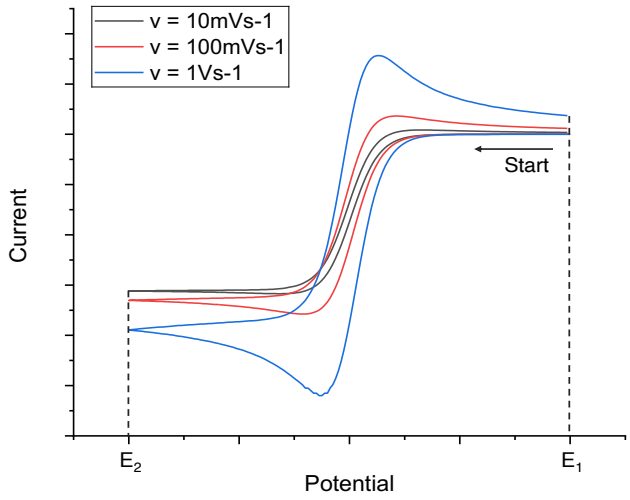

Figure 2.6: Voltammogram of a microelectrode comparing different scan rates. Graphs are generated using *FreeSim*[2].

2.2.3 Chronoamperometry

Chronoamperometry is another powerful technique for electrochemical experiments. This method involves applying a potential step to a working electrode, starting from a potential where no reactions occur, then shifting to a potential that can trigger a redox reaction of interest. Concurrently, the current is recorded as the potential is applied.

In this thesis, chronoamperometry is applied to macroelectrodes. The current response (due to redox reactions), triggered by the potential step, can be described by the Cottrell equation (equation (1.27)), which decays in inverse proportion to the square root of time. This decay is due to the insufficient diffusion of reactants to the electrode surface to sustain the reaction.

2.2.4 Biopotentiostat

In addition to the normal potentiostat (**Figure 2.1**), I applied a biopotentiostat consisting of two working electrodes to study the signal recording process. The two working electrodes on biopotentiostat can be separately controlled and simultaneously monitored. Hence, one working electrode (WE1) was applied with a potential step to mimic a local potential disturbance during neural activities, and the other working electrode (WE2) served as the recording electrode to monitor current changes. In this thesis, two wires of one tetrode were used as WE1 and WE2 (**Figure 2.7**).

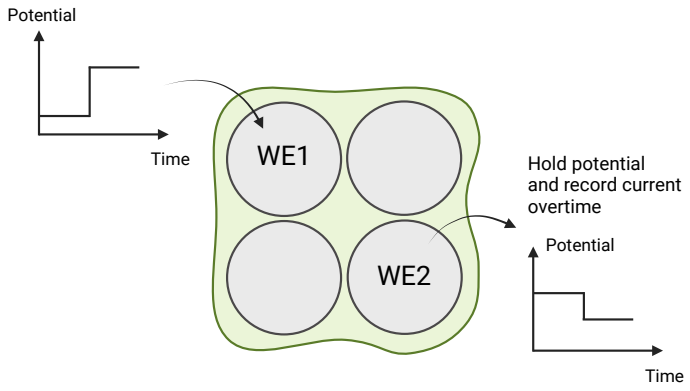

Figure 2.7: Bipotentiostat setup using a tetrode. One wire (WE1) on the tetrode functions as a signal generator, and the other one (WE2) functions as a signal recorder.

2.2.5 Electrochemical Instrumentation

Electrochemical experiments for polymer characterization and deposition were carried out using a μ-AutolabIII potentiostat/galvanostat (Autolab B.V., Utrecht, The Netherlands) controlled by NOVA software. Bipotentiostat experiments were conducted employing an Autolab PGSTAT30 (Autolab B.V., Utrecht, The Netherlands).

Table 2.2 lists the details of all the electrodes used in this thesis. Throughout experiments, the electrochemical cell was placed within a thermostated Faraday cage. The cell solution was maintained at 25 ± 1 °C and degassed with nitrogen before each electrochemical experiment.

Table 2.2: List of electrodes used in the thesis. Pt: Platinum; W: Tungsten; SCE: saturated calomel electrode; SHE: standard hydrogen electrode; d: diameter; A: area.

Type of electrodes	Electrode	Parameters	Supplier
Working electrode	Pt macrodisk	d = 1.66 mm	BASi, USA
	Pt single crystal	A ≈ 0.22 cm	/
	Pt insulated microwire	d = 25 or 15 μm	GoodFellow, UK
	W insulated microwire	d = 12.7 μm	California Fine Wire Company, USA
Reference electrode	SCE	+ 0.244 V vs. SHE	BASi, USA
Counter electrode	Graphite rod	/	/

2.2.6 Preparation of Insulated Microwire

All microwires used in the thesis were coated with insulation, exposing the conductive site only at the ends. Hence, they can be considered as microdisk electrodes. To make a connection with the Autolab, the insulation on one end of the microwire was gently removed by using a new, sharp scalpel. After the insulation layer was peeled off, the shiny metal underneath could be directly observed with the naked eye. The exposure of the metal was further confirmed by microscope.

The exposed end of the metal wire was then connected to a thicker and longer stainless-steel wire using silver epoxy (RS Components Ltd, UK), as depicted in **Figure 2.8** B and C. The connected wire was inserted through and fixed to a pipette head, where the pipette head was used to stabilize the wire and protect the wire body from bending and scratching during the experiments. The end of the stainless-steel wire (Figure 2.8 C) could then be easily connected to the electrochemical apparatus by using crocodile clips. The end of the microwire (**Figure 2.8** A) was cut with fine scissors (14568-12, German Stainless) to ensure a clean surface before each experiment.

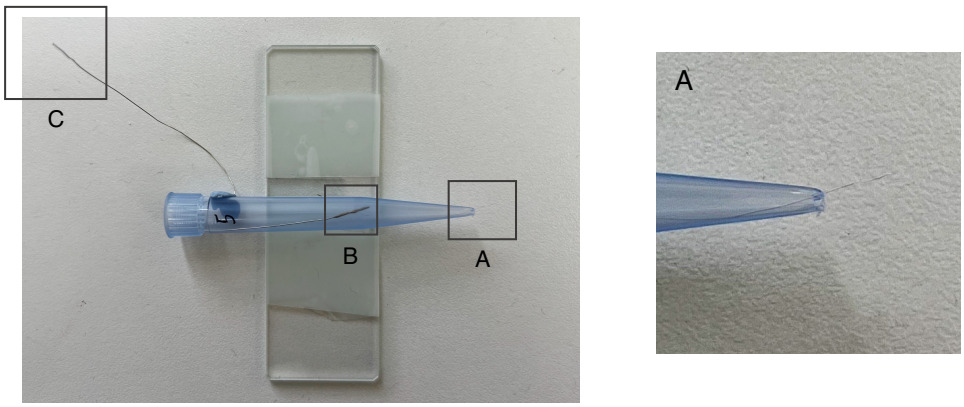

Figure 2.8: Setup for a microwire connection. **Box A:** Microwire end to be immersed into the solution (Zoom in is shown on the right). **Box B:** The connection between the stainless-steel wire and the microwire using silver epoxy. **Box C:** Stainless steel wire that can be clamped onto with a crocodile clip and connected to the electrochemical apparatus.

2.2.7 Fabrication and Preparation of a Tetrode

2.2.7.1 Tetrode Fabrication

The tetrode fabrication process is presented in **Figure 2.9**(a~c). A microwire of 20 to 30 cm in length was cut based on its intended use and the apparatus to which it was to be connected. The tape was used to fix both ends of the microwire together (**Figure 2.9**(a)), with one end (**Figure 2.9**(a), S) affixed to a rod attached to a clamp stand. The opposite free end (**Figure 2.9** (a), F) was positioned as shown in **Figure 2.9**(b). A small magnetic weight, with a hook at the top, was hung at the bottom of the wire in order to stretch four wire segments straight (**Figure 2.9**(b)). A magnetic stirrer plate was positioned beneath the weight to rotate the magnetic weight and twist the wires together at a consistent rate (**Figure 2.9** (c)). Before turning on the stirrer, it was ensured that the weight was centered on the stirrer plate to avoid wobbling and possible wire breakage. The twisting was stopped once sufficient tetrode length was achieved, leaving about 2 cm of untwisted wire near the rod. The stirrer plate was then carefully removed, allowing the wire to unwind slightly to alleviate stress, and the stirrer plate was replaced to stabilize the wire and the weight. Without this step, the wire might recoil when the weight is removed, leading to an undesired tetrode shape. A heat gun set to the appropriate temperature was used to melt the wire outer insulation slightly, causing the strands to fuse. For a W microwire insulated with HFV (Heavy Formvar, glass transition temperature at ca. 105˚C [3]), the heat gun was set to 200˚C, while for a Pt microwire insulated with polyimide, which has a higher glass transition temperature (ca. 220˚C [3]), the heat gun was at a temperature of ca. 300˚C. Note that the rod material should be heat-resistant, for example wood or glass, to prevent insulation material from melting onto the rod during the heat-curing process. After cooling the tetrode for a few minutes, sharp scissors were used to cut the end attached to the weight, followed by the top two ends.

2.2.7.2 Tetrode Preparation for Electrochemical Experiments

To connect a tetrode to the electrochemical apparatus, the insulation on the four tetrode free ends was removed using a scalpel. Similar to the single microwire attachment described in Section 2.2.6, all four wires of the tetrode were attached to four stainless steel wires (Figure 2.9 (d) C) respectively using silver epoxy. Pipette heads again were used to hold the stainless-steel wires, protect the connection, and stabilize the microwires. However, before making the connections, four pipette heads were first fixed together by placing a piece of Blu Tack (a moldable, clay-like, and pressure-sensitive adhesive produced by Bostik) to hold them together (**Figure 2.9**(d) B), after which stainless steel wires were inserted and connections made with the free ends of a tetrode. This arrangement of securing the four pipette heads prevents them from moving against each other during operation, which could potentially stretch the microwires and damage the tetrode. The final assembly is shown in **Figure 2.9**(d), and the tetrode head detail is illustrated in box A. The setup was allowed to dry overnight before connection testing or use.

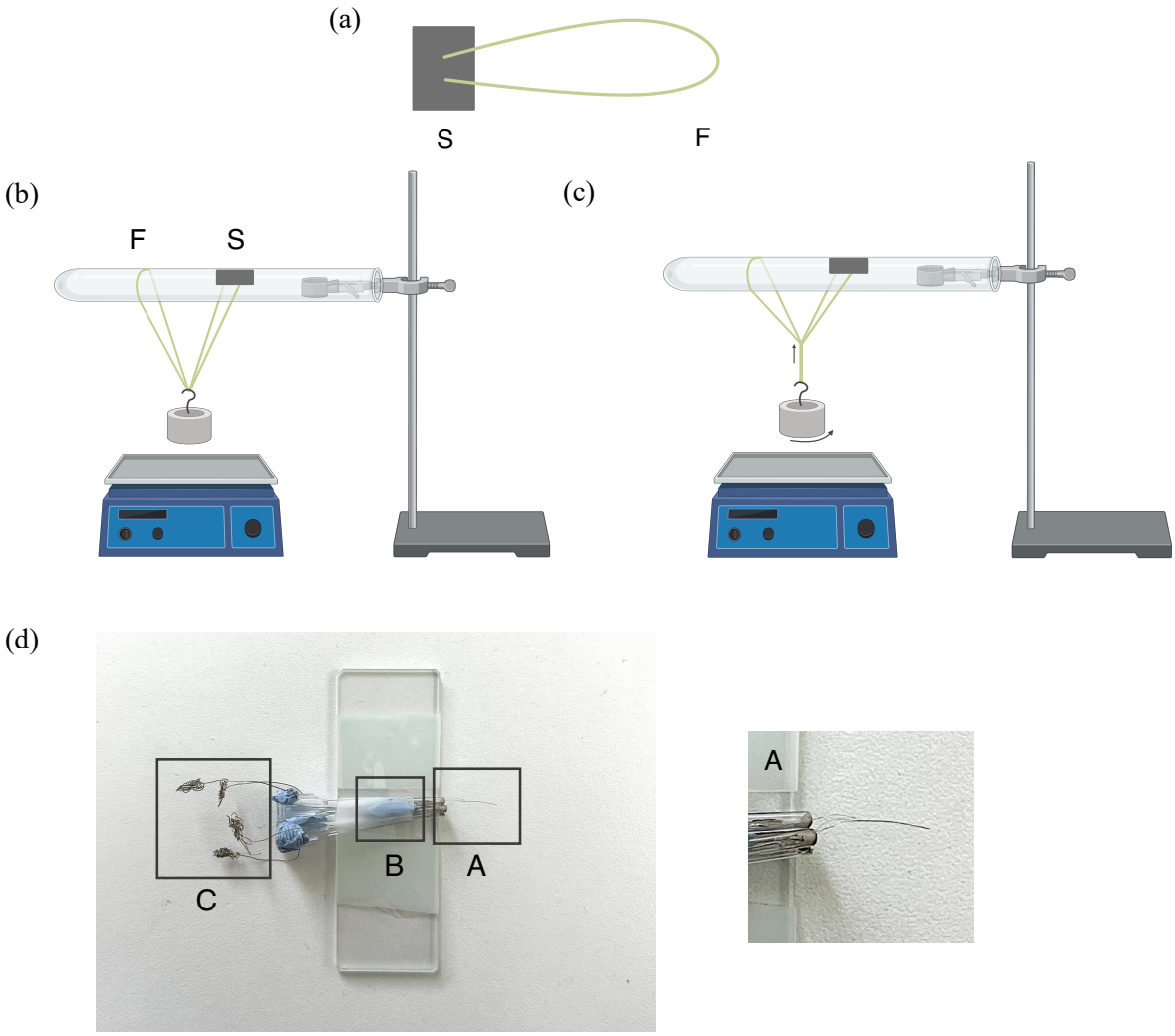

Figure 2.9: (a) A microwire fixed by tape. S represents the fixed end, and F represents the free end. **(b)** Tetrode fabrication setup. A glass tube is secured to a clamp stand to support the microwire. A magnetic weight, hooked at the bottom, ensures the wire segments are stretched, with a magnetic stirrer plate positioned underneath. **(c)** Turning on the stirrer plate causes the wires to twist into a single bundle. The twisting was stopped once the tetrode reached the desired length. **(d)** Tetrode connection setup. **Box A:** Tetrode end that will be immersed into the solution (Zoom in is shown on the right). **Box B:** Blu Tack (a moldable adhesive, Bostik) is placed in the middle to hold the pipette heads in place so that they will not slide over each other and break the tetrode. **Box C:** Stainless steel wires that connected via a crocodile clip to the electrochemical apparatus. (a~c) are created using BioRender.com.

2.3 Atomic Force Microscopy

Atomic Force Microscopy (AFM) is well-known for its high-resolution imaging of surface topography and force measurement, enabling the characterization of materials at the nano to micrometer scale. AFM is the primary tool used in this thesis for analyzing surface mechanical properties and for morphology imaging. A simplified AFM setup is illustrated in Figure 2.10(a). From the figure, the probe that interacts with the sample is known as the cantilever. One end of the cantilever is free and tipped, while the other end is connected to a piezoelectric actuator (piezo). The piezo helps in the movement of the cantilever relative to the sample, allowing for scanning and force measurement. At the free end of cantilever, a laser is reflected from the surface to a quadrant photodiode (PD). In the absence of bending, the laser spot is positioned at the center of the quadrant. During an AFM experiment, the cantilever is lowered towards the surface. At the proximity to the surface, the cantilever starts to bend in response to the tip-sample interaction. This causes the laser spot to shift, altering the potential difference across the PD, which is then converted into a measurement of cantilever deflection, z_c (unit: nm).

To prevent indefinite bending of the tip, a setpoint is manually established to control bending during scanning. Depending on the type of experiment, a setpoint could be deflection (in contact mode) or oscillation amplitude (in tapping mode) (Figure 2.10(b)). As shown in the graph (Figure 2.10(a)), there is a feedback loop connecting the PD and the piezo. If the PD detects signals above or below the setpoint, it adjusts the voltage across the piezo to extend or contract it until the signal matches the setpoint again.

Raw data obtained by AFM include the potential difference across the PD, piezo displacement, oscillation amplitude and phase, etc. In order to convert these data into more direct measures of tip/sample interaction, such as force, deflection, or indentation depth, knowledge of the cantilever's properties is required. Basic cantilever properties can be obtained through calibration.

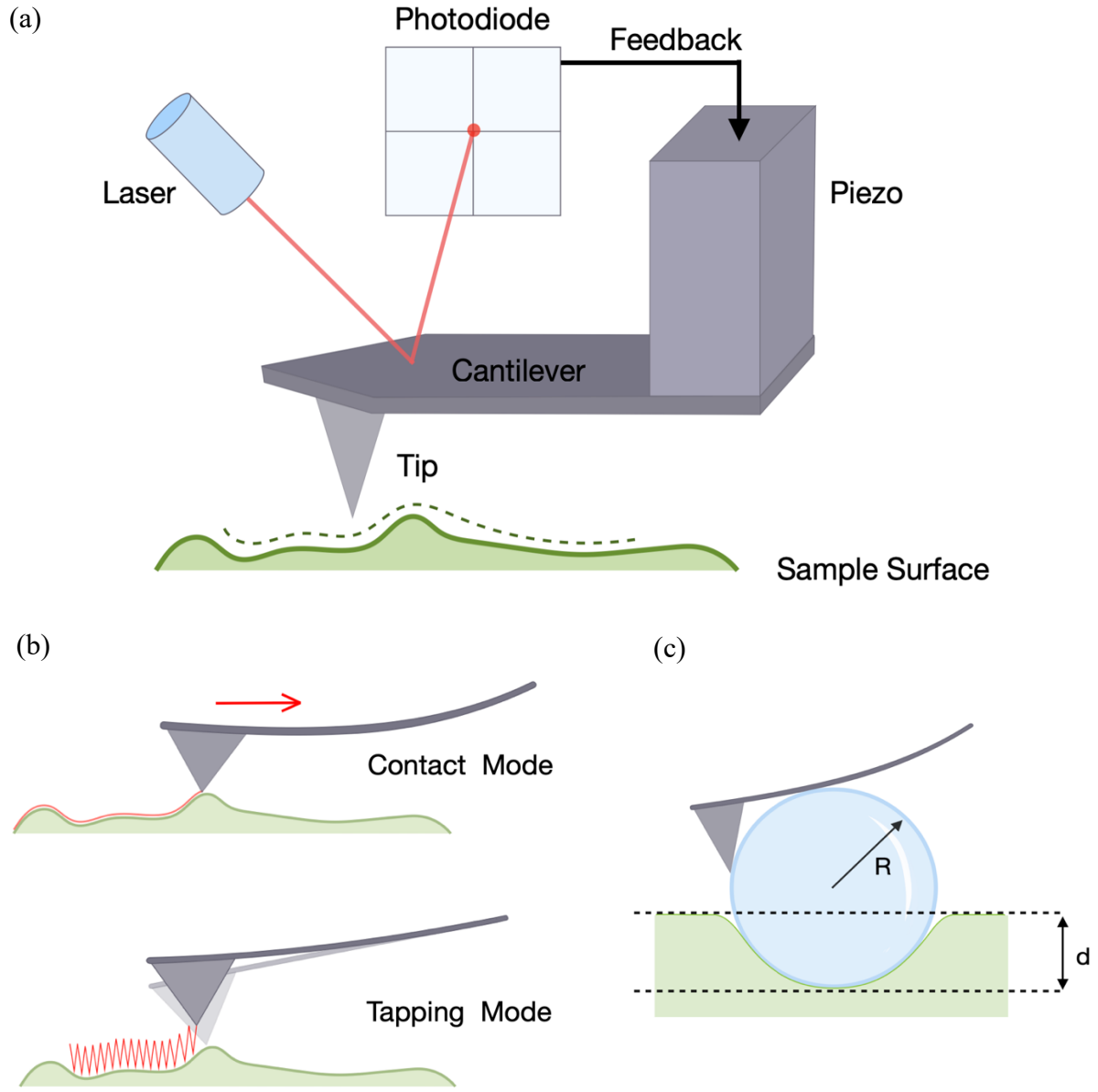

Figure 2.10: (a) AFM setup. The tip end interacts with the sample and the deflection z_c is detected by the laser spot on the photodiode (PD). PD is connected to the piezo to ensure a constant z_c. **(b)** Two modes of AFM [4]. In contact mode, tip scans across the surface at constant contact. Interaction is measured in terms of deflection and controlled by feedback. In tapping mode, cantilever vibrates at its resonance frequency and touches the surface very little. Oscillation amplitude reflects tip/sample interaction and is controlled by feedback loop [5]. **(c)** Spherical indenter. R: bead radius; d: indentation depth (denoted as δ in the following section).

2.3.1 Cantilever Calibration

Cantilever calibration is an essential preliminary step in most AFM measurements. Typically, the cantilever's stiffness (k_c,), resonance frequency (f_c,), quality factor (Q), and inverse optical lever sensitivity (InvOLS) must be calibrated prior to conducting an AFM experiment [6, 7]. InvOLS (unit: nm V^{-1}) allows the conversion of the potential difference measured across the PD into cantilever deflection (z_c) [6, 7]:

$$z_c = V_{PD} \times InvOLS \tag{2.11}$$

The conversion from deflection (z_c) to force utilizes Hooke's Law, where the interactive force (F) causing the bending is given by:

$$F = k_c z_c \tag{2.12}$$

The sample indentation depth (δ) is calculated as the difference between the piezo displacement (Z_p) and the cantilever deflection (z_c):

$$\delta = Z_p - z_c \tag{2.13}$$

In this thesis, two methods of cantilever calibration have been employed.

The first method is the GetReal™ method. It starts with positioning the tip far from the sample to avoid unwanted disturbances, and GetReal™ collects a thermal spectrum to obtain f_c and Q [6-8]. Following this, the Sader method is used to calculate the cantilever's stiffness (k_c) [6, 8-10], and the thermal noise method is utilized to determine the InvOLS [6, 8]. However, GetReal™ requires the input of cantilever properties (e.g. dimensions, shape) before calibration, limiting its use to pre-measured cantilevers [6]. This method is unsuitable for lab-modified or any other type of cantilever that is not recorded on the system. In this case, a second approach is suggested.

The second calibration method involves pressing the cantilever against a hard, non-sticky surface, such as a clean glass slide [6]. The stiffness of the indenting surface is chosen to greatly exceed that of the cantilever, ensuring that only the cantilever bends during this process. The InvOLS is calculated by dividing the distance the piezo extends towards the surface by the change in voltage on the PD [6]. Once the InvOLS is known, the cantilever is moved away from the surface to collect a thermal spectrum, which is used to determine f_c and Q [6, 11]. k_c is calculated using the thermal noise method [6, 11].

For both methods, a thermal spectrum is collected across a range of frequencies [6, 11]. A fast Fourier transform (FFT) is applied to identify and fit the peaks in the spectrum corresponding to the resonance frequency (f_c) of a cantilever. For each f_c, the quality factor (Q) is calculated by dividing the f_c by the half-width maximum of its corresponding peak [6, 11].

2.3.2 Cantilever Excitation – Photothermal Excitation

For an AFM, the cantilever can be excited indirectly by piezo actuation [12, 13]. However, when a cantilever is driven by piezoelectric excitation, especially in liquid, the resonances due to the piezo and other components of the experimental setup may appear in the thermal spectrum [12, 13]. These additional resonances complicate the identification of the true resonance frequency of a cantilever and introduce noise into the data [12, 13]. To improve these issues, more direct actuation methods are recommended to avoid spurious resonances.

One effective direct actuation method involves photothermal excitation (PTE) of the cantilever [14-20]. In this thesis, a blue laser (BlueDrive™, Oxford Instruments Asylum Research, wavelength = 405 nm) is employed [14-20]. The laser is focused near the fixed end of the cantilever. Cantilevers are typically constructed from layers of different materials. When pulses from the blue laser heat the cantilever locally, the differential thermal expansivity between the top layer coating and the underlying material causes the cantilever to bend and oscillate. The power of

the blue laser can be adjusted to control the desired frequency and amplitude of these oscillations [14-20].

2.3.3 AFM Contact Indentation and Relaxation Experiment

In this thesis, force indentation is measured using AFM contact mode (Figure 2.10(b)). The tip is lowered to make contact with the surface, pushed in until a predetermined threshold of force or indentation (a trigger point) is reached and then retract. Force and displacement data are recorded and analyzed using either the Hertz model (equation (1.35)) or the JKR model (equation(1.52)), depending on the adhesiveness of the material, to determine the Young's modulus (E) of the material, as discussed in Section 1.3.2.

In the relaxation experiment, the tip remains on the material surface for a certain period after reaching the trigger point before retracting. The relaxation time (τ) is determined by fitting the dwell section data to the models outlined in equations ((1.65) ~ (1.68)) from Section 1.3.3. Following the analysis, the goodness of fit (GoF) of each model is evaluated to determine the most accurate model (highest GoF) for describing the material.

For this thesis, in order to achieve model fitting assuming a spherical contact, cantilevers have been modified to incorporate a glass microsphere (diameter = 49.21 ± 0.72 μm, Whitehouse Scientific) at its end (Figure 2.10(c)). The choice of indenter shape affects the mathematical models due to geometric considerations [21]. Using a spherical indenter, rather than a sharp tip of an unmodified cantilever, provides several benefits. First, the spherical contact remains consistent throughout the experiment. However, for a sharp tip at shallow indentation depth, the interaction is approximated as conical contact [21], but it transitions to parabolic contact as the indent is deeper [21]. Therefore, using a sharp tip needs to consider changes of model at different depths. Second, the larger contact area with a microsphere mitigates the effects of adhesion, especially when testing soft materials like PDMS. With a sharp tip, there is a substantial risk that the tip may be stuck at the surface and difficult to withdraw.

2.3.4 AFM Tapping Mode: Topography Measurement

For morphological imaging, tapping mode AFM is employed (Figure 2.10(b)). In this mode, the cantilever is driven near its resonance frequency, with the feedback loop maintaining a constant oscillation amplitude. During scanning, the cantilever vibrates at a set amplitude and briefly touches the sample surface, minimizing contact time. This approach ensures that the tip remains mostly distant from the surface, avoiding the drag and potential rupture of the soft polymer surface often encountered in contact mode [22].

Similar to contact mode, tapping mode has a feedback loop that connects the PD and piezo, where the feedback loop ensures that the oscillation amplitude remains at the setpoint. The recorded change of height in the piezo reflects the change of height in the surface topography. Other than height information, tapping mode also captures variations in the phase difference (or phase shift) between the driving and recorded signals (Figure 2.11). These phase shifts provide insights into energy dissipation [23, 24]. For example, as shown in Figure 2.11, a flat surface will result in a uniform height image, whereas variations in material properties influence the extent of tip-surface interaction. These variations are reflected in the phase image. Softer and more adhesive materials may adhere to the tip (dissipating more energy), delaying its response and causing a pronounced phase shift. This difference is detected as a contrast in the phase signal (Figure 2.11). Therefore, phase information, combined with height data, can provide valuable information, particularly in studying inhomogeneous polymer networks [23, 25, 26].

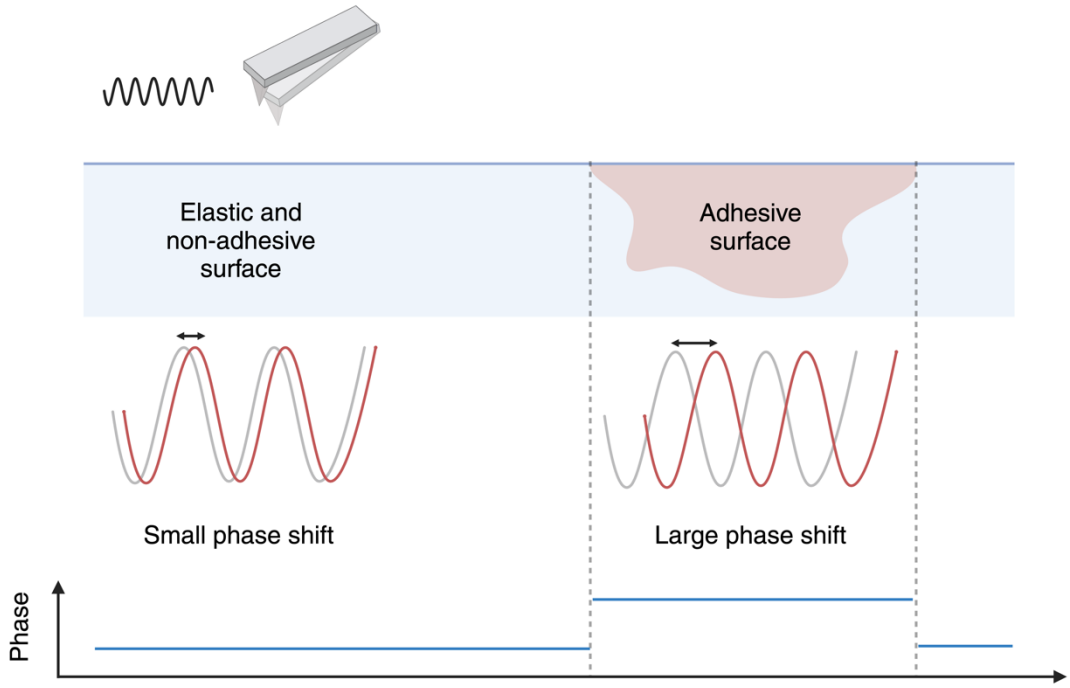

Figure 2.11: Illustration of an AFM conducting a tapping mode scan across a surface. At the elastic and non-adhesive sections (blue color), the response is rapid, resulting in a minimal phase shift between the input signal (grey line) and the recorded signal (red line). In contrast, at the adhesive region (brown color), the response is delayed, leading to a significant phase shift. The phase shifts along the surface are presented in the phase diagram, as shown at the bottom of the graph [27]. The adhesive areas exhibit a pronounced phase value relative to other regions.

2.4 Summary

Overall, this chapter introduces the chemicals, electrochemical methods, and AFM techniques employed in this thesis. In subsequent chapters, the conductive polymer PEDOT is first characterized using CV to understand the reaction mechanisms, followed by chronoamperometry for deposition. The PEDOT coatings are then imaged using AFM in tapping mode. A bipotentiostat is utilized to examine the recording processes. The mechanical properties of PDMS at the interface are assessed using AFM contact indentation and relaxation experiments. The specifics of these methods and analysis will be detailed in the upcoming chapters of the thesis.

References

(1) Compton, R. G.; Banks, C. E. *Understanding voltammetry, 3rd Edition*; World Scientific, 2018.

(2) Chen, H. *FreeSim*. https://github.com/nmerovingian/FreeSim (accessed 2024.05.23).

(3) *Enamel Insulation Specifications*. California Fine Wire, https://calfinewire.com/wp-content/uploads/Enamel-Insulation-Specs.pdf (accessed 2024 02.16).

(4) Asmatulu, R.; Khan, W. S. Chapter 13 - Characterization of electrospun nanofibers. In *Synthesis and Applications of Electrospun Nanofibers*, Asmatulu, R., Khan, W. S. Eds.; Elsevier, 2019; pp 257-281.

(5) Putman, C. A. J.; Vanderwerf, K. O.; Degrooth, B. G.; Vanhulst, N. F.; Greve, J. Tapping Mode Atomic-Force Microscopy in Liquid. *Appl Phys Lett* **1994**, *64* (18), 2454-2456.

(6) *Get Real - Automated Probe Calibration*. Oxford Instruments Asylum Research Forums, https://support.asylumresearch.com/articles/video-tutorials-aa/19721-getreal-automated-probe-calibration (accessed 2024).

(7) *Applications Guide Version 16 Revision*. Oxford Instruments Asylum Research Manual, (accessed 2024).

(8) Higgins, M. J.; Proksch, R.; Sader, J. E.; Polcik, M.; Mc Endoo, S.; Cleveland, J. P.; Jarvis, S. P. Noninvasive determination of optical lever sensitivity in atomic force microscopy. *Review of Scientific Instruments* **2006**, *77* (1).

(9) Sader, J. E.; Chon, J. W. M.; Mulvaney, P. Calibration of rectangular atomic force microscope cantilevers. *Review of Scientific Instruments* **1999**, *70* (10), 3967-3969.

(10) Sader, J. E.; Sanelli, J. A.; Adamson, B. D.; Monty, J. P.; Wei, X.; Crawford, S. A.; Friend, J. R.; Marusic, I.; Mulvaney, P.; Bieske, E. J. Spring constant calibration of atomic force microscope cantilevers of arbitrary shape. *Rev Sci Instrum* **2012**, *83* (10), 103705.

(11) Hutter, J.; Bechhoefer, J. Calibration of Atomic-Force Microscope Tips. *Review of Scientific Instruments* **1993**, *64*, 1868-1873.

(12) Rabe, U.; Hirsekorn, S.; Reinstädtler, M.; Sulzbach, T.; Lehrer, C.; Arnold, W. Influence of the cantilever holder on the vibrations of AFM cantilevers. *Nanotechnology* **2006**, *18*, 044008.

(13) Schäffer, T. E.; Cleveland, J. P.; Ohnesorge, F.; Walters, D. A.; Hansma, P. K. Studies of vibrating atomic force microscope cantilevers in liquid. *Journal of Applied Physics* **1996**, *80* (7), 3622-3627.

(14) Kiracofe, D.; Kobayashi, K.; Labuda, A.; Raman, A.; Yamada, H. High efficiency laser photothermal excitation of microcantilever vibrations in air and liquids. *Rev Sci Instrum* **2011**, *82* (1), 013702.

(15) Marti, O.; Ruf, A.; Hipp, M.; Bielefeldt, H.; Colchero, J.; Mlynek, J. Mechanical and thermal effects of laser irradiation on force microscope cantilevers. *Ultramicroscopy* **1992**, *42-44*, 345-350.

(16) Nishida, S.; Kobayashi, D.; Kawakatsu, H.; Nishimori, Y. Photothermal excitation of a single-crystalline silicon cantilever for higher vibration modes in liquid. *Journal of Vacuum Science & Technology B: Microelectronics and Nanometer Structures Processing, Measurement, and Phenomena* **2009**, *27* (2), 964-968.

(17) Ramos, D.; Tamayo, J.; Mertens, J.; Calleja, M. Photothermal excitation of microcantilevers in liquids. *Journal of Applied Physics* **2006**, *99* (12).

(18) Ratcliff, G. C.; Erie, D. A.; Superfine, R. Photothermal modulation for oscillating mode atomic force microscopy in solution. *Appl. Phys. Lett.* **1998**, *72* (15), 1911-1913.

(19) Umeda, N.; Ishizaki, S.; Uwai, H. Scanning attractive force microscope using photothermal vibration. *Journal of Vacuum Science & Technology B: Microelectronics and Nanometer Structures Processing, Measurement, and Phenomena* **1991**, *9* (2), 1318-1322.

(20) Labuda, A.; Hohlbauch, S.; Kocun, M.; Limpoco, F. T.; Kirchhofer, N.; Ohler, B.; Hurley, D. Tapping Mode AFM Imaging in Liquids with blueDrive Photothermal Excitation. *Microscopy Today* **2018**, *26* (6), 12-17.

(21) Popov, V. L.; He√ü, M.; Willert, E. *Handbook of Contact Mechanics: Exact Solutions of Axisymmetric Contact Problems*; Springer Berlin Heidelberg, 2019.

(22) Haugstad, G. *Atomic force microscopy : understanding basic modes and advanced applications*; John Wiley & Sons, Inc, 2012.

(23) Wang, Y.; Song, R.; Li, Y.; Shen, J. Understanding tapping-mode atomic force microscopy data on the surface of soft block copolymers. *Surface Science* **2003**, *530* (3), 136-148.

(24) Voïtchovsky, K.; Kuna, J. J.; Contera, S. A.; Tosatti, E.; Stellacci, F. Direct mapping of the solid–liquid adhesion energy with subnanometre resolution. *Nature Nanotechnology* **2010**, *5* (6), 401-405.

(25) YE, Z.; ZHAO, X. Phase imaging atomic force microscopy in the characterization of biomaterials. *Journal of Microscopy* **2010**, *238* (1), 27-35.

(26) Raghavan, D.; Gu, X.; Nguyen, T.; VanLandingham, M.; Karim, A. Mapping Polymer Heterogeneity Using Atomic Force Microscopy Phase Imaging and Nanoscale Indentation. *Macromolecules* **2000**, *33* (7), 2573-2583.

(27) *What are AFM phase images?* icspi, https://www.icspicorp.com/what-are-afm-phase-images/ (accessed 2024).

Chapter 3

Temporal Evolution of Mechanical Properties in PDMS: A Comparative Study of Elastic Modulus and Relaxation Time for Storage in Air and Aqueous Environment

Chapter 3 reports the mechanical studies on PDMS by employing AFM. PDMS is a soft, biocompatible polymer extensively employed in biomedical research, notable for its tunable mechanical properties achieved through cross-linking. While many studies have assessed the mechanical properties of PDMS utilizing macroscopic and microscopic methods, these analyses are often limited to freshly prepared samples. However, the mechanical properties of PDMS can be expected to change during prolonged exposure to water or air, such as interface polymer chain loosening or surface hardening, which are critical considerations in applications like cell culture platforms or microfluidic devices. This chapter presents a comprehensive 10-day investigation of the evolution of PDMS surface mechanical properties through AFM-based nano-indentation. I focused on the most commonly utilized crosslinker-to-base ratios of PDMS, 1:10 (r10) and 1:20 (r20), under conditions of air and deionized water storage. For r10 samples, a hardening process was detected, peaking at 2.12 ± 0.35 MPa within five days for those stored in air and 1.71 ± 0.16 MPa by the third day for those immersed in water. In contrast, r20 samples exhibited better stability, with an observed elastic modulus averaging 0.62 ± 0.06 MPa for air-stored and 0.74 ± 0.06 MPa for water-stored samples. Relaxation experiments, interpreted via the General Maxwell Model featuring two distinct component responses, a relatively consistent fast response τ_1 (on the order of 10^{-1} s), and a more variable, slower response τ_2 (on the order of 10 s), throughout the study period. The identification of two distinct relaxation times suggests the involvement of two disparate material property regimes in the relaxation process, implying changes in the surface material composition at the interface with air/water. These variations in

mechanical properties could significantly influence the long-term functionality of PDMS in various biomedical applications.

The work of **Chapter 3** has been published in the *Journal of the Mechanical Behavior of Biomedical Materials*. The project was carried out under the supervision of Prof. Sonia Contera. Dr. Casey Adam (now at Purdue University) and Henrik Rehnstrom helped me with the study of using AFM and the interpretation of experimental results.

3.1 Introduction

Polydimethylsiloxane (PDMS) is a member of the silicon polymers family [1]. The chemical formula of PDMS is $CH_3[Si(CH_3)_2O]_nSi(CH_3)_3$, where n is the number of repeating units. The structure of PDMS is shown in **Figure 3.1**. Commercially available PDMS is usually provided as a kit with two liquid components: a polymeric base and a curing agent [2]. Upon mixing, the vinyl end groups in the base react with the curing agent, leading to a three-dimensional crosslinked network via hydrosilylation reaction [2, 3]. Before crosslinking, the polymeric base is a viscous liquid [2], but once crosslinked, PDMS turns into a hydrophobic elastomer with a water contact angle larger than 100° [4, 5]. The stiffness of the elastomer can be tuned by varying the curing agent to base ratio [6].

PDMS has been widely used and characterized, especially in the context of micro-technologies for biomedical applications. For example, PDMS is used for fabricating microfluidic devices able to reach single molecule precision while still being a high throughput platform useful in fields such as drug delivery, DNA sequencing, and point-of-care testing [7-9]. Additionally, PDMS microfluidic devices are employed in creating lipid nanoparticles for pharmacological formulations [10]. PDMS also serves as a substrate for *in vitro* experiments, e.g. in hemodynamic [11] and stem cell differentiation studies [12-14].

The reason why PDMS is an attractive biomaterial can be attributed to multiple factors. First, PDMS is inexpensive and straightforward to manufacture. Uncrosslinked PDMS gels are viscous liquids [2], allowing them to fill any mould before the addition of the crosslinker retains the mould's structure. Furthermore, techniques such as lithography allow specific structuring of PDMS gels at high resolution, even to a few nanometers [15-17]. Secondly, PDMS is biocompatible and non-toxic[18], providing a suitable environment for living cells that can even be used for body implants [18, 19]. Thirdly, PDMS is optically transparent, allowing direct observation of processes inside, such as microparticle flow through PDMS scaffolds [20]. Moreover, PDMS has less autofluorescence than similar biocompatible polymers (e.g. PMMA) [21], meaning that fluorescence experiments can also be performed with PDMS constructs for experiments such as cell cytotoxicity tests, living cell imaging, and single molecular labelling [22-24]. Lastly, the surface of PDMS can be readily modified by UV [25, 26], ozone [25, 26], and plasma treatment [27]. Such surface modification changes the surface of PDMS from hydrophobic to hydrophilic [26], and can be used to enhance the attachment of other chemicals or cells [28], create multilayer PDMS devices [29], and improve water and air transportation which benefit applications like wound healing [30].

One of the key properties of PDMS is its tuneable mechanical properties, allowing PDMS to form both hard substrates, essential for chip manufacture, and soft substrates, beneficial to cell interactions. Therefore, numerous studies, both macroscale and microscale, have been undertaken to characterize the mechanical properties of PDMS. Data procured from macro or microscale tests are typically force-displacement curves [31]. To extract the elastic modulus from such curves, the data are fitted with contact mechanics models as discussed in Section 1.3.2 [32]. **Table 3.1** summarizes recent studies on the adhesion and mechanical properties of PDMS and its composite materials.

As shown in **Table 3.1**, macroscale tests include compression tests, tensile tests, and indentation with macroscale probes (1~5mm in size). Khanafer et al. [31] revealed at the microscale, PDMS stiffness saturated at a mixing ratio of 1:9 (crosslinker: base), beyond which the elastomer softened because excess cross-linker slowed the curing rate, leaving more base PDMS unreacted. Additionally, Kroner et al. [33] evaluated the macroscale adhesive properties of PDMS by performing indentation tests with flat and circular probes. They found that the reproducibility of adhesion measurements was heavily dependent on the tilting angle between the probe and the polymer surface, indicating that adhesion forces were contingent on the measurement geometry. In contrast, adhesion measurements obtained with spherical probes were less sensitive to surface alignment, whereas they may lose information on adhesion, especially with a patterned topography.

Macroscopic measurements, due to their limited spatial resolution, provide information on the bulk properties of materials but are less informative about variations on smaller scales. This is particularly relevant when nanomaterials, such as carbon nanotubes [34] or silica nanoparticles [35], are integrated into the PDMS matrix. In biological and biomedical contexts, where cellular interactions with PDMS involve forces on the nano-newton scale at the nano- and microscale [36], Atomic Force Microscopy (AFM) becomes a critical tool. Therefore, AFM is employed to elucidate mechanics at these scales with high-resolution.

Sharfeddin *et al.* [37] assessed the elastic modulus of PDMS gels with a range of base-crosslinker ratios, comparing their microscale and macroscale measurement results. Their study highlighted the nano-JKR test as a more appropriate method than macroscale tests for determining the elastic modulus of PDMS due to its consideration of surface adhesion forces. Beyond the crosslinker-to-base ratio and measurement methods, the medium surrounding PDMS gels also influences their mechanical properties. Kenry et al. [38] measured PDMS in a liquid medium comprising phosphate buffered saline (PBS) and 1% bovine serum albumin

(BSA), examining both the elastic modulus and creep response of PDMS gels of varying softness. Their finding revealed that PDMS with a higher stiffness had a shorter creep response than low-stiffness counterparts [38].

In addition to pure gel, PDMS materials often incorporate additional components to enhance functionality, such as carbon nanotubes [34] to improve electrical conductivity. However, the additional components can also alter the mechanical properties of PDMS gels. For example, Huang et al. [35] introduced hydrophilic silica nanoparticles (d≈16 nm) into PDMS and employed multi-frequency intermodulation AFM to map the mechanical properties and image the gel surface simultaneously. The nanoparticles caused pronounced local variation in hydrogel properties, marked by decreased local energy dissipation and increased stiffness [35]. Further exploring composite materials, Koetniyom et al. [39] compared Au or Ag PDMS composite surface root-mean-square roughness with that of the pure gel, reporting a considerably rougher composite surface with diminished surface adhesion.

Despite numerous studies quantifying the mechanics of PDMS, the majority focus on freshly produced samples, with limited research dedicated to tracking the evolution of these mechanical properties over time. This oversight is significant, particularly because PDMS is commonly used in biological contexts where its interactions with cells primarily occur at the micro and nanoscale within aqueous environments for extended periods lasting from days to weeks [12-14, 40].

For instance, PDMS is utilized in invasive operations such as catheters, flexible tubing, and breast implants due to its excellent flexibility and antibacterial properties [41, 42]. However, changes in its elasticity over time, attributed to environmental factors, can lead to stiffening or degradation [43]. At the macroscale, such stiffening could hinder a catheter's ability to navigate through narrow or delicate vascular passages, causing damage or discomfort. At the microscale, surface degradation could compromise the integrity of a material, increasing the risk of bacterial

infection at the interface with tissue and cells [44]. For non-invasive applications like wound healing patches [45], surface alternation can influence the longevity of the medical patch. Previous studies have pointed out that microbial surface colonization on PDMS can be significantly affected by mechanical deformation, particularly at sites with microcracks [44]. Thus, microscale mechanical studies are invaluable not only in assessing material durability but also in guiding strategies to facilitate device operation and minimize infection risks associated with material degradation or deformation. In the aspect of biomedical research, particularly in microfluidics, where surface properties are amplified at the microscale [46, 47]. Any change at the interface of PDMS, like surface polymer chain loosening due to prolonged swelling in solution, can alter the flow characteristics of fluids through these devices, thereby impacting their accuracy and reliability. While such changes might not be noticeable at the macroscale, they can be significant at smaller scales and, as such, should not be overlooked.

To better understand the interactions of materials at the micro and nanoscale, this article employs AFM indentations with and without dwells to measure and interpret the microscale mechanical properties of commonly used PDMS gels. I specifically analyze the elastic modulus and relaxation time of PDMS gels with a crosslinker-to-base ratio of 1:10 (r10) or 1:20 (r20) over a period of 10 days in both dry and swollen states. Furthermore, I expand the theoretical frameworks to study PDMS relaxation by fitting the data to the General Maxwell Model. My results could offer a deeper understanding of the nanoscale structure and mechanical properties of PDMS, which may provide insights into device failure that originates from surface alteration and degradation.

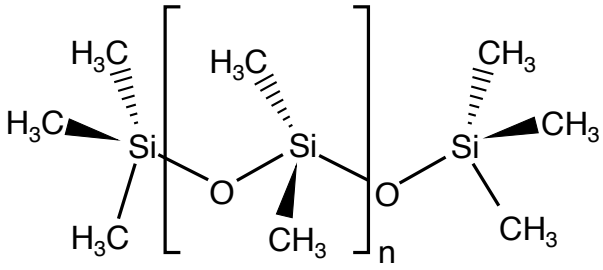

Figure 3.1: Chemical structure of Polydimethylsiloxane (PDMS). n denotes the number of repeating units.

Table 3.1: A summary of PDMS macroscopic and microscopic measurements. The ratios in brackets are the PDMS crosslinker-to-base ratio. a: np: nanoparticle, Ag: Silver, Au: Gold. b: d: diameter, r: radius.

Material [a]	Measurement	Probe Dimension [b]	Experiment Environment	Ref.
Pure PDMS (1:10, 1:9, 1:8, 1:7, 1:6)	Macroscopic Tensile test	/	In air	31
Pure PDMS (1:10)	Macroscopic Indentation test	Flat-ended cylindrical probe: d = 1mm Spherical probe: r = 2mm, 5mm	In air	33
Pure PDMS (1:10, 1:11.5, 1:16.5, 1:20, 1:30, 1:40, 1:50)	Macroscopic Tensile test, compression test	/	In air	37
	Microscopic Nanoindentation	Glass probe: d = 80mm	In air	
Pure PDMS (1:60, 1:80, 6:5, 5:5, 5:6)	Microscopic AFM indentation, creep test	Spherical cantilever tip: d = 20mm	In PBS + 1% BSA	38
Pure PDMS	Microscopic AFM indentation	Steel micro-spherical tip: d = 24mm	In air	48
Pure PDMS, PDMS/20%wt hydrophobic silicon np	Microscopic AFM tapping mode, multi-frequency Intermodulation AFM (ImAFM)	Cantilever tip r < 10nm	In air	35
Pure PDMS (1:10), PDMS (1:10)/Ag or Au np	Microscopic AFM tapping mode	/	In air	39

3.2 Materials and Methods

3.2.1 Materials

PDMS curing agents and base were purchased from Sylgard® 184 Dow-Corning Corporation and mixed in curing agent:base ratios of 1:10 and 1:20, referred to as r10 and r20, respectively. The base and curing agent were stirred manually until thoroughly combined, poured into circular polypropylene moulds (diameter = 8.0 ± 0.5 mm, depth = 3.0 ± 0.5 mm), then desiccated for a minimum of 30 minutes to ensure the removal of all air bubbles, producing homogeneous samples. Subsequently, samples were cured at 60 °C overnight. Post-curing, half of the samples were stored in air at room temperature, while the remaining half were immersed in deionized (DI) water, also at room temperature, in order to compare the swollen (wet) and non-swollen (dry) gel. All samples were stored for 10 days. The mechanical properties of each sample were measured by AFM on days 1, 3, 5, and 10.

3.2.2 Atomic Force Microscope

The mechanical properties of each PDMS sample were measured using an atomic force microscope (Cypher AFM, Asylum Research, Oxford Instruments, CA, USA). Olympus AC240TSA cantilevers with a 49.21 ± 0.72 μm glass microsphere (Whitehouse Scientific) attached to the tip were used. Cantilever stiffness was calibrated by indentation on a glass substrate and the Sader method as described in Section 2.3.3 [49] before any measurements were performed. Indentations were performed with and without dwells. For indentations without dwells, PDMS was indented to a force trigger point of 400 nN, and then the tip was immediately retracted. For indentations with dwells, once the 400 nN trigger point was reached, the probe remained on the surface for 2 s, maintaining a constant indentation depth, then retracted. The above procedures were repeated at at least three different points on the sample. Measurements were collected using

Igor Pro software (Oxford Instruments Asylum Research Version 16.26.227). Data were analyzed using Matlab, implementing a code based on the theory described in Section 1.3.2. All experiments were conducted in deionized (DI) water to eliminate the presence of an interfacial moisture layer that could confound the analysis of sample properties and adhesion. Furthermore, biomedical applications involve aqueous environments, so experiments in a liquid are more relevant to material applications.

3.3 Results and Discussion

3.3.1 Young's Modulus

In this section, I first revealed the observation of two distinct contact points presented in the approach curves of PDMS samples in Section 3.3.1.1. Then, Young's modulus was calculated and assessed for r10 and r20 PDMS in Section 3.3.1.2 and 3.3.1.3, respectively, by considering both contact points.

3.3.1.1 Contact Point Selection

During the indentation experiment, a gradual change was observed in the force-indentation curves with successive indentations at the same point on a PDMS sample, as shown in **Figure 3.2**. From **Figure 3.2**(a-d), the initial few indentations produced a small dip resembling a Hertzian contact, suggesting minimal adhesion between the tip and the sample. However, as more indentations were performed on the same spot, a hump appeared in the approach curves, and a second push-in dip could be observed. The hump stabilized by approximately the 5th indentation (**Figure 3.2**(e)). This phenomenon was consistently noted throughout the experiment, especially for the r10 PDMS starting from the 3rd day.

The hump observed in the approach curves suggests the presence of two contact points. The first contact point (before the hump) occurs when the tip initially touches the sample and

may result from interactions with the free polymer chains on the surface (in a depth of ca. 50nm ~ 200nm). As the tip passes through the surface chains, the force experienced by the cantilever slightly increases, giving rise to the hump. Once the tip penetrates deeper, it contacts the underlying bulk material, establishing a second contact point. After the second contact point, the force increases steadily, indicative of engaging with the more solid bulk material, until a maximum loading force is reached. The variation in curve shape between successive indentations is likely due to an inability of the loose polymer chains on the gel surface to rapidly return to their initial configuration [50]. In such a case, successive indentations gradually displace the loose top layer of PDMS, exposing the underlying polymer gel and resulting in the more pronounced second contact point after the hump (**Figure 3.2**(e-i)). It has been reported that free chains in a crosslinked network are likely to migrate and accumulate at the surface due to entropic effects [50, 51]. These free chains, in contact with air or water at the top interface, undergo various degrees of swelling and conformational changes [51], thereby exhibiting different mechanical properties compared to the underlying bulk. In addition to the variation between successive indentation curves, later indentations of the r10 sample (probing deeper PDMS layers) exhibited a larger area enclosed by the loading and unloading curves, showing adhesive forces acting over a broader range of indentation depths (**Figure 3.2**(d, e)). This suggests that adhesive forces are more prominent within the bulk of r10 PDMS gels than on the surface. These increased adhesion forces could be partly attributed to the increased contact surface area between the tip/sample as the tip enters deeper into the bulk gel [50].

Figure 3.3 illustrates variations in the calculated Young's modulus during successive indentations of a single point on r10 samples after storing in air for more than 3 days. Initially (orange lines, **Figure 3.3**), the Young's modulus either jumps or varies gradually during the consecutive indentations. These initial variations likely result from the tip pushing through the surface PDMS layer as the Young's modulus stabilizes once the secondary contact point

appears (blue lines **Figure 3.3**). Hence, in this paper, the first contact point (corresponding to the interface and to changing Young's moduli) is referred to as the 'minor contact', while the second (corresponding to indentations that result in a stable Young's modulus), formed after a few indentations, is referred to as the 'major contact'.

In contrast to r10 samples, multiple contact points in r20 samples occurred less often. The major contact point became noticeable after just one or two indentations (**Figure 3.5**(a,b)), and the its position remained fairly consistent (**Figure 3.5**(c~i). The increased stability of these curves resulted in a much more stable Young's modulus (**Figure 3.6**(j,k), without the variation observed in r10 samples (**Figure 3.3**).

The phenomenon of two contact points appearing upon sequential indentation of a single spot on a sample arises only after extended storage periods, mostly with r10 samples, varies locally, and cannot be detected through macroscopic measures. This observation suggests that long-term storage of r10 samples and r20 samples changes how the interface and bulk behave at the nanoscale and could thereby impact the function of such gels through time. Additionally, such a phenomenon has not been reported until now, in spite of the implications for PDMS material function and application through time.

3.3.1.2 r10 PDMS

Figure 3.4 shows how the Young's modulus from both the major and minor contacts of r10 samples varies over a 10-day period. Representative force-indentation curves for all samples are shown in Appendix B.1 and B.2. On the 1st day, neither air-stored nor DI water-stored r10 PDMS exhibited minor contacts (Figure B.1(a,b)). However, from the 3rd day onwards, two contact points became apparent, suggesting that the mechanical properties at the material surface had altered, distinguishing the interfacial/surface layer from the deeper bulk polymer, as detailed in the previous section.

The Young's modulus obtained from fits based on the major contact point exhibited a similar trend for r10 samples stored in air and in water (**Figure 3.4**). The Young's modulus of air-stored and DI water-stored samples increased until day 3 or 5, respectively, and started to decrease. The mean values of the Young's modulus of air-stored r10 PDMS increased from 0.63 ± 0.03 MPa to 1.28 ± 0.17 MPa, to 2.12 ± 0.35 MPa on days 1, 3, and 5, respectively, then decreased to a final value of 1.49 ± 0.36 MPa on day 10. This increase occurred faster for samples stored in DI water, peaking at 1.71 ± 0.16 MPa by day 3 then starting to decrease slowly to 1.51 ± 0.46 MPa by day 10. Previous studies of PDMS degradation suggest that the decrease in Young's modulus toward the end of the experiment largely arises from degradation of the cross-linker via hydrolysis [52]. Therefore, the drop in elasticity measured from the major contact point is likely caused by hydrolysis of the cross-linker in the bulk material. A potential explanation for the initial hardening might be that uncross-linked or loosely linked PDMS migrates to the surface of the gel [50, 51], leaving more firmly linked polymers in the bulk, and consequently increasing the bulk Young's modulus. As time progresses, and more cross-linker is degraded via hydrolysis, lost crosslinks begin to soften the bulk [52]. This crosslinker degradation starts earlier but is less pronounced in samples stored in DI water (-12% compared to the peak) compared to those stored in air (-30% compared to the peak), potentially because the water molecules enter the porous polymer matrix, support the gel structure and thereby moderating the Young's modulus decline.

The Young's modulus calculated from minor contact points decreased throughout the course of the experiment (**Figure 3.4**). For both air and water-stored PDMS. Elasticity calculated from the minor contact point was considerably lower than that from the major contact point, suggesting a softer layer of polymer brushes on the surface of PDMS [50, 51]. The continual decrease in elasticity of the top layer implies that the interface was already degrading by day 3

or maybe day 0, which might help explain why the surface layer was easier to push aside from day 3 onwards (as described in the previous section).

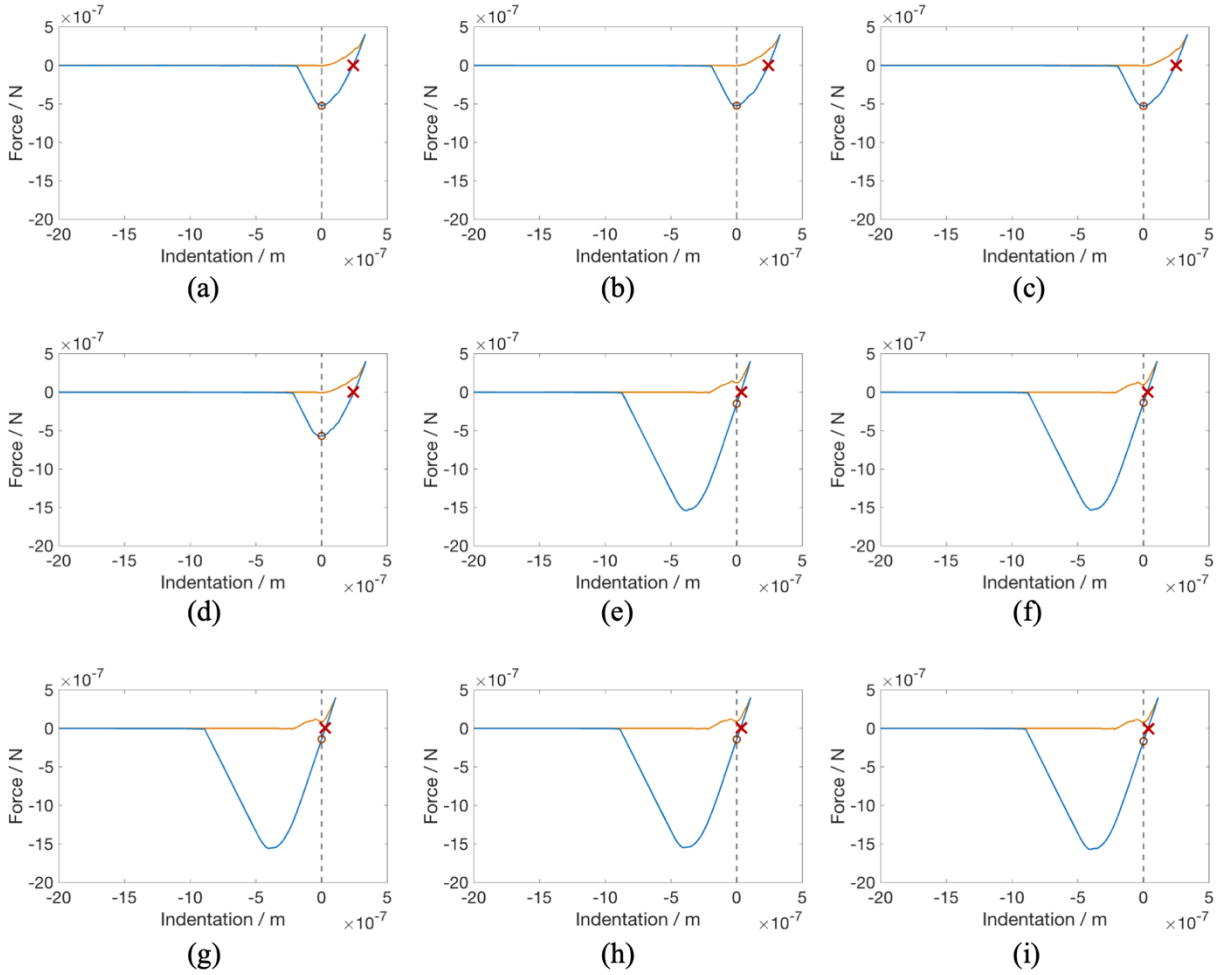

Figure 3.2: Successive force-indentation curves on a single point on an A-5D (air stored for 5 days) r10 PDMS sample. The orange line represents the loading curve, and the blue line denotes the retraction curve. Dashed vertical lines indicate the most prominent contact point, and its intersection with the retraction is marked by a circle (P_1 for the JKR model). The point with no force on the retraction curve (P_0 of the JKR model) is marked as a cross.

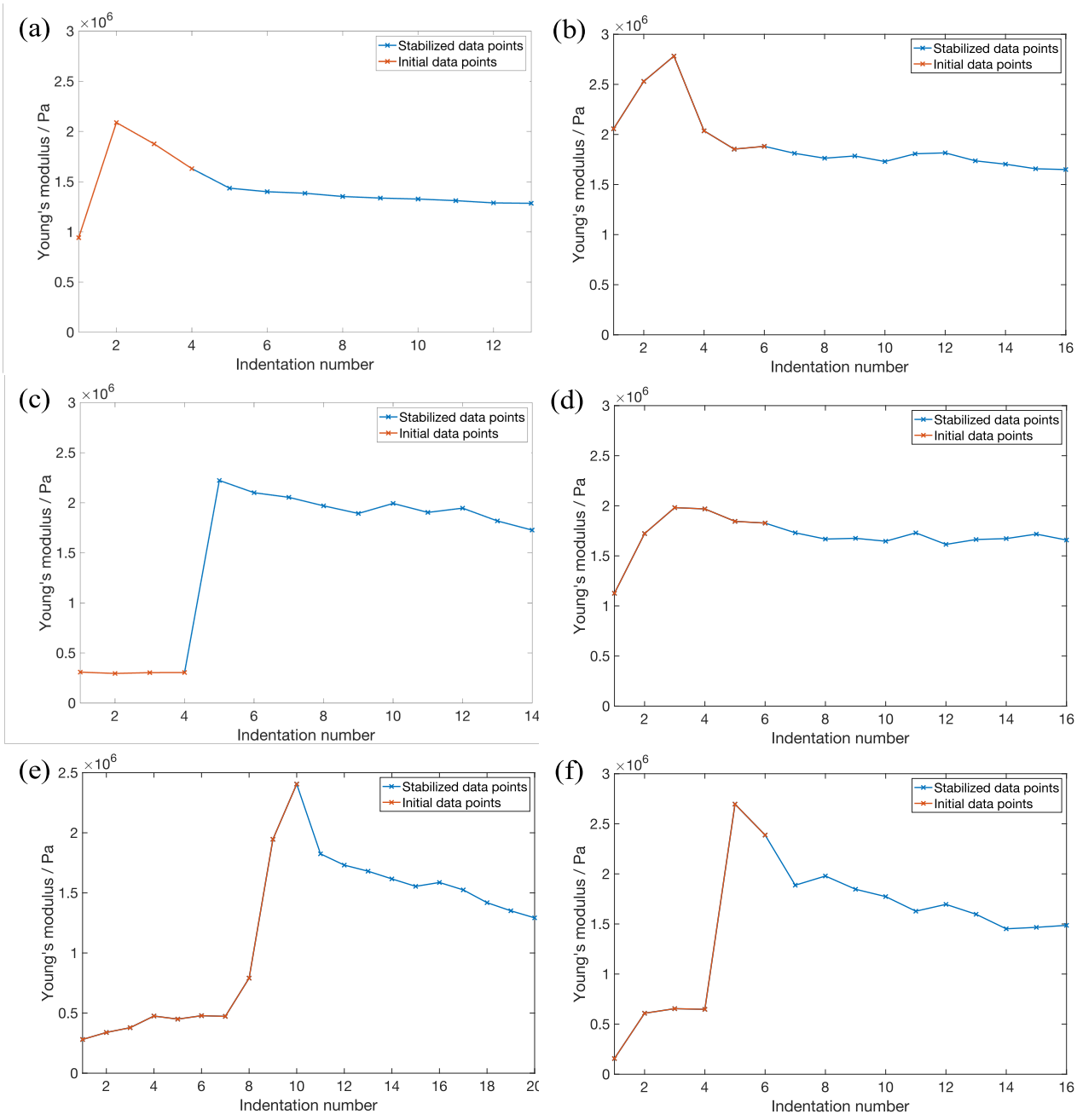

Figure 3.3: (a,c,e) The graphs correspond to the Young's modulus on successively indenting A-3D, 5D, and 10D r10 PDMS, respectively (air-stored for 3 days, 5 days, and 10 days). **(b,d,f)** The graphs correspond to the Young's modulus on successively indenting W-3D, 5D, and 10D r10 PDMS, respectively (DI water-stored for 3 days, 5 days, and 10 days).

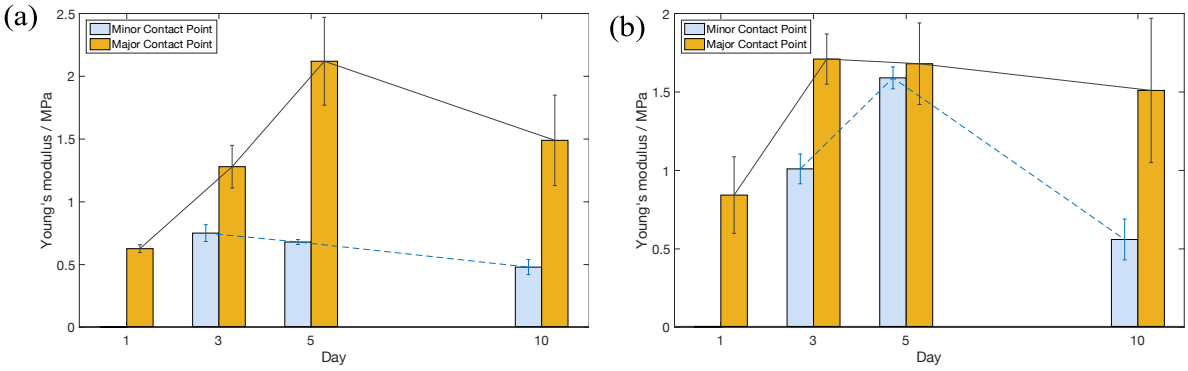

Figure 3.4: (a) The Young's modulus for air-stored r10 PDMS samples throughout 10 days. **(b)** The Young's modulus for DI water-stored r10 PDMS samples throughout 10 days.

3.3.1.3 r20 PDMS

As mentioned in **Section 3.3.1.1**, fewer r20 samples exhibited multiple contact points compared to r10 samples (**Figure 3.5**). Even on day 5, a major contact point became noticeable after just one or two indentations (**Figure 3.5**(a,b)), after which the major contact position remained relatively constant (**Figure 3.5**(c~i)). This behavior differs from that of r10, where the major contact point appeared after several indentations compared to just two for the r20, and a sudden shift from the minor to the major contact occurred (**Figure 3.2**, **Figure 3.3**). Although the approach curves before surface contact in both r10 and r20 samples are similar, suggesting that both samples have a loosely bound surface layer PDMS, the minor contact point of the r20 samples is much less pronounced than that of the r10 samples. Hence, unless there was a distinct shift in contact point after a few indentations, e.g., on r20 samples on day 10 (**Figure 3.6**(e,f)), the minor contact point was considered to be non-existent for most r20 samples.

While the position of the major contact point on r20 during successive indentation was stable, adhesion forces increased with the number of indents, as evidenced by the expanding area enclosed between the loading and retraction curves (**Figure 3.5**). The plateau at the bottom

of the retraction curves in **Figure 3.5**(g~i) occurred because adhesive forces were so strong that cantilever deflection reached its maximum (z_{c_max} ≈559 nm), thereby preventing the AFM from tracking time dynamics of the adhesion force until enough retraction occurred that the adhesive force decreased. Despite the increasing adhesion with successive indentations, the Young's modulus remained relatively constant for successive r20 sample indentations (**Figure 3.6**) because the position of the contact point and corresponding point (P_1) on the retraction curve did not vary substantially. Since the JKR model is based on point-fitting (using P_0 and P_1), the fit was unaffected by the increasing adhesion. As a result, Young's moduli of successive indentation on r20 samples were more stable in the first 5 days (**Figure 3.6** and Figure B.2) than r10 samples, and the observation of multiple contact points happened only on day 10 (Figure B.2(g,h)).

Over a longer timescale, the Young's modulus of r20 samples showed less variation compared to r10 samples within a 10-day period, as illustrated in **Figure 3.7**. The mean elastic modulus was 0.62 ± 0.06 MPa for samples stored in air, and 0.74 ± 0.06 MPa for samples stored in water over 10 days. Since r20 has a higher base-to-crosslinker ratio, it is likely that more free polymer chains are present than r10 samples, and hence, less of the sample is cross-linked, giving lower Young's modulus values than that of r10 samples. Additionally, with fewer crosslinks to lose as the crosslinker degrades, r20 samples would be more stable than r10 samples. Furthermore, since degraded PDMS residue shares identical chemical components with the original base polymer, [53] less cross-linking in r20 compared to r10 samples would mean less distinction between the degraded and the uncross-linked polymer, resulting in the apparent stability of the polymer even if crosslinks degrade.

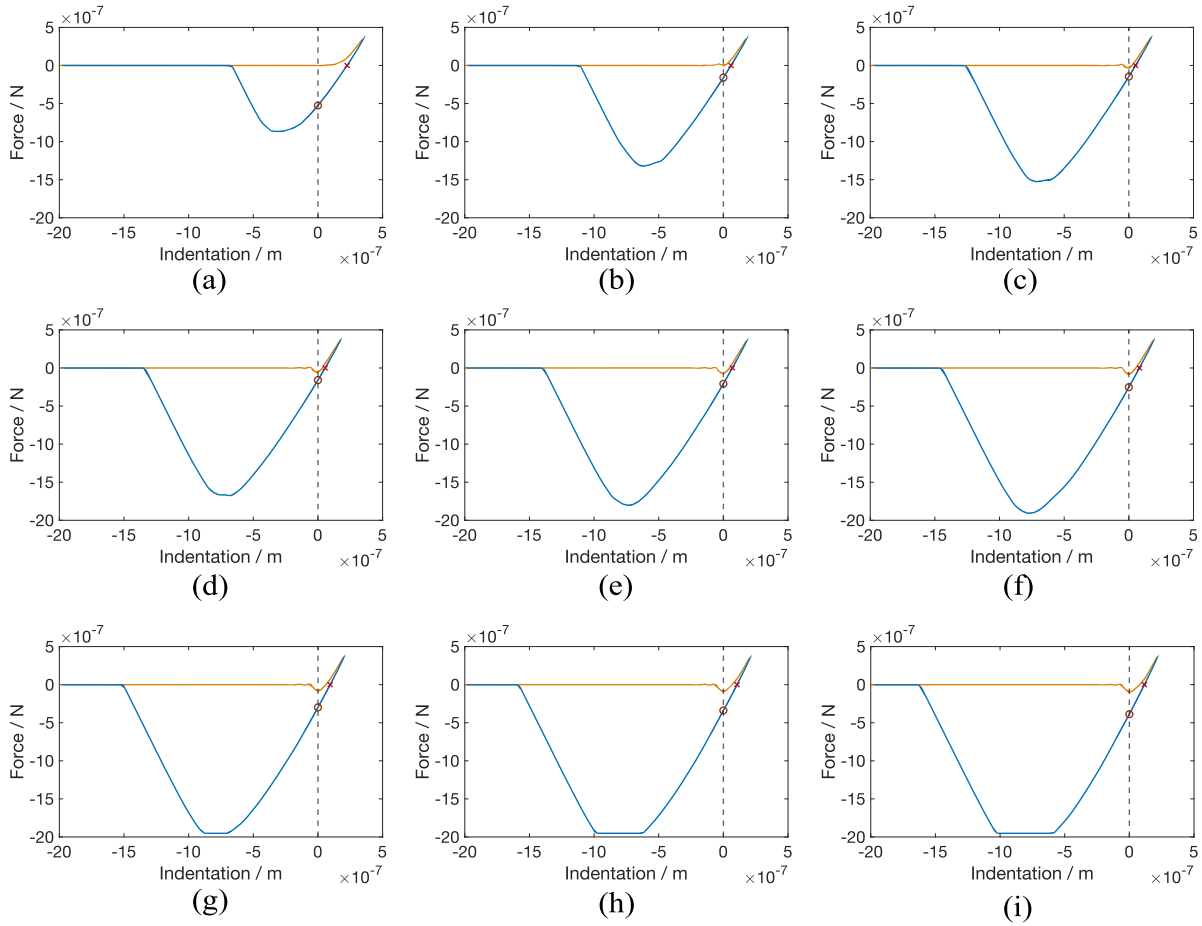

Figure 3.5: Successive force-indentation curves of a single point on an A-5D (air stored for 5 days) r20 PDMS sample. The orange line represents the loading curve, and the blue line denotes the retraction curve. Dashed lines indicate the position of the most prominent contact point, and its intersection with the retraction curve is marked by a circle (P_1 for the JKR model). The point with no force on the retraction curve (P_0 of the JKR model) is marked as a cross.

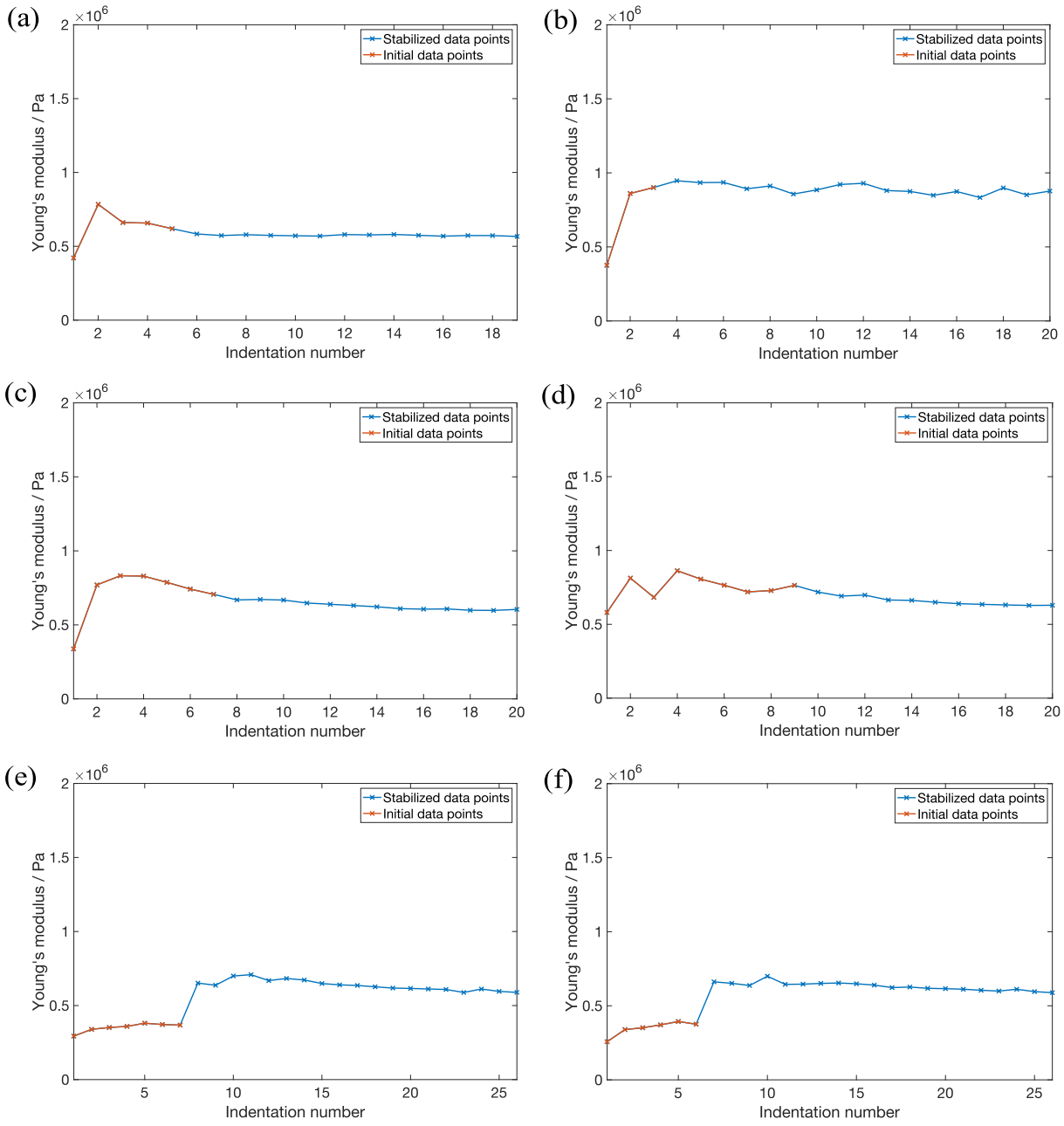

Figure 3.6: (a,c,e) The graphs correspond to the Young's modulus on successively indenting A-3D, 5D, and 10D r20 PDMS, respectively. **(b,d,f)** The graphs correspond to the Young's modulus on successively indenting W-3D, 5D, and 10D r20 PDMS, respectively.

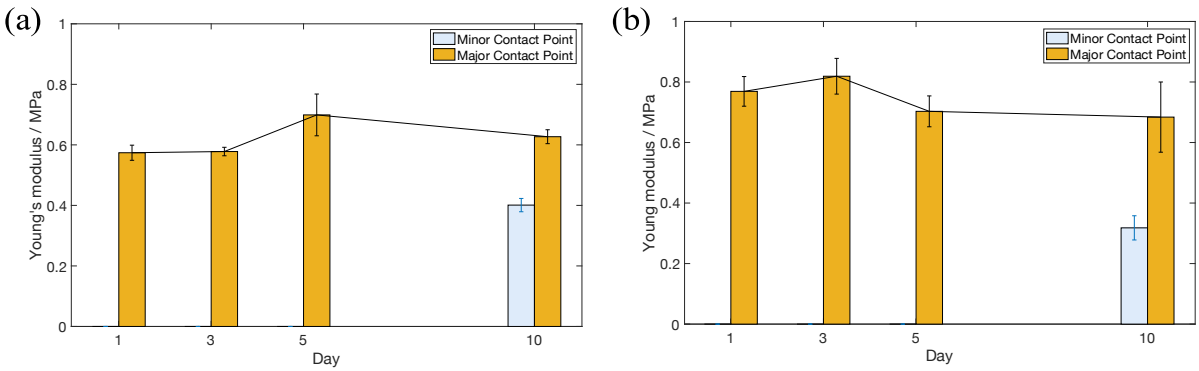

Figure 3.7:(a) The Young's modulus for air-stored r20 PDMS samples throughout 10 days. **(b)** The Young's modulus for DI water-stored r20 PDMS samples throughout 10 days.

3.3.2 Response Time

To determine the viscoelastic properties of the PDMS samples, relaxation experiments were performed to quantify sample response times and determine a model of linear viscoelasticity to describe the hydrogels. The relaxation time was obtained by extracting the exponential component of the Force-Time curves from the relaxation experiments (that is, the force vs indentation during a 2s dwell on the sample). I fit the data with four models, as mentioned in Section 1.3.3 (equation ((1.65) ~ (1.68)). The goodness of fit (R-squared values) for each equation was compared. As shown in Figure B.3 and Figure B.4 and Table B.1 and B.2 (Appendix Sections B.3 and B.4), the GMM-2 model best fits the data, which has been used to determine sample relaxation times.

3.3.2.1 r10 PDMS

Representative force relaxation graphs for all r10 samples are provided in the Appendix B.3 (Figure B.3). The General Maxwell Model with two components (GMM-2, as described by equation 1.68) provides the best fit for the relaxation curves during the 2-second dwell time for r10 PDMS stored in both air and DI water. The GMM-2 model exhibited the highest goodness-of-fit values (ESI Table S1) and, even by visual observation, was the most accurate (Figure

B.3), deviating the least from the original data compared to other models. Upon fitting, two coefficients, τ_1 and τ_2, are obtained, with τ_1 representing the shorter response time and τ_2 representing the longer response time. **Figure 3.8** illustrates a comparison of these two response times for r10 PDMS stored in air and in DI water over the 10-day period.

The presence of two distinct response times suggests that there are at least two dominant "materials" within the polymer, which could be various PDMS conformations, degrees of crosslinking, or solvent interactions inside the polymer matrix. Each of these responds differently to the continuous pressure applied by the AFM tip. From **Figure 3.8**(a), τ_1 is on the order of 10^{-1} s, indicating a fast response. τ_2 is in the order of 10 s, approximately 10^2 times greater than τ_1, suggesting the presence of a slower-responding material in the PDMS during relaxation. On average, τ_1 shows a similar trend under both storage conditions (0.25 ± 0.05 s for air-stored and around 0.22 ± 0.06 s for DI water-stored over 10 days.). However, τ_2 varies between samples stored in DI water or air. For the sample stored in DI water, τ_2 fluctuates but remains fairly constant around 20 s. In contrast, for the sample stored in air, τ_2 decreases noticeably over time, and on the 3rd day, the fitting of the parameter yields a negative value.

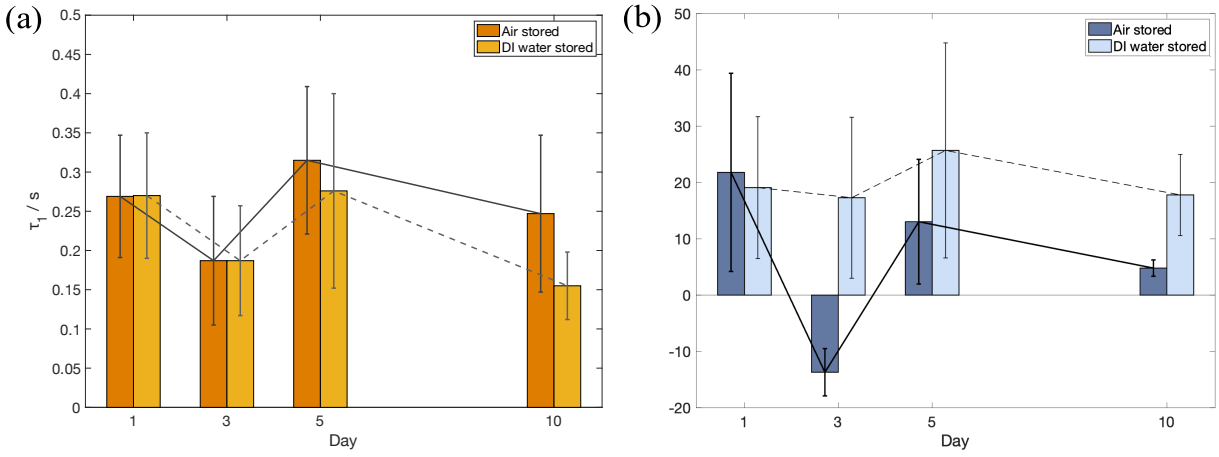

Figure 3.8: (a) The response time τ_1 for air stored and DI water stored r10 PDMS samples throughout 10 days. **(b)** The response time τ_2 for air stored and DI water stored r10 PDMS samples throughout 10 days.

The origin of this negative τ_2 can be attributed to the abnormal behavior observed in its relaxation curve (**Figure 3.9**, A-3D r10). Unlike other relaxation curves, where the force decreases gradually, the force instead increases. Such an increase suggests that the material was initially compressed and began to rebound back toward the tip, thereby requiring more force to maintain the same indentation depth. This increasing force begins after approximately 0.25 seconds of the dwell, around the time of τ_1 response ($\tau_1 = 0.19 \pm 0.082$ s), and thereafter, the other slower response material begins to dominate, moving towards the tip, pushing it upward. A possible explanation is that on the 3rd day, the surface layer started to become unstable. This notion is supported by the fact that the 3rd day was also the day when the second contact point appeared (**Figure 3.4**(a)). During the dwell on this altered surface layer, the tip reached the bulk material but was likely still influenced by the surface material as follows. In the initial few seconds of relaxation, corresponding to the τ_1 timescale, the tip compressed the more elastic bulk material. However, once the fast-responding materials finished responding, some of the loosely bonded PDMS or even water within the gel may flow back and interact with the tip, leading to an increased force required to maintain the indentation depth. After the 3rd day, the relaxation curve returned to normal behavior (decreasing force with time), potentially because the surface had finished degrading and was more stable.

3.3.2.2 r20 PDMS

Representative force relaxation graphs for all r20 samples are provided in the Appendix B.4 (Figure B.4). As with the r10 samples, the GMM-2 model is the most suitable for fitting the relaxation curves of r20 samples (Appendix B.4, Table B.2).

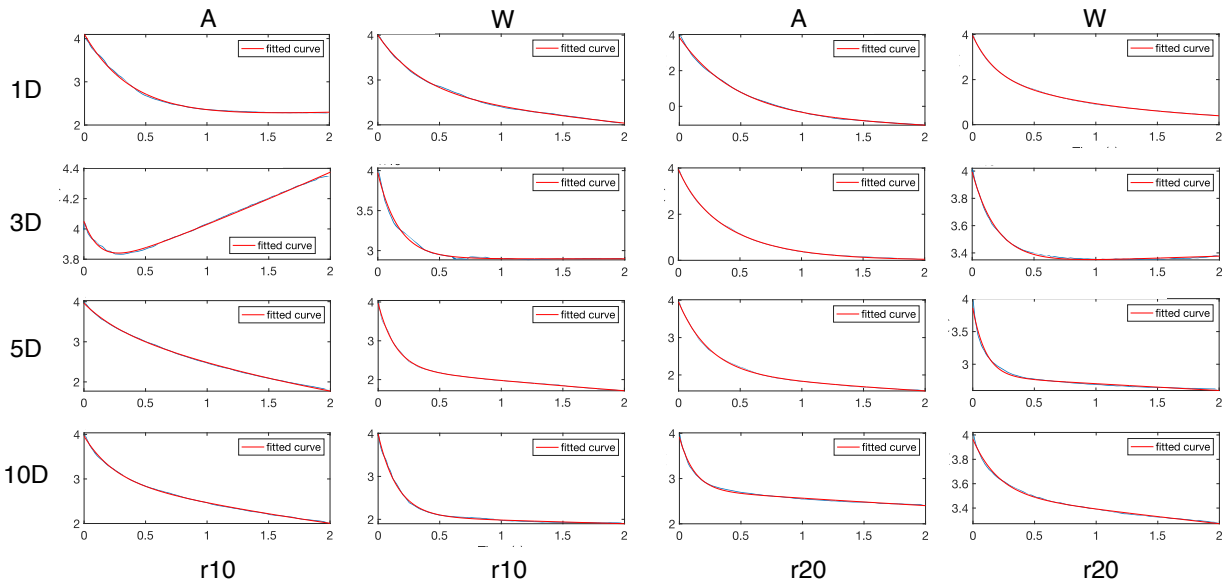

Figure 3.9: Summary of all relaxation curves: On each graph, the vertical axis represents the force (unit: 10^{-7} N), and the horizontal axis represents the dwell time (unit: s). As going down the row, the graphs represent an increasing number of storage days (from 1 day to 10 days). Each column represents a different PDMS sample as indicated at the top, where 'A' denotes air-stored and 'W' denotes DI water-stored."

For r20, τ_1 did not vary much with time (**Figure 3.10**(a)) and was on the same order of magnitude (10^{-1} s) as that of the r10 samples. However, τ_2 values of r20 samples exhibit more variability (**Figure 3.10** (b)) than that of r10 samples. As with r10 samples, relaxation curves exhibited abnormal behavior on the 3rd day. For example, the τ_2 value becomes very small for the air-stored r20 sample (τ_2 = 0.74 $\pm$0.56 s). Despite this small τ_2, the relaxation curve does not exhibit an increasing force like the r10 samples (Figure B.4, A-3D r20). Instead, a comparison of the dwell curves for A-1D r20 and A-3D r20 (**Figure 3.9**) shows that the final force required to maintain the indentation depth relaxed to a value near zero, which is the lowest among all the materials examined. Notably, for A-1D r20, the force even decreased to below zero, suggesting an attractive force from the PDMS that draws the tip inward. This complete relaxation (force approaching zero) was evident for the first 3 days in the air-stored r20 material and on the first day for the DI water-stored r20 material, indicating the adhesive and viscous

nature of r20 PDMS as a less cross-linked polymer. After day 3, the force required to maintain indentation depth for air-stored r20 returned to levels comparable to r10. However, for r20 stored in water (W-3D, 5D, 10D r20), the force at the end of relaxation was approximately 0.1 μN higher compared to all the other samples in **Figure 3.9**, except for the abnormal A-3D r10. This difference could be attributed to the poroelastic nature of PDMS. When submerged in solvent for an extended period, the less cross-linked PDMS swells [51], trapping solvent molecules within the polymer matrix and thereby altering the mechanical response of the material. Thus, during indentation, additional force is required to displace not only the polymer but also the trapped water molecules, requiring greater force to maintain the indentation depth. As suggested by previous research [54], two concurrent processes may occur during the indentation of elastomer gels. The first is the conformational change of the network, caused by the sliding of polymer chains or rotation at the connection joints [54]. The second process occurs if the material is immersed in a solvent, in which case the indentation will also cause migration of the solvent within the polymer matrix [54, 55]. These processes lead to viscoelasticity and poroelasticity, respectively, and are characterized by relaxation time and solvent diffusivity through the network [54]. To determine whether poroelasticity matters within the experimental timescale of this paper, the diffusion timescale needs to be compared with the dwell indentation period. The characteristic length for the AFM indentation experiment is about the size of glass bead attached at the tip head, $L_{bead} = 50$ μm. Taking a solvent diffusivity D as 10^{-9} m^2s^{-1} [54, 55], the timescale for solvent diffusion (t_{diff}) is approximately 2.5 s (calculated by equation (3.1)), which is comparable to the dwell time (t_{dwell} = 2 s).

$$t_{diff} = \frac{L_{bead}^2}{D} \tag{3.1}$$

Hence, as expected, poroelasticity and the entrapment of water molecules within the polymer network could contribute to the increased force observed in the relaxation experiments.

Therefore, assuming the polymer has been immersed in a solution for a sufficient period, the effects of poroelasticity likely manifest, resulting in a larger final relaxed force. From **Figure 3.9**, this effect appears to be more pronounced in less cross-linked and extended soaked PDMS, i.e., for W-3D, 5D, and 10D r20 samples, potentially because fewer crosslinks led to more free polymer chains where they swelled more when in contact with a solvent.

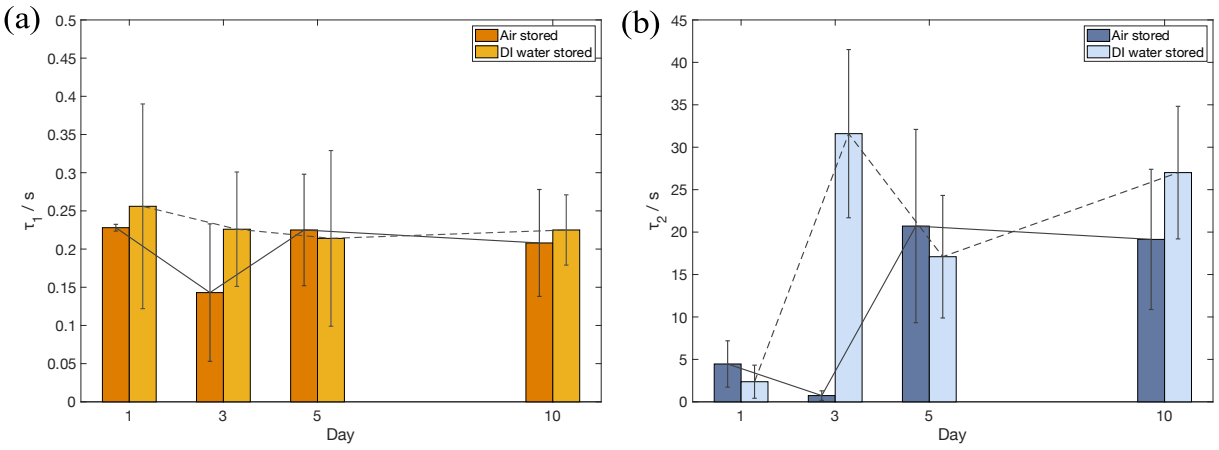

Figure 3.10: (a) The response time τ_1 for air-stored and DI water-stored r20 PDMS samples throughout 10 days. **(b)** The response time τ_2 for air-stored and DI water-stored r20 PDMS samples throughout 10 days.

3.4 Conclusion

This chapter evaluates the change in mechanical properties of PDMS with its most common crosslinker to base ratios (1:10, 1:20) when stored in air and DI water over a period of 10 days. AFM was utilized to measure Young's moduli and relaxation times of the samples through contact indentation and relaxation experiments. The r10 samples exhibited a hardening before the 5th and 3rd day for air and water stored samples, respectively. Then, there was a gradual softening due to degradation, whether stored in air or liquid. However, the decrease in elasticity was more pronounced in air, as indicated by the changes in Young's modulus.

Additionally, the occurrence of multiple contact points (minor and major) suggests the formation of interfacial and bulk layers in r10 starting at least from 3rd day. In contrast, r20 samples showed less variation in the Young's modulus and surface alternation.

Fitting relaxation curves showed that the GMM-2 model and its two response times best described the samples, suggesting that two predominate materials dominated the relaxation response. Apart from PDMS interactions, loosely crosslinked PDMS swelling in an aqueous environment for a long time could lead to two concurrent processes: solvent migration and polymer deformation. These processes may occur simultaneously due to their comparable timescales, which could affect the time response of the polymer to the surroundings.

Although PDMS is widely used in research and often for periods extending beyond a single day, most previous studies have conducted mechanical property measurements on freshly prepared polymers, overlooking changes in the subsequent days. This chapter of thesis addresses this gap, indicating that poroelastic and viscoelastic effects vary through time, which has important implications for material function in research and other applications that require the use of PDMS in air or aqueous environments over several days.

References

(1) Vlassov, S.; Oras, S.; Antsov, M.; Sosnin, I.; Polyakov, B.; Shutka, A.; Krauchanka, M. Y.; Dorogin, L. M. Adhesion and Mechanical Properties of PDMS-Based Materials Probed with AFM: A Review. *REVIEWS ON ADVANCED MATERIALS SCIENCE* **2018**, *56* (1), 62-78.

(2) Bardelli, T.; Marano, C.; Briatico Vangosa, F. Polydimethylsiloxane crosslinking kinetics: A systematic study on Sylgard184 comparing rheological and thermal approaches. *Journal of Applied Polymer Science* **2021**, *138* (39), 51013.

(3) Esteves, A. C. C.; Brokken-Zijp, J.; Laven, J.; Huinink, H. P.; Reuvers, N. J. W.; Van, M. P.; de With, G. Influence of cross-linker concentration on the cross-linking of PDMS and the network structures formed. *Polymer* **2009**, *50* (16), 3955-3966.

(4) Mata, A.; Fleischman, A. J.; Roy, S. Characterization of Polydimethylsiloxane (PDMS) Properties for Biomedical Micro/Nanosystems. *Biomedical Microdevices* **2005**, *7* (4), 281-293.

(5) Trantidou, T.; Elani, Y.; Parsons, E.; Ces, O. Hydrophilic surface modification of PDMS for droplet microfluidics using a simple, quick, and robust method via PVA deposition. *Microsystems & Nanoengineering* **2017**, *3* (1), 16091.

(6) Wang, Z.; Volinsky, A. A.; Gallant, N. D. Crosslinking effect on polydimethylsiloxane elastic modulus measured by custom-built compression instrument. *Journal of Applied Polymer Science* **2014**, *131* (22).

(7) Fujii, T. PDMS-based microfluidic devices for biomedical applications. *Microelectronic Engineering* **2002**, *61-62*, 907-914.

(8) Zhou, J.; Ellis, A. V.; Voelcker, N. H. Recent developments in PDMS surface modification for microfluidic devices. *Electrophoresis* **2010**, *31* (1), 2-16.

(9) Shakeri, A.; Khan, S.; Didar, T. F. Conventional and emerging strategies for the fabrication and functionalization of PDMS-based microfluidic devices. *Lab on a Chip* **2021**, *21* (16), 3053-3075.

(10) Maeki, M.; Fujishima, Y.; Sato, Y.; Yasui, T.; Kaji, N.; Ishida, A.; Tani, H.; Baba, Y.; Harashima, H.; Tokeshi, M. Understanding the formation mechanism of lipid nanoparticles in microfluidic devices with chaotic micromixers. *PLOS ONE* **2017**, *12* (11), e0187962.

(11) DOUTEL, E.; CARNEIRO, J.; OLIVEIRA, M. S. N.; CAMPOS, J. B. L. M.; MIRANDA, J. M. FABRICATION OF 3D MILI-SCALE CHANNELS FOR HEMODYNAMIC STUDIES. *Journal of Mechanics in Medicine and Biology* **2015**, *15* (01), 1550004.

(12) Béduer, A.; Vieu, C.; Arnauduc, F.; Sol, J.-C.; Loubinoux, I.; Vaysse, L. Engineering of adult human neural stem cells differentiation through surface micropatterning. *Biomaterials* **2012**, *33* (2), 504-514.

(13) Hashemzadeh, H.; Allahverdi, A.; Sedghi, M.; Vaezi, Z.; Tohidi Moghadam, T.; Rothbauer, M.; Fischer, M. B.; Ertl, P.; Naderi-Manesh, H. PDMS Nano-Modified Scaffolds for Improvement of Stem Cells Proliferation and Differentiation in Microfluidic Platform. *Nanomaterials* **2020**, *10* (4), 668.

(14) Wang, P.-Y.; Tsai, W.-B.; Voelcker, N. H. Screening of rat mesenchymal stem cell behaviour on polydimethylsiloxane stiffness gradients. *Acta Biomaterialia* **2012**, *8* (2), 519-530.

(15) Bender, M.; Plachetka, U.; Ran, J.; Fuchs, A.; Vratzov, B.; Kurz, H.; Glinsner, T.; Lindner, F. High resolution lithography with PDMS molds. *Journal of Vacuum Science & Technology B: Microelectronics and Nanometer Structures Processing, Measurement, and Phenomena* **2004**, *22* (6), 3229-3232.

(16) Koo, N.; Bender, M.; Plachetka, U.; Fuchs, A.; Wahlbrink, T.; Bolten, J.; Kurz, H. Improved mold fabrication for the definition of high quality nanopatterns by Soft UV-Nanoimprint lithography using diluted PDMS material. *Microelectronic Engineering* **2007**, *84* (5), 904-908.

(17) Lee, J.; Park, S.; Choi, K.; Kim, G. Nano-scale patterning using the roll typed UV-nanoimprint lithography tool. *Microelectronic Engineering* **2008**, *85* (5), 861-865.

(18) Kim, S.-J.; Lee, D.-S.; Kim, I.-G.; Sohn, D.-W.; Park, J.-Y.; Choi, B.-K.; Kim, S.-W. Evaluation of the biocompatibility of a coating material for an implantable bladder volume sensor. *The Kaohsiung Journal of Medical Sciences* **2012**, *28* (3), 123-129.

(19) Carta, R.; Jourand, P.; Hermans, B.; Thoné, J.; Brosteaux, D.; Vervust, T.; Bossuyt, F.; Axisa, F.; Vanfleteren, J.; Puers, R. Design and implementation of advanced systems in a flexible-stretchable technology for biomedical applications. *Sensors and Actuators A: Physical* **2009**, *156* (1), 79-87.

(20) Geoghegan, P. H.; Buchmann, N. A.; Spence, C. J. T.; Moore, S.; Jermy, M. Fabrication of rigid and flexible refractive-index-matched flow phantoms for flow visualisation and optical flow measurements. *Experiments in Fluids* **2012**, *52* (5), 1331-1347.

(21) Piruska, A.; Nikcevic, I.; Lee, S. H.; Ahn, C.; Heineman, W. R.; Limbach, P. A.; Seliskar, C. J. The autofluorescence of plastic materials and chips measured under laser irradiation. *Lab on a Chip* **2005**, *5* (12), 1348-1354.

(22) Ziolkowska, K.; Jedrych, E.; Kwapiszewski, R.; Lopacinska, J.; Skolimowski, M.; Chudy, M. PDMS/glass microfluidic cell culture system for cytotoxicity tests and cells passage. *Sensors and Actuators B: Chemical* **2010**, *145* (1), 533-542.
(23) Massalha, H.; Korenblum, E.; Malitsky, S.; Shapiro, O. H.; Aharoni, A. Live imaging of root–bacteria interactions in a microfluidics setup. *Proceedings of the National Academy of Sciences* **2017**, *114* (17), 4549-4554.
(24) Lee, J.-H.; Lee, S.-K.; Kim, J.-H.; Park, J.-H. Separation of particles with bacterial size range using the control of sheath flow ratio in spiral microfluidic channel. *Sensors and Actuators A: Physical* **2019**, *286*, 211-219.
(25) Song, J.; Tranchida, D.; Vancso, G. J. Contact Mechanics of UV/Ozone-Treated PDMS by AFM and JKR Testing: Mechanical Performance from Nano- to Micrometer Length Scales. *Macromolecules* **2008**, *41* (18), 6757-6762.
(26) Ma, K.; Rivera, J.; Hirasaki, G. J.; Biswal, S. L. Wettability control and patterning of PDMS using UV–ozone and water immersion. *Journal of Colloid and Interface Science* **2011**, *363* (1), 371-378.
(27) Mills, K. L.; Zhu, X. Y.; Takayama, S. C.; Thouless, M. D. The mechanical properties of a surface-modified layer on polydimethylsiloxane. *J Mater Res* **2008**, *23* (1), 37-48.
(28) Kuddannaya, S.; Chuah, Y. J.; Lee, M. H. A.; Menon, N. V.; Kang, Y.; Zhang, Y. Surface Chemical Modification of Poly(dimethylsiloxane) for the Enhanced Adhesion and Proliferation of Mesenchymal Stem Cells. *ACS Applied Materials & Interfaces* **2013**, *5* (19), 9777-9784.
(29) Zhang, M. Y.; Wu, J. B.; Wang, L. M.; Xiao, K.; Wen, W. J. A simple method for fabricating multi-layer PDMS structures for 3D microfluidic chips. *Lab on a Chip* **2010**, *10* (9), 1199-1203.
(30) Borde, A.; Larsson, M.; Odelberg, Y.; Hagman, J.; Löwenhielm, P.; Larsson, A. Increased water transport in PDMS silicone films by addition of excipients. *Acta Biomaterialia* **2012**, *8* (2), 579-588.
(31) Khanafer, K.; Duprey, A.; Schlicht, M.; Berguer, R. Effects of strain rate, mixing ratio, and stress–strain definition on the mechanical behavior of the polydimethylsiloxane (PDMS) material as related to its biological applications. *Biomedical Microdevices* **2009**, *11* (2), 503-508.
(32) Butt, H.-J.; Cappella, B.; Kappl, M. Force measurements with the atomic force microscope: Technique, interpretation and applications. *Surface Science Reports* **2005**, *59* (1), 1-152.

(33) Kroner, E.; Paretkar, D. R.; McMeeking, R. M.; Arzt, E. Adhesion of Flat and Structured PDMS Samples to Spherical and Flat Probes: A Comparative Study. *The Journal of Adhesion* **2011**, *87* (5), 447-465.
(34) Zhu, S.; Sun, H.; Lu, Y.; Wang, S.; Yue, Y.; Xu, X.; Mei, C.; Xiao, H.; Fu, Q.; Han, J. Inherently Conductive Poly(dimethylsiloxane) Elastomers Synergistically Mediated by Nanocellulose/Carbon Nanotube Nanohybrids toward Highly Sensitive, Stretchable, and Durable Strain Sensors. *ACS Applied Materials & Interfaces* **2021**, *13* (49), 59142-59153.
(35) Huang, H.; Dobryden, I.; Thorén, P. A.; Ejenstam, L.; Pan, J.; Fielden, M. L.; Haviland, D. B.; Claesson, P. M. Local surface mechanical properties of PDMS-silica nanocomposite probed with Intermodulation AFM. *Composites Science and Technology* **2017**, *150*, 111-119.
(36) Bajpai, A.; Tong, J.; Qian, W.; Peng, Y.; Chen, W. The Interplay Between Cell-Cell and Cell-Matrix Forces Regulates Cell Migration Dynamics. *Biophys J* **2019**, *117* (10), 1795-1804.
(37) Sharfeddin, A.; Volinsky, A. A.; Mohan, G.; Gallant, N. D. Comparison of the macroscale and microscale tests for measuring elastic properties of polydimethylsiloxane. *Journal of Applied Polymer Science* **2015**, *132* (42).
(38) Kenry; Leong, M. C.; Nai, M. H.; Cheong, F. C.; Lim, C. T. Viscoelastic Effects of Silicone Gels at the Micro- and Nanoscale. *Procedia IUTAM* **2015**, *12*, 20-30.
(39) Koetniyom, W.; Suhatcho, T.; Treetong, A.; Thiwawong, T. AFM force distance curve measurement for surface investigation of polymers compound blend with metal nanoparticles. *Materials Today: Proceedings* **2017**, *4* (5, Part 2), 6205-6211.
(40) Leclerc, E.; Sakai, Y.; Fujii, T. Cell Culture in 3-Dimensional Microfluidic Structure of PDMS (polydimethylsiloxane). *Biomedical Microdevices* **2003**, *5* (2), 109-114.
(41) Armugam, A.; Teong, S. P.; Lim, D. S. W.; Chan, S. P.; Yi, G.; Yew, D. S.; Beh, C. W.; Zhang, Y. Broad spectrum antimicrobial PDMS-based biomaterial for catheter fabrication. *Biomaterials Research* **2021**, *25* (1), 33.
(42) Lam, M.; Migonney, V.; Falentin-Daudre, C. Review of silicone surface modification techniques and coatings for antibacterial/antimicrobial applications to improve breast implant surfaces. *Acta Biomaterialia* **2021**, *121*, 68-88.
(43) Ramião, N. G.; Martins, P. S.; Barroso, M. L.; Santos, D. C.; Fernandes, A. A. In Vitro Degradation of Polydimethylsiloxanes in Breast Implant Applications. *Journal of Applied Biomaterials & Functional Materials* **2017**, *15* (4), e369-e375.
(44) van den Berg, D.; Asker, D.; Awad, T. S.; Lavielle, N.; Hatton, B. D. Mechanical deformation of elastomer medical devices can enable microbial surface colonization. *Sci Rep* **2023**, *13* (1), 7691.

(45) Hao-ran, L.; Xiao, L.; Xin-ye, N.; Hui-lin, Y.; Lei, Y. A novel hydrogel-polydimethylsiloxane elastomer for wound dressing application. *Ferroelectrics* **2018**, *523* (1), 104-111.

(46) Niculescu, A.-G.; Chircov, C.; Bîrcă, A. C.; Grumezescu, A. M. Fabrication and Applications of Microfluidic Devices: A Review. *International Journal of Molecular Sciences* **2021**, *22* (4), 2011.

(47) Ren, K.; Zhou, J.; Wu, H. Materials for Microfluidic Chip Fabrication. *Accounts of Chemical Research* **2013**, *46* (11), 2396-2406.

(48) Lin, L.-Y.; Kim, D.-E. Measurement of the elastic modulus of polymeric films using an AFM with a steel micro-spherical probe tip. *Polymer Testing* **2012**, *31* (7), 926-930.

(49) Sader, J. E.; Borgani, R.; Gibson, C. T.; Haviland, D. B.; Higgins, M. J.; Kilpatrick, J. I.; Lu, J.; Mulvaney, P.; Shearer, C. J.; Slattery, A. D.; et al. A virtual instrument to standardise the calibration of atomic force microscope cantilevers. *Review of Scientific Instruments* **2016**, *87* (9).

(50) Pickering, J. P.; Vancso, G. J. Influence of tip indentation depth on the adhesive behavior of viscoelastic polydimethylsiloxane networks studied by atomic force microscopy. *Macromolecular Symposia* **2001**, *167* (1), 189-199.

(51) Jopp, J.; Yerushalmi-Rozen, R. Autophobic Behavior of Polymers at the Melt−Elastomer Interface. *Macromolecules* **1999**, *32* (21), 7269-7275.

(52) Agaoglu, S.; Robles, M. C.; Smith, C. D.; Quake, S. R.; Araci, I. E. The effect of pre-polymer/cross-linker storage on the elasticity and reliability of PDMS microfluidic devices. *Microfluidics and Nanofluidics* **2017**, *21* (7), 117.

(53) Xiang, K.; Huang, G.; Zheng, J.; Wang, X.; xian Li, G.; Huang, J. Accelerated thermal ageing studies of polydimethylsiloxane (PDMS) rubber. *Journal of Polymer Research* **2012**, *19* (5), 9869.

(54) Hu, Y.; Suo, Z. Viscoelasticity and poroelasticity in elastomeric gels. *Acta Mechanica Solida Sinica* **2012**, *25* (5), 441-458.

(55) Hu, Y.; Chen, X.; Whitesides, G. M.; Vlassak, J. J.; Suo, Z. Indentation of polydimethylsiloxane submerged in organic solvents. *J Mater Res* **2011**, *26* (6), 785-795.

Chapter 4

Electrochemical and Nanostructural Characterization of Poly(3,4-ethylenedioxythiophene):Poly(styrenesulfonate) Films as Coatings for Neural Electrodes

Chapter 4 and **Chapter 5** report on the studies and characterization of poly(3,4-ethylenedioxythiophene) (PEDOT) using macroelectrodes and microelectrodes respectively. Following these studies, **Chapter 6** and **Chapter 7** explore and test the performance of PEDOT on tetrodes.

PEDOT, a well-characterized conducting polymer, has been applied for coating metal neural electrodes to improve their stimulating or recording performance. The coated electrodes possess advantages in better neuron attachment, lower impedance, and larger capacitance compared to the bare metal substrate due to the biocompatibility and porous surface of the polymer. However, the PEDOT-coated electrodes have frequently reported issues associated with mechanical instability, such as cracking and delamination. Solving this problem is crucial for stimulating electrodes, whereas a thick film is unnecessary for recording purposes. Moreover, the thickness control for the recording electrodes has rarely been investigated. In this chapter, I systematically studied and characterized PEDOT:PSS with CV and AFM to evaluate the electropolymerization of the polymer from the basic of its formation mechanism and analyze the surface morphology for a range of deposition times. The polymerization potential was obtained, and deposition charge density was optimized for recording neural electrodes. In addition, high-resolution AFM height and phase images reveal the heterogeneity of the polymer surface. The modified electrode was also tested for its electrochemical performance in a small potential window with both a standard electrochemical cell setup and stainless steel microscrews. The results showed that despite a shift of potential (0.42V) due to

the change of setup, the electrode functions well in the capacitive region without triggering redox reactions.

The work presented in **Chapter 4** has been published in *ACS Applied Polymer Materials* [1]. The project was conducted under the supervision of Prof. Richard Compton and Prof. Sonia Contera. Dr. Yuqi Chen assisted with the understanding and interpretation of the electrochemical analysis.

4.1 Introduction

Implantable neural devices are widely exploited in neuroscience research to probe electrically active cells [2]. However, due to their microscopic size and interfacial rigidity, many metal electrodes suffer from high impedance as well as being susceptible to surface fouling so limiting the signal-to-noise ratio and restricting the lifetime of implanted electrodes[2]. Since the development of conducting polymers (CPs) in the last century, broad attention has been given to electrode coatings on the surface of the electrodes to reduce these problems and to enhance the performance of neural electrodes. The layer of CP on the metallic or silicon substrate substantially reduces the impedance as the roughened, porous surface produces a larger electrochemical surface area [3]. The soft polymer layer also separates the hard substrate surface from the tissue, mitigating the immune response and there have even been reports of preferential in vitro and in vivo neuron growth[4]. Thanks to their superior conductivity, chemical stability[5], and biocompatibility, CPs have the potential to elevate the performance of traditional neural electrodes to new levels.

Poly(3,4-ethylenedioxythiophene) (PEDOT) is one of the most promising candidates for CP modified neural electrodes. PEDOT possesses good conductivity [5, 6] and has been shown in vitro to promote cell adhesion and exhibit low cytotoxicity [7], and little immune response following electrode insertion in vivo [8], which is crucial for long-term in vivo recording.

Common ways of PEDOT deposition include spin coating[9] and electropolymerization. However, for electrodes such as tetrodes, it is challenging to carry out spin coating, as cross-linking between the different recording sites can easily arise. Electropolymerization is a better and more controllable approach where the fabrication process can be tailored by tuning the polymerization conditions (potential/current, polymerization charge density, and dopant). **Table 4.1** summarizes several PEDOT electropolymerization methods.

Cui et al.[10] reported one of the earliest attempts at electrochemically depositing PEDOT onto a metal electrode for neuronal recordings. The coated electrode exhibited better electrical properties in terms of impedance and charge storage capacities compared to the bare electrodes. Their work focused on coating, particularly with stimulating electrodes [6], demonstrating that there is a charge injection limit with increasing thickness of the coating and that a thicker film is always accompanied by mechanical failure such as cracking and delamination. For recording electrode arrays, Ludwig et al.[11] showed that compared to uncoated sites, those coated with PEDOT provided higher quality recording in terms of better signal-to-noise ratio and a greater number of viable units registered. Moreover, they also found that the impedance decreased with increasing deposition but was limited for deposition charges larger than 260 $mCcm^{-2}$.

The mechanism of electropolymerization of PEDOT has been studied. The reaction scheme is shown in **Scheme 4.1**. Applying current or potential to the working electrode initiates the formation of the radical cation of the PEDOT monomer leading to the growth of the polymer film possibly via radical-radical dimerization followed by further electrochemical oxidation which with further addition of monomeric units forming oligomeric chains. The ultimate polymer chain is a combination of oligomeric and monomer radicals, with positive charges spread along the backbone. The charge requires the polymerization to be accompanied by the uptake of anions from the solution. Anions that have been used include perchlorate (ClO_4^-:), benzenesulfonate (BS), p-toluenesulfonate (pTS), dodecylbenzene sulfonate (DBS), and

tetrafluoroborate (BF_4^-) leading to different bulk properties [12, 13] but the use of polystyrene sulfonate(PSS) is common as is evident from **Table 4.1** partly due to the easy processability of the films [14] and partly since the synthesis is claimed to be green [14]. The transition of the growing polymer from the molecular to the macroscopic scale has been explored by Tamburri et al.[15] who discussed the growth mechanism of PEDOT in terms of polymer nucleation with the subsequent 3D growth blanketing the entire surface. Note that at high potentials the $PEDOT^+$ can undergo further oxidation, but the resultant products are complicated and have been covered by other literature [16, 17, 18]. Such overoxidation is likely to lead to irreversible chemical changes with a negative impact on essential properties notably conductivity [15, 16].

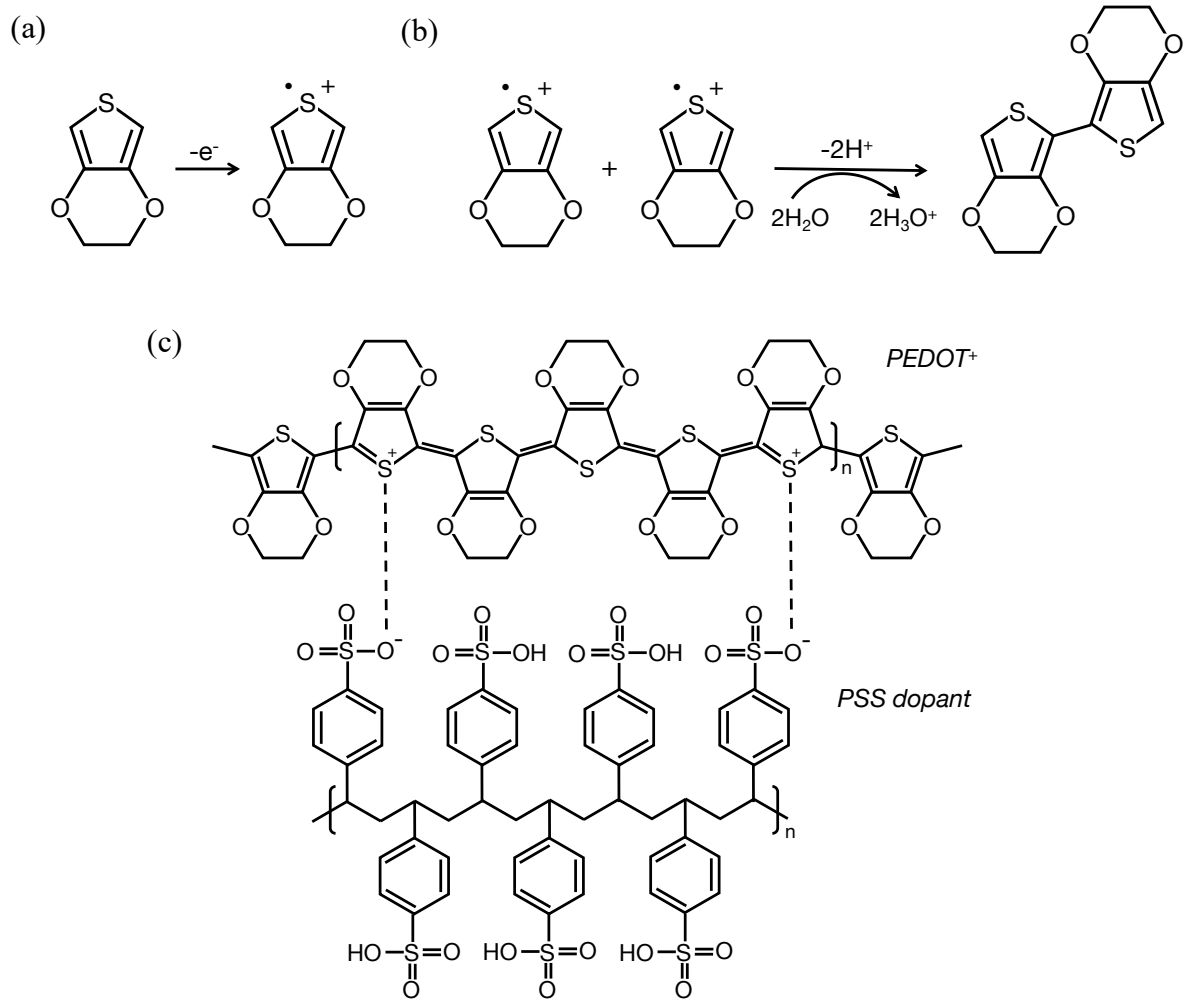

Scheme 4.1: Formation of PEDOT: PSS by electro-polymerization on the working electrode. The polymerization scheme starts with **(a)** monomers being initially oxidized at the working

electrode, and then **(b)** two oxidized monomers form a dimer. Dimers undergo further oxidation producing oligomeric radicals, which combine with other radicals in the end, **(c)** giving the polymer chain. The chain has a positively charged backbone and hence requires uptakes of PSS- or other anions from the solution to neutralize the charge. PEDOT: Poly(3,4-ethylene dioxythiophene); PSS: Polystyrene sulfonate.

PEDOT: PSS is attractive for biological applications because of its mixed ion-electron conductivity which is useful in converting biological signals (ionic motion) into electrical signals (electronic motion) [19]. The mixed conduction emerges from the two-phase nature of the material, where PEDOT-rich regions are embedded with PSS-rich regions [14]. The hydration of PSS is thought to help ion transport within the structure, and the aggregated PEDOT regions are responsible for hole transport [9, 14, 20]. PEDOT-rich and PSS-rich regions are interconnected, which implies the whole bulk is involved in the charge interaction giving rise to a volumetric capacitance. Furthermore, PEDOT:PSS possesses a relatively high specific capacitance originating from the large effective double-layer area due to its porous surface [9, 14, 20]. The capacity is thus closely related to material morphology.

The morphology reflects several factors, such as the polymerization method used, the solvent, and the choice of dopant. Castagnola et al. [21] investigated the effect of different electro-polymerization routes, where potential scanning approaches created the most homogeneous surface. However, very few researchers use this approach due to the uncontrollable current [22]. A range of dopants [12] and solvents [13] were also studied to address the issues of chemical and mechanical stability.

Whilst it has been established that PEDOT-modified electrodes demonstrate a lower impedance than bare electrodes (especially at low frequency, <100 kHz [6]), the main ongoing challenge relates to the mechanical stability of the film which is closely related to the film thickness. This is a particular problem for stimulating electrodes rather than recording

electrodes where in the former case thicker films are used to improve the charge injection capacity so that the injected charge is large enough to trigger neural membrane depolarization. On the other hand, a thick film is unnecessary for a recording electrode, in particular where little outperformance can be gained over the impedance. In addition, previous research has reported delamination and cracking problems associated with a thick coat, and reduced biocompatibility [6, 7, 22, 23]. For a film with charge deposition larger than 0.5 C cm^{-2}, PEDOT-coated electrodes showed no advantage over bare Pt in terms of biological benefit [7]. There is so far very little research about film thickness reported in the literature for recording electrodes. Other methods, notably incorporation of PEDOT:PSS hydrogel [24] to maintain film integrity is useful for macro sensor fabrication but not easy for microwire metal electrodes, especially those with closely packed detection spots (e.g. as in the tetrodes often used in vivo) where the hydrogel easily overgrows and cross-connects different detection points. Thickness control is an obvious gap in the published research and is an effective way to control and improve the film mechanical stability for recording electrodes. In addition, PEDOT as a volumetric capacitor, the morphological change post-implantation is crucial but has not been investigated.

In this chapter, the electro-deposition of PEDOT: PSS is systematically studied and characterized with Cyclic Voltammetry (CV) and Atomic Force Microscopy (AFM) from the perspective of use for neural electrodes in recording mode. The surface morphology is studied as a function of the conditions of deposition. The roughness of the surface is quantified; surface nanoscale heterogeneity is revealed and discussed. The surface morphology is assessed as a function of exposure to aqueous media in the form of deionized water and phosphate buffered solution (PBS) with the latter being a suitable medium for short-term in vitro characterization [26]. Electrochemical measurements, both Faradaic and capacitive, are investigated both with a well-defined reference electrode (a saturated calomel electrode) and with a stainless steel (SS) microscrew pseudo-reference electrode mirroring the typical approach adopted for in vivo

experiments (in rodents) where both such screws act both as reference and counter electrodes. The data collected could provide an essential basis for the use of PEDOT: PSS as a coating for neural metal electrodes particularly when used in recording mode.

Table 4.1: A summary of PEDOT:PSS electropolymerization methods.

Material[a]	Substrate[b]	Method	Voltage Applied[c]	Current Applied	Deposition Time	Ref
PEDOT:PSS	Au	Galvanostatic	/	0.5~2.0mAcm^{-2}	Charge deposition from 133~1667mC cm^{-2}	10
		Potentiostatic	1.1V (vs SCE)	/		
PEDOT:PSS	Pt	Galvanostatic	/	0.64mAcm^{-2}	10~500s	6
PEDOT:PSS PEDOT:Cl	Pt	Galvanostatic	/	0.2mAcm^{-2}	71~1071s	27
PEDOT:PSS	Pt, ITO[c]	Potentiostatic	0.0→0.5V for 10s 0.75→1.4V for 110s (vs SCE)	/	120s	15
PEDOT:PSS	Au	Cyclic Voltammetry	5~25mVs^{-1} -0.9V~1.2V (vs SCE)	/	/	21
		Potentiostatic	0.8V, 0.9V, 1.1V (vs SCE)	/	10~50s	
		Galvanostatic	/	0.03~0.5mAcm^{-2}	10~900s	
PEDOT:PSS	Glassy Carbon, Au	Potentiostatic	1V (vs Ag|AgCl)	/	Charge limited to 260mCcm^{-2}	28
PEDOT:PSS	Pt	Galvanostatic	/	0.5mAcm^{-2}	100~2000s	7
PEDOT:ClO_4 PEDOT:BS PEDOT:PTS PEDOT:DBS PEDOT:PSS	Pt	Galvanostatic	/	0.5mAcm^{-2}	33min20s	12

PEDOT:TEAP	Ir	Galvanostatic	/	0.5mAcm^{-2}	Charge deposition from 50~1000mCcm^{-2}	[11, 29]
PEDOT:BF_4	PtIr	Galvanostatic	/		Limit charge to 260mCcm^{-2}	[13]
PEDOT:PSS + MWCNT	Pt	Galvanostatic	/	0.02mAcm^{-2}	50~400s	[30]
		Potentiostatic	1V (vs Ag|AgCl)	/	50~400s	
PEDOT:PSS + MWCNT	Pt/Ir	Potentiostatic	1.3V (vs Ag|AgCl)	/	30s	[31]

[a] *PEDOT: Poly(3,4-ethylene dioxythiophene). PSS: Polystyrene sulfonate. TEAP: Tetraethylammonium perchlorate.* ClO_4^- *: perchlorate. BS: benzenesulfonate. pTS: p-toluenesulfonate. DBS: dodecylbenzene sulfonate.* BF_4^- *: tetrafluoroborate. MWCNT: Multi-walled Carbon Nanotube.*

[b] *Au: Gold. Pt: Platinum. ITO: Indium Tin Oxide. Ir: Iridium. Pt/Ir: Platinum/Iridium Alloy.*

[c] *SCE: Saturated Calomel Electrode. Ag|AgCl: Silver Chloride Electrode.*

4.2 Materials and Methods

4.2.1 Materials

3,4-ethylenedioxythiophene (EDOT, 97% purity), poly(sodium 4-styrenesulfonate) (NaPSS, average Mw = 70,000), and phosphate buffer saline(PBS) were purchased from Sigma Aldrich and used as received. Deionized water with a resistivity of 18.2 MΩ cm at 298 K (Millipore, Millipak Express 20, Watford, UK) was used.

A Pt macro disk ($Area = 0.02cm^2$) and a Pt single crystal (Miller indices (100), $Active\ Area \approx 0.22cm^2$) were used as working electrodes to perform electrochemical characterization and morphological studies.

4.2.2 Electropolymerization

Experiments were carried out in a thermostated Faraday cage using a μ-AutolabIII potentiostat /galvanostat (Autolab B.V., Utrecht, The Netherlands) with NOVA software. A standard three-electrode setup was employed with Pt as the working electrode, a saturated calomel electrode (SCE; BSi Inc., West Lafayette, IN, USA) as the reference electrode, and a graphite rod as the counter electrode. All working electrodes were washed with deionized water and dried with Nitrogen prior to electro-polymerization. The Pt macro disk was polished on soft lapping pads with alumina powder of decreasing size (1.0, 0.3, and 0.05μm; Buehler IL, U.K) each time before each experiment. The Pt single crystal electrode was cleaned by heating to red heat using a Bunsen burner for 10s to remove surface impurities.

The electro-polymerization was conducted potentiostatically in a solution containing 10mM EDOT and 0.1mM NaPSS (0.7% (w/v)) [15, 21]. Constant potentials with values between 0.5V to 1.5V were applied for 0.5s to 120s. The cell solution was kept at 25 $\pm$ 1˚C and degassed with nitrogen for 10 min before each electrochemical experiment.

4.2.3 Electrochemical Characterization

All the electrochemical characterizations were carried out in a three-electrode cell setup with either a saturated calomel electrode (SCE) as the reference electrode and a graphite rod counter electrode or, to mimic the in vivo setup, stainless steel microscrews (SS, M1.4) were used as the reference and counter electrodes. Electrodes were immersed in polymerization solution (10 mM EDOT and 0.1 mM NaPSS) or 0.1 mM NaPSS solution for investigation via cyclic voltammetry (CV) with a wide potential scanned between 0.5 V to 1.7 V and a scan rate of 50 mVs^{-1}. Small potential window scans from -100mV to 100mV with scan rates 25, 50, 100, and 200 mVs^{-1} in 0.01M PBS (0.01 M PBS is equivalent to the 1X PBS notation, and the ionic content is included in Table 5.1 of the next chapter for further analysis.) were undertaken to test electrode functioning in the range of neuronal activity.

To obtain the reference potential shift between the SCE/graphite setup and the SS/SS setup, both wide scans (-0.8 V to 2.0V) and small scans (-100 mV to 100 mV) were carried out separately with these two setups, immersing a modified Pt electrode (about 50 mC charge deposition) in 0.01 M PBS solution.

4.2.4 Morphological Characterization

The polymer film morphology was analyzed by Cypher atomic force microscopy (Cypher AFM, Asylum Research, Oxford Instrument, CA, USA). Olympus AC240TSA cantilevers (f_c~70 kHz, k_c~2.0 Nm^{-1}) were used to probe the surface. Images of topography and phase were acquired by tapping mode in deionized water or 0.01 M PBS and were collected and processed by Igor Pro software (Oxford Instruments Asylum Research). The cantilever was calibrated by the Sader method [32] and tuned before any test, so the phase was 90° when the cantilever was not in contact with the sample. During the tapping, the AFM operates in a small

amplitude range (<10 nm) [33]. The root-mean-square (RMS) roughness of each full image was calculated by the following equation:

$$R_{rms} = \sqrt{\frac{1}{N}\sum Y_i^2} \tag{4.1}$$

where R_{rms} is the RMS roughness, N is the number of data points and Y is the height value of each data point [34].

4.3 Results and Discussion

In this section, I first discuss the electrochemical properties of EDOT to determine the optimum coating potential. Subsequently, the selected voltage was applied to investigate the potentiostatic mode of coating for different deposition times and thus optimize the process. The film morphology, roughness, and stability were then investigated utilizing AFM in tapping mode. Finally, with the deposition potential and time optimized, the final modified electrode was tested in 0.01 M PBS as a good medium for short-term in vitro electrochemical characterization [26].

4.3.1 Electrochemical Characterization of EDOT

First, the electrochemical properties of EDOT in an aqueous solution were analyzed using cyclic voltammetry (CV). Initial CV scans started at a potential of 0.50 V (vs. SCE), swept anodically to 1.5 V, then swept cathodically to -0.80 V, and eventually returned to 0.50 V using a bare disc Pt electrode immersed in 10 mM EDOT and 0.1 mM NaPSS solution (**Figure 4.1**(a,b)). The choice of 0.5 V as the initial potential is to ensure no Faradaic reaction happens until the scan has reached higher potentials than the start potential. Otherwise, the resulting voltammogram would be distorted. For the anodic scan, a peak (P1) can be observed at around 1.4 V (vs. SCE), together with a shoulder (S1) in the proximity of 1.0 V. On the cathodic scan, a reduction peak P2 is seen with a peak potential of -0.55 V. The magnitude of this peak is

much smaller than the oxidation peak P1. To understand S1 and evaluate its nature, I recorded further CVs in which the maximum anodic potentials (E^+) were 0.50 V and 1.0 V, keeping the cathodic limit the same as before. The resultant CVs are compared and shown in **Figure 4.1**(a, b). The red line (E^+ = 0.5 V) has neither a reduction peak (P2) at -0.55 V nor a small oxidation peak at -0.42 V, implying no PEDOT formation at its maximum potential. For the reduction peak (P2) to be seen in the reverse scan, a threshold potential of ca. 1.0 V in the anodic scan is required. The presence of the reduction peak confirms there was Faradaic oxidation at S1.

Comparison with the literature [15] suggests that S1 corresponds to monomer oxidation and hence to the onset of polymerization.

Next, potential step chronoamperometry was applied to a solution of identical composition as used for the CV, with the value of the applied potential of the Pt electrode jumping from 0V (vs. SCE) to a fixed value ranging from 0.5 V to 1.5 V (**Figure 4.1**(c)). The total charge passed in the chronoamperograms up to a time of 120 seconds was calculated and summarized (**Figure 4.1**(d)). At low potentials, little current and hence charge was seen or passed in the chronoamperograms. After the onset of monomer oxidation around and near 1.0 V (vs. SCE), currents flow nearly steadily, with increasing charge and current seen for increasing potentials up to 1.0 V. Above this potential, the initially steady current dies away after prolonged electrolysis as is apparent in the current–time curve measured for a potential step to 1.1 V. This loss of electroactivity is especially apparent in **Figure 4.1**(d) where for potentials more anodic than 1.1 V the charge passed drops markedly. It is likely that for potentials of 1.1 V or more there is over-oxidation of the polymer film leading to irreversible chemical changes [15, 16] in addition to consumption of monomer.

To investigate this hypothesis further, the Pt electrode was coated in potentiostatic mode at 1.0 V for 120 s, transferred to a 0.1 mM NaPSS solution and a CV scanned (0.5 V→1.7 V→-0.8 V→0.5 V vs. SCE). The result is shown in **Figure 4.1**(e) and compared with the same scan

in a solution with the presence of 10 mM EDOT (**Figure 4.1**(f)). The former shows that the application of potential larger than 1.1 V to a pre-formed film completely destroyed the oxidative electroactivity. Therefore, after the first scan, the CV of the subsequent scan had little difference from a scan with a bare Pt in NaPSS. It is evident that the sustained application of an oxidizing potential in excess of ca. 1.0 V to the film causes over-oxidation and the loss of voltammetric signal likely due to the loss of film conductivity as observed by others [16].

It was concluded that for potentiostatic deposition the optimum potential was +1.0 V (vs. SCE) and that potentials in excess of this value caused an irreversible chemical change to the film. Next, I investigated the impact of the length of time of the deposition.

4.3.2 Morphological Characterization of EDOT

To optimize the coating time, an initial series of films were produced on a Pt single crystal (100) of size 0.22 cm^2 compatible with the AFM used for imaging the surfaces and for measuring their roughness. The procedures are illustrated in **Scheme 4.2**. In general, a potentiostatic deposition of PEDOT was performed on a Pt single crystal at 1V for a range of times depending on the particular test. After coating, the electrode was dipped in deionized water, blown with nitrogen to remove excess liquid, then left at room temperature for an hour or less depending on the exact experiments of interest before further testing. Note that beyond the coatings indicated in **Scheme 4.2**, thicker films have been made using a Pt macro disk electrode, but the surface was found to be mechanically fragile and, notably, easily cracked for example by simply blowing dry nitrogen over the surface (Appendix C Figure C.1). No such behavior was inferred for the coverage developed on my thinner layer coated electrodes. Film morphologies were observed in an aqueous environment formed from either a few drops of deionized water or PBS placed on the film before imaging using AFM tapping mode.

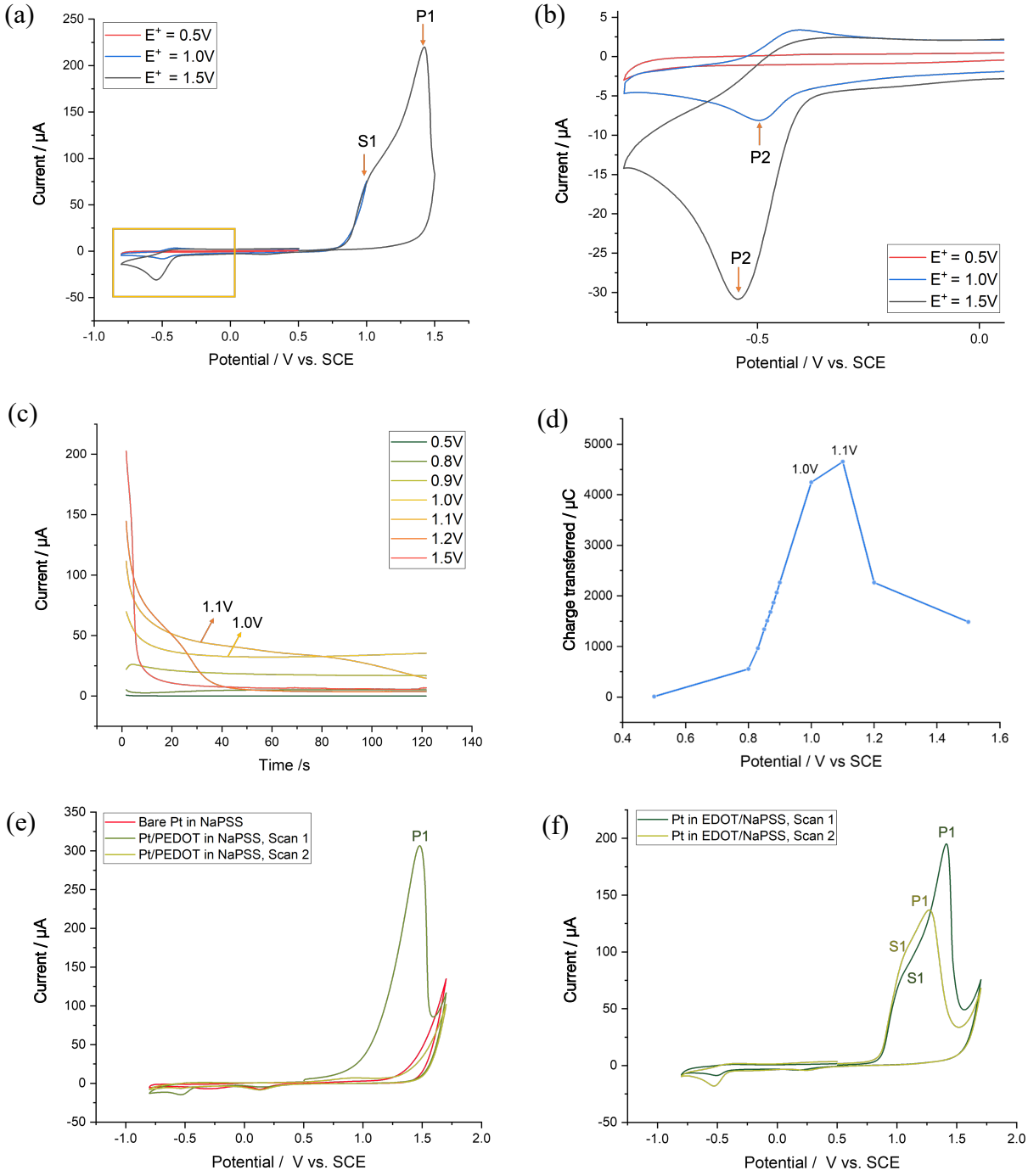

Figure 4.1: (a,b) CV of bare Pt disc electrode immersed in 10 mM EDOT and 0.1 mM NaPSS solution. The scan started at 0.5 V and was swept anodically up to different limits (E^+ = 0.5 V, 1.0 V, and 1.5 V vs. SCE), then reverse scanned to a fixed cathodic limit at -0.8V, and eventually returned to 0.5 V (0.5 V → E^+ → -0.8 V → 0.5 V vs. SCE). The yellow box for (a) is enlarged and shown in (b). **(c)** Chronoamperograms using the same electrode and solutions were recorded at potentials between 0.5 V and 1.5 V vs. SCE. **(d)** Variation of the amount of charge transferred during electropolymerization in (c) with potential 0.5 V ~ 1.5 V vs. SCE. **(e)**

Comparison of the CV of the modified Pt (green and yellow) and bare Pt (red) disc electrode in 0.1 mM NaPSS (0.5 V → 1.7 V → -0.8 V → 0.5V vs. SCE). **(f)** CV scans of a Pt disc electrode in 10 mM EDOT and 0.1 mM NaPSS (0.5 V → 1.7 V → -0.8 V → 0.5 V vs. SCE).

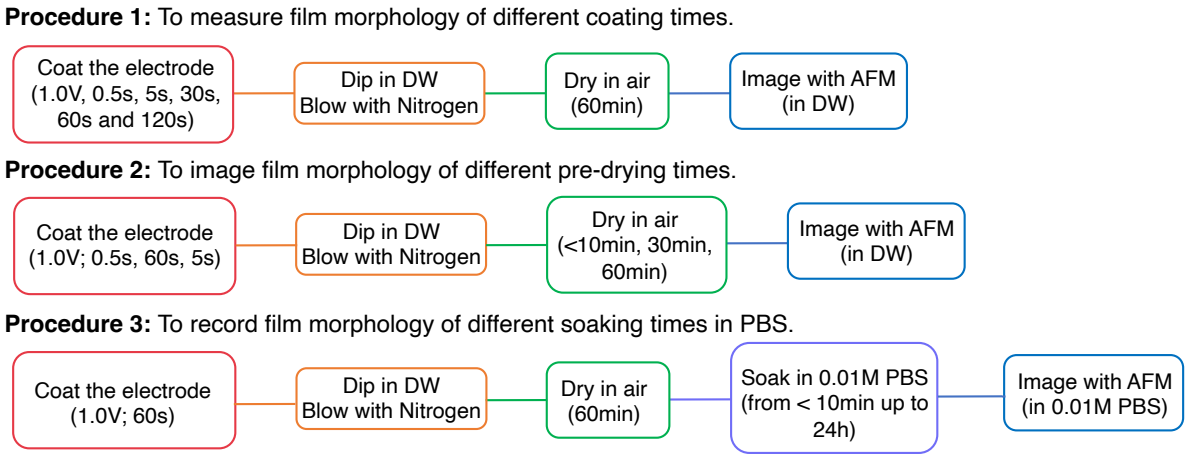

Scheme 4.2: The procedures for morphological characterization. DW: Deionized water. PBS: phosphate-buffered saline.

Note that all of the final imaging steps were carried out in aqueous conditions (deionized water or PBS). Performing the imaging in liquid provided several advantages notably giving higher resolution compared to those obtained in the air, where the resolution was compromised at a small scale because of a water moisture layer on the polymer surface makes the interaction potential between the tip and the sample more complex, decreasing resolution [35] (Appendix C Figure C.2(a)). In addition, in the in vivo environment, the ion species responsible for interaction are primarily provided by extracellular fluid (ECF), where a 0.01 M PBS can be useful as a short-term in vitro substitution for electrochemical and nanostructural characterization [26]. From the polymer deposition characterization point of view, the disadvantage of imaging in liquid was that the polymer would inevitably swell to a larger size than in air. To minimize such effects, I performed AFM imaging as fast as possible (within 30

min) after adding the liquid drop to the dried polymer. In addition, drying in the air before imaging also helps to better observe the small features. From Appendix C Figure C.2(b), the polymers were in circular shape (ca. 50 nm) until a drying time of 60 min where a finely meshed and porous structure (Appendix C Figure C.2(c)) similar to natural cotton balls (Appendix C Figure C.2(d)) could be observed.

For Procedure 1 and 2 (**Scheme 4.2**), the polymer was imaged in deionized water instead of PBS due to the much faster rate of swelling of the film in PBS. Given the same pre-drying time in the air (60 min) and the similar soaking time in solution (<10 min), the film roughness was larger in PBS than in deionized water (Appendix C Figure C.3). More direct visual evidence of swelling is shown in Appendix C Figure C.4(i) and Figure C.5(d), which indicate that the polymer swells into circular bulbs (ca. 50 nm) in PBS, but that a finely meshed and porous structure was visible in deionized water. The images in PBS are thought to be close to those expected for ECF. Procedure 3 was applied to keep track of polymer swelling in 0.01 M PBS from less than 10 min up to a prolonged period of 24 h. The final imaging was conducted in the same solution as the soaking to prevent disturbing the surface from changing the solution. The swelling of the film in PBS will reach an equilibrium which will be discussed in **section 4.3.2.3**.

Overall, in the context of the metal electrode for neuronal recording application environment, swelling of the pre-dried films following fabrication takes place. However, performing imaging in deionized water after a pre-drying period produced enhanced resolution and detail in the surface features, and imaging in 0.01 M PBS provided a satisfactory environment for transient studies. These approaches and initial observations gave a basis for recording the more detailed data given in the following sections.

4.3.2.1 Film Morphology of Different Coating Times

For the results reported in this section, Procedure 1 (**Scheme 4.2**) was followed. **Figure 4.2** summarizes the images for various coating times and at different magnification scales.

The images of the 0.5s coating surface in **Figure 4.2** reveal the very initial stages of polymer growth on a Pt substrate for the first time at high resolution (from 5×5 μm to 1×1 μm scan frames). The short-time deposition sample consisted of circular segments growing next to each other, enclosing a pore in the middle with an average depth of 6 nm (Appendix C Figure C.6). The presence of pores could lead to the exposure of the underlying Pt surface. For the 5s deposition sample, small granules (bright dots) can be observed, and they are connected by a finely meshed network. These grains are inferred to be growing polymer nuclei, PEDOT, embedded in the PSS matrix, as proposed previously [14, 15]. From the images, a large number of nuclei (ca. 15 ± 2 per μm^2) form within the first 5 s of growth (Appendix C Figure C.7) in contrast to observations using indium tin oxide [15] (ca. 4 ± 2 per μm^2) as the substrate where much fewer nuclei were observed indicating possible benefits of using platinum electrodes for reproducible and more homogeneous films. These nuclei grew in size as the deposition proceeded, and the average film thickness (**Table 4.2**) estimated from the amount of charge transferred) increased. **Figure 4.3** records the variation of surface RMS roughness with deposition time; the initial roughness is only about 1nm larger than the bare substrate, indicating a relatively flat surface for 0.5 s coating. For deposition time of 5 s or above the surface roughness reached a steady value.

To assess the coating coverage, the phase images of films formed by 0.5 s and 5 s coating were recorded as shown in **Figure 4.4**. Phase images contain information of the topography as well as the energy dissipation at the interface. The contrast in the phase signals gives insights into different types of materials over which the cantilever is being scanned, where a hard surface usually produces a higher phase signal compared to softer areas, and is related to the energy

dissipated at the interface [14, 36, 33]. Significant contrast between different areas was obtained in the 0.5 s coating (**Figure 4.4**(a)), in which the labeled points correspond to peaks of phase along the measurement line across the surface. The corresponding positions relate to the pores in the height image suggesting the Pt surface may be partially exposed at these sites. In the phase diagram recorded for the 5 s coating, although the line passes through several dark and bright regions (**Figure 4.4**(b)), their phase has little difference without any dominant peaks observed as in the 0.5 s image. The phase variation, in this case, is attributed to scanning through the PSS-rich and PEDOT-rich regions [14].

It has been reported that PEDOT: PSS cast onto a glass substrate [14] is a two-phase material consisting of PEDOT-rich and PSS-rich grains, where a PEDOT-rich grain is about 10~20 nm in size and PSS-rich grain is about 20~30 nm [14, 37]. The single grain size is similar to the phase variation period (16nm, evaluated by averaging the peak separation) along the drawn line imposed in **Figure 4.4**(b). Further zooming into the 5 s deposition image gives **Figure 4.5**(a, b), from which one can observe that bright regions in the height image (e.g. Box A) are dark in the phase image and vice versa (e.g. Box B). The inhomogeneous polymer surface is shown schematically in **Figure 4.5**(c). When the polymer is immersed in an aqueous environment, the PEDOT-dominant zones (Box B) are expected to be relatively hydrophobic in comparison to the PSS-dominated parts which are thought to take up water and hence are expected to swell and soften. The swelled polymer leads to higher height signals, but the soft areas are assigned to the dark phase signals. A rough estimation from **Figure 4.5**(a) suggests that the order of magnitude of a PEDOT-dominant region is about 70 nm, and the PSS-dominant region is about 80nm, which means every one of these regions consists of several PEDOT, PSS-rich grains.

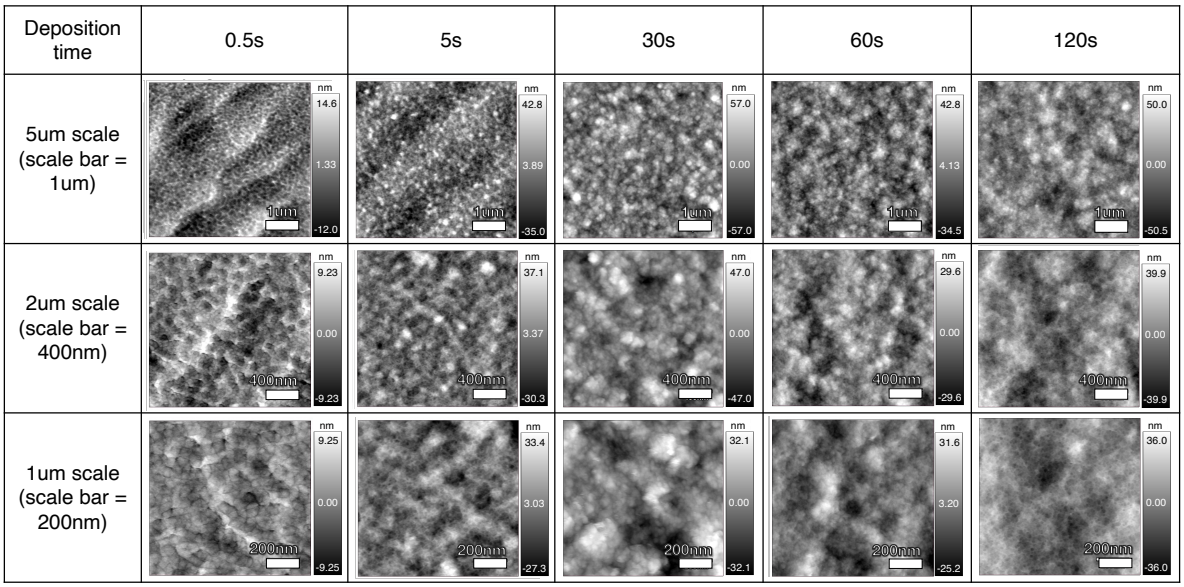

Figure 4.2: The morphology of PEDOT: PSS coated Pt electrode surfaces obtained by tapping mode AFM in deionized water. Deposition times range from 0.5 s to 120 s, and the images are magnified to different scales (5, 2, and 1 µm scan frames). The scale bars for the panel are 1µm, 400 nm, and 200 nm from the top to the bottom row respectively.

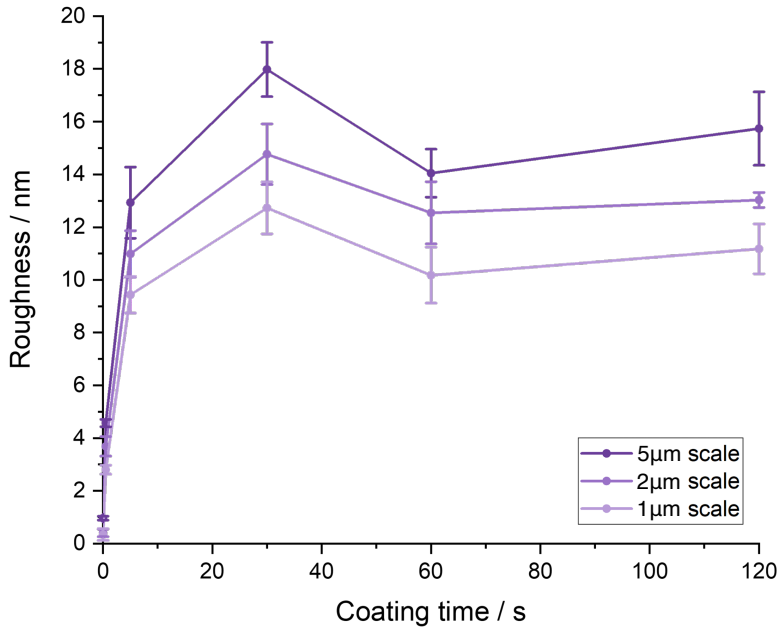

Figure 4.3: The RMS roughness of the PEDOT: PSS surfaces in Figure 4.2. The y-intercepts (coating time = 0 s) are the RMS roughness of the bare Pt electrodes. The error bars represent the surface roughness variation in three different spots on the film.

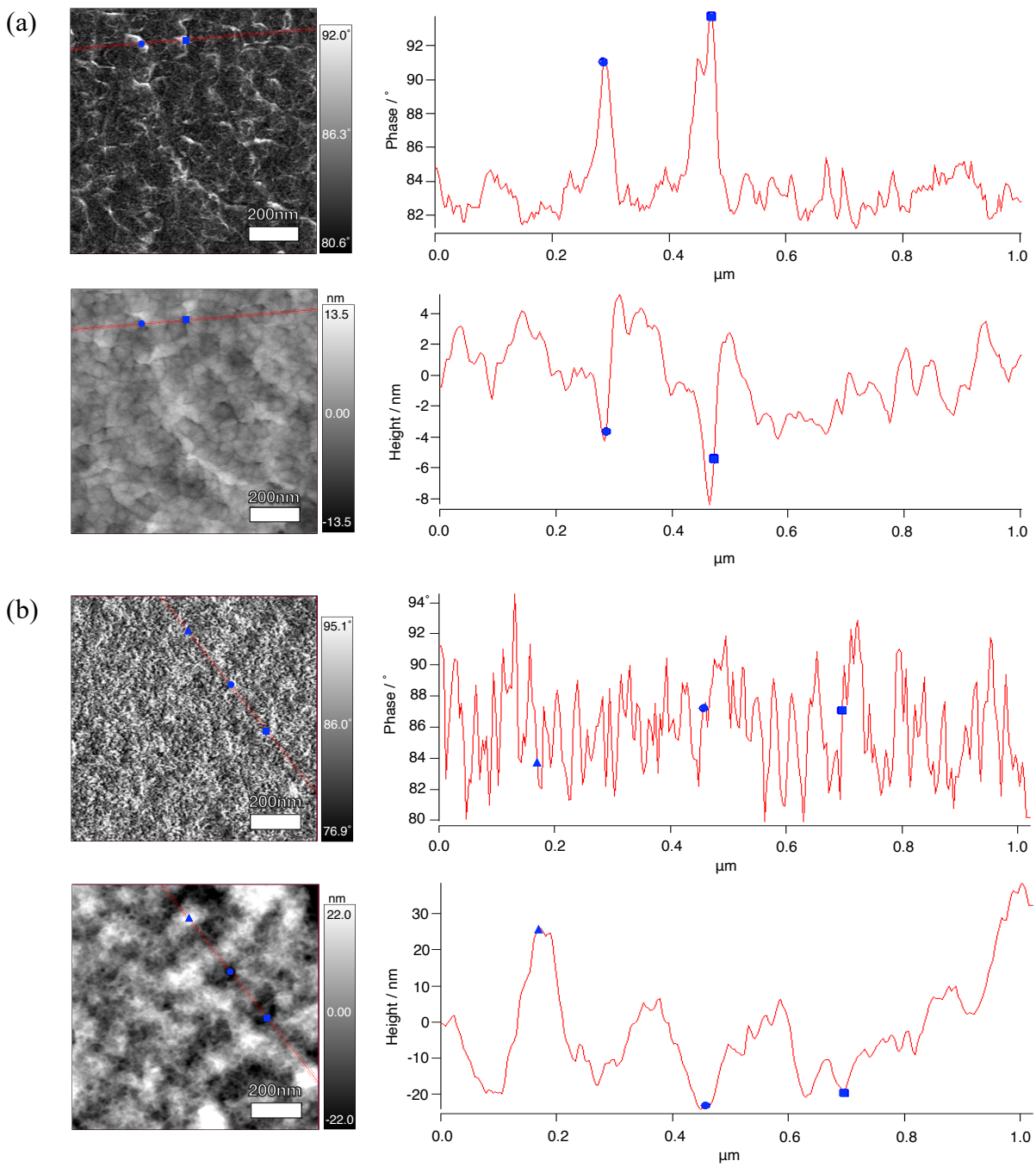

Figure 4.4: Top: Phase images and the corresponding phase variation along the red lines marked. **Bottom:** height images and the corresponding height variation along the red lines marked. Images were taken in DW with tapping mode AFM. All scale bars represent 200 nm. A red line is drawn to trace the height and phase variation across the surface, and the results are shown in the graphs on the right. **(a)** 0.5 s coating and dried in air for 1h. Two positions, corresponding to the peaks in phase data, are labeled by a circle and a square respectively. The peaks of the phase coincide with points close to the minima of the height. **(b)** 5 s coating and dried in air for 1h. The red line passes through several bright and dark regions in the height

image, but phase images illustrate less difference compared to (a), except the phase signal for the bright spot in the height image (triangle) is slightly lower than the phase of dark spots in the height image (sphere and square).

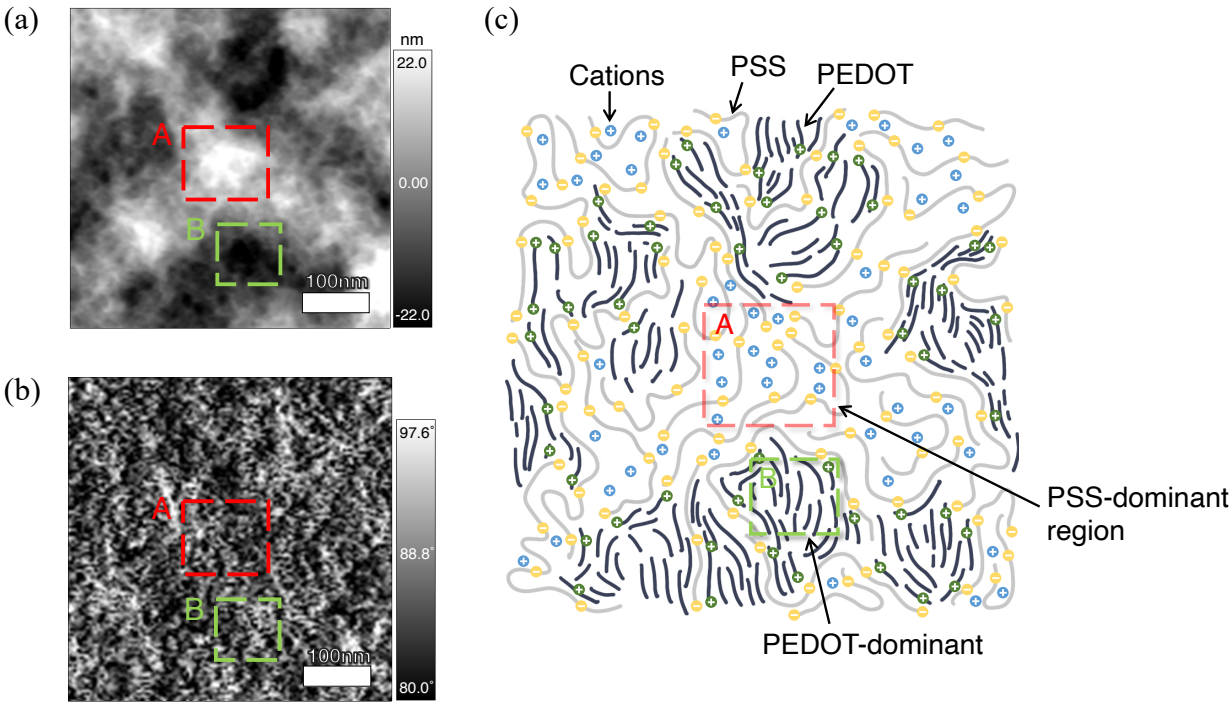

Figure 4.5: (a, b) Height and phase AFM images in deionized water: zoom in on the 5 s deposition surface. Scale bars: 100 nm. **(c)** Schematic generalization of the inhomogeneous distribution of material on the surface. Adapted with permission from [14] (Copyright 2017, John Wiley and Sons). Grey line and yellow charge: PSS^- chain and the excess charges on the chain. Dark line and green charge: $PEDOT^+$ polymer and its charge. Blue charge: cations in the solution. Box A: PSS-dominant region. Box B: PEDOT-dominant region.

Table 4.2: Summary of average charge transferred density during chronoamperometry, and estimation of average film thickness on the Pt electrode.

Coating time (s)	Average charge transferred density ($mCcm^{-2}$)	Estimation of average thickness[a] (nm)
0.500 ± 0.001	0.49 ± 0.04	3.2 ± 0.3
5.000 ± 0.001	4.6 ± 0.4	30 ± 3
30.000 ± 0.001	22 ± 2	150 ± 10
60.000 ± 0.001	47 ± 4	310 ± 30
120.000 ± 0.001	87 ± 7	570 ± 50

[a] *Assume the total volume of the polymer deposited evenly across the electrode substrate.*

4.3.2.2 Film Morphology Resulting from Different Pre-drying Times

In this section, Procedure 2 (**Scheme 4.2**) was followed to prepare the imaging samples.

The aim was to inspect the change of surface morphology over the drying time as it could provide information on how long time after coating should the neuronal probe be used biomedically and also to test the variation of surface roughness due to drying. The AFM images are shown in Appendix C Figure C.4, and the roughness is reported in **Figure 4.6**(a). The polymer swelling over a short time of drying (<60 min) was significant as the mesh-like structure disappeared and was replaced by circular bulbs on the surface (Appendix C Figure C.4). As a result of swelling, all the films exhibited increasing roughness with decreasing drying times in the air (**Figure 4.6**(a)). The roughness of the films formed by 5 s and 60 s of electro-deposition were similar throughout the drying time, but the 60 s film has its roughness variation within 1nm for all scales. Moreover, polymers were prone to adhere to the cantilever tip producing blurred images for a short drying period (Appendix C Figure C.4(a, e)). Therefore,

to have a film securely attached to the electrode, a long enough drying time needs to be allowed before any tests are made that might potentially rupture the surface.

4.3.2.3 Film Morphology of Different Soaking Times in PBS

In this section, Procedure 3 (**Scheme 4.2**) was followed to prepare the imaging samples.

The aim is to conduct a short-term in vitro characterization within an ionic solution, 0.01 M PBS functions as an appropriate medium. A 60 s coating by performing potentiostatic deposition was selected as it is the point where its roughness had reached its plateau value (**Figure 4.3** after 5 s) and had the least roughness variation with different drying times (**Figure 4.6**(a)).

From the AFM images (Appendix C, Figure C.5), the faster swelling rate compared to deionized water turned the polymer quickly into spherical shapes when put into PBS for less than 10min. The trend in **Figure 4.6**(b) suggests that with the prolonged soaking time, the polymer swelling will reach equilibrium as the roughness value (solid line) fluctuates around its average (dash line) for all scales throughout the soaking time. The results are expected as PBS contains a greater number of ions than deionized water, increasing the rate of cation uptake, and the leveling off of the roughness indicates a maximum extent of swelling where the polymer stops absorbing cations and water. The reproducibility of the film was also tested by drying a freshly coated film overnight and soaking it in PBS for 4 h. The roughness obtained was close to the same average value illustrated in **Figure 4.6**(b) across all the scales (Appendix C, Figure C.8).

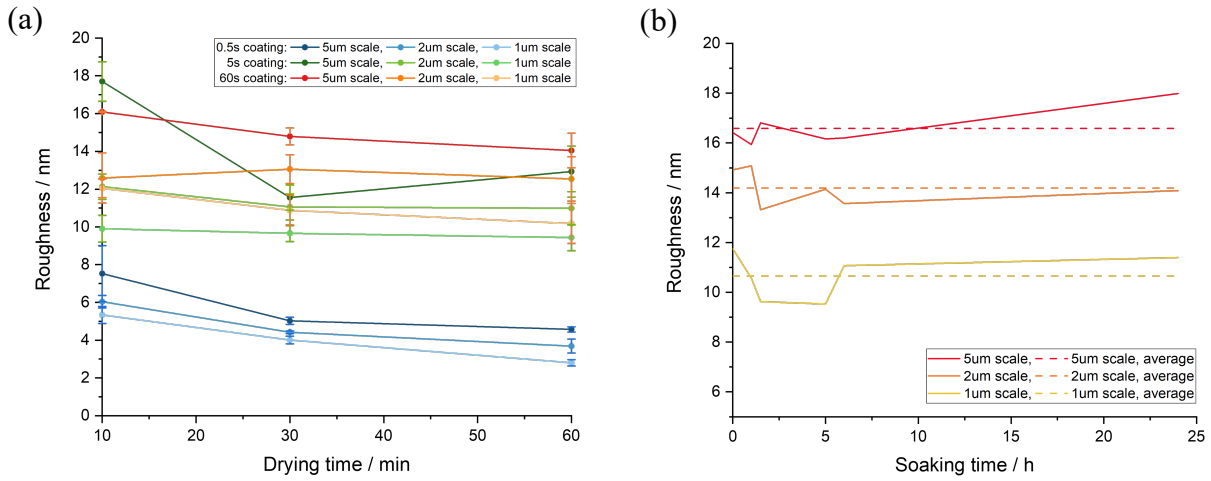

Figure 4.6: (a) The change of RMS roughness of different thickness PEDOT: PSS surfaces as dried in air. **(b)** 60 s coating, change in RMS roughness for a range of soaking times in 0.01 M PBS.

4.3.3 Electrochemical Test on a Modified Electrode

The previous section reported tests on electrodes coated with PEDOT: PSS and fabricated via potentiostatic electrodeposition at 1.0 V for a range of times (0.5 s~120 s). A preferred coating time of 60 s was established. To further test the performance of electrodes fabricated in this manner, a narrow CV scan was carried out to obtain capacitive data relevant to the recordings made when monitoring in vivo neuronal activity where the detected potential is usually tiny and within the range of -1.5 mV and +1.5 mV [38, 39].

To ensure complete coverage of the full range of likely potentials to be encountered in vivo, a CV was scanned between -100 mV to + 100 mV vs. SCE and tested with various scan rates of 25, 50, 100, and 200 mVs^{-1} for continuous 5 cycles. The resulting voltammograms are shown in **Figure 4.7**(a) revealing capacitive behavior within this potential window with a nearly rectangular-shaped CV without any discernable redox peaks. The 5 repeated scans in each case overlay well, indicating little variation on the electrode coating surface during the scan. The anodic currents were measured at 0V vs. SCE corresponding to the steady state plateau in

Figure 4.7(a) and plotted against the scan rate. The result shown in **Figure 4.7**(b) which displays a direct proportionality between the current and scan rate is consistent with a pure capacitive behavior of the modified electrode within the small potential window. The fitted straight line passes the origin with a slope of 0.450 ± 0.010 μF and $R^2 = 0.999$. From the gradient of the linear line, the specific capacitance can be obtained (2.0 ± 0.2 $mFcm^{-2}$). The significantly large value of the capacitance compared to that of the bare electrode surface (Appendix C, Figure C.9, ca. 80-folder larger) implies a large electrochemical surface area introduced by the porous structure polymer coated on the surface.

For many in vivo experiments, the electrode setup differs from a standard electrochemical cell setup. Stainless steel (SS) microscrews are commonly used as both reference and ground (counter) electrodes [40]. To compare the potentials measured using a SS microscrew as a pseudo reference electrode with that of a SCE, a wide scan (0.50 V → 2.0 V→ -0.80 V → 0.50 V) was scanned with a 60s-coated electrode immersed in 0.01 M PBS respectively using Graphite rod/SCE setup and SS/SS setups. A broad scan range was chosen to ensure the coverage of the oxidation peak of PEDOT, to facilitate the identification of the difference in reference potential compared to the SCE. **Figure 4.8**(a) shows a noticeable shift in the peak to more anodic values after changing the standard cell setup to the SS/SS setup. The shift in oxidation potential (ΔV) was 0.42 ± 0.01 V corresponding to the difference in the reference potential of the SS compared to the SCE. CVs corresponding to **Figure 4.7**(a) were also made using the SS/SS set up and converted to the SCE scale, as shown in **Figure 4.8**(b) demonstrating a satisfactory overlay.

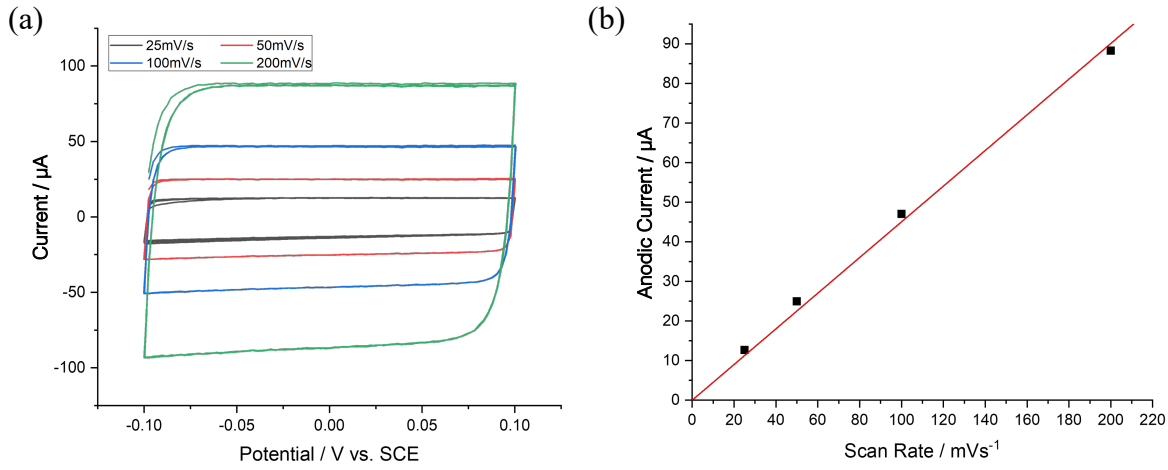

Figure 4.7: (a) CV of a Pt electrode formed by potentiostatic electrodeposition for 60 s immersed in 0.01 M PBS. The scan started at -0.10 V, was swept anodically up to 0.10 V and reverse scanned back to -0.01 V. The scan continued for a total of 5 cycles for each scan rate. **(b)** The anodic current in (a) measured at 0 V is plotted against the scan rate. The result is a straight line through the origin (Slope = 0.450 ± 0.010 µF and R^2 = 0.99858).

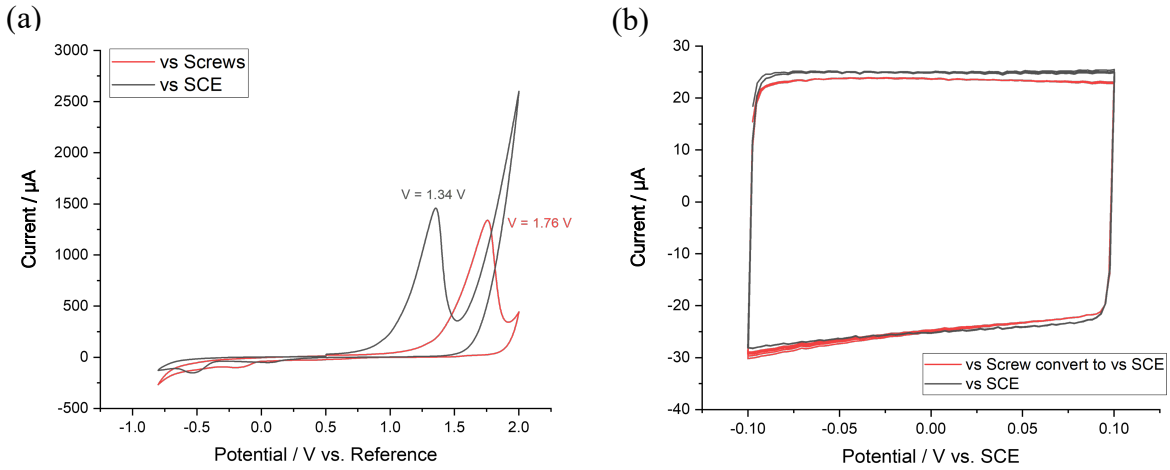

Figure 4.8: (a) CV of the 60s-coated Pt electrode immersed in 0.01 M PBS solution. The scan started at 0.50 V and was swept anodically up to 2.0 V, then reverse scanned to a cathodic limit at -0.80 V, and eventually returned to 0.50 V (0.50 V → 2.0 V→ -0.80 V → 0.50 V). A shift in the peak potential to anodic potentials can be observed, and the shift is ΔV=0.42 ± 0.01 V. **(b)** Small window CV scan of the 60s-coated Pt electrode immersed in 0.01 M PBS solution. The recorded potential vs. SS setup was converted to vs. SCE by subtracting ΔV found in (a). **Black line:** standard electrochemical cell setup with Graphite rod and SCE as the ground and reference electrode respectively. **Red line:** in vivo experimental setup with stainless steel microscrews (SS) as the ground and reference electrode.

4.4 Conclusions

The systematic electrochemistry and morphological studies reveal an optimum potential of 1 V for the electropolymerization of PEDOT:PSS and the subsequent surface roughness/morphology evaluation suggested 60 s as a preferable coating time corresponding to a charge deposition of ca. 50 mC $cm^{-2,}$ which represents a balance between depositing sufficient polymer to ensure that no part of the underlying electrode surface is exposed whilst maintaining the bulk and thickness of the coating in the interests of mechanical stability. Importantly, the high-resolution AFM images provide clear evidence of an inhomogeneous distribution of the PEDOT and PSS grains across the surface with an average size of ca. 16 nm. Last, measurements in both Faradaic and capacitive regions of the voltammetry with saturated calomel reference, and stainless-steel pseudo-reference electrodes show that reliable electrochemistry can be performed under in vitro conditions in which stainless steel electrodes are used as both (pseudo-)reference and counter electrode. The potential shift between the two electrodes is 0.42 V. Importantly, the electrode performance in the capacitive region is unaffected. Therefore, the neural electrode can function without triggering redox reactions altering surface chemistry with the use of a pseudo reference electrode despite the usual reservations.

Overall, the comprehensive study of PEDOT:PSS in this chapter provides a solid foundation for further investigation into polymer-electrode interfaces. The next chapter, **Chapter 5**, explores PEDOT variations with different dopants and details the adaptation of the coating technique from macroelectrodes to microelectrodes. The application of neural electrodes in the in vitro experiment, particularly focusing on PEDOT coatings, will be addressed in **Chapter 6.**

References

(1) Zhang, Y.; Chen, Y.; Contera, S.; Compton, R. G. Electrochemical and Nanostructural Characterization of Poly(3,4-ethylenedioxythiophene):poly(styrenesulfonate) Films as Coatings for Neural Electrodes. *ACS Applied Polymer Materials* **2023**, *5* (7), 5555-5566.

(2) Aqrawe, Z.; Montgomery, J.; Travas-Sejdic, J.; Svirskis, D. Conducting Polymers as Electrode Coatings for Neuronal Multi-electrode Arrays. *Trends in Biotechnology* **2017**, *35* (2), 93-95.

(3) Charkhkar, H.; Knaack, G. L.; McHail, D. G.; Mandal, H. S.; Peixoto, N.; Rubinson, J. F.; Dumas, T. C.; Pancrazio, J. J. Chronic intracortical neural recordings using microelectrode arrays coated with PEDOT–TFB. *Acta Biomater* **2016**, *32*, 57-67.

(4) Asplund, M.; Nyberg, T.; Inganäs, O. Electroactive polymers for neural interfaces. *Polymer Chemistry* **2010**, *1* (9), 1374-1391, 10.1039/C0PY00077A.

(5) Yamato, H.; Ohwa, M.; Wernet, W. Stability of polypyrrole and poly(3,4-ethylenedioxythiophene) for biosensor application. *J Electroanal Chem* **1995**, *397* (1), 163-170.

(6) Cui, X. T.; Zhou, D. D. Poly (3,4-ethylenedioxythiophene) for chronic neural stimulation. *IEEE Trans Neural Syst Rehabil Eng* **2007**, *15* (4), 502-508.

(7) Baek, S.; Green, R. A.; Poole-Warren, L. A. The biological and electrical trade-offs related to the thickness of conducting polymers for neural applications. *Acta Biomater* **2014**, *10* (7), 3048-3058.

(8) Luo, S.-C.; Mohamed Ali, E.; Tansil, N. C.; Yu, H.-h.; Gao, S.; Kantchev, E. A. B.; Ying, J. Y. Poly(3,4-ethylenedioxythiophene) (PEDOT) Nanobiointerfaces: Thin, Ultrasmooth, and Functionalized PEDOT Films with in Vitro and in Vivo Biocompatibility. *Langmuir* **2008**, *24* (15), 8071-8077.

(9) Dijk, G.; Ruigrok, H. J.; O'Connor, R. P. Influence of PEDOT:PSS Coating Thickness on the Performance of Stimulation Electrodes. *Adv Mater Interfaces* **2020**, *7* (16).

(10) Cui, X. Y.; Martin, D. C. Electrochemical deposition and characterization of poly(3,4-ethylenedioxythiophene) on neural microelectrode arrays. *Sensor Actuat B-Chem* **2003**, *89* (1-2), 92-102.

(11) Ludwig, K. A.; Uram, J. D.; Yang, J. Y.; Martin, D. C.; Kipke, D. R. Chronic neural recordings using silicon microelectrode arrays electrochemically deposited with a poly(3,4-ethylenedioxythiophene) (PEDOT) film. *J Neural Eng* **2006**, *3* (1), 59-70.

(12) Baek, S.; Green, R. A.; Poole-Warren, L. A. Effects of dopants on the biomechanical properties of conducting polymer films on platinum electrodes. *J Biomed Mater Res A* **2014**, *102* (8), 2743-2754.

(13) Bodart, C.; Rossetti, N.; Hagler, J.; Chevreau, P.; Chhin, D.; Soavi, F.; Schougaard, S. B.; Amzica, F.; Cicoira, F. Electropolymerized Poly(3,4-ethylenedioxythiophene) (PEDOT) Coatings for Implantable Deep-Brain-Stimulating Microelectrodes. *ACS Appl. Mater. Interfaces* **2019**, *11* (19), 17226-17233.

(14) Volkov, A. V.; Wijeratne, K.; Mitraka, E.; Ail, U.; Zhao, D.; Tybrandt, K.; Andreasen, J. W.; Berggren, M.; Crispin, X.; Zozoulenko, I. V. Understanding the Capacitance of PEDOT:PSS. *Adv Funct Mater* **2017**, *27* (28).

(15) Tamburri, E.; Orlanducci, S.; Toschi, F.; Terranova, M. L.; Passeri, D. Growth mechanisms, morphology, and electroactivity of PEDOT layers produced by electrochemical routes in aqueous medium. *Synthetic Metals* **2009**, *159* (5-6), 406-414.

(16) Du, X.; Wang, Z. Effects of polymerization potential on the properties of electrosynthesized PEDOT films. *Electrochim Acta* **2003**, *48* (12), 1713-1717.

(17) Kamensky, M. A.; Eliseeva, S. N.; Láng, G.; Ujvári, M.; Kondratiev, V. V. Electrochemical Properties of Overoxidized Poly-3,4-Ethylenedioxythiophene. *Russian Journal of Electrochemistry* **2018**, *54* (11), 893-901.

(18) Wang, D.; Pillier, F.; Cachet, H.; Debiemme-Chouvy, C. One-pot electrosynthesis of ultrathin overoxidized poly(3,4-ethylenedioxythiophene) films. *Electrochimica Acta* **2022**, *401*, 139472.

(19) Rivnay, J.; Owens, R. M.; Malliaras, G. G. The Rise of Organic Bioelectronics. *Chemistry of Materials* **2014**, *26* (1), 679-685.

(20) Rivnay, J.; Leleux, P.; Ferro, M.; Sessolo, M.; Williamson, A.; Koutsouras, D. A.; Khodagholy, D.; Ramuz, M.; Strakosas, X.; Owens, R. M.; et al. High-performance transistors for bioelectronics through tuning of channel thickness. *Sci Adv* **2015**, *1* (4).

(21) Castagnola, V.; Bayon, C.; Descamps, E.; Bergaud, C. Morphology and conductivity of PEDOT layers produced by different electrochemical routes. *Synthetic Metals* **2014**, *189*, 7-16.

(22) Rossetti, N.; Hagler, J.; Kateb, P.; Cicoira, F. Neural and electromyography PEDOT electrodes for invasive stimulation and recording. *J Mater Chem C* **2021**, *9* (23), 7243-7263.

(23) Green, R. A.; Hassarati, R. T.; Bouchinet, L.; Lee, C. S.; Cheong, G. L. M.; Yu, J. F.; Dodds, C. W.; Suaning, G. J.; Poole-Warren, L. A.; Lovell, N. H. Substrate dependent stability of conducting polymer coatings on medical electrodes. *Biomaterials* **2012**, *33* (25), 5875-5886.

(24) Zeng, Q.; Wu, T. Z. Enhanced electrochemical performance of neural electrodes based on PEDOT:PSS hydrogel. *J Appl Polym Sci* **2022**, *139* (13).
(25) Hong, G. S.; Lieber, C. M. Novel electrode technologies for neural recordings (vol 20, pg 330, 2019). *Nat Rev Neurosci* **2019**, *20* (6), 376-376.
(26) Boehler, C.; Carli, S.; Fadiga, L.; Stieglitz, T.; Asplund, M. Tutorial: guidelines for standardized performance tests for electrodes intended for neural interfaces and bioelectronics. *Nat Protoc* **2020**, *15* (11).
(27) Bobacka, J.; Lewenstam, A.; Ivaska, A. Electrochemical impedance spectroscopy of oxidized poly(3,4-ethylenedioxythiophene) film electrodes in aqueous solutions. *J Electroanal Chem* **2000**, *489* (1-2), 17-27.
(28) Carli, S.; Bianchi, M.; Zucchini, E.; Di Lauro, M.; Prato, M.; Murgia, M.; Fadiga, L.; Biscarini, F. Electrodeposited PEDOT:Nafion Composite for Neural Recording and Stimulation. *Adv Healthc Mater* **2019**, *8* (19), 1900765.
(29) Yang, J.; Kim, D. H.; Hendricks, J. L.; Leach, M.; Northey, R.; Martin, D. C. Ordered surfactant-templated poly(3,4-ethylenedioxythiophene) (PEDOT) conducting polymer on microfabricated neural probes. *Acta Biomater* **2005**, *1* (1), 125-136.
(30) Luo, X.; Weaver, C. L.; Zhou, D. D.; Greenberg, R.; Cui, X. T. Highly stable carbon nanotube doped poly(3,4-ethylenedioxythiophene) for chronic neural stimulation. *Biomaterials* **2011**, *32* (24), 5551-5557.
(31) Alba, N. A.; Du, Z. J.; Catt, K. A.; Kozai, T. D.; Cui, X. T. In Vivo Electrochemical Analysis of a PEDOT/MWCNT Neural Electrode Coating. *Biosensors (Basel)* **2015**, *5* (4), 618-646.
(32) Sader, J. E.; Borgani, R.; Gibson, C. T.; Haviland, D. B.; Higgins, M. J.; Kilpatrick, J. I.; Lu, J.; Mulvaney, P.; Shearer, C. J.; Slattery, A. D.; et al. A virtual instrument to standardise the calibration of atomic force microscope cantilevers. *Rev Sci Instrum* **2016**, *87* (9), 093711.
(33) Voïtchovsky, K.; Kuna, J. J.; Contera, S. A.; Tosatti, E.; Stellacci, F. Direct mapping of the solid–liquid adhesion energy with subnanometre resolution. *Nature Nanotechnology* **2010**, *5* (6), 401-405.
(34) *Igor Pro Manual Version 9*. 2017. https://www.wavemetrics.net/doc/IgorMan.pdf (accessed in 2024).
(35) Contera, S. A.; Voïtchovsky, K.; Ryan, J. F. Controlled ionic condensation at the surface of a native extremophilemembrane. *Nanoscale* **2010**, *2* (2), 222-229, 10.1039/B9NR00248K.
(36) Wang, Y.; Song, R.; Li, Y.; Shen, J. Understanding tapping-mode atomic force microscopy data on the surface of soft block copolymers. *Surface Science* **2003**, *530* (3), 136-148.

(37) Modarresi, M.; Mehandzhiyski, A.; Fahlman, M.; Tybrandt, K.; Zozoulenko, I. Microscopic Understanding of the Granular Structure and the Swelling of PEDOT:PSS. *Macromolecules* **2020**, *53* (15), 6267-6278.
(38) Xia, Z.; Arias-Gil, G.; Deckert, M.; Vollmer, M.; Curran, A.; Herrera-Molina, R.; Brosch, M.; Krug, K.; Schmidt, B.; Ohl, F. W.; et al. Electrochemical Roughening and Carbon Nanotube Coating of Tetrodes for Chronic Single-Unit Recording. *bioRxiv* **2019**, 738245.
(39) Marblestone, A. H.; Zamft, B. M.; Maguire, Y. G.; Shapiro, M. G.; Cybulski, T. R.; Glaser, J. I.; Amodei, D.; Stranges, P. B.; Kalhor, R.; Dalrymple, D. A.; et al. Physical principles for scalable neural recording. *Front Comput Neurosci* **2013**, *7*, 137.
(40) van de Ven, G. M.; Trouche, S.; McNamara, C. G.; Allen, K.; Dupret, D. Hippocampal Offline Reactivation Consolidates Recently Formed Cell Assembly Patterns during Sharp Wave-Ripples. *Neuron* **2016**, *92* (5), 968-974.

Chapter 5

Further Electrochemical Characterization of PEDOT with Different Dopants on Macro and Micro Electrodes.

Chapter 5 extends the studies from **Chapter 4**, further investigating PEDOT polymers doped with a different anion (chloride, Cl^-). Initially, this chapter systematically reports on the characterization of PEDOT:Cl on macroelectrodes. After understanding the reaction mechanisms, both PEDOT:PSS and PEDOT:Cl will be evaluated on microelectrodes made of different materials (Tungsten, Platinum) and sizes (10 μm ~ 25 μm in diameter).

The work presented in **Chapter 5** has been published in *ACS Applied Materials and Interfaces* [1]. The project was conducted under the supervision of Prof. Richard Compton and Prof. Sonia Contera. Dr. Yuqi Chen assisted with the understanding and interpretation of the electrochemical analysis.

5.1 Introduction

In the previous chapter, the mechanism of PEDOT:PSS electropolymerization and the deposition conditions using macro-electrodes were reported. The subsequent stage, reported in this chapter, involves transferring this coating to microelectrodes for actual neural recording applications. However, before this can be implemented, there are questions regarding the choice of materials for the microelectrodes and challenges posed by polymer overgrowth, which can lead to cross-connections between different recording sites.

First, consider the material choice. During the recording processes using neural electrodes, the primary challenges are the foreign body immune response and the need to maintain an optimum signal-to-noise ratio. The immune response is largely due to the non-biological interface between electrode materials and neural tissue, while the signal quality is affected by

electrode impedance. Consequently, biocompatibility and electrode-tissue impedance are critical criteria to consider when selecting materials for implantable electrodes [2-4].

Bio-incompatibility can primarily be attributed to the following factors: the mechanical mismatch between the probe materials and neural tissue, the chemical instability of the electrodes, the degradation of insulating layers, and the potential for infection through percutaneous leads — all of which may contribute to the instability and failure of neural recordings [3]. The use of materials harder than tissue during initial insertion inevitably causes shearing forces, but if a material is excessively rigid compared to that of brain tissue, it can further exacerbate the immune response by causing repetitive chronic damage, such as continuous friction and compression between the soft brain tissue and the rigid metal electrode could potentially cause long-term inflammation [3]. Moreover, an electrode inserted in tissue for a prolonged period can, in some cases, gradually be oxidized. In the extracellular aqueous environment, as detailed in Table 1.2, certain metals are prone to oxidation, which may result in cellular toxicity [3, 4]. Bad examples of metals for long-term usage include zinc (Zn) and magnesium (Mg), which quickly dissolve and degrade into their oxides or hydroxides (ZnO, $Zn(OH)_2$, $Mg(OH)_2$) in the brain (Dissolution rate for Zn and Mg = 0.5 ~ 3 μm h^{-1}) [4, 5]. Tungsten, although it dissolves slowly (Dissolution rate = 2×10^{-3} μm h^{-1}) [4, 5], its oxides are toxic to cells [6]. In comparison, stable metals like gold and platinum hardly dissolve [4]. Together, these two responses (physical damage in tissue and oxide formation on the electrode) may trigger a cascade of inflammation, leading to the development of a glial encapsulation around the implant [3]. This glial sheath acts as a barrier, impeding signal transmission to the electrode [3], potentially leading to the failure of many electrodes within weeks or months.

Numerous experiments have been conducted to evaluate biocompatible materials for both the metal components and the insulation of electrodes. The details of these studies are beyond the scope of this thesis, but comprehensive summaries can be found in the literature [2-4]. In

summary, based on the material and intended use, the most suitable metals for recording electrodes are platinum, iridium, rhodium, and gold [2]. For stimulating electrodes, the optimal choices are platinum, platinum-iridium alloy, gold, and rhodium [2]. The preferred candidates for insulating materials are polyimide and glass [2]. Moreover, with the development of semiconductor manufacture, silicon or silicon oxide based electrodes have also been a popular choice [3, 4].

Regarding electrode-tissue impedance, electrodes with larger contact areas usually exhibit lower impedance. This impedance can be reduced by simply using larger electrodes. However, there may be a trade-off between a larger electrode size and a reduced number of recording sites on a substrate. Therefore, other techniques have been introduced to improve electrode performance, such as surface roughening or applying coatings of rough materials like porous polymers or carbon nanotubes [7-9]. This suggests the use of a coat of conductive polymer (CP) on the electrode. A layer of a CP on the metallic or silicon substrate substantially reduces the impedance as the roughened, porous surface produces a larger electrochemical surface area [10]. The soft polymer layer also separates the hard substrate surface from the tissue, mitigating the immune response and there have even been reports of preferential in vitro and in vivo neuron growth [11]. Typical biocompatible CPs include poly(pyrrole) (PPY), polyanilines (PANI), and poly(3,4-ethylenedioxythiophene) (PEDOT) [8]. Due to their superior conductivity, chemical stability [12], and biocompatibility, CPs have the potential to elevate the performance of traditional neural electrodes to new levels.

Despite the benefits of CPs, their applications have been primarily limited to single, needle-like electrodes [13] or large, flat slides [14] rather than to densely packed electrode configurations such as tetrodes. This limitation is partly due to the challenges associated with polymer overgrowth, which can lead to cross-connection of detection sites. These challenges

can be overcome through thickness control and optimization. However, a direct method for detecting cross-connection is also essential.

Furthermore, as indicated in the previous chapter, Table 4.1, oxidized PEDOT can have a variety of dopants. Therefore, it is beneficial to compare PEDOT:PSS with other doped PEDOT to evaluate their performance. Given the ease and environmental friendliness of the synthetic procedure, chloride ion (Cl^-) is a suitable choice for a dopant. In the extracellular fluid environment, the significant concentration of Cl^- (ca. 113 mM, Table 1.2) could potentially enhance the suitability of the polymer film for in vivo applications.

Overall, in this chapter, the electrodeposition of PEDOT:Cl on a Pt macro disc electrode is first systematically studied and characterized using CV following similar procedures as in **Chapter 4**. This includes studies of the Pt electrode immersed in a monomer solution (EDOT/NaCl) and in solutions without the monomer (NaCl, Na_2SO_4, PBS) to understand the deposition process and the potentials at which reactions occur. Subsequently, the focus moves on to microelectrode studies. Individual W and Pt microwires are characterized using CV in solutions with and without the monomer EDOT present to understand their electrochemical processes. W was selected because it is one of the earliest materials applied to neural recording [15]. Pt was chosen for its extensive use in both recording and stimulating electrodes and its compatibility with PEDOT deposition [16-19], as demonstrated in the literature and the previous chapter (Table 4.1). Then, electropolymerization is then performed on Pt microwires, with the resulting coatings characterized and compared with findings on macroelectrodes. Lastly, and crucially, the established electropolymerization conditions are applied to the coating of tetrodes. Additionally, a novel and straightforward testing method closely related to the properties of PEDOT is introduced to assess polymer overgrowth and detect cross-connections between recording sites.

5.2 Materials and Methods

5.2.1 Macroelectrode Characterization with PEDOT:Cl

All electrochemical characterizations were carried out using a three-electrode cell setup, which comprised a Pt macro disk (area = 0.02 cm^2) as the working electrode, an SCE as the reference electrode, and a graphite rod as the counter electrode.

5.2.1.1 Pt in Background Electrolyte

The Pt macroelectrode was tested in background electrolytes without EDOT monomers: NaCl, Na_2SO_4, and PBS.

Electrodes were first immersed in 0.1 M NaCl, and a wide CV scan was conducted ranging from -0.8 V to E_{max}, where E_{max} varied from an open circuit potential (OCP) to 2.0 V (vs. SCE) at a scan rate of 50 mVs^{-1}. To compare the effect of Pt in solutions with different chloride ion concentrations, the experiment was repeated in 0.01 M PBS and 0.5 M Na_2SO_4. A comparison of their ionic concentrations is presented in **Table 5.1**. Note that PBS has a significant chloride concentration.

Table 5.1: The ionic composition of 0.01 M PBS, 0.1 M NaCl and 0.5 M Na_2SO_4.

Ion	PBS / M	NaCl / M	Na_2SO_4 / M
Na^+	0.138	0.1	0.5
Cl^-	0.14	0.1	/
K^+	0.0027	/	/
PO_4^{3-}	0.01	/	/
SO_4^{2-}	/	/	0.5

5.2.1.2 Pt in EDOT/NaCl

The bare Pt macroelectrode was immersed in a solution containing 10 mM EDOT and 0.1 M NaCl, and a wide CV scan was performed within the same potential window (-0.8 V to various E_{max}) at a scan rate of 50 mVs^{-1}. Following this PEDOT:Cl was potentiostatically deposited on the Pt electrode at various potentials for a duration of 120 s. The potentials for deposition were chosen based on the prior CV scan results (5.2.1.1) of the bare Pt electrode in the monomer solution. These modified Pt electrodes were transferred to a 0.1 M NaCl solution containing no EDOT, and a CV scan was conducted from -0.8 V to 2.0 V (vs. SCE) at a scan rate of 50 mVs^{-1}. This step was carried out to verify whether the polymer PEDOT:Cl was deposited onto the Pt disc; the presence of a polymer is indicated by a peak attributable to $PEDOT^+$ overoxidation, at a potential of ca 1.2 V as demonstrated in **Chapter 4** [20]. In the absence of polymer deposition, or if the polymer has already been overoxidized during the deposition process, no corresponding peak is observed during the anodic scan.

5.2.2 Microelectrode Characterization

All electrochemical characterizations were conducted using a three-electrode setup, as in Section 5.2.1, except that the working electrode was a W or Pt microwire electrode as listed in **Table 5.2**. The connection method of microwires to electrochemical apparatus has been introduced in **Chapter 2**, Section 2.2.6. The success of the connection can be evaluated by a rough scan with a CV to see if there is any current recorded.

5.2.2.1 W Characterization

Electrodes were immersed in solutions containing monomer (10 mM EDOT and 0.1 mM NaPSS) and without monomer (0.1 mM NaPSS), respectively. A CV scan was carried out, starting from OCP to 1.7 V (vs. SCE) and -0.8V (vs. SCE) at a scan rate of 50 mVs^{-1} and continuing for 5 successive cycles.

Table 5.2: List of microelectrode used.

Electrode	Insulation	Parameters	Supplier
Pt insulated microwire	Polyimide	d = 25 or 15 µm	GoodFellow, UK
W insulated microwire	Heavy Formvar (HFV)	d = 12.7 µm	California Fine Wire Company, USA

5.2.2.2 Pt Characterization in EDOT/NaPSS

The three-electrode setup described above was employed, with Pt microwire as the working electrode. Two different diameters of Pt microelectrodes were employed with diameters (d) 15 and 25 µm. It should be noted that the 15 µm microwire was only used to compare the effect of wire size on the CV scan in EDOT/NaPSS, as it has a radius comparable to the previously used W microwire (d = 12.7 µm), making it useful for comparing and understanding the electrochemical processes at this size scale. However, since Pt is softer compared to W and such thin and soft wires are known to be easily bent during implantation surgery, causing unwanted challenges, it was not utilized for further tests on galvanostatic deposition or implantation. Thus, most comparisons between macro and microwires were made using the 25 µm diameter wires.

A bare Pt microelectrode was immersed in a solution of 10 mM EDOT and 0.1 mM NaPSS, and a CV scan was conducted from OCP to 2.0 V (vs. SCE), and then to -0.8 V (vs. SCE). This procedure was repeated for both sizes of Pt microwires. Subsequently, the 25 µm diameter microwire was cut to expose fresh Pt, and placed into a solution containing only the background electrolyte of 0.1 mM NaPSS. The outcomes of these scans were compared with those obtained using a macroelectrode to, first, understand the electrochemical processes occurring and, second, deduce the optimal coating conditions for the microelectrode.

A galvanostatic deposition was carried out using a current of 20 nA for 13 s on the 25 μm Pt microelectrode. The conditions were chosen to maintain the deposition charge density at approximately 50 mC cm^{-2}, consistent with findings from previous macroelectrode studies[20]. Following this, the modified Pt microwire was immersed in a 10 mM NaPSS solution to conduct a CV scan ranging from OCP to 1.35 V (vs. SCE) and then to 0 V (vs. SCE).

5.2.2.3 Pt Characterization in EDOT/NaCl

The same setup as described in Section 5.2.2.2 was employed using 25 μm diameter Pt electrodes.

A bare Pt microelectrode was first immersed in a solution of 0.1 M NaCl, where a CV scan was conducted from OCP to 1.7 V (vs. SCE), and then to -0.8 V (vs. SCE). This procedure was repeated for solutions of 0.01 M PBS, 0.5 M Na_2SO_4, and 10 mM EDOT with 0.1 M NaCl, respectively, to evaluate the effects of different chloride concentrations and the presence of EDOT monomer on the Pt microelectrode.

Subsequently, to optimize the deposition conditions, a range of fixed currents ranging between 15 nA and 28 nA was chosen for the galvanostatic coating in 10 mM EDOT and 0.1 M NaCl. The experiment was repeated in a solution containing only 0.1 M NaCl to assess whether the change of potential was due to chloride oxidation or EDOT oxidation.

Following the optimization steps, a coating condition of 20 nA for 13 s was selected to be consistent with the previous method on PEDOT:PSS. The PEDOT:Cl-coated Pt microwire was then immersed in 0.01 M PBS to test the coating by searching for any PEDOT overoxidation peak with a CV scan spanning from 0 V to 1.5 V (vs. SCE) over 3 successive cycles. For comparison, the Pt microwire was then cut and coated with PEDOT:PSS using the same conditions as before (20 nA, 13 s) and this modified microwire underwent the same CV scan in 0.01 M PBS for 3 cycles.

5.2.3 Tetrode Cross-Connection Check

Detailed tetrode fabrication procedures have been introduced in Chapter 2, Section 2.2.7. Before initiating the coating process, a small segment from the head of the tetrode was carefully cut and affixed to an SEM specimen stub using an adhesive carbon tab. This wire segment was positioned at the edge of the specimen stub to facilitate observation. SEM images were captured for W tetrodes after the heat-curing process [21]. Images of Pt tetrodes, both with and without heat curing, were similarly recorded. The coating scheme for a tetrode follows exactly the method in Section 5.2.2.2 and 5.2.2.3, but runs individually on each wire. The cross-connection check for polymer overgrowth can be done via electrochemical methods or direct inspection spectroscopic methods.

5.2.3.1 Electrochemical Method

Initially, the Pt tetrode was immersed in a solution containing 0.1 mM NaPSS. Three successive CV scans from OCP to 1.5 V (vs. SCE) and back to OCP were conducted for two wires on the tetrode, respectively, designated as Wire 1 and Wire 2. Wire 1 was selected for coating, while Wire 2 was to remain bare, and their CV scans would be compared once again in 0.1mM NaPSS after coating. The tetrode was then placed in a solution containing 10 mM EDOT and 0.1 mM NaPSS. Wire 1 underwent galvanostatic deposition at 20 nA for 13 s. The wire was then gently dipped into deionized water to wash away any excess monomer solution from the surface before being returned to the NaPSS solution for a post-coating test. The same CV sweep conducted prior to coating was repeated, allowing the results to be overlaid and compared.

To test for unwanted cross-connections between different Pt wires in the tetrode after coating, the tetrode was then immersed in 0.1 mM NaPSS and a CV scan was performed for each wire within the same potential window as before (OCP → 1.5 V → OCP). If any cross-

connection exists, one CV scan in NaPSS will disrupt the polymer electroactivity on any connected wire, thus eliminating the overoxidation peak. If the process is successful, four distinct oxidation peaks should be evident during the post-coating scans, one for each electrode contacted.

5.2.3.2 Spectroscopic analysis

For more direct visual evidence, deposition was performed on three of the four discs. The resulting tetrode was then cut and meticulously affixed to a specimen stub for SEM and EDX analysis. Additionally, the tetrode segment could be examined under an optical microscope to assess the coating. In both cases, the coated end must be delicately handled and oriented toward the camera for clear visualization, enabling the coated cross-section of the tetrode to be clearly seen. This allows for a direct comparison with the cross-section of the bare tetrode.

5.3 Results and Discussion

5.3.1 Macroelectrode Characterization

In this section, the Pt macro disc electrode is systematically studied and characterized in background electrolytes (in NaCl, PBS, Na_2SO_4. Section 5.2.3.1) and in monomer solutions (in EDOT/NaCl. Section 5.2.3.2). The aim is to understand the reactions that happen within the potential range of interest.

5.3.1.1 Pt Macroelectrode in Background Electrolyte

It has been reported that Pt itself may undergo oxidation [22, 23], or chloride ions may be oxidized at a Pt electrode [22, 24, 25]. Therefore, before placing Pt in the coating solution (EDOT/NaCl), it is essential to first determine if any Pt-based reactions occur within the potential range of interest and, second, if reactions occur, to identify the products and understand the underlying reactions.

To start with, the Pt macroelectrode was immersed in 0.1 M NaCl. An initial CV scan was made (OCP → E_{max} = 2.0 V → -0.8 V→ OCP). Starting the sweep at OCP ensures that no Faradaic reaction occurs at the start of the scan until any higher potential is reached. In **Figure 5.1**(a, b), an anodic peak (P1) is observed at approximately 1.35 V, and two cathodic peaks (P1' and H) appear around 0.9 V and 0.1 V, respectively. To further investigate P1, the procedure was repeated with E_{max} values of OCP, 1.0 V, and 1.5 V (vs. SCE), as shown in **Figure 5.1**(a, b). A comparison of the different E_{max} scans suggests that P1 could correspond to chloride oxidation on the Pt surface. P1' is identified as the reduction peak corresponding to P1 since P1' is absent from the reverse scan when the voltage is lower than the potential of P1 (indicated by the blue and green lines in **Figure 5.1**(b)). The peak H was inferred to be due to hydrogen adsorption [23], as it remains even when the CV scan maximum potential is OCP (**Figure 5.1**(b), green line).

To further validate the identification of these peaks, the Pt electrode was placed in 0.01 M PBS or 0.5 M Na_2SO_4, respectively, and the above experiments were repeated. The CV scans (PBS in **Figure 5.1**(c), Na_2SO_4 in **Figure 5.1**(d)) show that all three peaks are observed in PBS when E_{max} is sufficiently high, while only the peak H is present during the reverse scan in Na_2SO_4, regardless of E_{max}. This indicates that the P1 and P1' pair only emerge in the presence of chloride ions and when the potential exceeds 1.35 V. The distinction between the P1 and P1' pair is more apparent when overlaying their CV scans up to 2.0 V (**Figure 5.1**(e)), where no significant oxidation is observed in the Na_2SO_4 scan around 1.35 V (**Figure 5.1**(d)), and the reduction peak P1' is only seen in PBS and NaCl. Additionally, overlaying the CV scans up to 1.0 V (**Figure 5.1**(f)) reveals a small signal (S1) during the positive scan, which could correspond to Pt oxidation [22, 23].

The reaction of chloride ions at the electrode is described by equation (5.1) [22], where E^0 is the standard electrode potential for the reaction. The reaction mechanism for chloride ions on

Pt is a two-step process, as suggested by previous studies [22, 24]. Chloride ions are reported to first form a bond with Pt through the removal of one electron (equation (5.2)), followed by the metal-chloride bond reacting with another chloride ion to regenerate the Pt and form chlorine (equation (5.3)) [22].

$$2Cl^- \leftrightarrow Cl_2 + 2e^- \qquad (E^0 = 1.359\,V) \tag{5.1}$$

$$Cl^- + Pt \leftrightarrow PtCl + e^- \tag{5.2}$$

$$Cl^- + PtCl \leftrightarrow Pt + Cl_2 \tag{5.3}$$

At potentials lower than 1.0 V, the following reactions happen and lead to the formation of platinum hydroxide and monoxide (equation (5.4)(5.5)) [22]

$$Pt + H_2O \leftrightarrow Pt - OH + H^+ + e^- \tag{5.4}$$

$$Pt - OH \leftrightarrow PtO + H^+ + e^- \tag{5.5}$$

Overall, as supported by the literature [22] and my experiments, P1 and P1' can be assigned as the peaks for chloride oxidation and its reversal, respectively. The formation of Pt hydroxide and monoxide occurs between 0.5 V and 1.0 V, and this process results in a small shoulder (S1) in **Figure 5.1**(f), which is relatively minor compared to the chloride oxidation (P1). Lastly, peak H can be attributed to hydrogen adsorption on Pt, as evidenced by its consistent presence across all CV scans in various solutions (PBS, NaCl, Na_2SO_4).

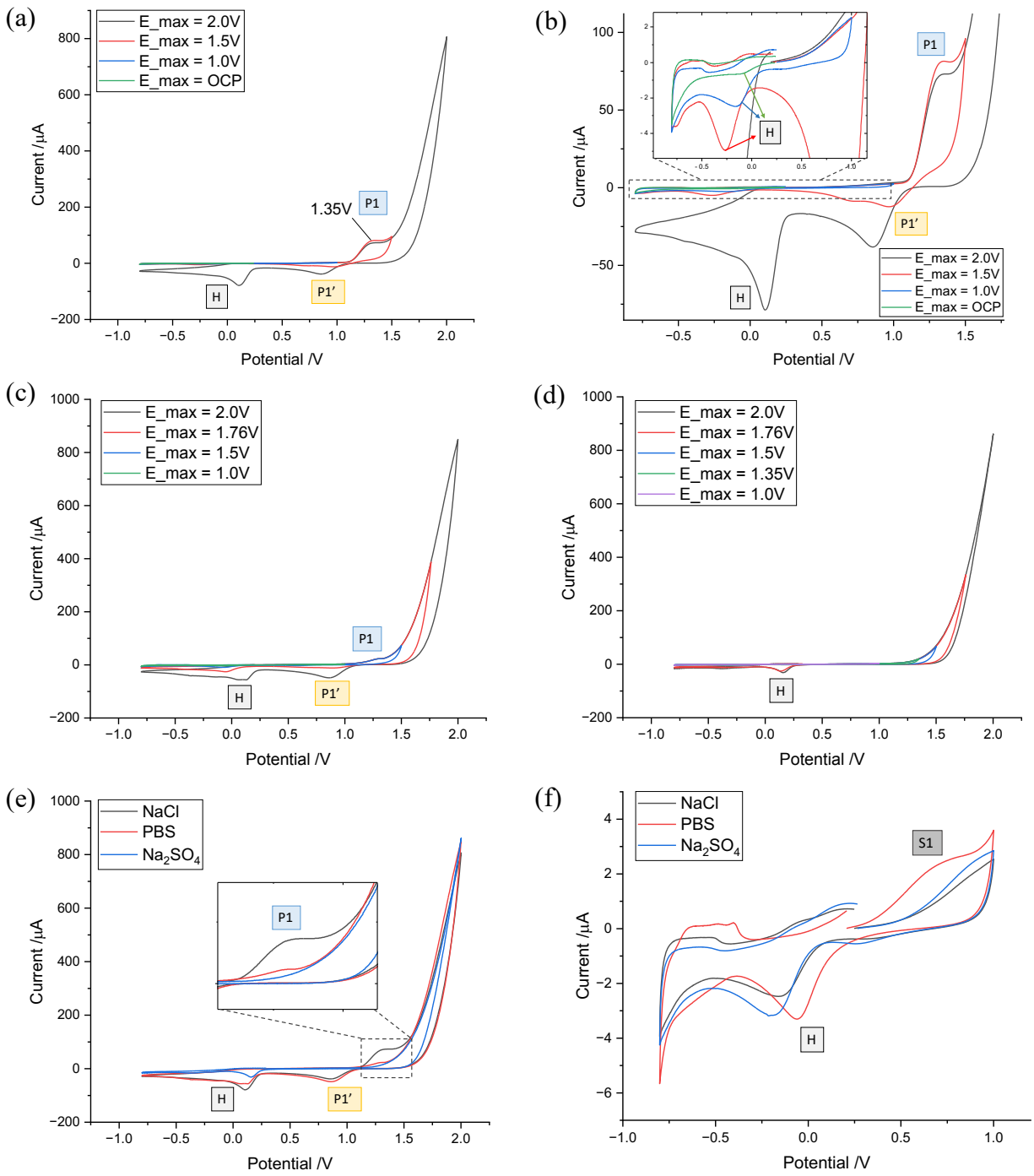

Figure 5.1: CV scan of bare Pt macroelectrode from the OCP → E_{max} → -0.8V → OCP (scan rate v = 50 mVs^{-1}) **(a,b)** in 0.1M NaCl. (b) is the zoom-in of (a) **(c)** in 0.01 PBS, **(d)** in 0.5M Na_2SO_4. **(e)** Comparison of the CV scan with E_{max} = 2.0V. **(f)** Comparison of the CV scan with E_{max} = 1.0V. **P1, P1':** Chloride oxidation and reduction; **H**: Hydrogen adsorption; **S1**: Pt oxidation. OCP is the open circuit potential, which is around 0V vs. SCE. All potentials are reported relative to the SCE.

5.3.1.2 Pt Macroelectrode in EDOT/NaCl

After identifying the potential where Pt is reactive with chloride in the solution as reported in section 5.3.1.1, CV scans of Pt in EDOT/NaCl were conducted to understand the electrodeposition process in aqueous media.

A CV scan was first conducted with a Pt macroelectrode in a solution of 10 mM EDOT and 0.1 M NaCl, starting from OCP scanning up to a maximum potential of 2.0 V (vs. SCE) and then reversing to a potential -0.8 V (vs. SCE). In this way, it was possible to identify potential(s) where electrode reactions happen and hence deduce the potential for electro-polymerization. The CV is shown in **Figure 5.2**(a), where two peaks, P1 and P2, can be observed at 1.53 V and 1.21 V, respectively. P1 is assigned to chloride oxidation at Pt with a peak potential of 1.53 V which compares to ca 1.35 V seen in pure 0.1 M NaCl (**Figure 5.1**(a). It is inferred that the presence of the polymer layer slows the reaction. P2 is therefore assigned to a mixture of EDOT oxidation and PEDOT overoxidation of PEDOT. These two reactions are not resolved in EDOT/NaPSS solution [20], but in EDPT/NaCl they merge into a single peak.

To confirm whether P2 is indeed due to mixture of EDOT oxidation and subsequent over-oxidation, the electrode was cleaned, and the same experiment repeated but with various E_{max} values below 1.5 V (that is below P1). The results of these CV scans are overlaid in **Figure 5.2**(b). Evidence of over-oxidation at P2 (1.21 V) is indicated by the presence of a P2' reduction peak, observable only when E_{max} exceeds the P2 peak value (**Figure 5.2**(b), black line). The E_{max} of 1.35 V was intentionally chosen as it was the previously observed potential for chloride ion oxidation (**Figure 5.1**(a)). If chloride oxidation were occurring, a corresponding reduction peak would be expected around 0.9 V during the cathodic sweep. However, no such reduction is observed, further suggesting that the oxidation peak P2 is due to EDOT oxidation and overoxidation rather than a chloride reaction. Note that the peak P2" seen in the range of -0.1 V to -0.2 V is a reduction peak which is present for all E_{max} values equal to or greater than 1.0

V, as shown by the black, green, and red lines in **Figure 5.2**(b). Although P2" is too small to be conclusively characterized, it suggests, even if it is associated with the polymer reduction that the majority of the oxidation process is irreversible and implies that the oxidation of EDOT occurs around 1.0 V to 1.1 V, aligning with my previous experiments [20]. More significantly, this indicates that for PEDOT subjected to scanning at potentials below those needed for over-oxidation (< 1.2 V), there is little, if any, sign of any reduction during the reverse scan. Thus, the oxidation of EDOT in NaCl results in the formation of PEDOT:Cl ($PEDOT^+$ with the dopant Cl^-), which does not undergo reduction on the reverse scan. In essence, no PEDOT is formed with the expulsion of the chloride on the reductive scans.

Next, different coating potentials were selected based on the peak values (P1, P2 = 1.21 V, 1.53 V) observed in **Figure 5.2**(a) and previous knowledge of PEDOT oxidation at 1.0V [20]. Potentiostatic deposition was performed, and the results are shown in **Figure 5.2**(c). When the modified Pt electrodes were immersed in a monomer-free solution (0.1 M NaCl), only the potentiostatic deposition at 1.0 V displayed an overoxidation peak at approximately 1.25 V (**Figure 5.2**(d), red line). It was noticed that for all modified electrodes, no peak was observed around 1.35 V, which corresponds to chloride oxidation on bare Pt. This suggests the presence of a polymer layer, either PEDOT (E = 1.0 V) or over-oxidized PEDOT (E = 1.21 V and 1.53 V), covering the Pt surface and inhibiting the chloride oxidation.

Overall, the above experiment indicates that the potential for EDOT/NaCl electro-polymerization occurs around 1.0 V to 1,1V. Beyond ca. 1.2 V (P2), the reaction forms a mix of PEDOT and over-oxidized PEDOT. Chloride oxidation is not a concern at this stage, as it is shifted to a higher potential of around 1.5 V due to the presence of the polymer layer. Once covered by the polymer, chloride ions cannot as easily access the Pt substrate as compared to a bare electrode, and consequently, no chloride oxidation peak is observed, which could otherwise be confused with the over-oxidation peak of PEDOT.

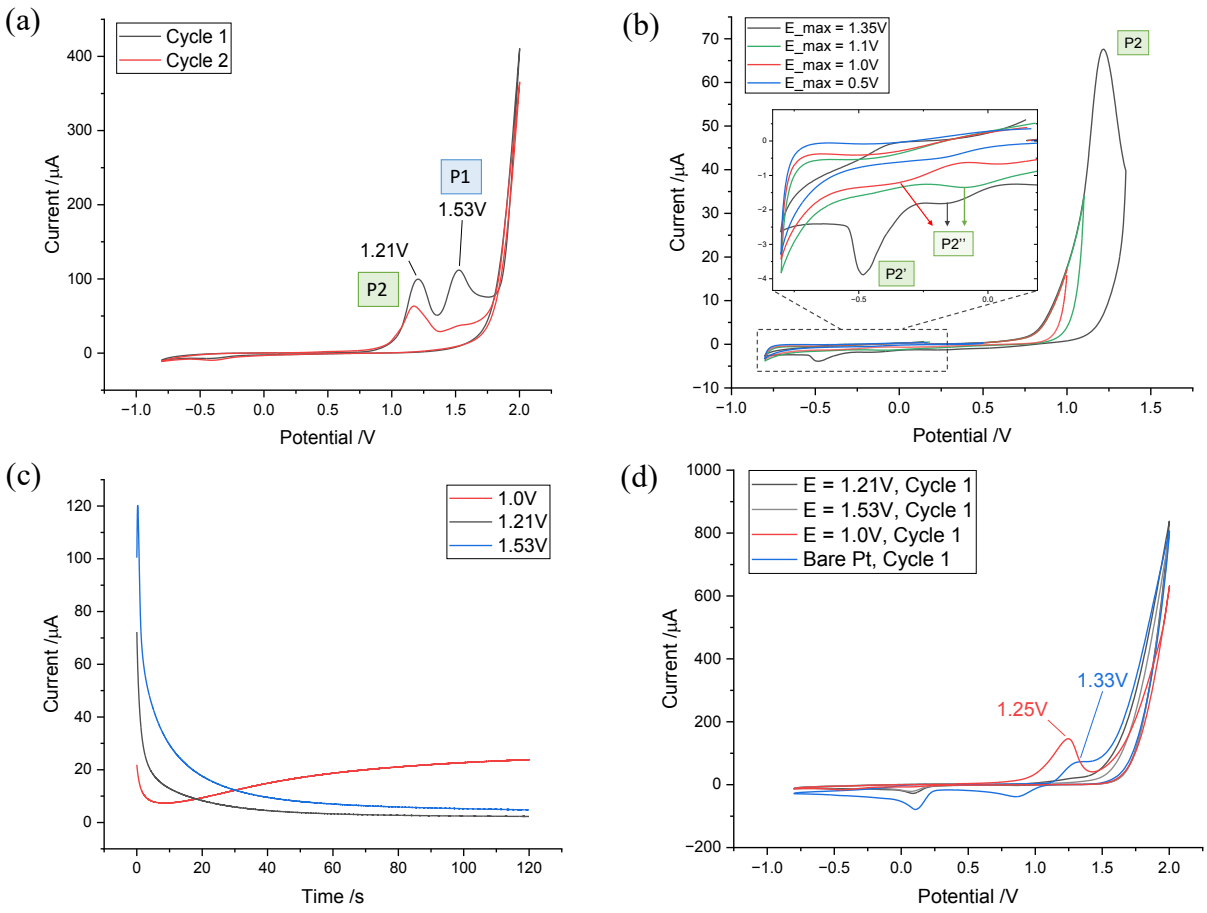

Figure 5.2: (a, b) CV scan of a bare Pt macroelectrode from OCP → E_{max} → -0.8V → OCP in 10 mM EDOT and 0.1 M NaCl (scan rate v = 50 mVs^{-1}). E_{max} = 2.0 V for (a) and 0.5 V ~ 1.35 V for (b). **(c)** Chronoamperograms using the same electrode and solution were recorded at potentials of E = 1.0 V, 1.21 V, and 1.53 V for 120 s. **(d)** CV scan of modified and bare Pt electrodes in 0.1 M NaCl, scanning from OCP → 2.0 V (vs. SCE) → -0.8 V (vs. SCE) → OCP (scan rate v = 50 mVs^{-1}). All potentials are reported relative to the SCE.

5.3.2 W Microelectrode Characterization

Tungsten (W) has frequently been used for implanted electrodes [2, 26]. However, it has been reported that tungsten oxidation and resulting dissolution products are toxic and compromise the long-term viability of the implants [6]. Therefore, it is useful to see if tungsten can be coated with PEDOT without triggering the formation of any oxides and subsequent corrosion, thereby avoiding the production of toxic products and enhancing the device longevity in implant applications.

A CV scan from 0.5 V to 1.0 V in 0.01 M PBS was carried out to test the wire connection. A bad connection will result in a purely noisy current fluctuating around 0 A (**Figure 5.3**(a); a good connection, however, will exhibit a much higher and stable current (**Figure 5.3**(b)).

To characterize the W microwires, a CV scan was recorded starting from OCP to 1.7 V (vs. SCE), then reversed to -0.8 V (vs. SCE), and finally returned to the initial OCP value in a solution containing both 10 mM EDOT and 0.1 mM NaPSS, as well as in a solution with only the background electrolyte 0.1 mM NaPSS. From **Figure 5.3**(c, d), both scans exhibit a peak around 0.5 V (P_w1) during the initial cycle, which then shifts to approximately 0.9 V (P_w1') in subsequent cycles. P_w1 and P_w1' are assigned to tungsten oxidation. These two peaks appear at similar potentials and peak heights in both scans, regardless of the presence of the monomer EDOT. In contrast, P_w2 (ca 1.5 V) is only present in the scan in EDOT/NaPSS (**Figure 5.3**(c)), indicating it is a peak resulting from a combination of EDOT oxidation and PEDOT overoxidation, as discussed below. The merging of EDOT and PEDOT oxidation reactions on the W electrode is clearer when comparing that with the CV scans in EDOT/NaPSS using Pt microwires in the later section (Section 5.3.3.1).

Therefore, unlike the previous results with Pt in EDOT/NaCl (Section 5.2.1.2), where chloride oxidation on Pt only occurs at potentials beyond polymer formation, W oxidation appears to occur prior to polymer deposition and continues post-polymer formation. The current

generated by such oxidation (P_w1) is not negligible compared to the polymer oxidation peak (P_w2), suggesting that the product might be a mixture of W oxides and PEDOT. Previous studies have suggested several possible reactions at the W surface (equation (5.6)(5.7)) [6, 27, 28], but the precise electrochemical reactions remain unclear [6].

$$W + 4H_2O \rightarrow WO_4^{2-} + 8H^+ + 6e^- \quad (5.6)$$

$$WO_3 + H_2O \rightarrow WO_4^{2-} + 2H^+ \quad (5.7)$$

Moreover, the challenge of preventing oxidation cannot mitigated by PEDOT deposition. Consequently, subsequent sections will focus on Pt, a better candidate for implant microelectrode [6] and for surface modification, where no oxidation except for polymer formation is expected within the potential range of interest.

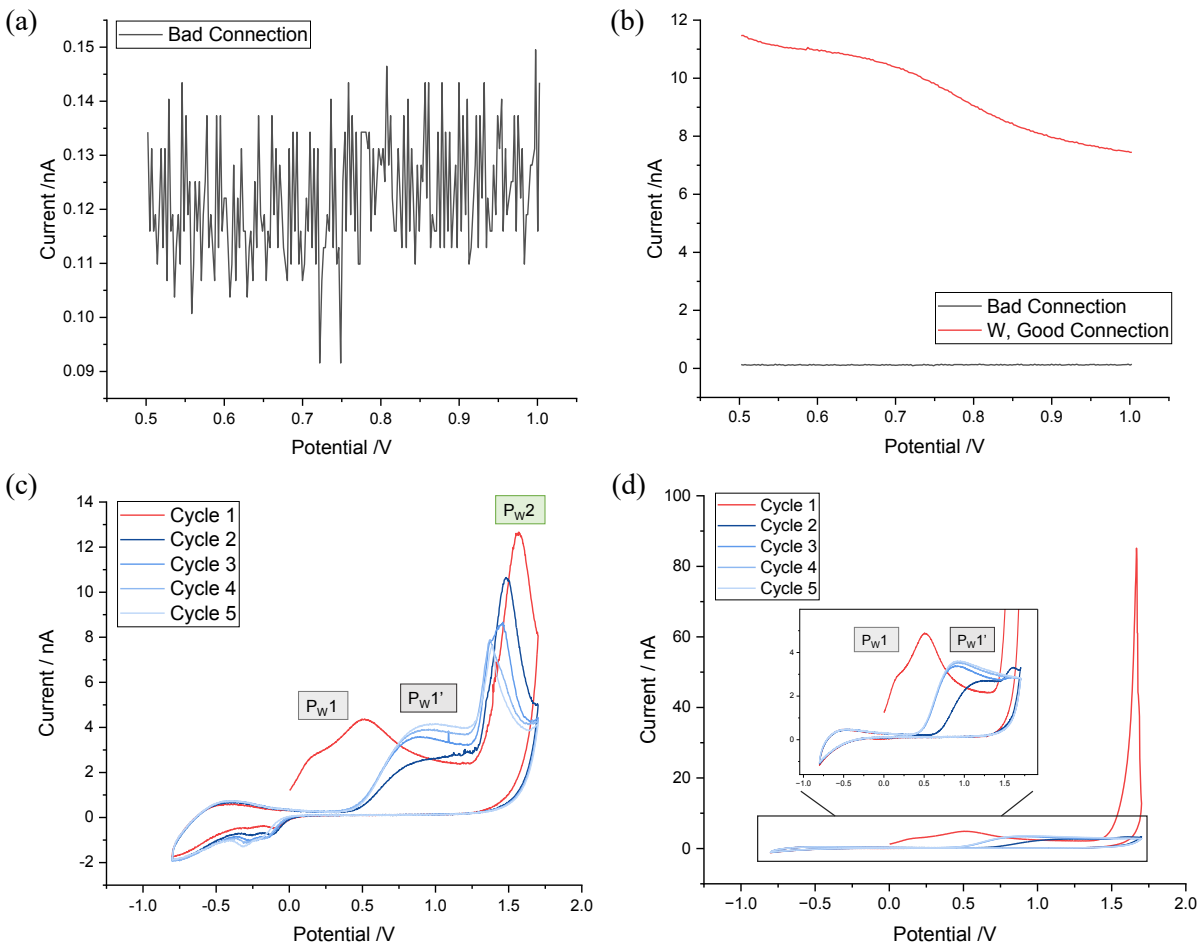

Figure 5.3:(a) Example CV for a "bad" W wire connection. **(b)** Contrast between "good" and "bad" connections to W wires. **(c~d)** CV scan of bare W microwire (d = 12.7 μm) from the OCP → 1.7 V → -0.8V → OCP **(c)** in 10 mM EDOT and 0.1 mM NaPSS. **(d)** in 0.1 mM NaPSS. **P_w1, P_w1':** W oxidation. **P_w2:** Mix of EDOT oxidation and PEDOT overoxidation. Scan rate *v* = 50 mVs^{-1} for all the above scans. All potentials are reported relative to the SCE.

5.3.3 Pt Microwire Characterization

In the first part of this section (Section 5.3.3.1), I first explore via CV the effect of different Pt electrode sizes on the electro-oxidation of EDOT in NaPSS. Subsequently, a galvanostatic deposition is performed on Pt microelectrodes. The coatings are characterized in the background electrolyte containing only NaPSS, and the results compared with those from the macroelectrode [20], particularly focusing on the charge associated with polymer overoxidation.

After testing with EDOT/NaPSS, the Pt microelectrode is used to explore the EDOT/NaCl in Section 5.3.3.2. Galvanostatic deposition conditions for EDOT/NaCl are also examined. Finally, the results of different polymer coatings (PEDOT:PSS and PEDOT:Cl) are compared.

5.3.3.1 Pt Microwire in EDOT/NaPSS

The voltammograms recorded at both Pt microwires (d = 15 and 25 μm) in the monomer solution from OCP to 1.7 V and back to -0.8 V. These results are presented together with previously reported macroelectrode data [20] (**Chapter 4**) in **Figure 5.4**(a). The major oxidation peak (P) shifts more negative potentials as the dimensions of the wire get smaller. This might be caused by the different diffusion to and from micro- and macro-disk electrodes with the greater current density seen at microelectrodes leading to the more rapid completion of the process. A shoulder (S) was observed beside the major peak for Pt (d = 25 μm) (**Figure 5.4** (a)), similar to what is seen for the macroelectrode, where the shoulder (S) represents EDOT polymerization, and the major peak (P) is the PEDOT overoxidation. The shoulder is not visible

for the smaller Pt wire (d = 15 μm) due to the shift of P with potential. The observations help explain why in the case of W microwire (d = 12.7 μm), the P_w2 in **Figure 5.4**(c) is concluded to be a combination of EDOT polymerization and PEDOT overoxidation.

Next, CV scans of bare 25 μm Pt micro and macro electrodes in 0.1 mM NaPSS were conducted and are displayed in **Figure 5.4**(b, c). The current density in the microelectrode scan (**Figure 5.4**(b)) is significantly higher than that in the macroelectrode (**Figure 5.4**(c)), as anticipated. However, the major electrochemical reactions remain consistent; both electrode types exhibit Pt oxide formation within the potential range of 0.5 V to 1.0 V vs. SCE and reduction around 0.0 V vs. SCE. Based on the CV results, I transitioned to using the galvanostatic deposition method instead of potentiostatic deposition to prevent PEDOT overoxidation while ensuring that the charge deposition per unit area remains constant.

The choice of galvanostatic deposition maintained the same current density as that used in the macroelectrode deposition ($\sigma_{ave} = 50\, mCcm^{-2}$). The monomer oxidation on the macroelectrode was observed at a potential of ca 1.0V with a current of ca. 80 μA [20]. Therefore the current density during oxidation (J_{ox}) can be calculated as in the following (equation (5.8)) which can then be employed to determine the current (I_{dep}) and duration (t_{dep}) for deposition on the 25 μm microelectrode (equation (5.9)(5.10)):

$$J_{ox} = \frac{I_{ox}}{A_{macro}} = \frac{80\mu A}{0.02cm^2} = 4mAcm^{-2} \tag{5.8}$$

$$I_{dep} = J_{ox} \times A_{micro} = 4mAcm^{-2} \times \left(\frac{25\times10^{-4}cm^{-2}}{2}\right)^2 \times \pi \approx 20\text{nA} \tag{5.9}$$

$$t_{dep} = \frac{\sigma_{ave}}{J_{ox}} = \frac{50mCcm^{-2}}{4mAcm^{-2}} \approx 13s \tag{5.10}$$

The galvanostatic deposition was applied to a Pt microwire (d = 25 μm) with a current of 20 nA for 13 s, as shown in **Figure 5.5**(a), resulting in a final charge density of around 50 $mCcm^{-2}$. The deposition was repeated for three independent trials, and the resulting deposition curves demonstrated a high level of consistency.

The coated Pt microwire was then placed in 0.1 mM NaPSS for a CV scan starting from OCP and up to 1.35 V (vs. SCE) and reversed back to -0.8 V (vs. SCE) for successive 3 cycles. The results are overlaid with the macroelectrode scans, ranging from OCP to 1.7 V (vs. SCE), as shown in **Figure 5.5**(b). These potential ranges were chosen to capture the entire overoxidation peak without reaching a potential that is high enough to cause solvent breakdown.

As illustrated in **Figure 5.5**(b), both the micro and macro electrodes exhibit an overoxidation peak in the first cycle, with no peak observed in subsequent scans due to the destruction of PEDOT electrical properties from overoxidation [20, 29, 30], preventing further electrochemical reactions. Notably, a shift in the overoxidation peak to less positive potentials occurs, analogous to the shift of the major oxidation peak observed in **Figure 5.4** (a) as the electrode size decreases. Further, the first cycle scans of the micro and macro electrodes were extracted and are presented in **Figure 5.5**(c) and **Figure 5.5**(d), respectively with the aim of comparing the charge transferred during the overoxidation process to approximately estimate the amount of polymer deposited. After baseline subtraction (indicated by the red lines), the areas under the curves were calculated. The outcomes reveal that the areas of the overoxidation peaks for the micro (Area ≈ 3.2 $mQcm^{-2}$) and macro (Area ≈ 2.8 $mQcm^{-2}$) electrodes are comparable, suggesting that the degree of overoxidation is similar and that the intended charge density deposition was successfully achieved.

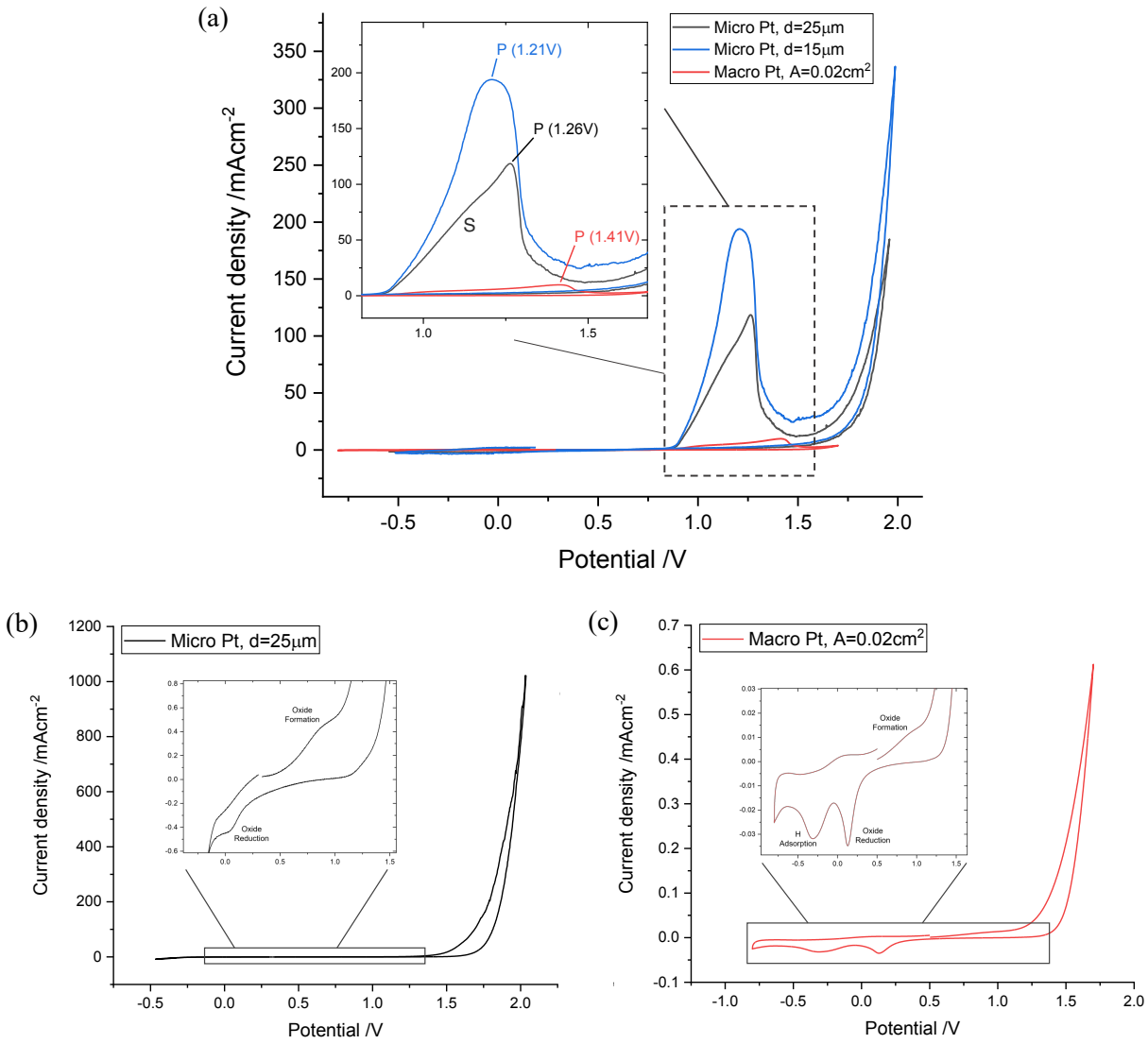

Figure 5.4 : (a) CV scan from OCP→ 2.0V → -0.5V → OCP was conducted for Pt microwires of d = 25 µm and 15 µm in solution containing 10 mM EDOT and 0.1 mM NaPSS. The results are overlayed with the previous macroelectrode CV scan, which ranged from -0.7 V to 1.7 V. **(b)** CV scan from OCP → 2.0V → -0.5V → OCP using Pt microwire with d = 25 µm, **(c)** CV scan from OCP → 2.0V → -0.8V → OCP using Pt macroelectrode with area A = 0.02 cm^2. Scan rate v = 50 mVs^{-1} for all the above scans. All potentials are reported relative to the SCE.

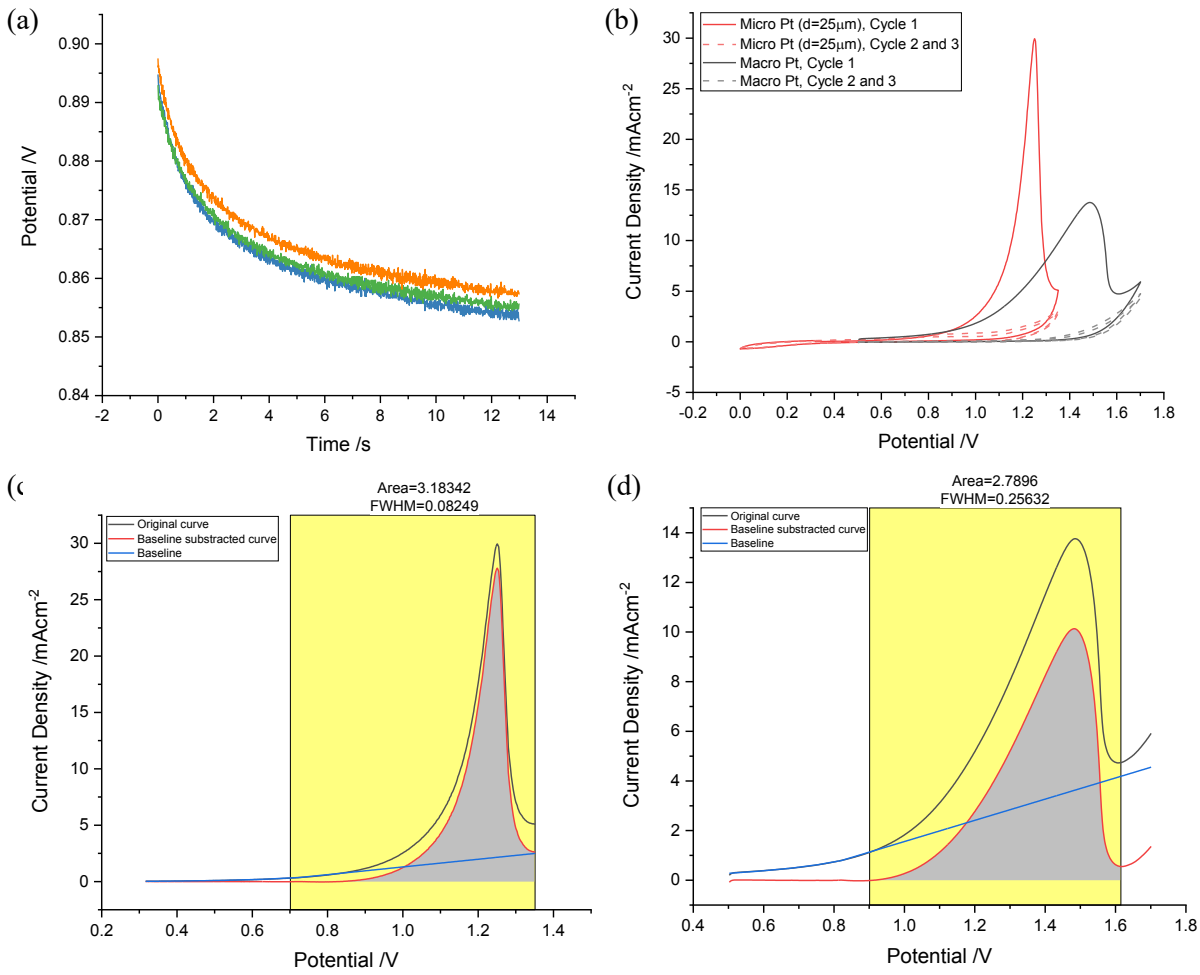

Figure 5.5: (a) Galvanostatic deposition of three independent trials. **(b)** On microelectrode, CV scans from OCP → 1.35V → 0V → OCP. On macroelectrode, CV scans from OCP →1.7V →OCP. **(c)** The area under the microelectrode overoxidation peak (Area ≈ 3.2 $mQcm^{-2}$), **(d)** The area under the macroelectrode overoxidation peak (Area ≈ 2.8 $mQcm^{-2}$). Scan rate ν = 50 mVs^{-1} for all the above CV scans. All potentials are reported relative to the SCE.

5.3.3.2 Pt Microwire in EDOT/NaCl

The CV scans of the bare Pt microwire in 0.1 M NaCl, 0.01 M PBS, 0.5 M Na_2SO_4, and 10 mM EDOT with 0.1 M NaCl are summarized in **Figure 5.6**(a). As seen in **Figure 5.6**(a), peak P2 (ca 1.21 V) represents PEDOT overoxidation, while P1 (ca 1.35 V) corresponds to chloride oxidation, similar to the findings discussed with the macroelectrode in Section 5.3.1.1. The difference in the scale of P1 in non-EDOT solutions compared to **Figure 5.1**(e) and **Figure 5.2**(a) is attributed to the higher current densities on the microelectrode compared to the macro disk, which leads to a shorter timescale for completing the process. When comparing scans between the micro and macro electrodes in EDOT/NaCl, the deposition of the polymer quickly covered the small cross-section of the microwire, thereby inhibiting the chloride reaction and resulting in a much smaller P1 in **Figure 5.6**(a) compared to **Figure 5.2**(a).

Next, a freshly cut Pt microwire was placed in a solution of 10 mM EDOT and 0.1 M NaCl to test the galvanostatic deposition conditions with currents ranging from 15 nA to 28 nA for 20 s. As illustrated in **Figure 5.6**(b), similar galvanostatic curves were observed for currents within the 15 nA to 22 nA range. For currents higher or equal to 23nA, the reaction potential increased. In particular, the potential shifted to above 1.3 V, which is near the chloride oxidation potential at the Pt surface. To ascertain whether this increase was related to chloride oxidation, the galvanostatic experiments were repeated in 0.1 M NaCl. The results, illustrated in **Figure 5.6**(c), show a consistent increasing trend in potential, implying that this phenomenon could be due to chloride oxidation on the Pt. Thus, a current between 15 nA and 22 nA is more suitable for electropolymerization, especially since the potential in this current range is between 1.0 V and 1.1 V, which corresponds to the range for monomer oxidation alone, as mentioned in Section 5.3.1.2.

Given the negligible differences when selecting a current between 15 nA and 22 nA, and for consistency with the deposition conditions of PEDOT:PSS (Section 5.3.3.1), a deposition

current of 20 nA for 13 s was chosen for subsequent experiments. The PEDOT:Cl-coated Pt microwire was then immersed in 0.01 M PBS, and the CV was compared with that for PEDOT:PSS-coated Pt microwire. Their galvanostatic curves are shown in **Figure 5.6**(d), and their CV scans in 0.01 M PBS are presented in **Figure 5.6**(e). From **Figure 5.6**(e), overoxidation peaks are observable for both types of polymer-coated electrodes, with their peak positions aligning with each other very well at around 1.2 V, indicating that EDOT was successfully oxidized in both cases to form either PEDOT:Cl or PEDOT:PSS on the Pt surface.

Comparison of the micro and macro electrode CV scans in solutions containing with EDOT monomer, reveals much higher current densities at the microelectrode disc. This leads to more rapid completion of electrochemical processes, where the effect is more obvious in smaller diameter electrodes (12.7 μm W and 15 μm Pt) resulting in the merging of oxidation and overoxidation peaks. Consequently, the galvanostatic deposition method was chosen to prevent PEDOT overoxidation, with a current of 20 nA for 13 s being selected to ensure that the charge deposition per unit area achieves an average density of $\sigma_{ave} = 50\, mCcm^{-2}$. Electropolymerization using this method to deposit PEDOT:PSS and PEDOT:Cl on Pt was tested in PBS. The presence of overoxidation peaks in both cases was successfully used to fingerprint successful coating. Thus, in the subsequent section, this galvanostatic deposition condition is maintained and applied to a Pt tetrode.

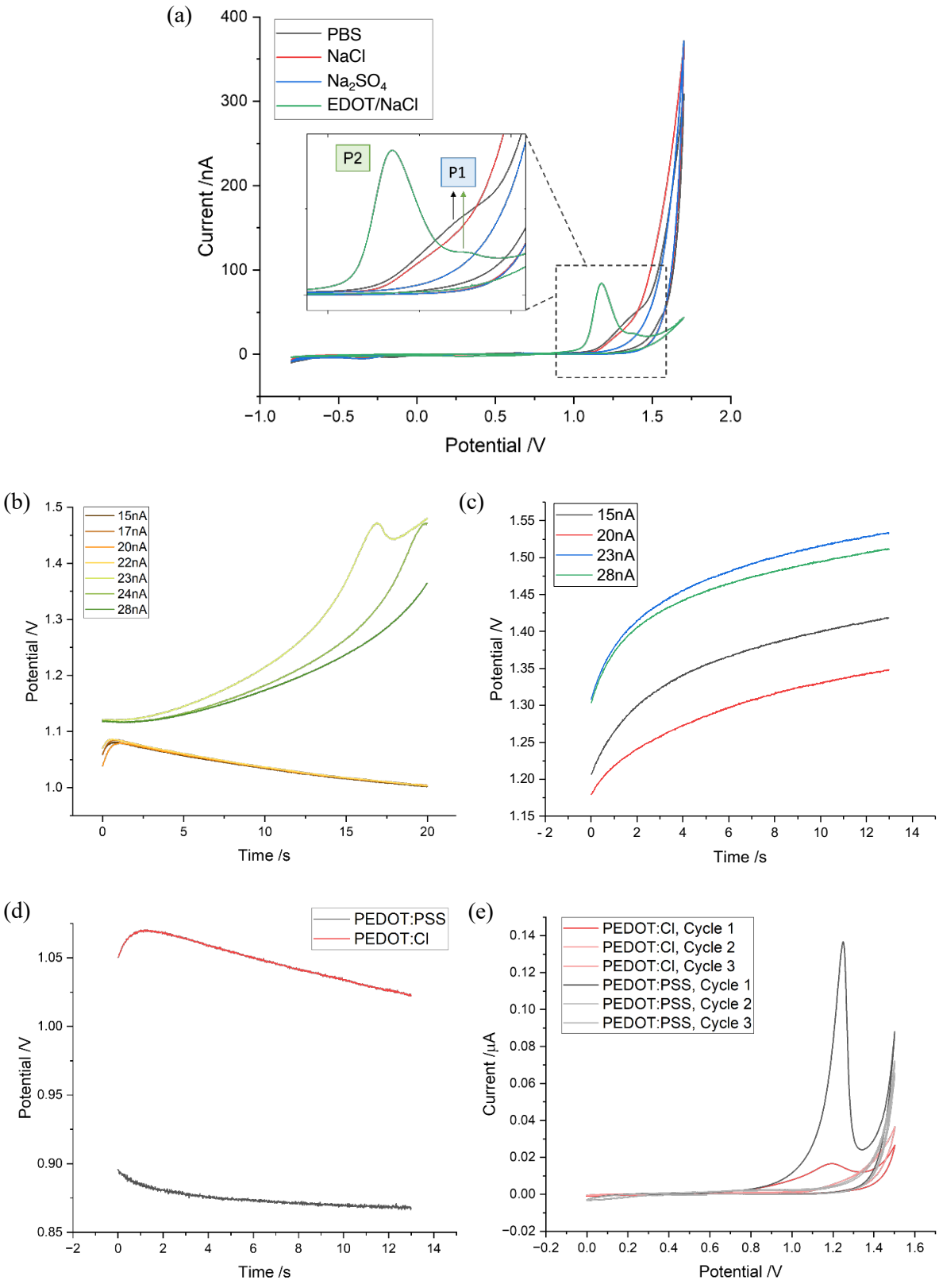

Figure 5.6: (a) Comparison of the CV scans from OCP → 1.7V →-0.8V → OCP using Pt microelectrode (d = 25 µm) in 0.01 M PBS, 0.1 M NaCl, 0.5 M Na_2SO_4, and 10 mM EDOT with 0.1 M NaCl, respectively. **(b)** Galvanostatic deposition of Pt immersed in 10 mM EDOT

and 0.1 M NaCl, holding current at different values for 20 s. **(c)** Galvanostatic deposition of Pt immersed in 0.1 M NaCl, holding current at different values for 13 s. **(d)** Galvanostatic deposition of Pt immersed in 10 mM EDOT and 0.1 M NaCl or 10 mM EDOT and 0.1 mM NaPSS. Coating conditions were both 20 nA for 13 s. **(e)** Three successive CV scans of PEDOT:Cl and PEDOT:PSS coated Pt immersed in 0.01 M PBS for a CV scan OCP →1.5 V → 0 V → OCP. Scan rate v = 50 mVs^{-1} for all the above CV scans. All potentials are reported relative to the SCE.

5.3.4 Tetrode

To have a visual representation of the structure of a bare tetrode, SEM images of both the tetrode body and its cross-sections were captured and are presented in **Figure 5.7**. W tetrodes have insulation made of Heavy Formvar (HFV), which can be melted and fused together using a heat gun at 200˚C (**Figure 5.7**(a)). In contrast, a Pt tetrode, as shown in **Figure 5.7**(c), shows no melting of the polyimide insulation at this temperature. However, after heat curing at approximately 300˚C, the four Pt wires are tightly packed together, as illustrated in Figures S9(d, e). Moreover, the tetrode body does not exhibit significant alterations after heating, as evidenced by comparing **Figure 5.7**(e, f) with the non-heated example in **Figure 5.7**(b).

5.3.4.1 Cross Connection Test – Electrochemical Method

CV scans of a coated (Wire 1) and an adjacent bare wire (Wire 2) in 0.1mM NaPSS were compared before and after polymer deposition. As illustrated in **Figure 5.8**(a), after Wire 1 was coated with PEDOT:PSS, a significant peak corresponding to polymer overoxidation is evident in the first CV scan cycle. In the subsequent cycles, the scans align resemble those seen before coating, indicating that polymer electroactivity was destroyed in the first scan, rendering the response indistinguishable from that of bare Pt. The CV scans of the uncoated Wire 2, depicted

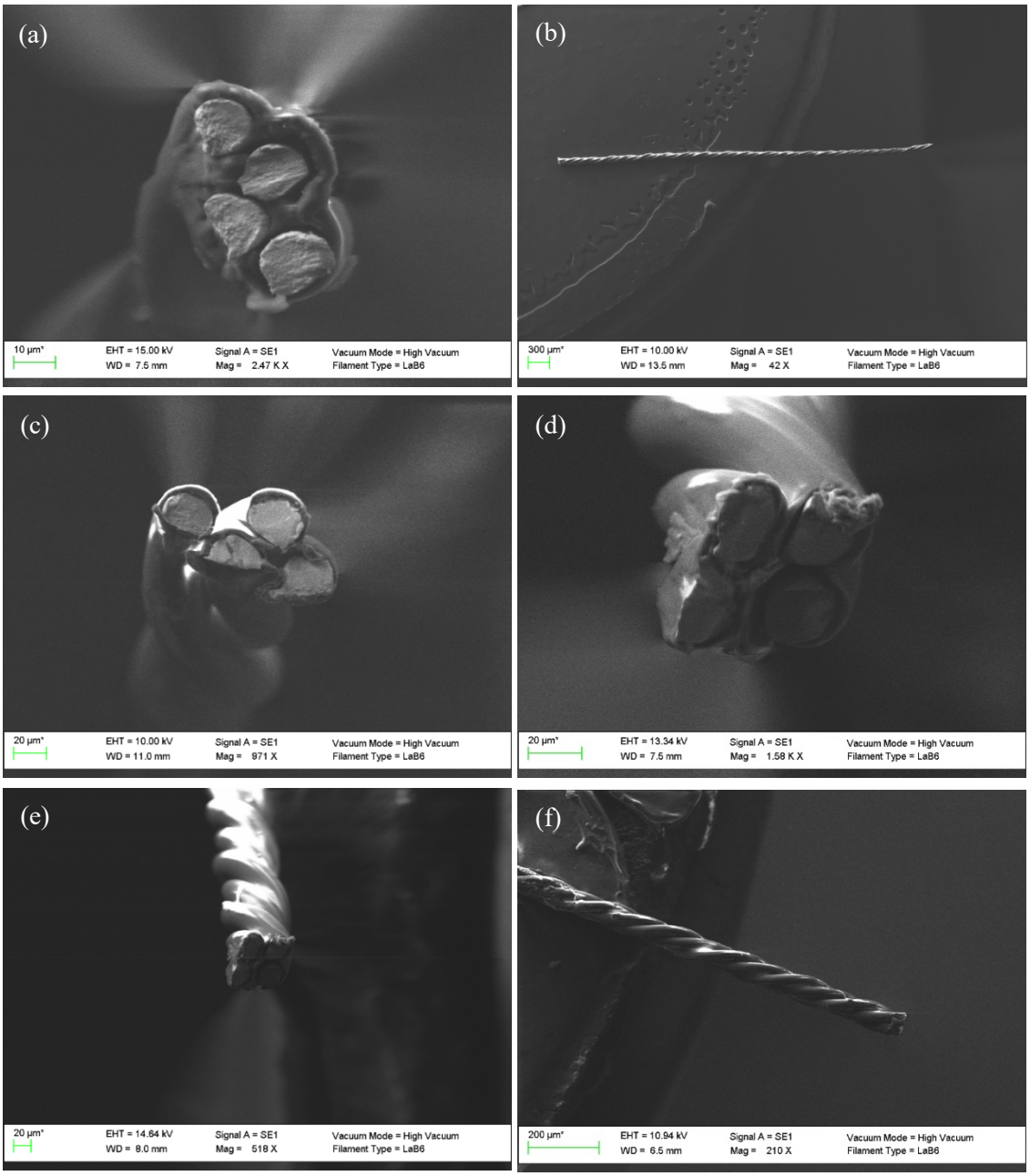

Figure 5.7: (a) W tetrode with heat curing at 200˚C. The outer insulation (HFV) is fused together, and the four wires are closely packed. **(b,c)** Pt tetrode without heat curing, body, and cross-section images. Four wires split at the end of the tetrode. **(d~f)** Pt tetrode with heat curing at 300 ˚C, cross-section, and body images. The Pt wires are closely packed.

in **Figure 5.8**(b), show minimal difference before and after the coating of Wire 1. This demonstrates that individual tetrode discs can be coated without affecting neighboring discs. The slight increase observed in Wire 2 (at ca 1.0 V, **Figure 5.8**(b)) after coating Wire 1 is attributed to EDOT adsorption rather than overgrowth. Otherwise, scanning Wire 1 would have completely eliminated any peaks in Wire 2.

Subsequently, all wires were coated in sequence (noted as Wires 1 to 4). Their galvanostatic deposition curves, presented in **Figure 5.8**(c), show a relatively consistent initiation point, indicating that the polymerization commenced on the Pt substrate without any previous potential overgrowth. All four wires exhibit overoxidation peaks in the first cycle of their CV scans in NaPSS (**Figure 5.8**(d)), and the subsequent cycles (**Figure 5.8**(e)) confirmed that all polymer-associated electroactivity was eradicated. These findings confirm that the destruction of polymer on one tetrode disc did not impact the others, suggesting that the coatings are independent on each wire without any electrical cross-connection. Moreover, the uniformity in the height and shape of all four overoxidation peaks (**Figure 5.8**(d)) suggests that a consistent level of deposition was achieved.

5.3.4.2 Cross Connection Test – Spectroscopic Analysis

Three of the four wires on the tetrode were coated, and their characterizations are presented in **Figure 5.9**. It is challenging to determine from the SEM image alone (**Figure 5.9** (a)) whether the surface is covered with PEDOT. However, EDX provides insights into the elements present on the surface (**Figure 5.9** (d)). The EDX spectra of the coated discs, as shown in **Figure 5.9** (d), revealed the presence of carbon (C) and oxygen (O) elements, while the bare and partially exposed electrodes exhibited significant peaks for platinum (Pt). The high levels of aluminum (Al) observed originate from the sample stage. Optical microscopy offered more direct visual evidence; the bare Pt appears shiny, whereas the PEDOT-covered surfaces are dull (Figures

S11(b, c)). Additionally, Figures S11(b, c) clearly show that the PEDOT adhered well to the plates without encroaching onto the other discs.

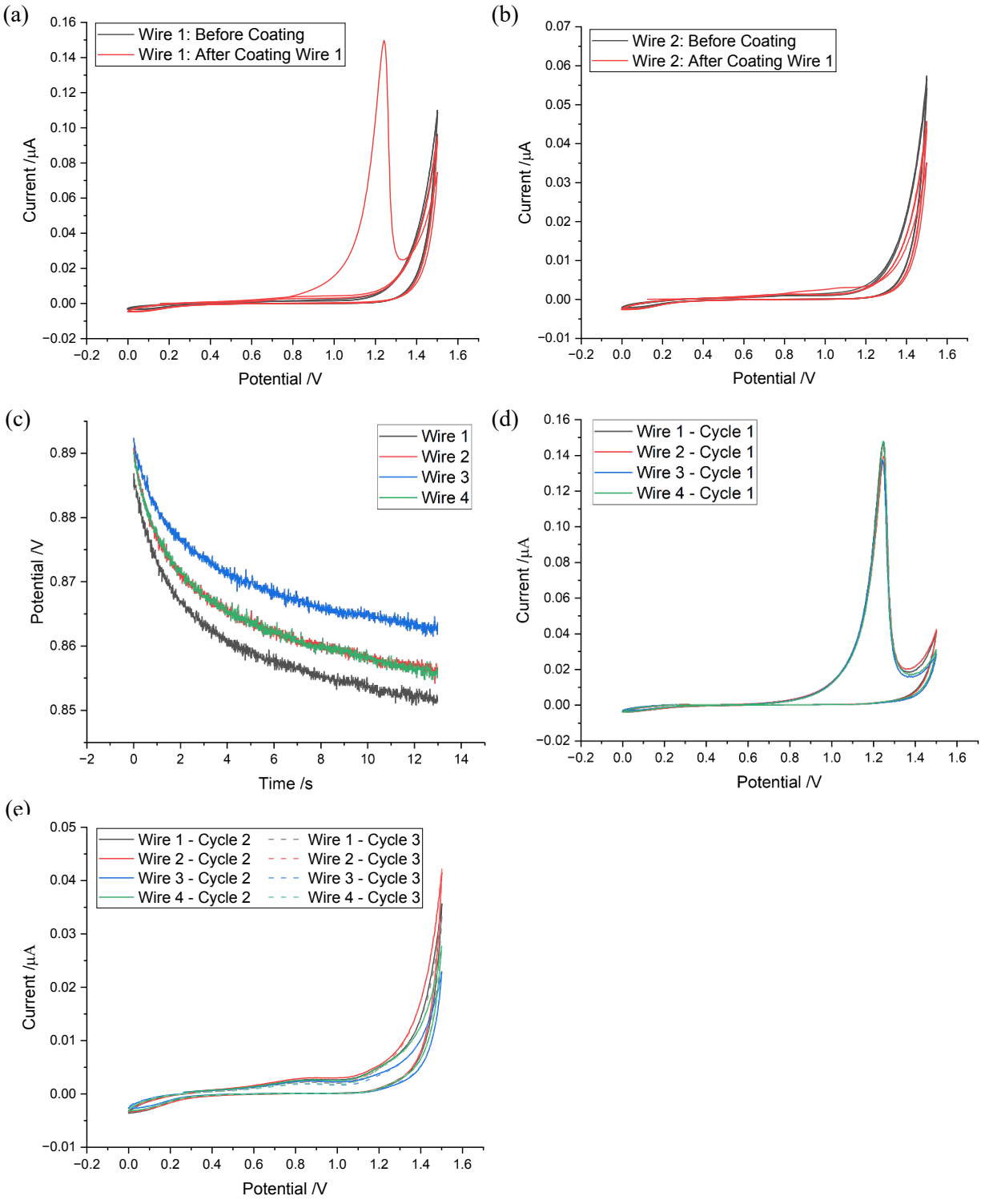

Figure 5.8: (a) CV scan of wire 1 before and after coating in 0.1mM NaPSS (OCP → 1.5 V →OCP). **(b)** CV scan in 0.1 mM NaPSS of wire 2 before and after coating wire 1 (OCP → 1.5

V →OCP). (The other bare wires had similar results as Wire 2). **(c)** Galvanostatic deposition of all four wires at 20 nA for 13 s. **(d, e)** The CV scan for all four wires in 0.1 mM NaPSS (OCP → 1.5 V →OCP). **(d)** The first cycle of the CV. Overoxidation peaks can be observed for all wires. **(e)** Second (solid lines) and third cycles (dashed lines) of CV scan for all four wires. Scan rate v = 50 mVs^{-1} for all the above CV scans. All potentials are reported relative to the SCE.

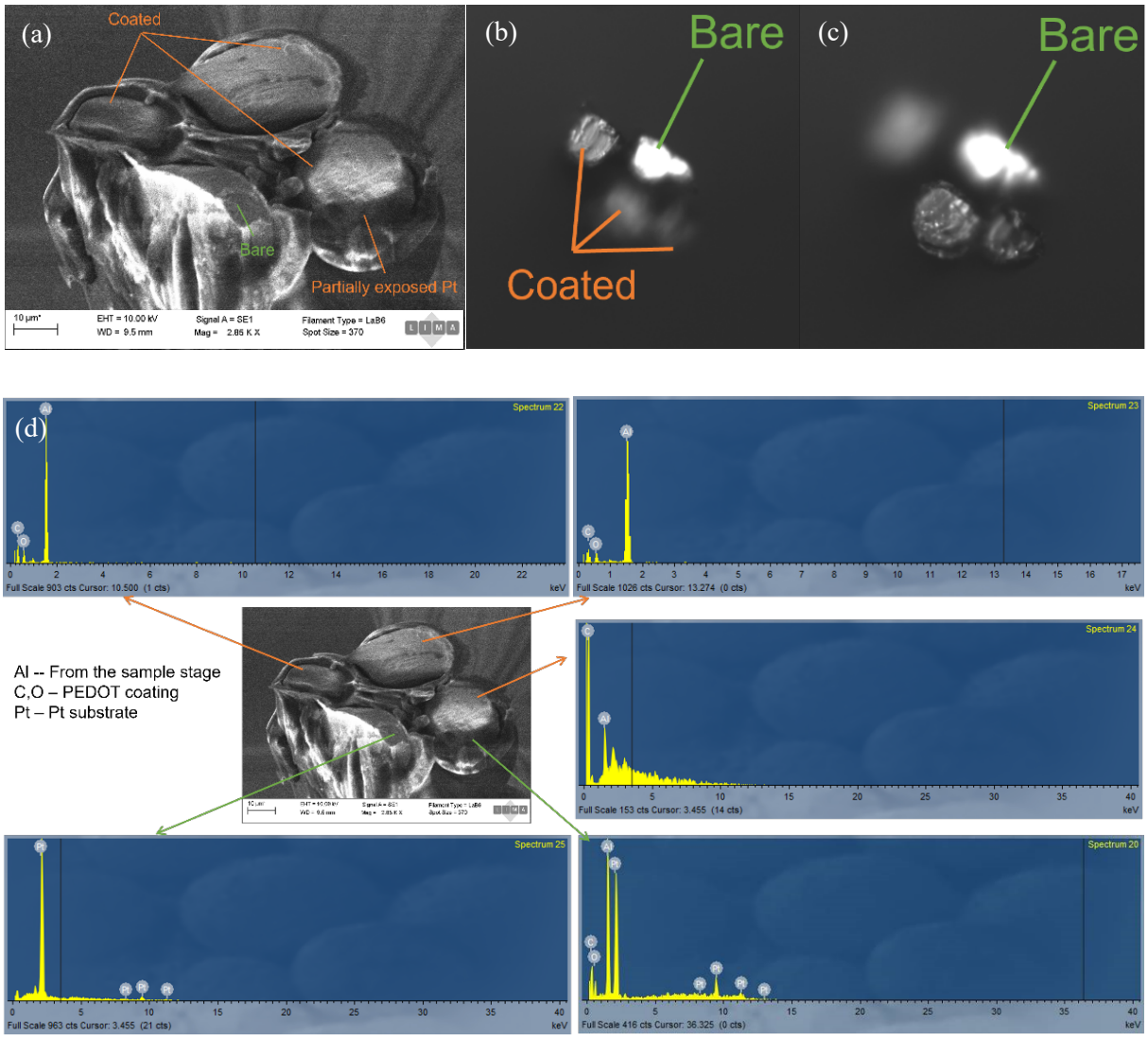

Figure 5.9: (a) SEM image of partially coated Pt tetrode. **(b,c)** Optical microscope image of partially coated Pt tetrode. **(d)** EDX for analyzing elements on the surface as shown in (a).

5.4 Conclusions

Building on the works reported in the previous chapter, this chapter has further evaluated PEDOT polymers with different dopants, Cl^-. Similar to PEDOT:PSS, PEDOT:Cl has its polymerization initiated at a potential around 1.0 V to 1.1 V, and an overoxidation happens at ca. 1.2 V. However, the presence of chloride ions in the solution introduces an additional oxidation peak at approximately 1.5 V due to chloride oxidation. This chloride oxidation can be suppressed once the Pt substrate is coated with the polymer, which restricts access to chloride ions.

Contrasting W and Pt, the key difference is the oxidation of W, which happens prior to the EDOT oxidation and cannot be mitigated by a polymer coating. Consequently, the resultant electrode consists of both oxide and PEDOT, making it difficult to characterize and unsuitable for neural electrode applications.

Comparing macro and micro Pt electrodes, analysis of the charge transferred under the overoxidation peak indicates a similar level of oxidation on both electrodes. Therefore, a similar method can be employed for coating microelectrodes and tetrodes. Moreover, as demonstrated by the cross-connection test, the chosen amount of deposition (50 mC cm^{-2}) effectively adheres to each individual recording site without causing polymer overgrowth and cross-connection within the tetrode.

In summary, this chapter has systematically tested not only the polymer but also the electrode material for tetrode fabrication. The method for tetrode coating and the subsequent cross-connection test offers a straightforward approach for any microelectrode array subjected to PEDOT deposition or any conductive polymer whose properties change beyond a certain potential threshold. The coating scheme is applied in the next chapter to assess polymer performance on a tetrode in vitro and explore the recording processes at the electrode/polymer interface.

References

(1) Zhang, Y.; Chen, Y.; Contera, S.; Compton, R. G. Double Electrode Experiments Reveal the Processes Occurring at PEDOT-Coated Neural Electrode Arrays. *ACS Appl. Mater. Interfaces* **2024**, *16* (22), 29439-29452.

(2) Geddes, L. A.; Roeder, R. Criteria for the selection of materials for implanted electrodes. *Ann Biomed Eng* **2003**, *31* (7), 879-890.

(3) Hong, G.; Lieber, C. M. Novel electrode technologies for neural recordings. *Nature Reviews Neuroscience* **2019**, *20* (6), 330-345.

(4) Feiner, R.; Dvir, T. Tissue–electronics interfaces: from implantable devices to engineered tissues. *Nature Reviews Materials* **2017**, *3* (1), 17076.

(5) Yin, L.; Cheng, H.; Mao, S.; Haasch, R.; Liu, Y.; Xie, X.; Hwang, S.-W.; Jain, H.; Kang, S.-K.; Su, Y.; et al. Dissolvable Metals for Transient Electronics. *Advanced Functional Materials* **2014**, *24* (5), 645-658.

(6) Patrick, E.; Orazem, M. E.; Sanchez, J. C.; Nishida, T. Corrosion of tungsten microelectrodes used in neural recording applications. *Journal of Neuroscience Methods* **2011**, *198* (2), 158-171.

(7) Rossetti, N.; Hagler, J. E.; Kateb, P.; Cicoira, F. Neural and electromyography PEDOT electrodes for invasive stimulation and recording. *Journal of Materials Chemistry C* **2021**, *9* (23), 7243-7263, 10.1039/D1TC00625H.

(8) Peng, C.; Jin, J.; Chen, G. Z. A comparative study on electrochemical co-deposition and capacitance of composite films of conducting polymers and carbon nanotubes. *Electrochimica Acta* **2007**, *53* (2), 525-537.

(9) Xia, Z.; Arias-Gil, G.; Deckert, M.; Vollmer, M.; Curran, A.; Herrera-Molina, R.; Brosch, M.; Krug, K.; Schmidt, B.; Ohl, F. W. Electrochemical Roughening and Carbon Nanotube Coating of Tetrodes for Chronic Single-Unit Recording. *bioRxiv* **2019**, 738245.

(10) Charkhkar, H.; Knaack, G. L.; McHail, D. G.; Mandal, H. S.; Peixoto, N.; Rubinson, J. F.; Dumas, T. C.; Pancrazio, J. J. Chronic intracortical neural recordings using microelectrode arrays coated with PEDOT–TFB. *Acta Biomater* **2016**, *32*, 57-67.

(11) Asplund, M.; Nyberg, T.; Inganäs, O. Electroactive polymers for neural interfaces. *Polymer Chemistry* **2010**, *1* (9), 1374-1391, 10.1039/C0PY00077A.

(12) Yamato, H.; Ohwa, M.; Wernet, W. Stability of polypyrrole and poly(3,4-ethylenedioxythiophene) for biosensor application. *J Electroanal Chem* **1995**, *397* (1), 163-170.

(13) Bodart, C.; Rossetti, N.; Hagler, J. E.; Chevreau, P.; Chhin, D.; Soavi, F.; Schougaard, S. B.; Amzica, F.; Cicoira, F. Electropolymerized Poly(3,4-ethylenedioxythiophene) (PEDOT) Coatings for Implantable Deep-Brain-Stimulating Microelectrodes. *ACS Applied Materials & Interfaces* **2019**, *11* (19), 17226-17233.
(14) Dijk, G.; Ruigrok, H. J.; O'Connor, R. P. Influence of PEDOT:PSS Coating Thickness on the Performance of Stimulation Electrodes. *Adv Mater Interfaces* **2020**, *7* (16), 2000675.
(15) Hubel, D. H. Tungsten microelectrode for recording from single units. *Science* **1957**, *125* (3247), 549-550.
(16) Cui, X. T.; Zhou, D. D. Poly (3,4-ethylenedioxythiophene) for chronic neural stimulation. *IEEE Trans Neural Syst Rehabil Eng* **2007**, *15* (4), 502-508.
(17) Luo, X.; Weaver, C. L.; Zhou, D. D.; Greenberg, R.; Cui, X. T. Highly stable carbon nanotube doped poly(3,4-ethylenedioxythiophene) for chronic neural stimulation. *Biomaterials* **2011**, *32* (24), 5551-5557.
(18) Baek, S.; Green, R. A.; Poole-Warren, L. A. The biological and electrical trade-offs related to the thickness of conducting polymers for neural applications. *Acta Biomater* **2014**, *10* (7), 3048-3058.
(19) Baek, S.; Green, R. A.; Poole-Warren, L. A. Effects of dopants on the biomechanical properties of conducting polymer films on platinum electrodes. *J Biomed Mater Res A* **2014**, *102* (8), 2743-2754.
(20) Zhang, Y.; Chen, Y.; Contera, S.; Compton, R. G. Electrochemical and Nanostructural Characterization of Poly(3,4-ethylenedioxythiophene):poly(styrenesulfonate) Films as Coatings for Neural Electrodes. *ACS Applied Polymer Materials* **2023**, *5* (7), 5555-5566.
(21) Van de Ven, G. M.; Trouche, S.; McNamara, C. G.; Allen, K.; Dupret, D. Hippocampal offline reactivation consolidates recently formed cell assembly patterns during sharp wave-ripples. *Neuron* **2016**, *92* (5), 968-974.
(22) Patil, R. S.; Juvekar, V. A.; Naik, V. M. Oxidation of Chloride Ion on Platinum Electrode: Dynamics of Electrode Passivation and its Effect on Oxidation Kinetics. *Industrial & Engineering Chemistry Research* **2011**, *50* (23), 12946-12959.
(23) Puglia, M. K.; Bowen, P. K. Cyclic Voltammetry Study of Noble Metals and Their Alloys for Use in Implantable Electrodes. *ACS Omega* **2022**, *7* (38), 34200-34212.
(24) Dickinson, T.; Greef, R.; Wynne-Jones, L. The kinetics of the chlorine electrode reaction at a platinum electrode. *Electrochimica Acta* **1969**, *14* (6), 467-489.
(25) Chen, Y.; Compton, R. G. Direct Electrochemical Analysis in Seawater: Evaluation of Chloride and Bromide Detection. *Chemosensors* **2023**, *11* (5), 297.

(26) Williams, J. C.; Rennaker, R. L.; Kipke, D. R. Long-term neural recording characteristics of wire microelectrode arrays implanted in cerebral cortex. *Brain Research Protocols* **1999**, *4* (3), 303-313.
(27) Kelsey, G. S. The anodic oxidation of tungsten in aqueous base. *Journal of the Electrochemical Society* **1977**, *124* (6), 814.
(28) Lillard, R.; Kanner, G.; Butt, D. The nature of oxide films on tungsten in acidic and alkaline solutions. *Journal of the Electrochemical Society* **1998**, *145* (8), 2718.
(29) Tamburri, E.; Orlanducci, S.; Toschi, F.; Terranova, M. L.; Passeri, D. Growth mechanisms, morphology, and electroactivity of PEDOT layers produced by electrochemical routes in aqueous medium. *Synthetic Metals* **2009**, *159* (5), 406-414.
(30) Du, X.; Wang, Z. Effects of polymerization potential on the properties of electrosynthesized PEDOT films. *Electrochimica Acta* **2003**, *48* (12), 1713-1717.

Chapter 6

Double Electrode Experiments Reveal the Processes Occurring at PEDOT-Coated Neural Electrode Arrays

Chapter 6 implements the methods established in **Chapter 4** and **Chapter 5** for tetrode fabrication and coating. Furthermore, this chapter also introduces the use of in vitro double electrode experiments to mimic the responses of neural electrodes with a focus on signal-recording electrodes modified with PEDOT. Specifically, potential steps on one unmodified electrode in an array are used to identify the responses for PEDOT doped with different anions and compared with that of a bare Pt electrode. The response is shown to be related to the rearrangement of ions in solution near the detector electrode resulting from the potential step, with a current transient seen at the detector electrode. A rapid response for PEDOT doped with chloride ions (ca. 0.04 s) was observed and attributed to the fast movement of chloride ions in and out of the polymer film. In contrast, PEDOT doped with PSS^- responds much slower (ca. 2.2 s), and the essential immobility of polyanion constrains the direction of current flow.

The work presented in **Chapter 6** has been published in *ACS Applied Materials and Interfaces* [1]. The project was conducted under the supervision of Prof. Richard Compton and Prof. Sonia Contera. Dr. Yuqi Chen assisted with the understanding and interpretation of the electrochemical analysis.

6.1 Introduction

Neuronal activity in the central nervous system gives rise to transmembrane currents that can be detected by electrodes in the extracellular medium. These “electrical recordings” are used by neuroscientists to investigate the processes underlying neuronal communication and computation[2]. Significant research has focused on developing neural recording electrodes to

collect and interpret these signals in the brain. Extracellular recording started with a tungsten microwire electrode [3], advancing to silicon probes, among which the Michigan array [4, 5] and Utah array [6, 7] are the most widely used. The Michigan array consists of a single or several long "shanks" [5] with distributed recording sites. The Utah array is a 10x10 array of silicon needles on a large silicon base. Subsequent developments include tetrodes, formed by twisting microwires together [8, 9], and more recently, flexible polymer electrode arrays such as NeuroGrid [10, 11] and mesh electronics [12, 13]. A summary of the various electrodes is presented in **Table 6.1**.

As mentioned in Section 1.1.2, the signals or spikes recorded by extracellular electrodes are generated by ion flow induced near active neurons. Extracellular recordings typically embrace signals from multiple neurons within a proximal range (up to around 140 μm) [2, 14]. Hence, a single detection channel can capture signals from various neurons. If the spikes have minimal overlap so that they can be temporally resolved [15], then active neurons can be located using triangulation methods by analyzing the amplitudes of the wavefronts from different channels [9]. Additionally, the distinct shape of each action potential helps in identifying individual neurons [9, 15]. Silicon probes, usually with numerous detection sites (ranging from 8 to 1024 recording sites [2, 16, 17]), are designed to capture as many signals as possible, and such oversampling can facilitate spike separation and assignment [2]. However, their relatively large physical size poses challenges, causing tissue damage, particularly when penetrating deep into the brain [2, 16]. For instance, a Michigan array is often approximately 120 μm in width and 15 to 50 μm in thickness [18], and a Utah array has 100 silicon needles (around 80~100 μm thick at base [6, 7, 16]) projecting from a large substrate (4.2 × 4.2 mm) [6]. This penetration can lead to inflammation and glial encapsulation that prevents external signals from reaching the electrode [2, 16, 19]. To address these issues, recent developments in electrode technology have focused on creating more physically flexible designs. For example, NeuroGrid is a flexible organic material-based interface array [10], whereas this flexible electrode film primarily allows for the

detection of superficial cortical neuron signals [10]. To facilitate deep-brain measurement, an innovative approach has been the development of injectable neural mesh. This mesh-like structure can be injected into a specific brain region by using a syringe, but the position can no longer be altered post-injection [12, 13].

The tetrode, a now well-established method, consists of four insulated microwires twisted together, with metal exposed only at the tip (**Figure 6.1**(a)). The diameter of a single microwire is typically around 12 to 25 μm [20-22], making the tetrode significantly thinner than a silicon probe, which enables it to reach deep brain regions with minimal damage. Although a single tetrode has only four recording sites, a specially designed drive can hold multiple tetrodes arranged in a custom configuration [23, 24]. This allows for recordings across widely distributed structures, and the drive facilitates vertical adjustments of each tetrode, both before and during recordings [24]. Advances in drive design now permit compatibility with complex animal movements [20, 21] as well as wireless data logging [23], enabling observations of natural and free behaviors. Nevertheless, tetrodes still face an immune response by the brain due to their mechanical mismatch. The mechanical mismatch between the tetrode's body and the brain tissue can be mitigated by using more bendable materials, such as platinum or platinum-iridium, instead of tungsten wires [22]. Further improvement can be offered by modification with coating with a soft, biocompatible conductive polymer, such as PEDOT.

Although PEDOT-coated electrodes have seen widespread application, the mechanisms underlying signal recording at the polymer-metal interface remain insufficiently understood. To clarify these mechanisms, this chapter introduces an in vitro experiment utilizing a bipotentiostat and a tetrode to explore the electrical response within the polymer film created by neural signals. During extracellular recording, signals arise due to the depolarization of neuron membranes, which causes local ion flux [25]. To simulate this neuronal activity, the potential of one electrode (WE1) within the tetrode is rapidly altered to replicate the

depolarization changes of active neurons (**Figure 6.1**(b)). Meanwhile, the response of a nearby second electrode (WE2) within the same tetrode is monitored (**Figure 6.1**(b)). In this way, the complex ionic conduction environment in the brain can be simplified, but the essence of signal recording is preserved and can be investigated. In particular, the sensitivity and magnitude of the response of the monitoring electrode (WE2) can be compared and contrasted for different surface modifications. Thus, the in vitro experiments that explore how an electrode reacts to adjacent potential disturbances can serve as a basis for understanding signal recording in vivo, offering insight into the process at the metal-polymer interface and so giving a basis for the design and functionality of future neural recording devices.

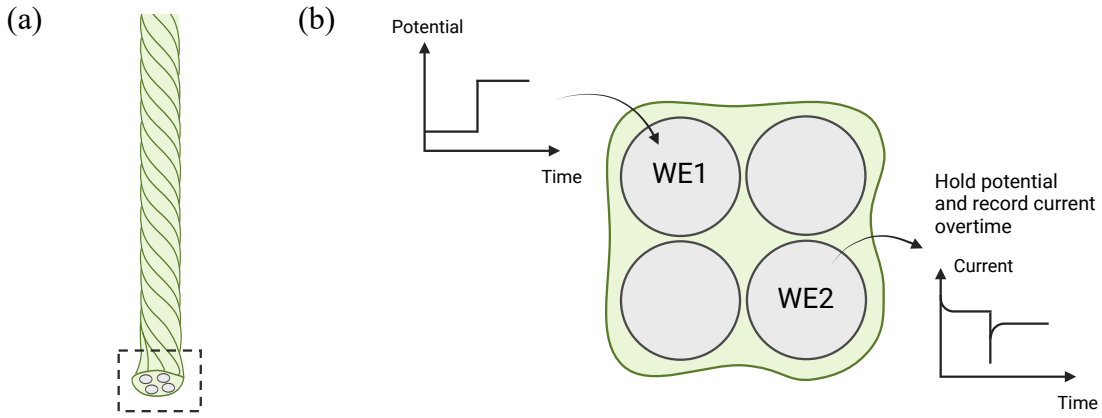

Figure 6.1: (a) Schematic tetrode. The green color indicates the outer insulation layer. The metal, depicted in grey, is only exposed at the tip. The boxed section is enlarged and shown in (b) **(b)** Setup to mimic neural recording. A stepped potential is applied to one of the wires on tetrode (WE1), mimicking neural activity. The response experienced by one other wire (WE2) is monitored over time.

Table 6.1: Summary of neural electrodes.

Electrode Techniques	Description	Function	Refs
Tungsten microwire electrode	One of the earliest types of neuron electrodes was reported to have a sharpened tip with a submicrometer diameter, enabling it to record signals from small neurons and axons in the mammalian brain.	Recording	3
Michigan array	The Michigan array consists of one to several long shanks, with recording sites distributed along each shank. Typically, the shank width is 120 μm, and its thickness ranges from 15 to 50 μm.	Recording and stimulating	4, 5, 18
Utah array	The Utah array consists of 100 microelectrodes arranging in a 10×10 pattern. These silicon needles typically have a length of a few millimeters, projecting from a silicon base, with a dimension of approximately 4.2×4.2 mm.	Recording and stimulation	6, 7, 16
Tetrode	Tetrode is formed by twisting four insulated microwires together. The microwire diameter usually ranges from 12 to 25 μm.	Recording	8, 9
NeuroGrid	NeuroGrid consists of electrodes on a flexible and soft polymer substrate, which enables surface-level large-scale monitoring of neural activities. The polymer film is typically a few micrometers thick.	Recording	10, 11
Mesh electronics	Mesh electronics feature a soft, tissue-like design, with probes approximately the size of neuron soma, interconnected by mesh-like structured nanowires. The implantation process involves syringe injection to ensure minimal invasiveness.	Recording and stimulation	12, 13

6.2 Materials and Methods

6.2.1 Electrode Coating and Characterization

Electrochemical experiments introduced in **Section 6.2.1** were carried out with a standard three-electrode setup connected to a μ-AutolabIII potentiostat/galvanostat (Autolab B.V., Utrecht, The Netherlands) controlled by NOVA software.

The aim of electrode characterization in this chapter is to identify a region of potential where no electrochemical reactions occur, ensuring it is suitable for conducting potential-step experiments. Therefore, all observed changes in current can be attributed to ionic movement rather than redox processes.

6.2.1.1 Electropolymerization

The electropolymerization was conducted galvanostatically in a solution of 10 mM EDOT and 0.1 mM NaPSS [0.7% (w/ v)] [26], or 10 mM EDOT and 0.1 M NaCl [27]. A constant current of 20 nA was applied for 13 s to achieve an average charge deposition density of 50 $mCcm^{-2}$ following the protocol presented in **Chapter 5**.

6.2.1.2 Bare Pt Characterization:

To identify a potential range for Pt in 0.01 M PBS in which undesired Faradaic activity was present, a bare Pt microwire was immersed in 0.01 M PBS, and a CV scan was performed. The scan range was from OCP to various potentials (0.2~1.0V vs. SCE) and then to -0.2 V (vs. SCE), returning to OCP at the end with a scan rate of 50 mV/s.

6.2.1.3 Coated Pt Characterization:

For characterization of the coated Pt in 0.01 M PBS and for identifying ranges of potential in which no undesired Faradaic processes took place, a PEDOT:PSS or PEDOT:Cl coated Pt microwire was immersed in 0.01 M PBS. A CV scan was executed from OCP to different upper

limits (0.5/1.0/1.5V vs. SCE) and then to -0.2 V (vs. SCE), and back to OCP at a scan rate of 50 mV/s.

6.2.2 Potential Step Experiments with a Bipotentiostat

Experiments described in **Section 6.2.2** were carried out using an Autolab PGSTAT30 (Autolab B.V., Utrecht, The Netherlands). A four-electrode setup was utilized. Two wires of the tetrode (WE1 and WE2) served as the two working electrodes. An SCE was used as the reference electrode, and a graphite rod functioned as the counter electrode. The experimental procedure is illustrated in **Figure 6.2**.

6.2.2.1 Collection Efficiency Measurements

A bare Pt tetrode was immersed in a 1 mM hexaammineruthenium(III) chloride solution with 0.1 M KCl as a supporting electrolyte. A CV scan on two selected wires was made from 0.2 V (vs. SCE) to -0.5 V (vs. SCE) with a potential reversal back to 0.2 V (vs. SCE) at a scan rate of 25 mVs^{-1} to obtain near steady-state currents for Ru^{2+} oxidation (E1) and Ru^{3+} reduction (E2). The surface of the tetrode was refreshed by cutting before continuing. On WE1, a linear sweep was conducted from E1 to E2 at a scan rate of 5 mVs^{-1}, while WE2 was held at the potential of E1. The following reactions happen at each electrode:

At WE1: $$Ru(NH_3)_6^{3+}(aq) + e^- \rightarrow Ru(NH_3)_6^{2+}\ (aq) \quad (6.1)$$

At WE2: $$Ru(NH_3)_6^{2+}(aq) \rightarrow Ru(NH_3)_6^{3+}\ (aq) + e^- \quad (6.2)$$

The process is illustrated in **Figure 6.2**(a). Current was recorded at both WE1 and WE2 to calculate the collection efficiency (N) using equation (6.3) [28, 29]. The collection efficiency (N) measures the ratio of Faradaic current at a detector electrode (WE2) to that at the generator electrode (WE1) [28, 29]. In this way, the fraction of the Ru^{2+} species generated at WE1 that have been transported to the 'detector' electrode WE2 is quantified:

$$N = \frac{I_{det}}{I_{gen}} = \frac{I_{WE2}}{I_{WE1}} \tag{6.3}$$

6.2.2.2 Potential Step Experiments with a Tetrode

Potential step experiments were conducted using two electrodes within a tetrode. One of these with either a bare Pt (**Figure 6.2**(b)) or a polymer-coated electrode (**Figure 6.2**(c, d)) acting as a detector electrode (WE2), with the other electrode (WE1) used to generate signals to mimic neural action. The bare or partially coated tetrode was immersed in 0.01 M PBS. WE2 was maintained at potentials of 0.15 V, 0.25 V, or 0.35 V (vs. SCE), while a stepped potential was applied to WE1 starting from 0.25 V with a jump to potentials in the range -0.5 V ~ 1.0 V (vs. SCE). Each step typically was 10 s in duration. Some recorded currents, notably those from polymer-modified surfaces, exhibited fluctuations. In these cases, the data were smoothed using MATLAB.

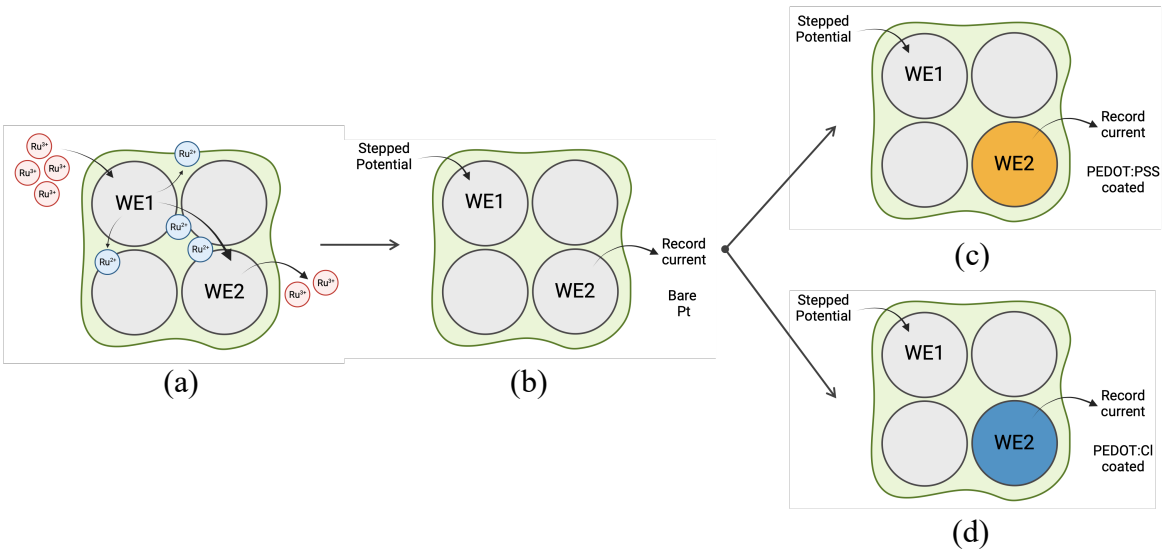

Figure 6.2: Experiment arrangement. **(a)** Setup to measure the collection efficiency**.** Initially, only Ru^{3+} is in the solution, and both electrodes are held at a potential corresponding to the transport limited formation of Ru^{3+} so that no current flows. When the potential at WE1 is swept to the reduction potential, Ru^{2+} is gradually produced, some of which diffuses towards WE2 where Ru^{2+} is oxidized. In this way, WE2 "collects" some of the Ru^{2+} formed at WE1, leading

to the current recorded at WE2. **(b)** Potential step experiment with a bare Pt electrode. A potential step is applied to WE1 and the response is simultaneously recorded at WE2. **(c, d)** The potential step experiment setup with WE2 coated with (c) PEDOT:PSS and (d) PEDOT:Cl.

6.3 Results and Discussion

In this section, two wires of a tetrode are utilized to simulate the signal recording process and to understand the interactions at the interface. These wires are designated as WE1 and WE2, with WE1 functioning as a signal generator and WE2 serving as a signal recorder. Initially, a model system is used to quantify the diffusion of material generated on WE1 via reduction and then collected and oxidized on WE2. The ratio of the currents is known as the collection efficiency, N ($0 < N < 1$). Upon confirming that diffusion to an adjacent electrode is significant ($N > 0$), a series of potential steps is applied to WE1, and the response on WE2 is monitored in 0.01M PBS. This procedure is conducted successively with WE2, using bare Pt, PEDOT:PSS-coated Pt, and PEDOT:Cl-coated Pt, to compare and elucidate the ion movements responsible for the signal generation.

6.3.1 Collection Efficiency Measurements

A bare Pt tetrode was immersed in a solution with 1 mM hexaammineruthenium(III) chloride and 0.1M KCl, and an initial potential scan was performed on two selected wires, starting from 0.2 V and scanning cathodically to -0.5 V before returning to 0.2 V (vs. SCE). The resulting CV scans, as illustrated in **Figure 6.3**(a), show near zero current regions at more positive potentials and transport controlled regions at sufficiently negative potentials; a half wave potential for the Ru^{2+}/ Ru^{3+} redox couple was estimated (ca. -0.15 V vs. SCE) which is in good agreement with literature reports [30].

Subsequently, the tetrode was freshly cut to expose clean Pt to the solution. Both wires were connected to the bipotentiostat, with WE2 held at a potential (E1) of 0.05 V (vs. SCE) throughout the experiment, while WE1 underwent a linear potential scan from E1 to E2 (-0.35 V vs. SCE) corresponding to transport-controlled reduction of Ru^{3+}. The resulting currents on WE1 (red line) and WE2 (blue line) are presented in **Figure 6.3**(b). Initially, the current signals at WE1 and WE2 were near zero because the solution contained only $Ru^{3+,}$ and both electrodes were at the oxidation potential, precluding any reaction. However, as the potential on WE1 was swept towards E2, Ru^{2+} began to form at WE1 (equation (6.1)), as indicated by the increasingly negative current (red line). WE2, in turn, captured the diffused Ru^{2+}, triggering oxidation (equation (6.2)) and leading to an influx of Faradaic current, as evidenced by the rising potential (blue line) towards more positive values.

By comparing the current recorded on WE1 and WE2, the efficiency of the Ru^{2+} collected on WE2 from WE1 can be calculated using equation (6.3), which graphically is the gradient of **Figure 6.3**(c). The ratio of the currents is known as the collection efficiency, N, where $0 < N < 1$ with the fraction 1-N reflecting material generated at WE1, which is lost to the bulk solution. **Figure 6.3**(c) shows that the collection efficiency $N = 0.12 \pm 0.04$ which relates to the specific electrodes studied as the electrode size can vary within the array. To estimate the distance between electrode discs, as depicted in **Figure 6.3**(d), with each wire having a radius (R) of 12.5 μm and an insulation thickness (t) of 5 μm, the adjacent (a) and diagonal (b) distances to neighboring electrodes was calculated as the following:

$$a = (R + t) \times 2 \; = \; 35.0 \; \mu m \tag{6.4}$$

$$b = (R + t) \times 2\sqrt{2} \approx 49.5 \; \mu m \tag{6.5}$$

The findings show that changes on one tetrode disc can affect an adjacent disc, with around 10% of the ions diffusing to neighboring electrodes. Additionally, the distances between discs, whether adjacent or diagonal, are within the range for extracellular recording (< ca. 140 μm [2,

[14]). This encourages the use of potential step experiments using the tetrode to mimic neuronal recording as described in the next section.

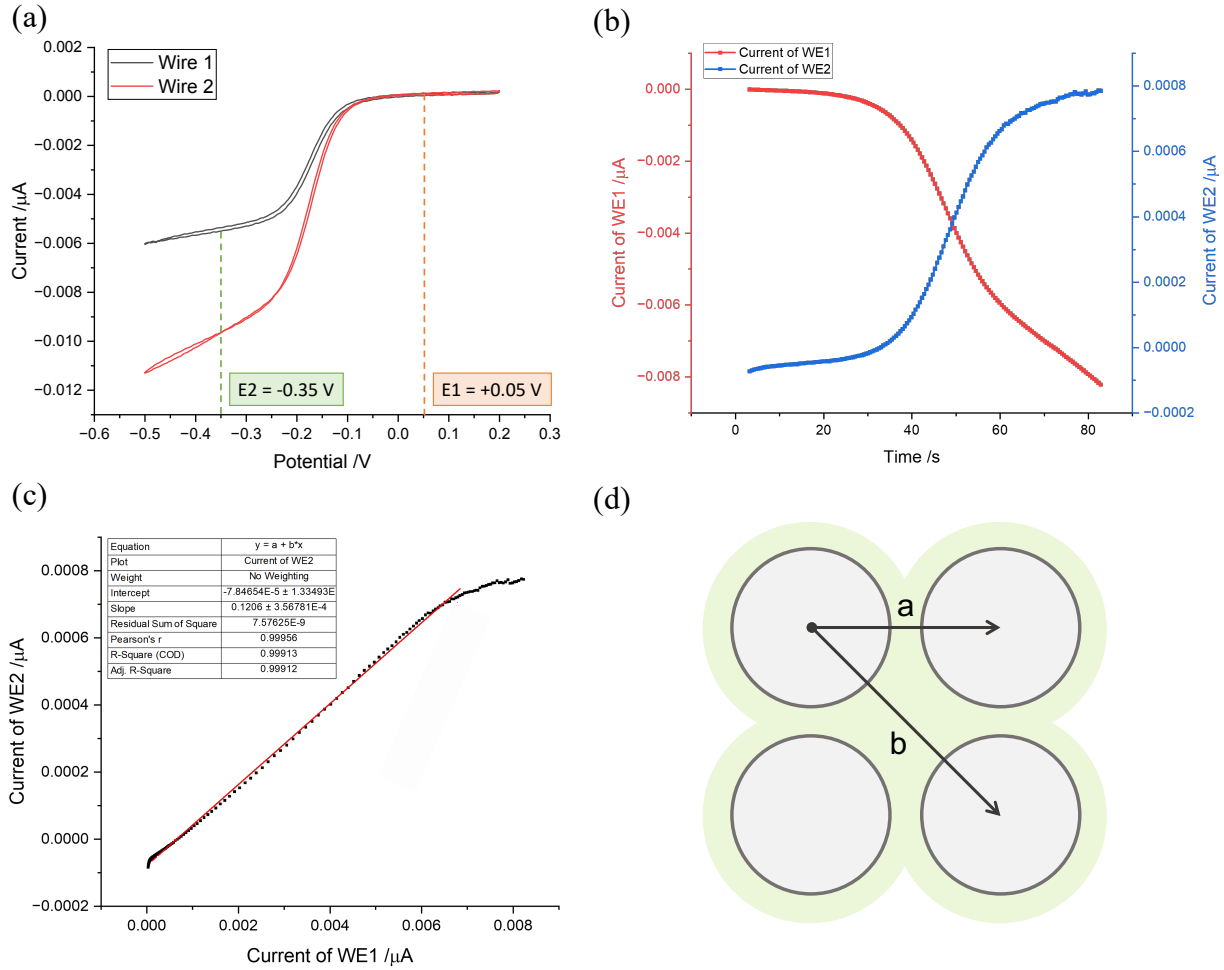

Figure 6.3: (a) CV scan of Pt tetrode wires from 0.2 V →-0.5 V → 0.2 V in 0.1 mM hexaammineruthenium(III) chloride solution with 0.1 M KCl as a supporting electrolyte (scan rate, v = 25 mVs^{-1}). **(b)** The current recorded on WE1 and WE2 when a slow linear sweep (v = 25 mVs^{-1}) of potential on WE1 is made from an oxidation potential (0.5 V) to a reducing potential (-0.35 V) while holding the potential on WE2 constant at an oxidizing potential of 0.5 V. **(c)** The plot of current on WE2 against WE1 is fitted with a linear line (red line), and the gradient is used to obtain the collection efficiency. **(d)** Graphic illustration of the tetrode cross-section. 'a' denotes the length of the adjacent discs, and 'b' denotes the diagonal distance between discs. All potentials are reported relative to the SCE.

6.3.2 Potential Step Experiments on a Bare Tetrode

This section explores how the current detected on a single electrode within a tetrode array responds to a potential step on a nearby electrode, providing a basis for understanding the responses induced by neural potential transients.

Before initiating the potential step experiments, it is necessary to identify a potential range that avoids undesired (electro-)chemical reactions that would generate unwanted Faradaic currents, for example, due to solvent decomposition or surface oxide formation. A CV scan was conducted on a bare Pt microwire immersed in 0.01 M PBS, setting the potential window from a fixed minimum of -0.2 V to a range of maximum potentials between 0.2 V and 1.0 V (vs. SCE) with the aim of locating a region for Pt in PBS in which Faradaic activity is absent and only capacitive charging observed. As indicated by the yellow box in **Figure 6.4**(a), a potential range from 0.1 V to 0.4 V (vs. SCE) was identified in which no current peaks or shoulders were observed, suggesting the absence of electrochemical reactions. Consequently, the initial potential for the stepped potential on WE1 and the holding potential on WE2 were selected within this range. Starting potentials (V_i) of 0.15 V, 0.25 V, and 0.35 V were chosen to be evenly distributed within the unreactive region. The final potential (V_f) was set to span the entire range from 0.1 V to 0.4 V. The experimental procedure is detailed in **Scheme 6.1**. The currents recorded on WE2 are presented in **Figure 6.4**(b~d). Observations from **Figure 6.4**(b~d) reveal a consistent pattern: if the final potential is more positive than the initial potential ($V_f > V_i$, orange arrow), the current on WE2 exhibits a rapid negative pulse before gradually returning to a steady-state current. Conversely, if the final potential is more negative than the initial potential ($V_f < V_i$, green arrow), the current on WE2 shows a rapid positive pulse, also decaying to a steady-state level over time.

To better understand the process, the current responses on electrodes for potential steps from 0.25 V to 0.1 V and 0.4 V were studied in further detail (**Figure 6.5**). **Figure 6.5** (a)

displays the current only on WE2, where distinct positive and negative current pulses are evident for different final potentials. Then, to examine the current response on both electrodes, the currents on WE1 (red line) and WE2 (blue line) are overlaid for each case of the pulse (0.25 V → 0.1 V/0.4 V) in **Figure 6.5**(b, c). Noting the absence of Faradaic activity, the currents must reflect the attraction and/or repulsion of ions at the electrodes, the nature of which can be inferred from the chemical composition of the solution and the direction of current flow. The ionic composition of PBS is detailed in **Table 6.2**, alongside a comparison with extracellular fluid (ECF) and artificial cerebrospinal fluid (ACSF). Schematic illustrations of the inferred ionic movement near the electrode surface are presented in **Figure 6.5**(d~i).

Initially (t < 10s), before the change of potential, both working electrodes attain a near steady-state current close to zero following the formation of the double layer and any other surface processes (**Figure 6.5**(d, g)). When the final potential (V_f) is more positive than the initial (V_i) (**Figure 6.5**(e)), the positive charge near the WE1 surface is repelled once the potential step occurs (**Figure 6.5**(e)), producing a large and sudden positive increase in the current on WE1 (**Figure 6.5**(b), red line). Concurrently, this pulse also disrupts the ion distribution at the adjacent WE2, leading to an influx of positive charges and a decrease in detected current, which corresponds to the outward flow of positive charge from the electrode (**Figure 6.5**(b), blue line; **Figure 6.5**(h)). Eventually, the current reaches a steady value due to the completion of a new ion distribution around the electrode. After sufficient time, a small steady state background current on both electrodes flows, giving the long and flat tail at the end. Conversely, when V_f is more negative than V_i (**Figure 6.5**(c)), a rapid influx of positive charge towards WE1 occurs (**Figure 6.5**(f)), resulting in a negative spike in current (**Figure 6.5**(c), red line). Simultaneously, positive ions near WE2 are drawn towards WE1, increasing the positive charge outflow at WE2, and thus a larger current is observed (**Figure 6.5**(c), blue line; **Figure 6.5**(i)).

It is important to note that the transient spikes are attributable to ion movement within the diffusion layer when there is a sudden change in applied potential, while the flat steady-state current at the extremities is the Faradaic current due to trace amounts of electrolysis at the surface.

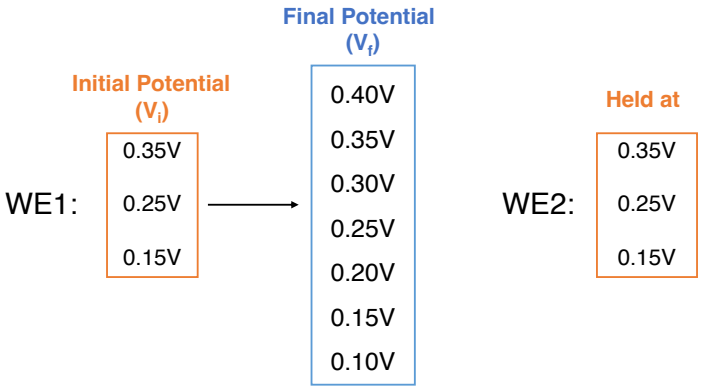

Scheme 6.1: Potential step experiment using bare Pt in 0.01 M PBS. A series of potential steps are applied to the working electrode 1 (WE1) with all potentials within the range of the region without Faradaic activity. The potential of the working electrode 2 (WE2) is fixed at the starting potential of WE1. All potentials are reported relative to the SCE.

Table 6.2: The ionic composition of 0.01 M PBS, extracellular fluid (ECF), and artificial cerebrospinal fluid (ACSF). The ionic compositions of PBS and ACSF (catalog number: 352525ML, Fisher Scientific) are obtained from the product information from their supplier.

Ions	0.01 M PBS / mM	ECF / mM [31]	ACSF / mM
Na^+	138	147	150
Cl^-	140	113	155
K^+	2.70	2.90	3.0
PO_4^{3-}	10.0	0.358	1.0
Ca^{2+}	/	1.14	1.4
Mg^{2+}	/	1.10	0.8
HCO_3^-	/	23.3	26

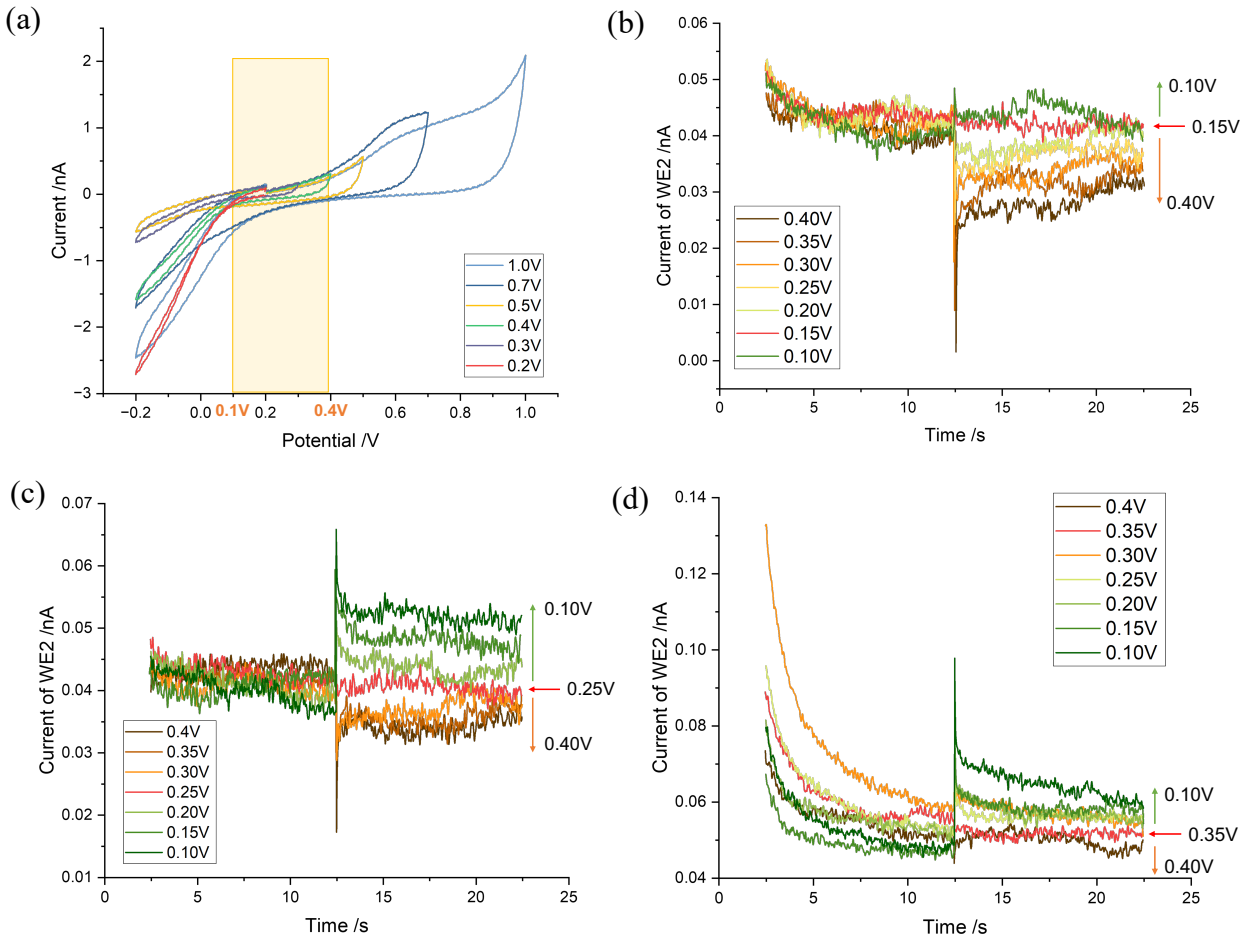

Figure 6.4: (a) CV scan of a bare Pt microwire in 0.01 M PBS from OCP → 0.2 ~ 1.0 V→ -0.2 V→ 0.2V. The region without Faradaic activity is highlighted in yellow (0.1 V ~ 0.4 V) (scan rate, v = 50 mVs^{-1}). **(b, c, d)** Current detected on WE2 when a potential step was applied to WE1 (0.15 V / 0.25 V / 0.35 V → 0.10 ~ 0.40 V), holding WE2 at 0.15 V / 0.25 V / 0.35 V respectively. The red arrow represents the potential at which WE2 was held. The green arrow indicates the direction of the final potential is more negative than the WE2 potential, while the orange arrow indicates the opposite. All potentials are reported relative to the SCE.

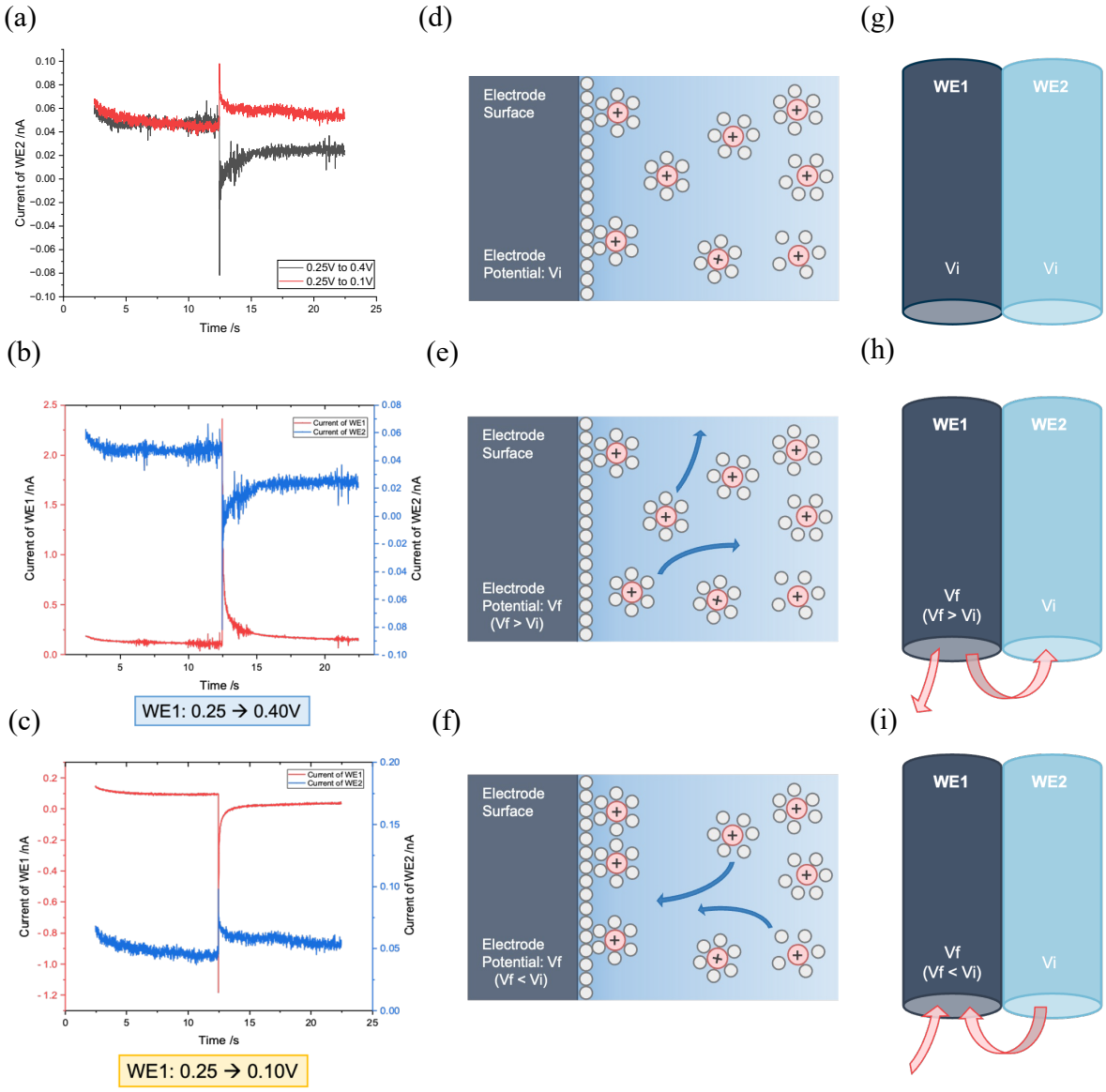

Figure 6.5: Left column: (a) Current transients recorded on WE2 for potential steps on WE1 from 0.25 V → 0.1 V and 0.4 V. **(b, c)** Current transients on WE1 (red line) and WE2 (blue line) for WE1 stepped **(b)** from 0.25 V to 0.4 V, (c) from 0.25 V to 0.1 V. All potentials are reported relative to the SCE. **Middle column:** Schematic showing inferred ion motion on the WE1 surface. **(d)** Initial double layer, **(e, f)** Ion movement when the final potential is more positive or more negative than the initial potential, positive charges are repelled away from or attracted to the surface, creating a positive or negative current pulse on WE1. **Right column:** Coupled response between WE1 and WE2. The pink arrow indicates the direction of cation flow. **(g)** Initially, both electrodes have a double layer reflecting the potential of the electrode. **(h, i)** Early in the transients, the charges near WE1 are repelled/attracted over a short timescale, so that ion movement near WE2 is the inverse to that of WE1, producing an opposite direction of the current pulse. V_f denotes the final stepped potential, V_i represents the initial potential.

6.3.3 Potential Step Experiments on PEDOT-Coated Tetrodes

Potential step experiments were carried out in which WE2 was coated with a PEDOT polymer using different dopants: PSS^- or Cl^-, and the results compared to those of bare Pt.

6.3.3.1 Identifying Faradaically Unreactive Regions

Prior to initiating the stepped potential experiment, so as to identify start and end potentials for the steps, the signal-receiving electrode (WE2) was subjected to a series of CV scans extending from the OCP to various maximum potentials (E_{max}). **Figure 6.6**) shows the CV scans for the PEDOT-coated electrodes, where the non-Faradaic regions are indicated in the yellow boxes (-0.5 V to 1.0 V vs. SCE).

From these experiments, WE1 was set to a fixed initial potential of 0.25 V (vs. SCE), selected as this is the potential in the middle of the unreactive range (as in section 6.3.2) and close to the OCP of Pt in 0.01 M PBS (ca. 0.2 V vs. SCE). A broad range of final potentials, from -0.5 V to 1.0 V (vs. SCE), was investigated. This potential range was chosen based on the unreactive range identified for PEDOT-coated Pt in PBS (**Figure 6.6**). The potential on WE2 was held constant at 0.15 V, 0.25 V, and 0.35 V (vs. SCE), as in section 6.3.2. The experimental procedures are outlined in **Scheme 6.2**.

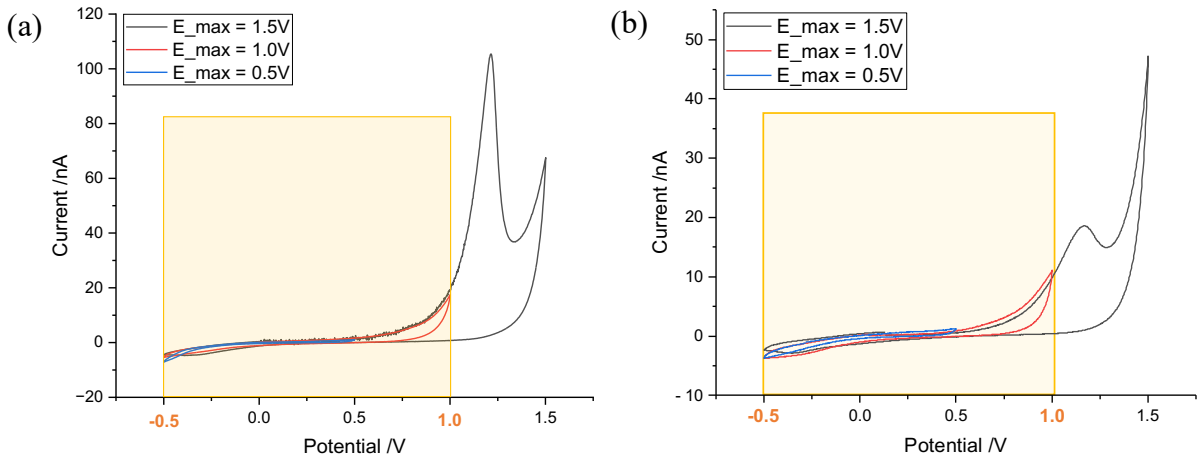

Figure 6.6: CV scan from OCP → E_{max} → -0.5 V was employed using (scan rate v = 50 mVs^{-1}). **(a)** PEDOT:PSS coated, **(b)** PEDOT:Cl coated microwire immersed in 0.01 M PBS. For both polymers, -0.5V to 1.0V is a safe region without triggering any Faradaic current. All potentials are reported relative to the SCE.

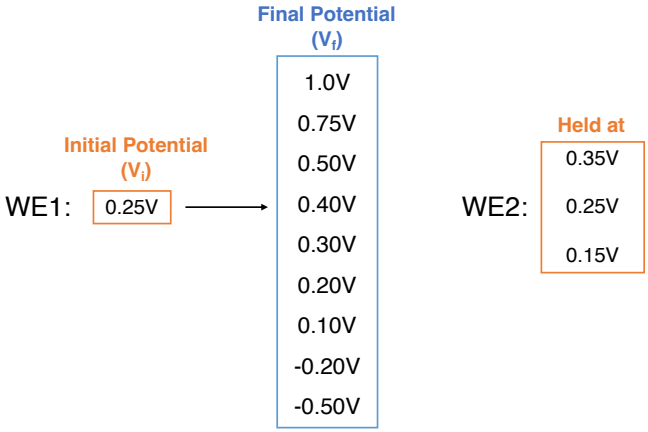

Scheme 6.2: Potential step experiment using a PEDOT-coated Pt in 0.01 M PBS. A potential step was applied to the working electrode 1 (WE1) with a fixed starting point to a range of final potentials. The potential of the working electrode 2 (WE2) was fixed at 0.15 V, 0.25 V, or 0.35 V. All potentials are reported relative to the SCE.

6.3.3.2 Data Smoothing

For electrodes coated with PEDOT, recorded currents demonstrate greater variability than those from bare Pt electrodes. The raw transients have significant noise, making overlaying and comparison challenging. Consequently, data were smoothed using MATLAB. The smoothing parameter (p_s = 0.999991) was tuned to preserve the prominent data features while enhancing presentation clarity. Examples of the smoothed data are depicted in **Figure 6.7**(a~d), using data from a PEDOT:PSS coated electrode. Post-smoothing, the data from the PEDOT:PSS coated WE2 are much clearer, maintaining crucial information preceding and following the application of the potential step (**Figure 6.7**(a, b)), thus simplifying comparison with a bare Pt WE2 (**Figure 6.7**(c, d)). Although PEDOT:Cl shows less variation than PEDOT:PSS, smoothing was also

found to benefit the data analysis (**Figure 6.7**(e, f)). Therefore, all the stepped potential graphs presented in the following sections have been smoothed to allow clearer observation.

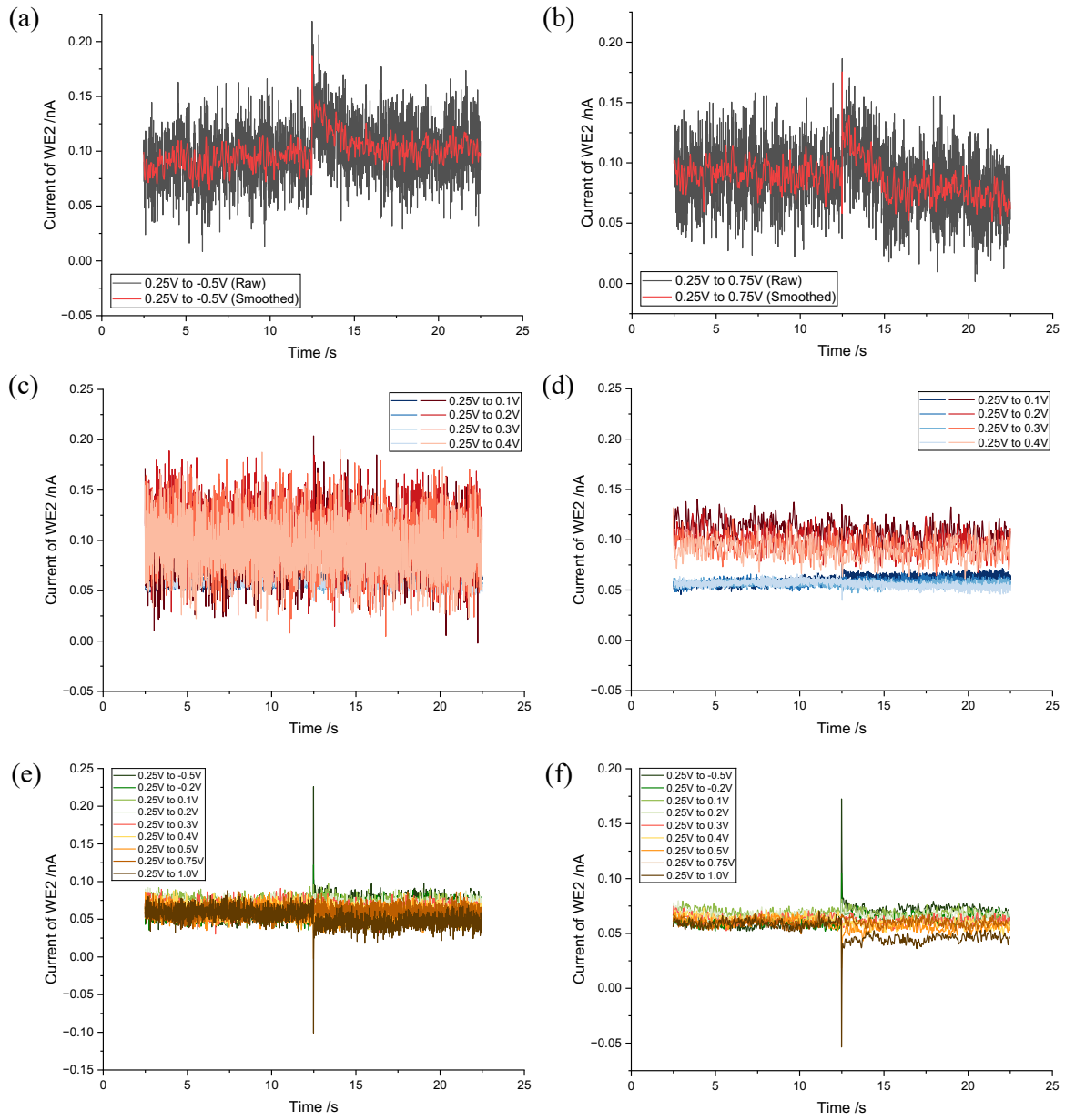

Figure 6.7: (a, b) Comparison of the raw (black line) and smoothed (red line) data of PEDOT:PSS coated WE2 (WE2 held at 0.25 V). **(c, d)** Comparison between the bare (blue lines) and PEDOT:PSS (red lines) coated WE2 recorded data (WE2 held at 0.25 V), where PEDOT:PSS data was unprocessed in (c) and smoothed in (d). **(e, f)** PEDOT:Cl potential step data (WE2 held at 0.25 V), where (e) is the unprocessed raw data and (f) is smoothed. All potentials are reported relative to the SCE.

6.3.3.3 PEDOT:PSS Coated Tetrode

Following the same procedure as the bare Pt, the non-reactive potential range for PEDOT:PSS-coated Pt microwire was determined to be from -0.5 V to 1.0 V (vs. SCE) (**Figure 6.6**(a)). After coating WE2 with PEDOT:PSS, the potential step experiment was carried out, and the procedure was repeated with a bare Pt tetrode for comparison. The recorded current on WE2 after data smoothing is presented in **Figure 6.8**.

In **Figure 6.8**(a, c, e) (left column), the spikes observed in WE2 are relatively minor or barely noticeable when the end potential on WE1 approximates the starting value of 0.25V (e.g. V_f = 0.2 V ~ 0.4 V). In contrast, **Figure 6.8**(b, d, f) (right column) show more pronounced spikes when the potentials on WE1 finished at values significantly different from 0.25 V (e.g. V_f = -0.2 V, -0.5 V, 0.75 V, and 1.0 V). This pattern was consistent across both bare and coated electrodes.

Furthermore, comparing the coated and the bare Pt electrodes, the coated electrodes detected more positive current than the bare ones, in particular when WE2 was held at 0.15 V and 0.35 V. The final steady-state currents showed that the more negative the final potential relative to the initial, the more positive the final steady-state current, and vice versa, which is consistent with the observation with bare Pt (**Figure 6.4**(b~d)). However, the most significant contrast is that the spikes for PEDOT:PSS-coated Pt consistently showed only positive current values, irrespective of the final potential, in contrast to both the positive and negative currents seen with bare Pt.

To discern which component of the polymer contributes to the unidirectional current flow, PEDOT:PSS coated electrodes were examined more closely. Note that the polymer comprises $PEDOT^+$, facilitating hole transport, and PSS^-, with the latter more involved in ion transport [32-34]. With the aim to study the origin of the unidirectional current from either $PEDOT^+$ or PSS^-, the PEDOT:PSS was firstly coated onto WE2, then applied a CV scan ranging from OCP to

(a)

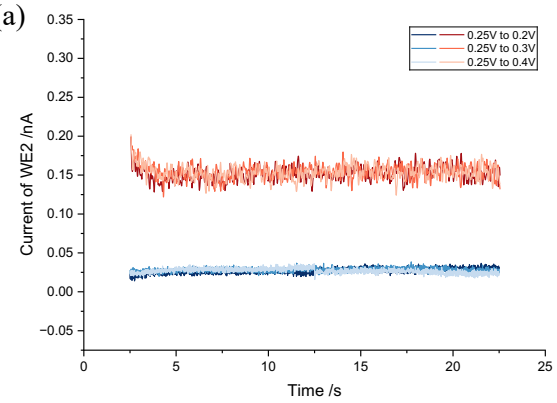

WE1: 0.25 →-0.5~1.0V; **WE2: 0.15V**

(b)

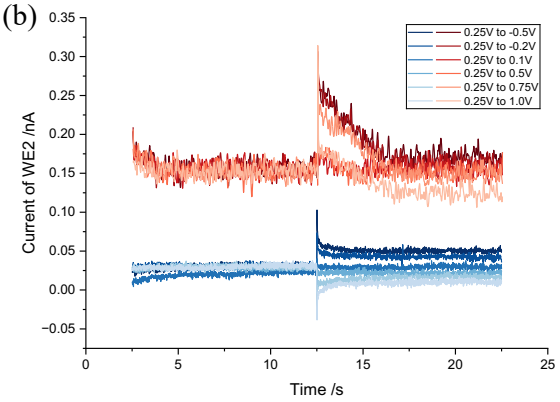

WE1: 0.25 →-0.5~1.0V; **WE2: 0.15V**

(c)

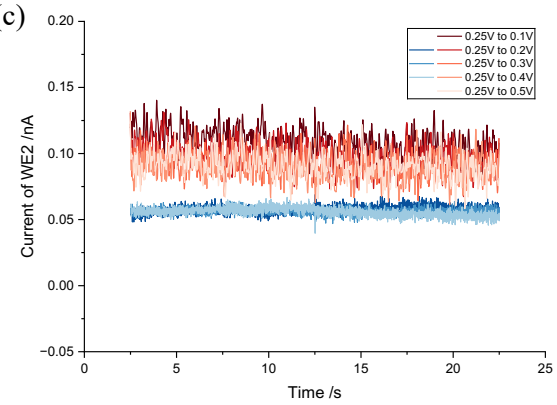

WE1: 0.25 →-0.5~1.0V; **WE2: 0.25V**

(d)

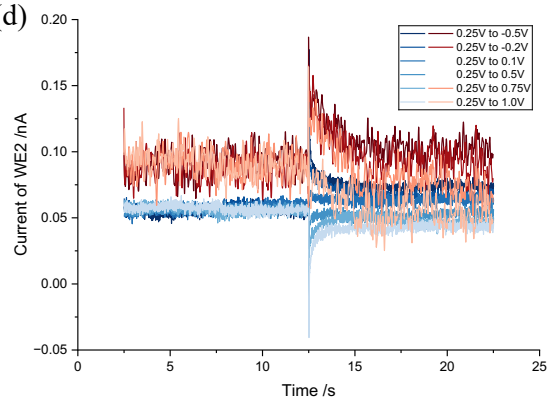

WE1: 0.25 →-0.5~1.0V; **WE2: 0.25V**

(e)

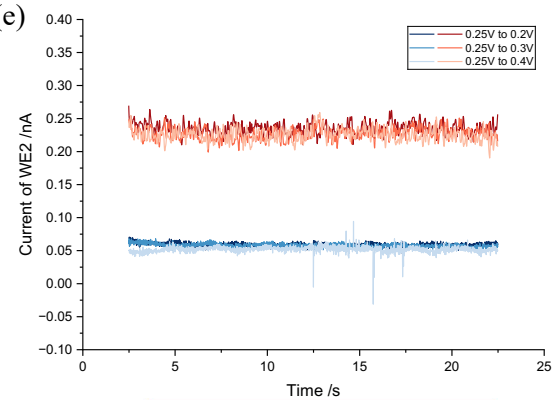

WE1: 0.25 →-0.5~1.0V; **WE2: 0.35V**

(f)

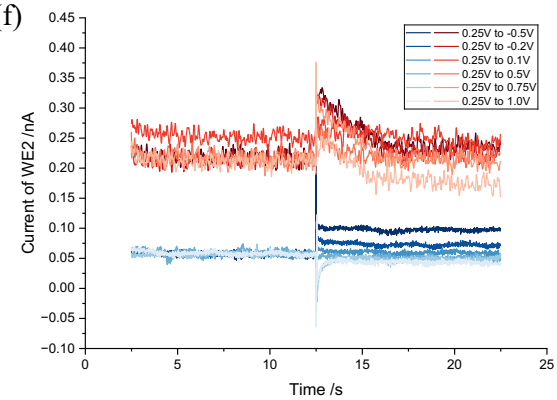

WE1: 0.25 →-0.5~1.0V; **WE2: 0.35V**

(g)

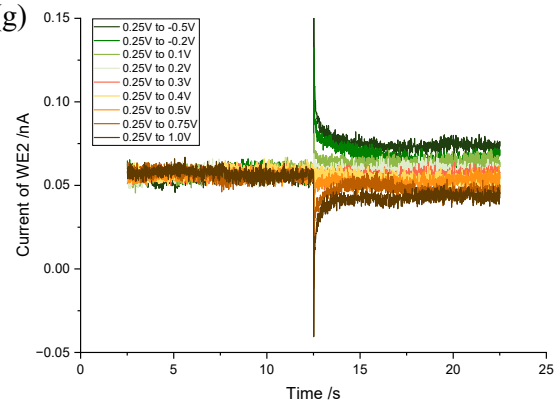

(h)

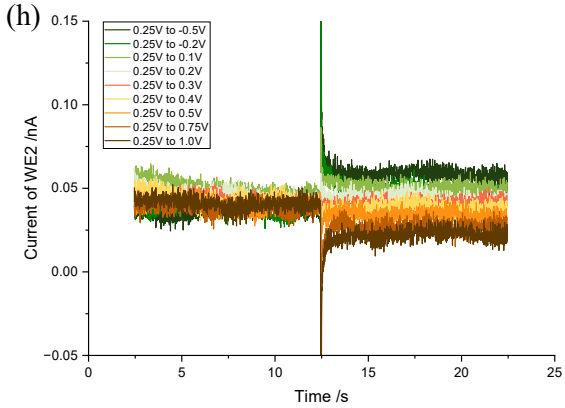

Figure 6.8: (a~f) The current recorded on WE2, where WE2 was held at 0.25 V/0.15 V/0.35 V, respectively, and the potential on WE1 jumped from 0.25 V to a range of final potentials. The left column graphs (a, c, e) illustrate the situations where the potential step on WE1 triggered little response on WE2. The right column graphs (b, d, f) include the potential steps that led to significant responses on WE2. *Blue lines:* Bare Pt. *Red lines:* PEDOT:PSS coated Pt. **(g, h)** Potential step experiment with WE2 held at 0.25 V, and WE1 jumped from 0.25 V to a range of values, using **(g)** a bare tetrode and **(h)** an overoxidized PEDOT coated tetrode. All potentials are reported relative to the SCE.

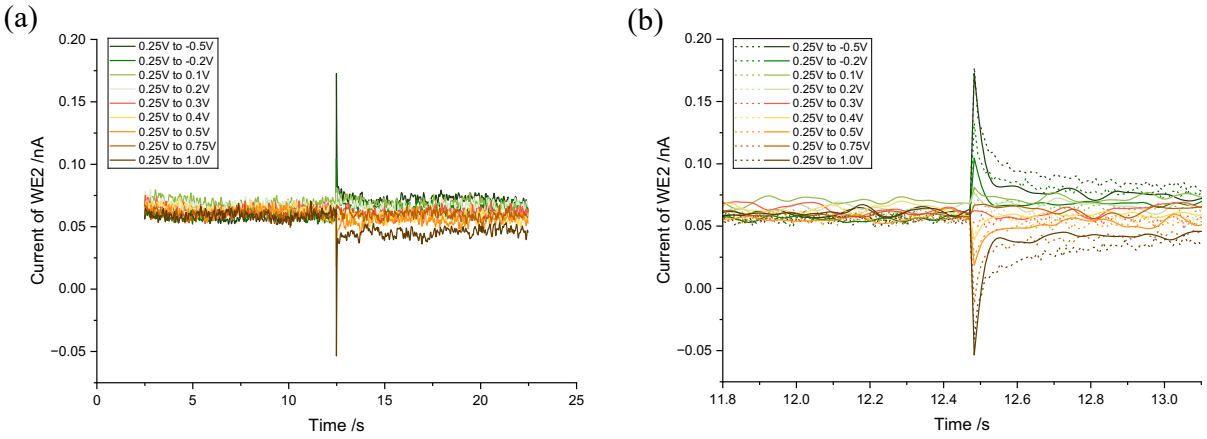

Figure 6.9: The current recorded on WE2, where WE2 was held at 0.25 V, respectively, and the potential on WE1 jumped from 0.25 V to a range of final potentials. **(a)** WE2 was coated with PEDOT:Cl. **(b)** Zoom in and comparison of the current immediately before and after the potential step between the PEDOT:Cl coated and the bare WE2. *Solid line:* PEDOT:Cl coated. *Dashed line*: Bare Pt. All potentials are reported relative to the SCE.

1.5V (vs. SCE) to over-oxidize the $PEDOT^+$. The overoxidation step destroyed the $PEDOT^+$ electrical conductivity, changing the polymer film charge structure, and the process is known to involve counter-ion flux (PSS^-) leaving the film [35]. The potential step experiment was then conducted with WE2 held at 0.25 V, and the current observed on WE2, as shown in **Figure 6.8**(g), exhibited little difference from that of bare Pt (**Figure 6.8**(h)), suggesting that the presence of PSS^- may account for the unidirectional current flow. Therefore, further research

was pursued to evaluate the impact of dopants by doping $PEDOT^+$ with another ion, Cl^-, for comparison.

6.3.3.4 PEDOT:Cl Coated Tetrodes

Similarly, the non-reactive region for PEDOT:Cl coated Pt in 0.01M PBS was determined to be between -0.5 V and 1.0 V (vs. SCE) (**Figure 6.6**(b)). Following the same methodology in **Scheme 6.2**, a potential step experiment was performed.

Similarly to what was observed with PEDOT:PSS, a small potential step (V_f = 0.2 V ~ 0.4 V) produced only a minor current pulse, whereas larger potential changes led to more pronounced current pulses. The results are detailed in the Appendix D, section D.1. After the coating, the final steady-state current values for WE2 at 0.15 V and 0.35 V were more positive than those for a bare Pt electrode, while the current with WE2 held at 0.25 V was generally comparable to that of a bare Pt electrode. Most notably, the current flow in both positive and negative directions was restored (**Figure 6.9**(a)), with the current direction depending on the initial and final potentials, the same pattern as observed with the bare Pt in Section 6.3.2. Additionally, both the pulse and subsequent recovery of the double layer occurred at a noticeably faster rate for the PEDOT:Cl coated electrode compared to the bare Pt. This is evident in **Figure 6.9**(b), where the capacitive decay indicated by solid lines (PEDOT:Cl coated) was quicker than that indicated by dashed lines (bare Pt), and the steady-state current was rapidly restored following the potential step.

On the basis of the above and noting that the bidirectional pulse can be restored either by excluding PSS^- through overoxidation or by employing alternative counterions such as Cl^-, it can be concluded that the unidirectional current flow is associated with the presence of PSS^- in the polymer matrix. The insensitivity of PSS^- to anion movement is likely due to its large chain structure and strong doping with $PEDOT^+$ (as depicted in Chapter 4, Scheme 4.1), which inhibits its mobility in and out of the polymer, thus affecting signal transmission. Conversely,

the smaller Cl^- ions can move more freely into and out of the film, enhancing signal transmission. Additionally, the presence of Cl^- in both the film and the solution could promote signal propagation, potentially leading to a more rapid signal response.

6.3.4 Comparison of Transient Responses at Different Electrodes

To gain further insights and quantify ion movements at the polymer-solution interface, the current recorded at WE2 after the application of the potential step was approximately fitted with an exponential decay curve using the following equation:

$$I = I_0 + A_1 exp\left(-\frac{t}{t_1}\right) \tag{6.6}$$

I_0 represents the steady-state current after the potential step. t_1 is the response time, reflecting how ions around WE2 respond to the sudden potential change at WE1. A_1 indicates the direction and implies the size ($I_0 + A_1$) of the resulting current, where a positive A_1 suggests a positive current, and vice versa. It is important to note that the fitting of equation (6.6) focuses on the transient decay following the initial rapid spike (< 0.02 s). Additionally, to avoid tiny current pulses and so to better fit the exponential curves, large potential steps were chosen to obtain significant responses. Specifically, V_f was chosen to satisfy $|V_f - V_i| > 0.35$ V, with V_i = 0.25 V (**Table 6.3**).

6.3.4.1 Potential Step Data Analysis and Preprocessing

The data fitting was performed using the software Origin 2024.

Noting the noisy nature of the recorded current and the approximation of applying equation (6.6), the R-square value for fitting was generally controlled to be around 0.5. However, for very noisier data, notably WE2 coated with a polymer film, the variance of the raw data is much higher, causing the R-square for fitting the original data to be lower. Hence, in this case, both the raw data and its smoothed data were fitted with equation (6.6), with the latter one to double-check the validity of the fitting.

Figure 6.10 presents a summary of the data preprocessing for the bare Pt WE2 electrode. Given that the current typically returns to a steady state approximately 2 s after a change in potential on WE1, extending the data fitting to the full 10 s is unnecessary and shows minimal difference from a 4 s data fit (**Figure 6.10**(a, b)). The fitting parameters (I_0, t_1 , A_1) for both the 10 s and 4 s datasets closely align, as indicated in the tables below the graphs, with minor variances falling about the error margins of each other.

The low R-Square value originates from the inherent noise in the recorded signals. To improve the quality and check the reliability of the fitting, data were smoothed using MATLAB with a smoothing parameter of p_s = 0.9999 (**Figure 6.10**(c)), followed by fitting with equation (6.6) in Origin. As shown in the table in **Figure 6.10**(d), the R-Square value improved to 0.864, and all fitting parameters remained consistent with those obtained from the raw data fitting (**Figure 6.10**(b)). For example, the response time of the smoothed data ($t_1^{smoothed} \approx 0.22 \pm 0.01\, s$) aligns with the response time derived from raw data ($t_1^{raw} \approx 0.24 \pm 0.04\, s$). Furthermore, some datasets exhibit minimal fluctuations (**Figure 6.10**(e, f)), thus their fitting results do not necessitate additional validation through smoothing.

Similar procedures were repeated for PEDOT:PSS and PEDOT:Cl data. The details of the pre-processing and fitting are included in the Appendix D, Section D.2.

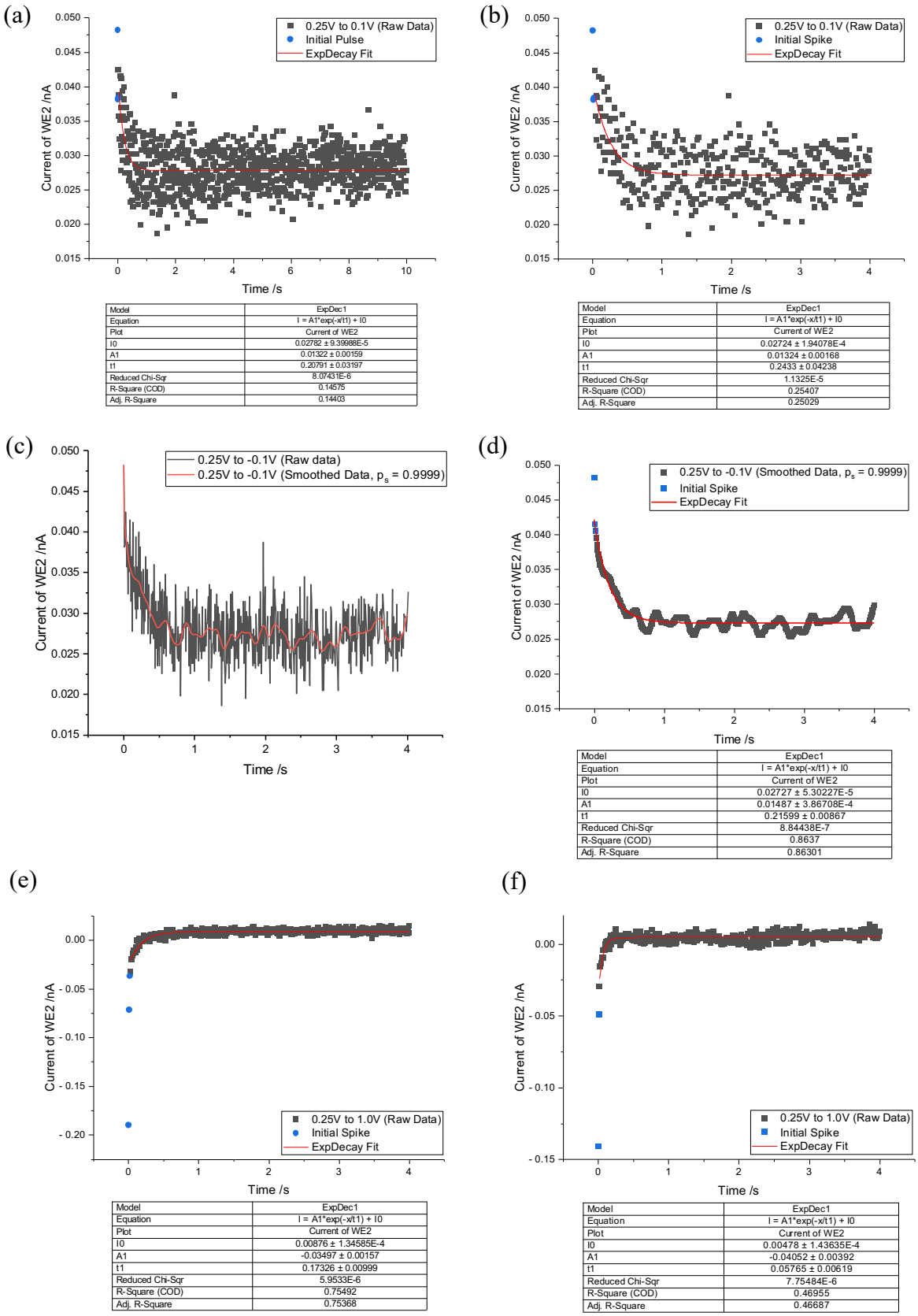

Figure 6.10: (a, b) 10 s and 4 s data for currents recorded at WE2 following a potential step at WE1 from 0.25 V to -0.1 V. WE2 was held at 0.25 V. **(c)** Comparison of the smoothed data

and the raw data. The smoothing parameter p_s = 0.9999. **(d)** Curve fitting of the smoothed data in (c). The fitting parameters (I_0, t_1 and A_1) are all within the error range of that presented in the table in (b). **(e, f)** Less noisy data. WE2 was held at (e) 0.25 V, (f) 0.35 V. All potentials are reported relative to the SCE.

Table 6.3: The potential step experiments for WE1 when WE2 is a PEDOT-coated electrode. All potentials are reported relative to the SCE.

WE1 Initial Potential, V_i / V	WE1 Final Potential, V_f / V	Potential Step Size, $V_f - V_i$ / V
0.25	-0.5	-0.75
	-0.35	-0.6
	-0.25	-0.5
	-0.2	-0.45
	-0.1	-0.35
	0.6	0.35
	0.7	0.45
	0.75	0.5
	0.85	0.6
	1.0	0.75

6.3.4.2 Comparison of the Fitting Results

The results of the parameters A_1, I_0, and t_1 are summarized in **Figure 6.11**.

From **Figure 6.11**(a), it can be seen that PEDOT:PSS coated electrodes consistently produce only positive pulses, and the A_1 values are invariably with a value of 0.022 ± 0.001 s across all transients. In contrast, both PEDOT:Cl-coated and bare Pt electrodes exhibit bidirectional transient decays, their A_1 values hence could be positive or negative depending on the potential step. However, the average magnitude of $|A_1|$ is generally larger for PEDOT:Cl coated Pt than for bare Pt, with differences of approximately 0.012, 0.016, 0.030 nA, increasing

with the WE2 holding potential from 0.15 V to 0.35 V. Observing the steady-state current I_0 post-potential step application in **Figure 6.11**(b), it is evident that for WE2 = 0.15 V and 0.35 V, the values follow the trend PEDOT:PSS > PEDOT:Cl > Bare Pt, reflecting relative amounts of trace Faradaic currents. For WE2 = 0.25V, the steady state current is comparable for PEDOT:PSS and PEDOT:Cl, which could be attributed to varying background effects and/or the different morphology of the polymer materials. Lastly, **Figure 6.11**(c) compares the response times, t_1, for the transient decay of the three different WE2 electrodes. From the graphs, PEDOT:Cl (blue lines) response is the quickest (average 0.04 ± 0.02 s) followed by bare Pt (black lines, average 0.22 ± 0.04 s) and the movement of ions in PEDOT:PSS (red lines) takes the longest time of an average 2.2 ± 0.2 s. Furthermore, the response time was compared with the estimated timescale of pure one-dimensional diffusion between WE1 and WE2:

$$\tau = \frac{\lambda^2}{2D} \tag{6.7}$$

With an approximate value of $D = 10^{-9}$ $m^2 s^{-1}$ which is typical for ions in aqueous solution and $\lambda = 35 \sim 50$ μm (using the length of a and b in **Figure 6.3**(d)), the diffusion response time τ is calculated to be between 1.3 s and 0.6 s from equation (6.7). This diffusion response time is on the same order of magnitude as that of bare Pt. The presence of the polymer with different dopants modifies the response time from free diffusion by either one order of magnitude less or more, and these differences may arise from the mobility of the anions within the polymer matrices (estimated thickness is of ca. 0.3 μm) and their capacity to enter and exit the polymer. Specifically, the presence of Cl^- dopant accelerates the response to approximately within an order of 10^{-1} s, suggesting high ion mobility, while PSS^- extends the response to an order of magnitude of around 10 s, indicative of hindered ionic movement. In this case, it is possible that the response time reflects ion motion within pores or channels within the polymer film so restricting the current flow, whilst in the case of films containing Cl^- the response of WE2 is

controlled by the exchange of Cl^- into and out of the film where they are present at a concentration of ca. 0.1 M in PBS (as shown in **Table 6.2**) and estimated from the charge passed in the film growth to be around 18 M in the doped film.

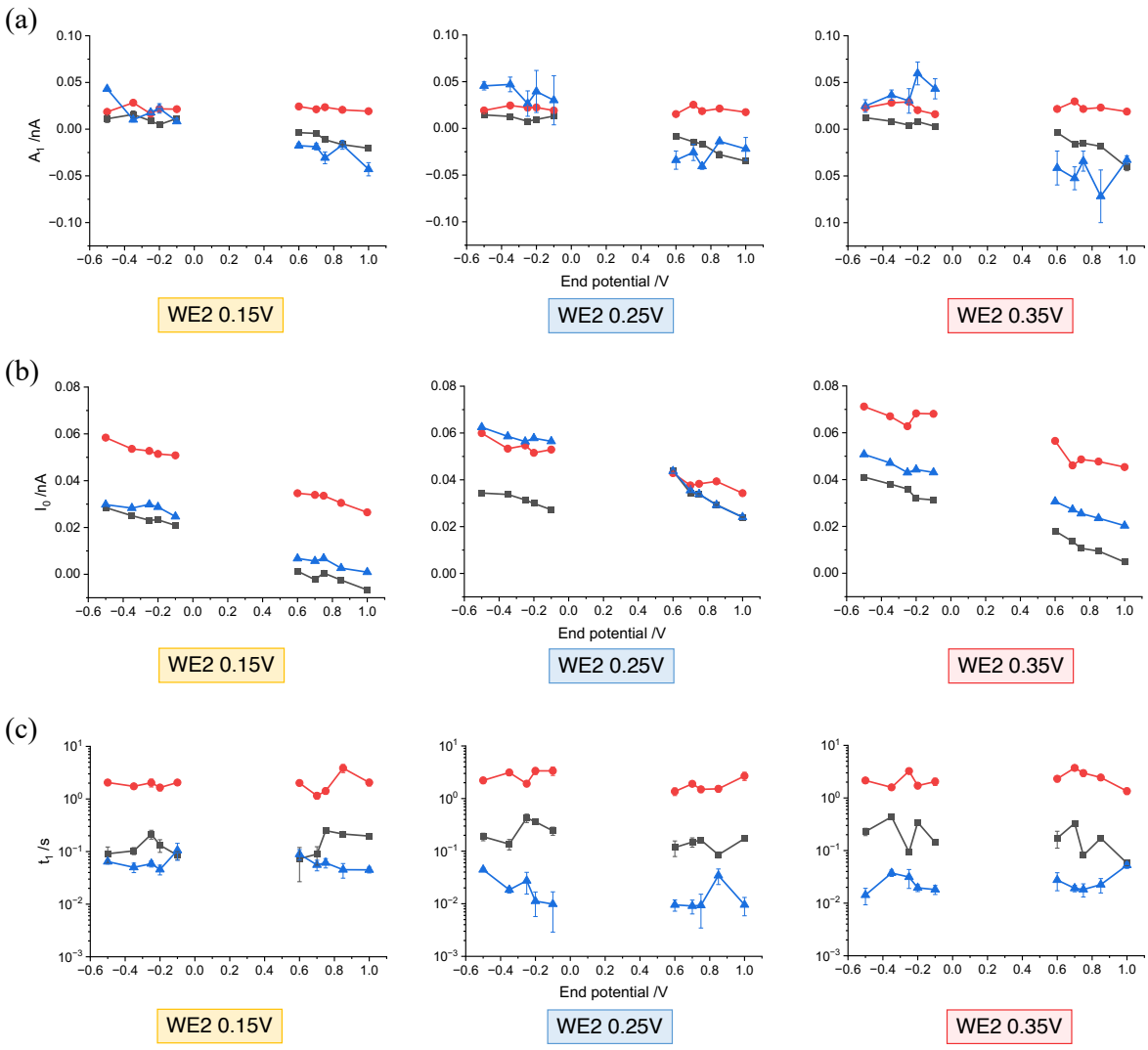

Figure 6.11: The results of the fitting parameter using equation (6.6) on the potential step experiments, where WE2 was held at 0.25 V/0.15 V/0.35 V, respectively, and the potential on WE1 jumped from 0.25 V to a range of end potentials (-0.5 V ~ 0.1 V and 0.6 V~1.0 V). **(a)** Comparison of the fitting parameter A_1. **(b)** Comparison of the steady-state current I_0. **(c)** Comparison of the response time t_1. *Black line:* Bare Pt. *Red line:* PEDOT:PSS coated. *Blue line:* PEDOT:Cl coated. All potentials are reported relative to the SCE.

6.4 Conclusions

In summary, the potential step results revealed that the choice of PEDOT dopant affects the responses to the ions near the electrode-polymer interface. For PEDOT:PSS, the strong interaction between the lengthy $PEDOT^+$ chains and PSS^- restrains the polyanion mobility leading to a slow response time and intrinsic insensitivity to anion flows. Conversely, for PEDOT:Cl, the small Cl^- ions, which are present in both the polymer film and the environment solution, diffuse faster, both in solution and inside the film, thus resulting in a quicker response.

Overall, from Chapters 4 to 6, the polymerization mechanisms, reaction principles, and both electrochemical and morphological properties of PEDOT have been systematically explored and discussed. Each chapter builds on the findings of the previous, establishing a comprehensive foundation for subsequent investigations. The next chapter introduces a pilot in vivo study that applies PEDOT coatings, aiming to evaluate their biocompatibility and applicability in practical settings. Furthermore, the chapter will also explore future directions of this research.

References

(1) Zhang, Y.; Chen, Y.; Contera, S.; Compton, R. G. Double Electrode Experiments Reveal the Processes Occurring at PEDOT-Coated Neural Electrode Arrays. *ACS Appl. Mater. Interfaces* **2024**, *16* (22), 29439-29452.

(2) Hong, G.; Lieber, C. M. Novel electrode technologies for neural recordings. *Nature Reviews Neuroscience* **2019**, *20* (6), 330-345.

(3) Hubel, D. H. Tungsten microelectrode for recording from single units. *Science* **1957**, *125* (3247), 549-550.

(4) Wise, K. D.; Angell, J. B.; Starr, A. An integrated-circuit approach to extracellular microelectrodes. *IEEE transactions on biomedical engineering* **1970**, (3), 238-247.

(5) Kipke, D. R.; Vetter, R. J.; Williams, J. C.; Hetke, J. F. Silicon-substrate intracortical microelectrode arrays for long-term recording of neuronal spike activity in cerebral cortex. *IEEE Trans Neural Syst Rehabil Eng* **2003**, *11* (2), 151-155.

(6) Campbell, P. K.; Jones, K. E.; Huber, R. J.; Horch, K. W.; Normann, R. A. A silicon-based, three-dimensional neural interface: manufacturing processes for an intracortical electrode array. *IEEE Transactions on Biomedical Engineering* **1991**, *38* (8), 758-768.

(7) Campbell, P. K.; Jones, K. E.; Normann, R. A. A 100 electrode intracortical array: structural variability. *Biomed. Sci. Instrum* **1990**, *26*, 161-165.

(8) McNaughton, B. L.; O'Keefe, J.; Barnes, C. A. The stereotrode: A new technique for simultaneous isolation of several single units in the central nervous system from multiple unit records. *Journal of Neuroscience Methods* **1983**, *8* (4), 391-397.

(9) Gray, C. M.; Maldonado, P. E.; Wilson, M.; McNaughton, B. Tetrodes markedly improve the reliability and yield of multiple single-unit isolation from multi-unit recordings in cat striate cortex. *Journal of neuroscience methods* **1995**, *63* (1-2), 43-54.

(10) Khodagholy, D.; Gelinas, J. N.; Thesen, T.; Doyle, W.; Devinsky, O.; Malliaras, G. G.; Buzsáki, G. NeuroGrid: recording action potentials from the surface of the brain. *Nature neuroscience* **2015**, *18* (2), 310-315.

(11) Vetter, R. J.; Williams, J. C.; Hetke, J. F.; Nunamaker, E. A.; Kipke, D. R. Chronic neural recording using silicon-substrate microelectrode arrays implanted in cerebral cortex. *IEEE transactions on biomedical engineering* **2004**, *51* (6), 896-904.

(12) Liu, J.; Fu, T.-M.; Cheng, Z.; Hong, G.; Zhou, T.; Jin, L.; Duvvuri, M.; Jiang, Z.; Kruskal, P.; Xie, C. Syringe-injectable electronics. *Nature nanotechnology* **2015**, *10* (7), 629-636.

(13) Hong, G.; Yang, X.; Zhou, T.; Lieber, C. M. Mesh electronics: a new paradigm for tissue-like brain probes. *Current opinion in neurobiology* **2018**, *50*, 33-41.
(14) Buzsáki, G. Large-scale recording of neuronal ensembles. *Nature neuroscience* **2004**, *7* (5), 446-451.
(15) Rossant, C.; Kadir, S. N.; Goodman, D. F.; Schulman, J.; Hunter, M. L.; Saleem, A. B.; Grosmark, A.; Belluscio, M.; Denfield, G. H.; Ecker, A. S. Spike sorting for large, dense electrode arrays. *Nature neuroscience* **2016**, *19* (4), 634-641.
(16) Ferguson, M.; Sharma, D.; Ross, D.; Zhao, F. A Critical Review of Microelectrode Arrays and Strategies for Improving Neural Interfaces. *Adv Healthc Mater* **2019**, *8* (19), e1900558.
(17) Rios, G.; Lubenov, E. V.; Chi, D.; Roukes, M. L.; Siapas, A. G. Nanofabricated neural probes for dense 3-D recordings of brain activity. *Nano letters* **2016**, *16* (11), 6857-6862.
(18) Thompson, C. H.; Riggins, T. E.; Patel, P. R.; Chestek, C. A.; Li, W.; Purcell, E. Toward guiding principles for the design of biologically-integrated electrodes for the central nervous system. *J Neural Eng* **2020**, *17* (2), 021001.
(19) Polikov, V. S.; Tresco, P. A.; Reichert, W. M. Response of brain tissue to chronically implanted neural electrodes. *Journal of Neuroscience Methods* **2005**, *148* (1), 1-18.
(20) Van de Ven, G. M.; Trouche, S.; McNamara, C. G.; Allen, K.; Dupret, D. Hippocampal offline reactivation consolidates recently formed cell assembly patterns during sharp wave-ripples. *Neuron* **2016**, *92* (5), 968-974.
(21) Battaglia, F. P.; Kalenscher, T.; Cabral, H.; Winkel, J.; Bos, J.; Manuputy, R.; van Lieshout, T.; Pinkse, F.; Beukers, H.; Pennartz, C. The Lantern: An ultra-light micro-drive for multi-tetrode recordings in mice and other small animals. *Journal of Neuroscience Methods* **2009**, *178* (2), 291-300.
(22) Xia, Z.; Arias-Gil, G.; Deckert, M.; Vollmer, M.; Curran, A.; Herrera-Molina, R.; Brosch, M.; Krug, K.; Schmidt, B.; Ohl, F. W. Electrochemical Roughening and Carbon Nanotube Coating of Tetrodes for Chronic Single-Unit Recording. *bioRxiv* **2019**, 738245.
(23) Omer, D. B.; Maimon, S. R.; Las, L.; Ulanovsky, N. Social place-cells in the bat hippocampus. *Science* **2018**, *359* (6372), 218-224.
(24) Voigts, J.; Newman, J. P.; Wilson, M. A.; Harnett, M. T. An easy-to-assemble, robust, and lightweight drive implant for chronic tetrode recordings in freely moving animals. *Journal of neural engineering* **2020**, *17* (2), 026044.
(25) Israel, Z.; Burchiel, K. *Microelectrode recording in movement disorder surgery*; Thieme, 2004.

(26) Zhang, Y.; Chen, Y.; Contera, S.; Compton, R. G. Electrochemical and Nanostructural Characterization of Poly(3,4-ethylenedioxythiophene):poly(styrenesulfonate) Films as Coatings for Neural Electrodes. *ACS Applied Polymer Materials* **2023**, *5* (7), 5555-5566.
(27) Bobacka, J.; Lewenstam, A.; Ivaska, A. Electrochemical impedance spectroscopy of oxidized poly(3,4-ethylenedioxythiophene) film electrodes in aqueous solutions. *Journal of Electroanalytical Chemistry* **2000**, *489* (1-2), 17-27.
(28) Barnes, E. O.; Lewis, G. E. M.; Dale, S. E. C.; Marken, F.; Compton, R. G. Generator-collector double electrode systems: A review. *Analyst* **2012**, *137* (5), 1068-1081, 10.1039/C2AN16174E.
(29) Bard, A. J.; Faulkner, L. R. *Electrochemical Methods: Fundamentals and Applications, 2nd Edition*; John Wiley & Sons, Incorporated, 2000.
(30) Wang, Y.; Limon-Petersen, J. G.; Compton, R. G. Measurement of the diffusion coefficients of [Ru(NH3)6]3+ and [Ru(NH3)6]2+ in aqueous solution using microelectrode double potential step chronoamperometry. *Journal of Electroanalytical Chemistry* **2011**, *652* (1), 13-17.
(31) Boehler, C.; Carli, S.; Fadiga, L.; Stieglitz, T.; Asplund, M. Tutorial: guidelines for standardized performance tests for electrodes intended for neural interfaces and bioelectronics. *Nature Protocols* **2020**, *15* (11), 3557-3578.
(32) Dijk, G.; Ruigrok, H. J.; O'Connor, R. P. Influence of PEDOT:PSS Coating Thickness on the Performance of Stimulation Electrodes. *Adv Mater Interfaces* **2020**, *7* (16), 2000675.
(33) Volkov, A. V.; Wijeratne, K.; Mitraka, E.; Ail, U.; Zhao, D.; Tybrandt, K.; Andreasen, J. W.; Berggren, M.; Crispin, X.; Zozoulenko, I. V. Understanding the Capacitance of PEDOT:PSS. *Adv Funct Mater* **2017**, *27* (28), 1700329.
(34) Rivnay, J.; Leleux, P.; Ferro, M.; Sessolo, M.; Williamson, A.; Koutsouras, D. A.; Khodagholy, D.; Ramuz, M.; Strakosas, X.; Owens, R. M.; et al. High-performance transistors for bioelectronics through tuning of channel thickness. *Sci Adv* **2015**, *1* (4), e1400251.
(35) Kovács, N.; Ujvári, M.; Láng, G. G.; Broekmann, P.; Vesztergom, S. Characterization of the Capacitance of a Rotating Ring–Disk Electrode. *Instrumentation Science & Technology* **2015**, *43* (6), 633-648.

Chapter 7

Pilot In Vivo Experiments

Following the comprehensive material studies in **Chapter 4** to **Chapter 6**, it is important to evaluate how PEDOT polymers perform in authentic application environments, particularly regarding their biocompatibility. **Chapter 7** presents a pilot in vivo study involving the implantation of electrodes in a mouse, with signal recording conducted five weeks post-surgery. A preliminary analysis was performed to assess the recording quality of PEDOT-coated electrodes. However, given the nature of in vivo experiments, the conditions could not be as tightly controlled as in vitro setups. Despite these limitations, the foundational work discussed in this chapter is encouragingly positive and will likely stimulate further research.

The in vivo experiment result of this chapter has been published in *ACS Applied Materials and Interfaces* [1]. The project was conducted under the supervision of Prof. Richard Compton and Prof. Sonia Contera. The surgery and neural signal processing were conducted in collaboration with Prof. David Dupret (Oxford Nuffield Department of Clinical Neurosciences) and members of his group, Dr. Katja Hartwich, Dr. Vitor Lopes dos Santos, and Dr. Tabitha Broadbelt.

7.1 Materials and Methods

7.1.1 Tetrode Drive Fabrication

The assembly of the complete implant device consists of tetrode fabrication, loading of the tetrode into the drive, and tetrode coating. The following sections detail these procedures separately.

7.1.1.1 Tetrode and Drive Fabrication

For the tetrodes loaded into the drive, the lengths were slightly longer than those typically used for electrochemical analysis to ensure they could pass through the guide tube and extend through the top lid (**Figure 7.1**). Therefore, each microwire was cut to a length approximately equal to that of an A4 paper (ca. 297 mm), following the tetrode fabrication methods described in **Chapter 2, Section 2.2.7**. Completion of the fabrication of the tetrode was realized at the same time as the drive fabrication and loading procedure. The latter were carried out by Dr. Katja Harwich from the neuroscience group. A loaded drive is shown in **Figure 7.1**. Subsequent to the loading of all tetrodes, the top lid (**Figure 7.1**(a, c)) was pushed down to close the drive. Any excess lengths of the protruding free ends at the top lids were cut, and tetrode tips at the bottom ends (**Figure 7.1**(b, d)) were trimmed to ensure that the electrodes recorded signals at consistent depths. Tetrodes were prepared and positioned as detailed in **Figure 7.2**. For ease of operation, the uncoated electrodes were placed in the middle of the drive, and the coating process was applied to the outermost tetrodes on the drives (**Figure 7.2**).

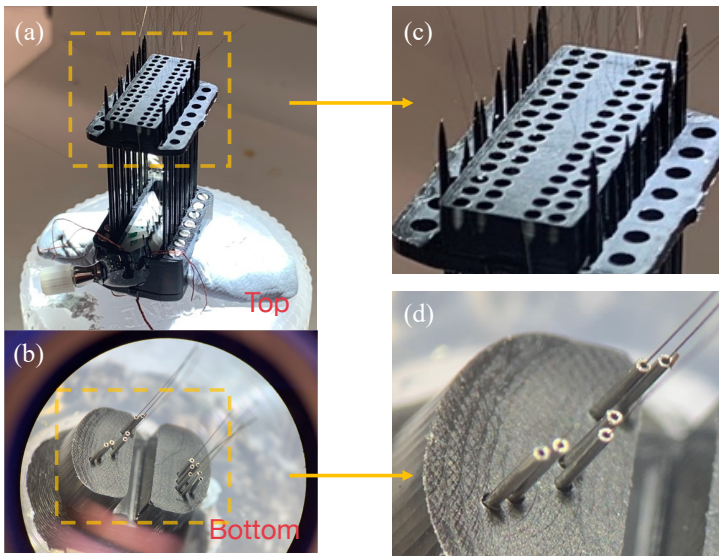

Figure 7.1: The tetrode-loaded drive. **(a)** Top view. The yellow box (zoom in at (c)) indicates the lid that would be pressed down to close and secure the tetrode after loading. **(b)** Bottom

view. The tubes were arranged in a specific configuration for targeting particular brain regions The yellow box (zoom in at (d)) indicates the guiding tubes.

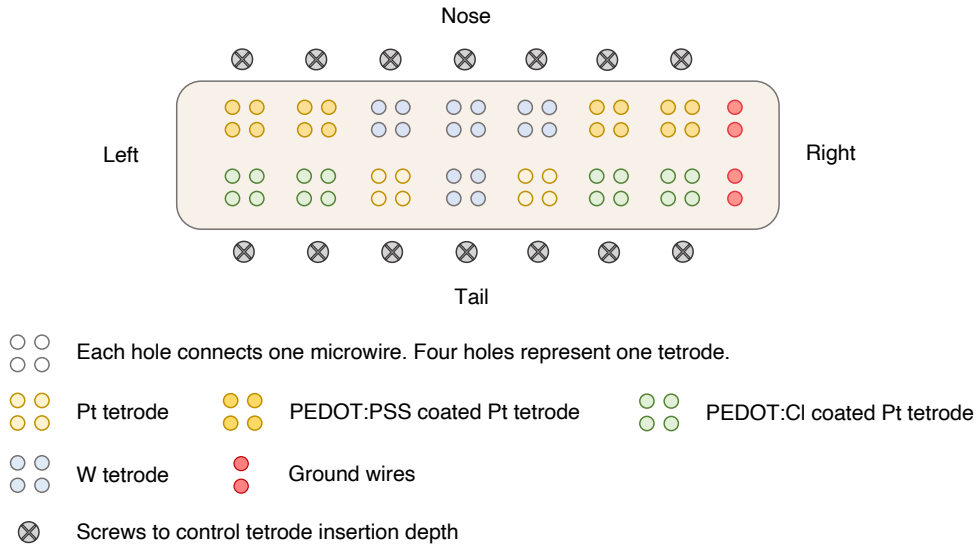

Figure 7.2: Tetrode loading and coating scheme.

7.1.1.2 Tetrode Coating

Connecting the drive to electrochemical devices was achieved using an array of pins (**Figure 7.3**), each of which was inserted into a hole on the drive's top lid (**Figure 7.1**(a, c)). Each pin was connected to one wire of the tetrode, and hence four pins correspond to one tetrode.

Four stainless steel wires were separately soldered onto four pins. It is important to ensure that the soldering does not cause any interconnection between sites (**Figure 7.3**(b)). The connected pins were then inserted into the holes corresponding to the tetrodes designated for coating. The drive was securely held with a clamp. A beaker containing the coating solution was placed on an adjustable stand to control the immersion depth of the tetrode ends in the solution. Extra care was taken to prevent the ends of different tetrodes from sticking together, ensuring that the coating was applied independently.

The coating scheme follows exactly that used for the microwire coating in previous chapters. Electropolymerization was conducted galvanostatically in a solution of 10 mM EDOT and 0.1 mM NaPSS, or 10 mM EDOT and 0.1 M NaCl. A constant current of 20 nA was applied

for 13s to achieve an average charge deposition density of 50 mC cm^{-2}. After coating all the desired tetrodes, they were gently dipped in deionized waters to wash away excess coating solutions.

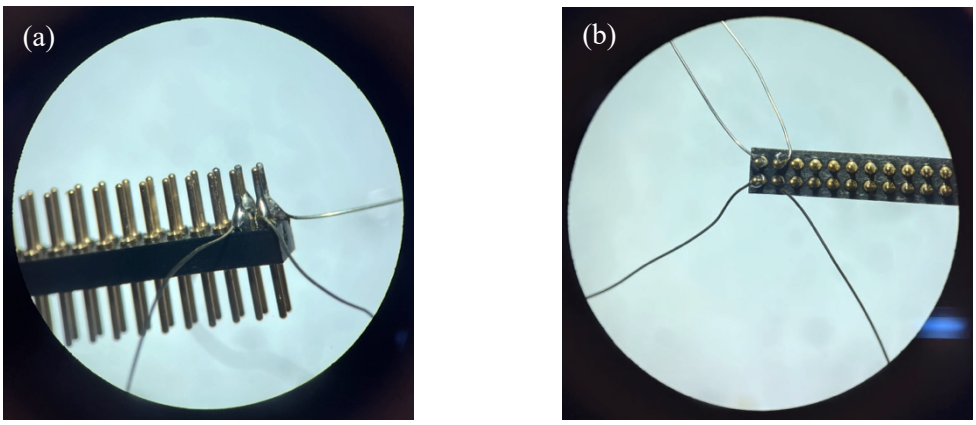

Figure 7.3: Pins soldered with stainless steel wires. **(a)** Side View. **(b)** The top view was taken to check if there was any interconnection between the pins.

7.1.2 In Vivo Experiments

One lab-raised adult mouse was implanted with a single microdrive containing 14 independently movable tetrodes (**Figure 7.2**). To allow recovery from the surgery, the recording started by the end of the fifth week after the implantation. The surgery and recording procedures reflect previous studies [2, 3], and was carried out by Prof. David Dupret's group in strict accordance with the Animals (Scientific Procedures) Act, 1986 (United Kingdom), with a final ethical review by the Animals in Science Regulation Unit of the UK Home Office. The details of the surgery and data processing scheme are included in Appendix E.

7.2 Results and Discussion

A pilot experiment utilizing a coated tetrode was conducted to assess the biocompatibility of PEDOT-coated Pt electrodes and compared to that of bare Pt electrodes. The electrode was implanted in the mouse brain for five weeks prior to initiating recordings at the hippocampal

layers. All polymer-coated electrodes successfully recorded signals, indicating good biocompatibility. Compared to bare Pt in this trial of experiment, the PEDOT-coated electrodes demonstrated enhanced capability to distinguish between neuronal signals. Specifically, the maximum number that the PEDOT:PSS tetrode could distinguish was up to six single-unit recordings, while PEDOT:Cl identified and differentiated seven distinct action potentials from neurons. In contrast, a bare Pt electrode was only able to maximally differentiate spike signals from four neurons.

In addition, to compare the consistency of single-unit recording signals, a comparison factor waveform score (wv_{score}) was introduced [3] :

$$wv_{score} = \sqrt{\sum_{i=1}^{n} \frac{(w_i/\sigma_{wi})^2}{n}} \tag{7.1}$$

where w_i is the value of mean waveform of a sample i, σ_{wi} is the standard deviation across all spike of sample i, and n is the number of waveform samples [3]. **Figure 7.4**(a, b) presents examples of low and high wvscore, respectively. To understand these figures, it can be considered as how the mean waveform (represented by the thick, darker line) compares to the distribution of all waveforms (illustrated by the lighter background band). **Figure 7.4**(b) shows a narrower band, suggesting a smaller deviation, which could indicate less noise and more consistent recordings over time. In contrast, **Figure 7.4**(a) displays a wider background band relative to the mean waveform, suggesting greater variation during recording and reduced consistency.

The average wv_{score} of all recorded units was PEDOT:Cl (1.2 ± 0.2) ~ Pt (1.2 ± 0.1) > PEDOT:PSS (1.1 ± 0.2). Considering PEDOT:Cl and PEDOT:PSS recorded more neuronal signals of different sources, the slightly larger error bar accounts for the variety of signals recorded. The results of wv_{score} for PEDOT:Cl and PEDOT:PSS in comparison with all the wv_{score} are presented in **Figure 7.5**.

Overall, due to the nature of in vivo experiments, as opposed to in vitro, the neuronal signals generated cannot be identical each time. The recorded waveform largely depends on the proximity and the orientation of the neuron relative to the electrode, and the number of signals recorded can also be significantly influenced by the distribution of neurons. Given the complexities of the extracellular environment, a straightforward comparison is challenging, and further studies are required to elucidate the processes occurring in vivo. However, the results from this pilot study have confirmed the biocompatibility of the material and provide confidence and guidance in further investigation and experimental design.

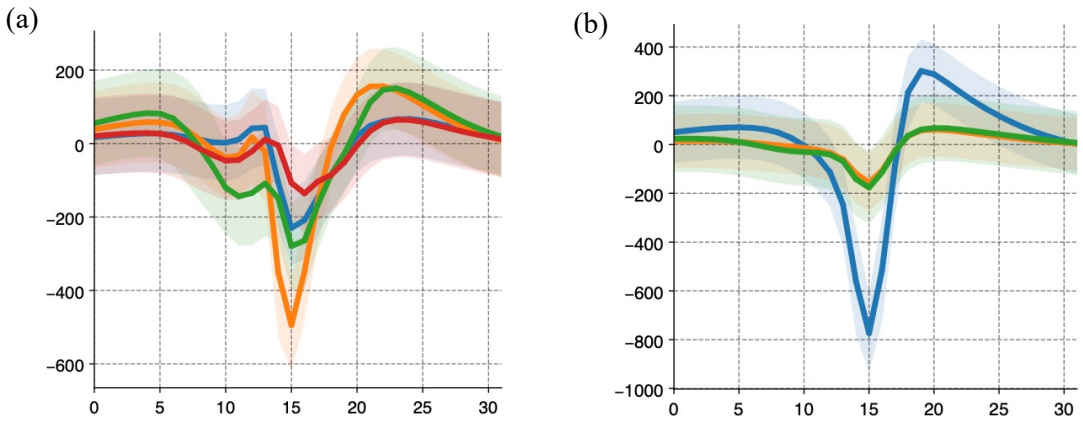

Figure 7.4: Example of **(a)** low wvscore (0.64) and **(b)** high wvscore (1.44).

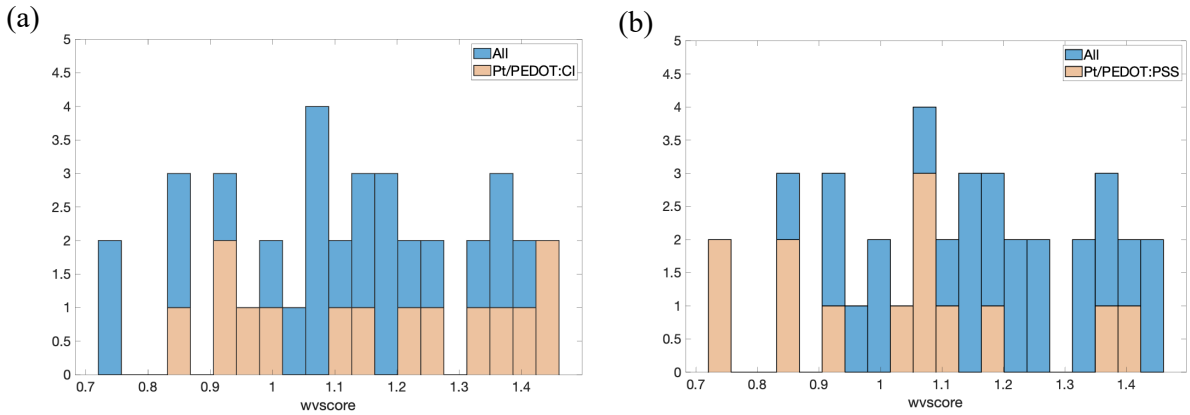

Figure 7.5: Histogram of all the wvscores obtained from single-unit recording. The blue bins represent the wvscore from all the recordings. The pale orange bins represent the wvscore obtained with **(a)** PEDOT:Cl coated tetrode; **(b)** PEDOT:PSS coated tetrode.

7.3 Conclusions

In conclusion, the in vivo experiment further validates the coated tetrode method introduced in previous chapters. The distinct signals on every recording channel indicate no cross-connections occurred. Moreover, this pilot in vivo experiment proves the biocompatibility of both PEDOT:PSS and PEDOT:Cl coatings. Despite the challenges associated with the complex environment during in vivo experiments, this work effectively demonstrates the applicability of these techniques, which could significantly contribute to the development and enhancement of future neural interface devices.

References

(1) Zhang, Y.; Chen, Y.; Contera, S.; Compton, R. G. Double Electrode Experiments Reveal the Processes Occurring at PEDOT-Coated Neural Electrode Arrays. *ACS Appl. Mater. Interfaces* **2024**, *16* (22), 29439-29452.

(2) Van de Ven, G. M.; Trouche, S.; McNamara, C. G.; Allen, K.; Dupret, D. Hippocampal offline reactivation consolidates recently formed cell assembly patterns during sharp wave-ripples. *Neuron* **2016**, *92* (5), 968-974.

(3) Vítor, L.-d.-S.; Demi, B.; David, D. Spatio-temporal organization of network activity patterns in the hippocampus. *bioRxiv* **2023**, 2023.2010.2017.562689.

Chapter 8

Summary and Future Work

Since the initial development of neural electrodes in the last century [1], significant advances have been made in this field. Neural electrodes have evolved from purely metallic materials, such as tungsten, gold, and platinum [1, 2], to silicon-based materials [3-8] and, most recently, biocompatible polymers like PEDOT and PDMS [9-15]. These devices have been utilized not only for a broad range of neuroscience research, such as studies on memory formation and brain activity during sleep and wakefulness [16, 17], but also for medical applications addressing conditions such as Parkinson's and Alzheimer's diseases [18-23]. Although the techniques continue to evolve, knowledge about the fundamental processes underpinning their measurement is limited. The objective of the work reported in this thesis was to understand the processes occurring at the polymer/solution and polymer/electrode interfaces and to develop methods that improve the performance and biocompatibility of neural electrodes (specifically tetrodes). To achieve this goal, electrochemical methods such as cyclic voltammetry (CV) and biopotentiostat techniques were extensively applied to characterize materials and study ionic responses at the interface. Additionally, atomic force microscopy (AFM) was employed to examine the mechanical properties of interfaces and the topography of polymer surfaces at the micro and nanoscales, aligning with the scale at which cellular interactions occur.

The initial consideration in enhancing neural electrodes was the selection of materials. Polydimethylsiloxane (PDMS) and poly(3,4-ethylenedioxythiophene) (PEDOT) were chosen for detailed investigation. Both materials have broad applications. PDMS was selected for its ease of fabrication, compatibility with various materials such as carbon nanotubes (CNT), biocompatibility, and tunable mechanical properties. PEDOT was chosen for its excellent conductivity, biocompatibility, and functional flexibility, and hence, it can be applied to many

surfaces. Both materials have been used extensively in biosensor applications, which made them suitable starting points for this project

After fabrication, both materials were examined using AFM. As PEDOT is porous and can easily stick to the tip (Appendix C, **Figure** C.2(a)), indentation experiments were unsuitable. However, its mechanical properties could be quantitatively inferred from the tapping mode phase image. Conversely, PDMS was thoroughly examined with AFM to study interface interactions and material mechanical properties through indentation and relaxation experiments.

In **Chapter 3**, experiments tracked the evolution of surface Young's modulus and relaxation time over 10 days with PDMS (with 1:10 and 1:20 base to crosslinker ratio, denoted as r10 and r20) stored in either deionized water or air. The results indicated a gradual hardening process at the surface, followed by degradation after the fifth day (**Figure** 3.4, **Figure** 3.7). More importantly, after prolonged storage, two contact points were observed during indentation, especially for r10 samples, suggesting that the AFM tip encountered two distinct material layers. This hypothesis was substantiated by fitting the relaxation curves, where the general Maxwell model with two arms (GMM2) provided the best fit. This suggests the presence of two dominant materials influencing the relaxation processes, giving rise to two relaxation times. The two distinct materials could be attributed to surface layer degradation caused by hydrolysis, resulting in a loosened surface layer of polymer brushes that created a disturbing initial contact. When the tip penetrated this region, it encountered more stable bulk mechanical properties. These findings have minimal impact on macroscopic measurements and appear only after prolonged storage ($\geq$ 2 days). Thus, they have been overlooked by previous studies that focused either on macroscopic properties or freshly produced materials. Future research could use these results as a guideline for PDMS storage and application, particularly when used in microscale environments such as microfluidic channels.

After studying the mechanical properties of PDMS using AFM, it was observed that the mechanical characteristics of polymer interfaces in solution vary over time. Consequently, attention was given to surface changes under different conditions when examining PEDOT in **Chapter 4**.

Due to its conductivity, PEDOT can be synthesized from its monomer via electropolymerization. The material was meticulously characterized using both electrochemical methods and AFM. CV scans performed with a Pt macroelectrode in EDOT and NaPSS solution clarified the reaction mechanism: EDOT oxidizes around 1.0 V to form PEDOT:PSS, and overoxidation occurs at about 1.4 V (vs. SCE). Subsequent AFM examinations showed that similar to PDMS, PEDOT:PSS surfaces underwent changes depending on the storage conditions due to polymer swelling. Being a volumetric conductor, the properties of PEDOT:PSS heavily depend on its structure and morphology. The surface morphology is influenced by the environmental conditions (e.g. in an aqueous environment or in air, does the solution contain ions or is deionized) and thickness. Hence, different thickness polymers were tested with AFM and stored in different conditions (PBS, EDOT/NaPSS, deionized water, air). The AFM results in deionized water revealed a heterogeneous surface characterized by PSS-rich areas intertwined with PEDOT-rich regions. The swelling also affects the polymer stability in terms of its roughness changes. The final optimized coating, assessed via morphological and electrochemical analysis, suggests a charge deposition of about 50 mC cm^{-2}, which showed better film stability across all tested conditions (**Figure** 4.1, **Figure** 4.3, **Figure** 4.6). Following up with a comparison to a bare Pt electrode, a significant enhancement in capacitance (80 times larger than bare) was observed. In addition, measurements using stainless steel as the pseudo-reference electrode, typically used for in vivo experiments, reveal results equivalent to tests using SCE, except for a shift of potential of ca 0.42 V. This indicates that electrochemical data

obtained under in vitro conditions can inform in vivo experiments, confirming PEDOT as a promising material for further study.

As introduced in Chapter 4 (Table 4.1), PEDOT can be doped with different counter ions. Besides PEDOT:PSS, PEDOT:Cl was also selected for comparison to assess the functionality of PEDOT. In **Chapter 5**, similar electrochemical characterization procedures were conducted using Pt macroelectrodes in EDOT and NaCl solutions. CV scans across various potential ranges identified three oxidation processes: EDOT oxidation at ca. 1.0 V, PEDOT overoxidation at ca. 1.2 V, and chloride oxidation on Pt at ca. 1.5 V (vs. SCE). The additional chloride oxidation on Pt is suppressed once the polymer layer forms on the surface, as the film restricts chloride access to the underlying electrode. Since the coating potential is lower than the chloride oxidation potential, the underlying Pt remains unaffected. Following characterizations on Pt macroelectrodes, the next step involved transferring the deposition scheme to microelectrodes. The coating process was initially applied to a single microelectrode to compare the charge density transferred with that of a macroelectrode during overoxidation. Results showing similar levels of oxidation (both ca. 3 mQ cm^{-2}) suggest a successful transfer of coating methods. A major challenge was applying the coating to closely packed electrodes within a tetrode. Therefore, a novel testing method for electrode interconnections was introduced. This method uses the overoxidation properties of PEDOT. Furthermore, this method will likely generally apply to any polymer exhibiting electrochemical property changes beyond a certain potential. For PEDOT, after overoxidation, its electrical activity is destroyed, and further scanning of the coated electrode in a non-monomer-containing solution will not generate additional oxidation peaks. Hence, if a wide-range CV scanning of one electrode does not affect adjacent electrodes, then scanning each of the four electrodes independently should yield distinct four overoxidation peaks, which is an indication of no interconnections (**Figure** 5.8 (d)). In addition to electrochemical testing, further optical, SEM, and EDX analyses

corroborated that the coating scheme can be transferred to a tetrode without causing any interconnections.

Building on the work presented in the previous chapters, **Chapter 6** applied PEDOT:PSS and PEDOT:Cl coating to tetrodes. Furthermore, potential step experiments employing a biopotentiostat were used to evaluate ionic responses at the polymer/electrode interface when there was a potential disturbance at proximity. The responses were compared between coated electrodes and bare electrodes. The potential disturbance was controlled in a range where it would not trigger any chemical reactions on either the bare or coated recording electrodes. Hence, the observed responses were only due to ionic motion, reflecting ion redistribution at the interface to form the double layer. The results demonstrated that the response of ion movement on a bare electrode (0.22 ± 0.04 s) has little difference as compared to free diffusion, whereas the response is slower in PEDOT:PSS (2.22 ± 0.19 s) and much faster in PEDOT:Cl (0.04 ± 0.02 s). These differences were attributed to the polymer and are particularly influenced by the dopants used. As discussed in Chapter 4 (Scheme 1 and **Figure** 4.5), PEDOT:PSS consists of entangled long polymeric networks of $PEDOT^+$ and PSS^-, which restrict the mobility of the polyanion, leading to a slow response time. In comparison, for PEDOT:Cl, the small Cl^- ions, present in both the polymer film and the surrounding solution (PBS), can diffuse more rapidly and freely, both in solution and within the film, resulting in a quicker response.

Although rigorously controlled experiments were conducted in various in vitro setups throughout the previous chapters, in vivo experiments were essential, particularly for testing the biocompatibility of the polymers. **Chapter 7**, therefore, describes a pilot in vivo experiment in which coated tetrodes were implanted into a mouse brain, with signal recordings taken in the fifth week post-surgery. During this period, no acute symptoms were observed, and signals were successfully collected from both coated and bare Pt electrodes. A preliminary analysis was conducted using the wvscore (equation 7.1), and the results showed that PEDOT:Cl ($1.2 \pm$

0.2) ~ Pt (1.2 ± 0.1) > PEDOT:PSS (1.1 ± 0.2). However, due to the complexities involved in the in vivo experiments, a more definitive conclusion regarding the effects of coated vs. uncoated electrodes on signal quality requires more sophisticated electrode configurations and additional experimental trials. Nevertheless, biocompatibility has been examined and proven, laying the fundamental works for additional research involving coated electrodes.

In conclusion, this thesis began with characterization of material properties and then progressed to investigations of interface processes. Both surface mechanical evolution and ionic responses in widely used polymers (PDMS, PEDOT) have been thoroughly examined. From a mechanical perspective, this work has, for the first time, revealed how interface mechanical properties evolve at the microscale and nanoscale, highlighting the formation of distinct surface layers in contact with air or water. The novel approach of coating tetrodes with PEDOT:PSS and PEDOT:Cl, as detailed in this thesis, has not been previously reported. Most importantly, the introduction of a method to prevent interconnections addresses significant concerns associated with coating densely packed microelectrode arrays with polymers. Additionally, the use of a bipotentiostat has provided, for the first time, direct evidence of how polymers influence ion movement at the polymer/electrode interface, which could potentially be used to improve neural recording using these materials and is worth further investigation. With this foundational knowledge, the work can be extended to many future studies, which will be discussed in subsequent sections.

8.1 Future Works

8.1.1 PDMS and PEDOT to Improve Tetrode Biocompatibility

Biocompatibility of the tetrode tip section has been enhanced through PEDOT coating, while the tetrode body's compatibility can be improved by coating with soft PDMS to better match the mechanical properties of brain tissue. Additionally, PDMS serves as an effective

barrier against bacterial infections, making it suitable for surgical usage. The coating process involves dipping the tetrode into PDMS gel, followed by curing in an oven to solidify the gel. The end of the coated tetrode is then cut to expose the metallic tip for subsequent PEDOT coating.

However, two challenges can arise during this process: 1. Potential Sticking Between Tetrode Rods; 2. Control of PDMS Coating Thickness and Uniformity

For the first problem, as tetrodes are closely positioned on the drive, they may stick together during the dip-coating process, particularly when removed from the gel. Surface tension can also cause PDMS to drip at the tip, increasing the likelihood of adherence to adjacent tetrodes. This issue can be mitigated by using drives that are less densely loaded with tetrodes, although this may reduce the number of recording sites per experiment and necessitate a trade-off between biocompatibility and data quantity. For the second issue, challenges in controlling the thickness and uniformity of the coating can be addressed by using an electronically controlled stage to precisely manage the dipping and withdrawal speeds. With sufficient experimentation and calibration, the coating thickness could be controlled.

8.1.2 Potential Step Experiment for Stimulation

From Chapter 6, the potential step experiment was utilized to evaluate the influence of polymers on recording sites. Pt electrodes have been used not only as recording materials but also frequently as stimulating electrodes. Furthermore, PEDOT is a commonly used material for stimulating electrodes to enhance capacitance and charge injection capabilities [24, 25]. However, the impact of the polymer on stimulation signals has not been directly tested.

The potential step experiment could be extended to assess polymer performance during stimulation (**Figure 8.1**). In this setup, WE1 would be coated with PEDOT polymers and subjected to a stimulation pulse, while WE2 would function as the recording site to capture the resultant signal, as it would be received in vivo by a neuron. Comparisons could also be made

with bare Pt and Pt with different doped PEDOT. It has been reported that PEDOT:PSS films often crack after repeated stimulation pulses, where the stimulation potential is often larger than the overoxidation potential (> 1.4 V vs. SCE) [25]. Previous literature attributes this to mechanical instability caused by thick films and also the irreversibility of electrochemical change in PEDOT:PSS due to overoxidation [24, 25]. However, there is a possibility that the cracking could be due to the repetitive expulsion of PSS^- from the film under applied potential, potentially stretching and deforming the film. No studies have yet explored the use of PEDOT with smaller dopants in stimulating electrodes (e.g. PEDOT:Cl). The mobility of Cl^- in PEDOT:Cl, as discussed in Chapter 6, may lead to different outcomes, which is worth further studying.

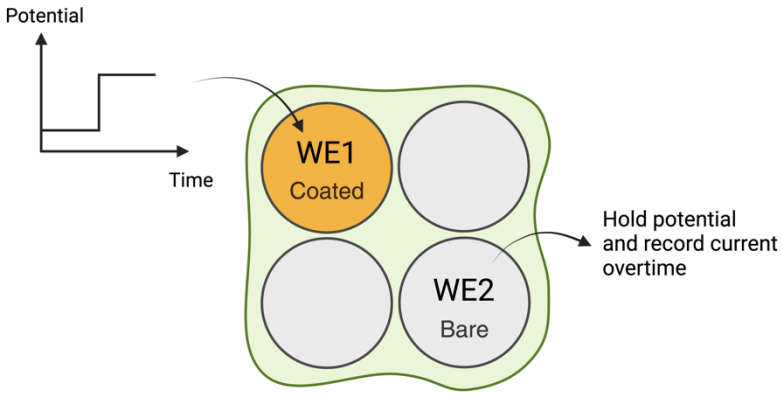

Figure 8.1: Potential step experiment with the biopotentiostat step up to test polymer coating on stimulating effects.

8.1.3 Further In Vivo Experiments

During in vivo recording, even within the same tetrode, different channels capture signals with distinct shapes. Slight alterations in the orientation and distance of an electrode relative to the neuron can impact the signal shape. Furthermore, the recorded signal is measured in terms of voltage, which indirectly reflects ionic movement, unlike the direct current response observed in in vitro tests. Nevertheless, in vivo experiments are essential for advancing the understanding of interface processes.

The challenges involved in the in vivo experiments come from two factors: 1. Difficulty in fair comparison; 2. Complex in vivo environment; 3. Signal filtering.

To address the first issue, fair comparisons can be improved by positioning implants with symmetrical electrode configurations on both hemispheres of the mouse's brain. Recording from symmetric channels enables a comparative analysis. However, achieving precise symmetry in implant placement is challenging due to surgical complexities and potential displacement by brain tissue. Nevertheless, statistically significant conclusions can be drawn if a sufficient number of trials are conducted.

The second issue relates to the complex in vivo environment, where other species (e.g. collagen, polyanions, fibers, etc. [26]) and mechanical squeezing with brain tissue may disrupt recording processes. An improved in vitro simulation to simply in vivo cases might involve recording in extracellular fluid (ECF) or artificial cerebrospinal fluid (ACSF) with neurons cultured on a Petri dish. However, recording lab-cultured neurons links to the third challenge, signal filtering.

Standard hippocampal recording filters might exclude signals of differing shapes that could originate from neurons in other layers, potentially disrupting focused analyses [27]. However, this would lead to a loss of information. In an in vitro setting, the filtering scheme needs to be revised and refined. When neurons are cultured on a Petri dish, their orientation and distribution are more random and non-uniform, as shown in some lab-grown neuron samples (**Figure 8.2**). A step-by-step filtering approach can be employed, starting with a single isolated neuron and progressing to low-density and then high-density neuron populations. This process could be enhanced by machine learning to optimize signal analysis. However, this method requires extensive training datasets to develop effective filtering principles without overlooking critical features.

Overall, conducting further in vivo experiments involves methodical setups for symmetric implantation, controlled in vitro testing, and step-by-step filtering processes that may integrate machine learning to improve signal analysis. By implementing these strategies, better in vivo interface studies can be achieved.

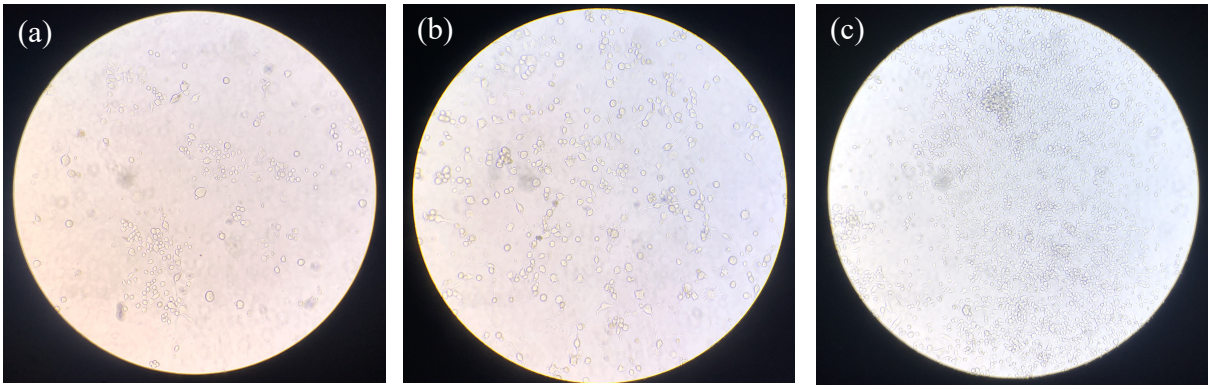

Figure 8.2: Lab cultured neurons with **(a)** low density; **(b)** medium density; **(c)** high density. Cells differentiated from F11, which is a somatic cell hybrid of a rat embryonic dorsal root ganglion and mouse neuroblastoma cell [28].

References:

(1) Hubel, D. H. Tungsten microelectrode for recording from single units. *Science* **1957**, *125* (3247), 549-550.

(2) Geddes, L. A.; Roeder, R. Criteria for the selection of materials for implanted electrodes. *Ann Biomed Eng* **2003**, *31* (7), 879-890.

(3) Hong, G.; Lieber, C. M. Novel electrode technologies for neural recordings. *Nature Reviews Neuroscience* **2019**, *20* (6), 330-345.

(4) Feiner, R.; Dvir, T. Tissue–electronics interfaces: from implantable devices to engineered tissues. *Nature Reviews Materials* **2017**, *3* (1), 17076.

(5) Campbell, P. K.; Jones, K. E.; Huber, R. J.; Horch, K. W.; Normann, R. A. A silicon-based, three-dimensional neural interface: manufacturing processes for an intracortical electrode array. *IEEE Transactions on Biomedical Engineering* **1991**, *38* (8), 758-768.

(6) Campbell, P. K.; Jones, K. E.; Normann, R. A. A 100 electrode intracortical array: structural variability. *Biomed. Sci. Instrum* **1990**, *26*, 161-165.

(7) Wise, K. D.; Angell, J. B.; Starr, A. An integrated-circuit approach to extracellular microelectrodes. *IEEE transactions on biomedical engineering* **1970**, (3), 238-247.

(8) Kipke, D. R.; Vetter, R. J.; Williams, J. C.; Hetke, J. F. Silicon-substrate intracortical microelectrode arrays for long-term recording of neuronal spike activity in cerebral cortex. *IEEE Trans Neural Syst Rehabil Eng* **2003**, *11* (2), 151-155.

(9) Peng, C.; Jin, J.; Chen, G. Z. A comparative study on electrochemical co-deposition and capacitance of composite films of conducting polymers and carbon nanotubes. *Electrochimica Acta* **2007**, *53* (2), 525-537.

(10) Cui, X. T.; Zhou, D. D. Poly (3,4-ethylenedioxythiophene) for chronic neural stimulation. *IEEE Trans Neural Syst Rehabil Eng* **2007**, *15* (4), 502-508.

(11) Luo, X.; Weaver, C. L.; Zhou, D. D.; Greenberg, R.; Cui, X. T. Highly stable carbon nanotube doped poly(3,4-ethylenedioxythiophene) for chronic neural stimulation. *Biomaterials* **2011**, *32* (24), 5551-5557.

(12) Baek, S.; Green, R. A.; Poole-Warren, L. A. The biological and electrical trade-offs related to the thickness of conducting polymers for neural applications. *Acta Biomater* **2014**, *10* (7), 3048-3058.

(13) Baek, S.; Green, R. A.; Poole-Warren, L. A. Effects of dopants on the biomechanical properties of conducting polymer films on platinum electrodes. *J Biomed Mater Res A* **2014**, *102* (8), 2743-2754.

(14) Barshutina, M. N.; Kirichenko, S. O.; Wodolajsky, V. A.; Lopachev, A. V.; Barshutin, S. N.; Gorsky, O. V.; Deriabin, K. V.; Sufianov, A. A.; Bulgin, D. V.; Islamova, R. M.; et al. PDMS-CNT composite for soft bioelectronic neuronal implants. *Composites Part B: Engineering* **2022**, *247*, 110286.
(15) Guo, L.; Guvanasen, G. S.; Liu, X.; Tuthill, C.; Nichols, T. R.; DeWeerth, S. P. A PDMS-Based Integrated Stretchable Microelectrode Array (isMEA) for Neural and Muscular Surface Interfacing. *IEEE Transactions on Biomedical Circuits and Systems* **2013**, *7* (1), 1-10.
(16) Viventi, J.; Kim, D.-H.; Vigeland, L.; Frechette, E. S.; Blanco, J. A.; Kim, Y.-S.; Avrin, A. E.; Tiruvadi, V. R.; Hwang, S.-W.; Vanleer, A. C.; et al. Flexible, foldable, actively multiplexed, high-density electrode array for mapping brain activity in vivo. *Nature Neuroscience* **2011**, *14* (12), 1599-1605.
(17) El-Gaby, M.; Reeve, H. M.; Lopes-dos-Santos, V.; Campo-Urriza, N.; Perestenko, P. V.; Morley, A.; Strickland, L. A. M.; Lukács, I. P.; Paulsen, O.; Dupret, D. An emergent neural coactivity code for dynamic memory. *Nature Neuroscience* **2021**, *24* (5), 694-704.
(18) McIntyre, C. C.; Thakor, N. V. Uncovering the Mechanisms of Deep Brain Stimulation for Parkinson's Disease through Functional Imaging, Neural Recording, and Neural Modeling. **2002**, *30* (4-6), 249-281.
(19) Velisar, A.; Syrkin-Nikolau, J.; Blumenfeld, Z.; Trager, M. H.; Afzal, M. F.; Prabhakar, V.; Bronte-Stewart, H. Dual threshold neural closed loop deep brain stimulation in Parkinson disease patients. *Brain Stimulation* **2019**, *12* (4), 868-876.
(20) Swann, N. C.; De Hemptinne, C.; Miocinovic, S.; Qasim, S.; Ostrem, J. L.; Galifianakis, N. B.; San Luciano, M.; Wang, S. S.; Ziman, N.; Taylor, R. Chronic multisite brain recordings from a totally implantable bidirectional neural interface: experience in 5 patients with Parkinson's disease. *Journal of neurosurgery* **2017**, *128* (2), 605-616.
(21) Ning, S.; Jorfi, M.; Patel, S. R.; Kim, D. Y.; Tanzi, R. E. Neurotechnological Approaches to the Diagnosis and Treatment of Alzheimer's Disease. *Front Neurosci* **2022**, *16*, 854992.
(22) Chang, C. H.; Lane, H. Y.; Lin, C. H. Brain Stimulation in Alzheimer's Disease. *Front Psychiatry* **2018**, *9*, 201.
(23) Wellman, S. M.; Coyne, O. A.; Douglas, M. M.; Kozai, T. D. Y. Aberrant accumulation of age- and disease-associated factors following neural probe implantation in a mouse model of Alzheimer's disease. *J Neural Eng* **2023**, *20* (4).
(24) Cul, X. T.; Zhou, D. D. Poly (3,4-ethylenedioxythiophene) for chronic neural stimulation. *IEEE Trans. Neural Syst. Rehabil. Eng.* **2007**, *15* (4), 502-508.

(25) Dijk, G.; Ruigrok, H. J.; O'Connor, R. P. Influence of PEDOT:PSS Coating Thickness on the Performance of Stimulation Electrodes. *Adv. Mater. Interfaces* **2020**, *7* (16).
(26) Wiig, H.; Swartz, M. A. Interstitial Fluid and Lymph Formation and Transport: Physiological Regulation and Roles in Inflammation and Cancer. *Physiological Reviews* **2012**, *92* (3), 1005-1060.
(27) Vítor, L.-d.-S.; Demi, B.; David, D. Spatio-temporal organization of network activity patterns in the hippocampus. *bioRxiv* **2023**, 2023.2010.2017.562689.
(28) *F11*, Culture Collections, https://www.culturecollections.org.uk/nop/product/f11-4 (accessed 2024).

Appendices

A. Chapter 1 and 2 Appendix

A.1. Electrochemical Equilibrium -- Derivation of the Nernst Equation

Consider a reaction between A and B,

$$A^z(aq) + e^-(m) \underset{k_a}{\overset{k_c}{\rightleftharpoons}} B^{z-1}(aq) \quad \text{(A1.1)}$$

To account for both chemical and electrical energies of the species, the electrochemical potential ($\bar{\mu}_j$ for species j) is introduced and defined as:

$$\bar{\mu}_j = \mu_j + Z_j F\phi \quad \text{(A1.2)}$$

$$\mu_j = \mu_j^0 + RTln\frac{[\,j\,]}{[\,]_0} \quad \text{(A1.3)}$$

The first term, μ_j, in equation (A1.2) represents the chemical potential. If j is in solution phases, μ_j can be calculated for an ideal solution using equation (A1.3), where $[\,]_0$ is the standard concentration (1 mol dm^{-3}) ang μ_j^0 is the standard chemical potential. In the case of pure solid or liquid $\mu_j \approx \mu_j^0$. The second term, $Z_j F\phi$, in equation (A1.3) represents the electrical potential of j, where Z_j is the charge on j, F is the Faraday constant, and ϕ is the potential of the phase in which j resides (e.g. ϕ_s if j is in solution, ϕ_m if j is in electrode). For a reaction in equilibrium (equation A1.1):

$$\bar{\mu}_{A^z} + \bar{\mu}_{e^-} = \bar{\mu}_{B^{z-1}} \quad \text{(A1.4)}$$

Substitution of the expression for the electrochemical potential for each species using equation (A1.2) (A1.3) and rearrangement gives:

$$F(\phi_M - \phi_s) = (\mu_{A^z}^0 + \mu_{e^-}^0 - \mu_{B^{z-1}}^0) + RTln\frac{[A^z]}{[B^{z-1}]}$$

$$\phi_M - \phi_s = \frac{\Delta\mu^0}{F} + \frac{RT}{F} ln \frac{[A^z]}{[B^{z-1}]} \quad \text{(A1.5)}$$

where $\Delta\mu^0 = \mu^0_{A^z} + \mu^0_{e^-} - \mu^0_{B^{z-1}}$ is a constant at given temperature and pressure. Equation (A1.5) is known as the Nernst equation in an ideal solution, describing the electrochemical equilibrium between the redox couple A^z/B^{z-1}. However, in reality, the reactants' 'activity' needs to be considered to account for the ion-ion and ion-solution interaction in non-ideal situations. Thus, the activity (a_j) and activity coefficient (γ_j) are introduced:

$$a_j = \gamma_j C_j \quad \text{(A1.6)}$$

Replacing the concentration in equation (A1.5) with the activity (equation (A1.6)) gives the non-ideal case,

$$\begin{aligned} \phi_M - \phi_s &= \frac{\Delta\mu^0}{F} + \frac{RT}{F} ln \frac{a_{A^z}}{a_{B^{z-1}}} \\ &= \frac{\Delta\mu^0}{F} + \frac{RT}{F} ln \frac{\gamma_{A^z}[A^z]}{\gamma_{B^{z-1}}[B^{z-1}]} \end{aligned} \quad \text{(A1.7)}$$

$\phi_M - \phi_s$ represents the potential difference between the metal and solution at the interface of an electrode. However, measuring the potential difference at a single electrode-solution interface directly is not feasible, but the change of potential between two electrodes can be measured and quantified as below:

$$E = (\phi_M - \phi_s)_{WE} - (\phi_M - \phi_s)_{RE} \quad \text{(A1.8)}$$

Therefore, a reference electrode, as a second electrode, is necessary for electrochemical measurement. Furthermore, as $(\phi_M - \phi_s)_{RE}$ is a constant value, expanding $(\phi_M - \phi_s)_{WE}$ using equation (A1.7) and combining all the constant terms into E_0, leads to

$$E = E_0 + \frac{RT}{F} ln \frac{\gamma_{A^z}[A^z]}{\gamma_{B^{z-1}}[B^{z-1}]} \quad \text{(A1.9)}$$

Further arrangement with E_0 and the activity coefficients gives

$$E = \left(E_0 + \frac{RT}{F} ln \frac{\gamma_{A^z}}{\gamma_{B^{z-1}}}\right) + \frac{RT}{F} ln \frac{[A^z]}{[B^{z-1}]}$$

$$E = E_f^0 + \frac{RT}{F} ln \frac{[A^z]}{[B^{z-1}]} \quad \text{(A1.10)}$$

where

$$E_f^0 = E_0 + \frac{RT}{F} ln \frac{\gamma_{A^z}}{\gamma_{B^{z-1}}} \quad \text{(A1.11)}$$

The Nernst equation is thus modified to equation (A1.10) and E_f^0 represents the formal potential.

To be more specific, as the value of $(\phi_M - \phi_s)$ for a RE is a constant, in the case of Saturated Calomel Electrode (SCE), the dynamic equilibrium at SCE is

$$\frac{1}{2} Hg_2Cl_2(s) + e^-(m) \rightleftharpoons Hg(l) + Cl^-(aq) \quad \text{(A1.12)}$$

As the system is at equilibrium the electrochemical potentials can be equated using equation (A1.4)

$$\frac{1}{2} \bar{\mu}_{Hg_2Cl_2} + \bar{\mu}_{e^-} = \bar{\mu}_{Hg} + \bar{\mu}_{Cl^-} \quad \text{(A1.13)}$$

For pure solids and liquids as they have unit activity, $\mu_j \approx \mu_j^0$. For reactants in solution, equation (A1.3) is applied. Overall, the electrochemical potential for each species can be expressed as the following:

$$\bar{\mu}_{Hg_2Cl_2} = \mu^0_{Hg_2Cl_2} \quad \text{(A1.14)}$$

$$\bar{\mu}_{e^-} = \mu_{e^-} - F\phi_M \quad \text{(A1.15)}$$

$$\bar{\mu}_{Hg} = \mu^0_{Hg} \quad \text{(A1.16)}$$

$$\bar{\mu}_{Cl^-} = \mu^0_{Cl^-} + \frac{RT}{F} ln \frac{[Cl^-]}{[\ ]_0} - F\phi_S \quad \text{(A1.17)}$$

Substituting equations (A1.14~1.17) into equation (A1.13), yields

$$\frac{1}{2} \mu^0_{Hg_2Cl_2} + (\mu_{e^-} - F\phi_M) = \mu^0_{Hg} + (\mu^0_{Cl^-} + \frac{RT}{F} ln[Cl^-] - F\phi_S) \quad \text{(A1.18)}$$

Rearrange the equation and obtain:

$$\phi_M - \phi_S = \frac{\Delta\mu^0}{F} - \frac{RT}{F} ln[Cl^-] \quad \text{(A1.19)}$$

As the concentration of chloride is held constant in SCE and $\Delta\mu^0$ is a constant, $\phi_M - \phi_S$ for SCE is a constant throughout the experiment.

A.2. Mass Transport – Derivation of the Cottrell Equation

As mentioned in the main text, Fick's First Law and Second Law (in 1D) are as follows:

$$J(x) = -D\frac{\partial C}{\partial x} \quad \text{(A1.21)}$$

$$\frac{\partial C}{\partial x} = D\frac{\partial^2 C}{\partial x^2} \quad \text{(A1.22)}$$

To solve Fick's Second Law, consider a case where at an electrode surface ($x = 0$), no reactions occur before a potential is applied *($t = 0$)*, resulting in no change in concentration. Once the potential is applied at $t = 0$, either a reduction or oxidation reaction is initiated leading to a gradual consumption of materials near to the electrode surface over time. Assuming all reactants which reach the electrode are electrolyzed, the following boundary conditions are applied:

$$t = 0, \text{ at all } x, \ C = C^* \quad \text{(A1.23)}$$

$$t > 0, \text{ at } x = 0, \ C = 0 \quad \text{(A1.24)}$$

$$t > 0, \text{ at } x \to \infty, \ C = C^* \quad \text{(A1.25)}$$

To facilitate the equation solving, a variable Γ is introduced and defined as

$$\Gamma = x/2\sqrt{Dt} \quad \text{(A1.26)}$$

The new boundary conditions relative to Γ are:

$$t = 0, \text{ at all } x, C = C^* \longrightarrow \Gamma \to \infty \quad \text{(A1.27)}$$

$$t > 0, \text{ at } x = 0, C = 0 \longrightarrow \Gamma = 0 \quad \text{(A1.28)}$$

$$t > 0, \text{ at } x \to \infty, C = C^* \longrightarrow \Gamma \to \infty \quad \text{(A1.29)}$$

Replacing x by the new variable Γ in equation (A1.22),

$$\frac{\partial \Gamma}{\partial x} = \frac{1}{2\sqrt{Dt}}, \quad \frac{\partial^2 \Gamma}{\partial x^2} = 0 \tag{A1.30}$$

$$\frac{\partial \Gamma}{\partial t} = \frac{-1}{2t}\frac{x}{2\sqrt{Dt}} = \frac{-1}{2t}\Gamma \tag{A1.31}$$

Hence

$$\frac{\partial C}{\partial t} = \frac{dC}{d\Gamma}\frac{\partial \Gamma}{\partial t} = \frac{-1}{2t}\Gamma\frac{dC}{d\Gamma} \tag{A1.32}$$

$$\frac{\partial C}{\partial x} = \frac{dC}{d\Gamma}\frac{\partial \Gamma}{\partial x} = \frac{dC}{d\Gamma}\frac{1}{2\sqrt{Dt}} \tag{A1.33}$$

$$\frac{\partial^2 C}{\partial x^2} = \frac{d^2 C}{d\Gamma^2}\frac{\partial \Gamma}{\partial x}\frac{\partial \Gamma}{\partial x} + \frac{dC}{d\Gamma}\frac{\partial^2 \Gamma}{\partial x^2} = \frac{d^2 C}{d\Gamma^2}\frac{1}{4Dt} \tag{A1.34}$$

Substituting equations (A1.32~A1.34) into Fick's second law (equation (A1.22):

$$\frac{-1}{2t}\Gamma\frac{dC}{d\Gamma} = D\frac{d^2 C}{d\Gamma^2}\frac{1}{4Dt}$$

$$\frac{d^2 C}{d\Gamma^2} + 2\Gamma\frac{dC}{d\Gamma} = 0 \tag{A1.35}$$

The solution to this differential equation has the form of

$$\frac{dC}{d\Gamma} = ae^{-\Gamma^2} \tag{A1.36}$$

Integrating both sides of equation (A1.36) and applying the boundary conditions (equation (A1.27~A.1.29)) gives:

$$\int_C^{C^*} dC = \int_\Gamma^\infty ae^{-\Gamma^2} d\Gamma$$

$$C^* - C = \int_0^\infty ae^{-\Gamma^2} d\Gamma - \int_0^\Gamma ae^{-\Gamma^2} d\Gamma \tag{A1.37}$$

When $\Gamma = 0$, $C = 0$,

$$C^* = \int_0^\infty ae^{-\Gamma^2} d\Gamma = a\frac{\sqrt{\pi}}{2} \tag{A1.38}$$

Therefore equation (A1.37) can be rewritten as

$$C^* - C = C^* - C^* \frac{2}{\sqrt{\pi}} \int_0^{\Gamma} e^{-\Gamma^2} d\Gamma$$

$$C = C^* \frac{2}{\sqrt{\pi}} \int_0^{\Gamma} e^{-\Gamma^2} d\Gamma \quad \text{(A1.39)}$$

From Fick's First Law, consider:

$$J = D \frac{\partial C}{\partial x}\Big|_{x=0} = D \frac{1}{2\sqrt{Dt}} \frac{dC}{d\Gamma}\Big|_{\Gamma=0}$$

$$= D \frac{1}{2\sqrt{Dt}} C^* \frac{2}{\sqrt{\pi}}$$

$$J = \frac{\sqrt{D} C^*}{\sqrt{\pi t}} \quad \text{(A1.40)}$$

Substituting *J* in equation (A1.40) into *I* = *nFAJ* results in the Cottrell equation:

$$I = \frac{nFA\sqrt{D} C^*}{\sqrt{\pi t}} \quad \text{(A1.41)}$$

A.3. Macroelectrode CV Reversibility

The competition between the electrode kinetics and mass transport gives rise to different extents of reversibility on a CV observed. To quantify this, the electrochemical rate constant k^0 (discussed Section 1.2.2.2) is compared with the rate of mass transport m_T defined as:

$$m_T = \frac{D}{d} \quad \text{(A1.42)}$$

where *D* is the diffusion coefficient and *d* is the diffusion later thickness.

Considering only the order of magnitude, the time required to scan the voltammogram at which there is a current flow can be related as [1]

$$t \sim \frac{RT}{Fv} \quad \text{(A1.43)}$$

From equation (1.25) (Section 1.2.3.1), $d \sim \sqrt{Dt}$, and again considering only order of magnitude estimation, substituting *d* and *t* into equation (A1.42) gives:

$$m_T \sim \sqrt{\frac{DFv}{RT}} \tag{A1.44}$$

The Matsuda and Ayabe parameter (Λ), which can be understood as a ratio of k^0 and m_Γ, is introduced to define the limits of reversibility [1, 2]:

$$\Lambda = \frac{k^0}{\sqrt{\frac{DFv}{RT}}} \tag{A1.45}$$

Full mathematical evaluations are given in Matsuda and Ayabe's paper [2]. By using Λ, the following ranges for different extents of reversibility on a macroelectrode are suggested:

(1) Reversible, $k^0 >> m_\Gamma$:

$$\Lambda \geq 15, \quad k^0 \geq 0.3\sqrt{v} \tag{A1.46}$$

(2) Quasi-reversible:

$$15 > \Lambda > 10^{-3}, \quad 0.3\sqrt{v} > k^0 > 2 \times 10^{-5}\sqrt{v} \tag{A1.47}$$

(3) Irreversible, $k^0 << m_\Gamma$:

$$\Lambda < 10^{-3}, \quad k^0 \leq 2 \times 10^{-5}\sqrt{v} \tag{A1.48}$$

B. Chapter 3 Appendix

Appendix B includes detailed AFM indentation curves obtained from experiments in Chapter 3. Section B.1 and B.2 display representative force-indentation graphs for r10 and r20 PDMS samples. Section B.3 and B.4 include representative dwell-indentation graphs for r10 and r20 PDMS, and tables of mean R-squared value for the dwell curve fitting.

B.1. Representative Force-Indentation Graphs for r10

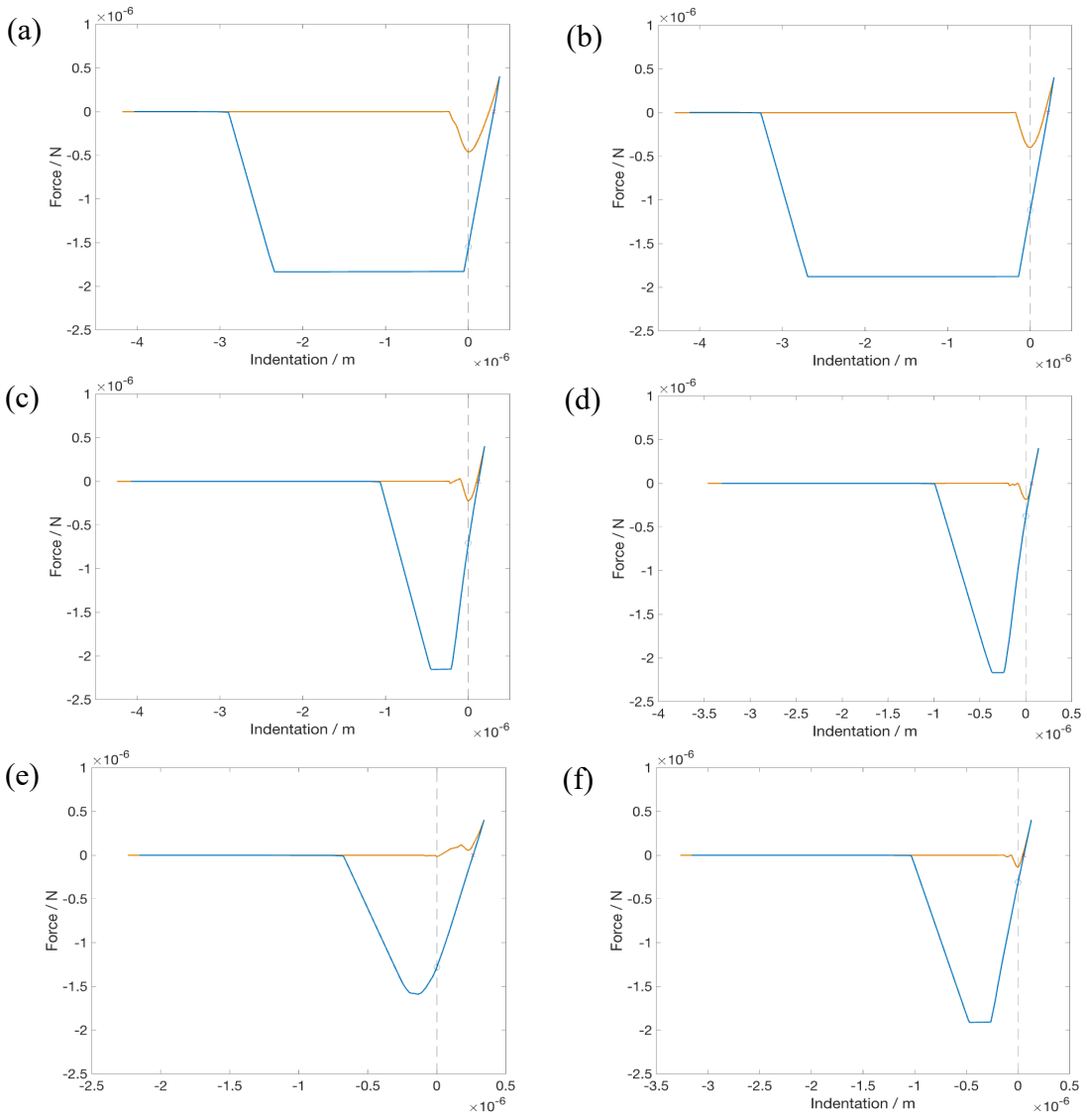

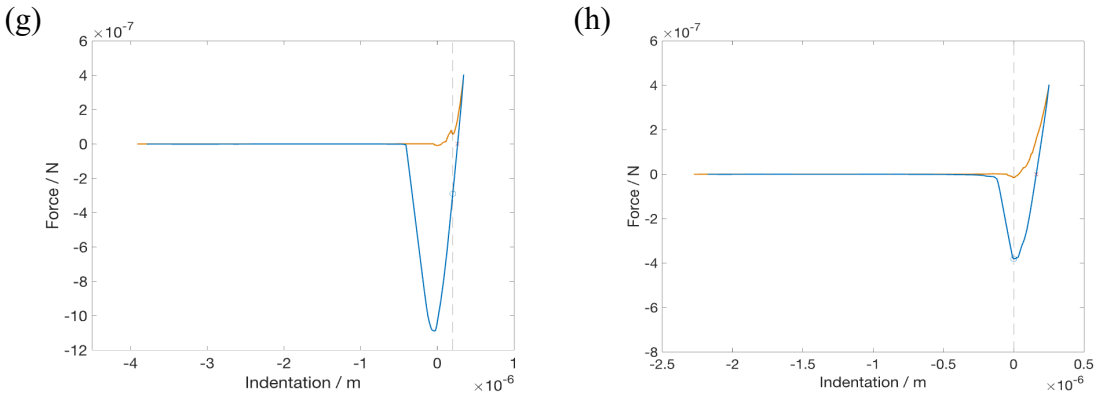

Figure B.1: (a,c,e,g) Force-indentation graphs for A-1D,3D,5D,10D r10 PDMS. (b,d,f,h) Force-indentation graphs for W-1D,3D,5D,10D r10 PDMS.

B.2. Representative Force-Indentation Graphs for r20

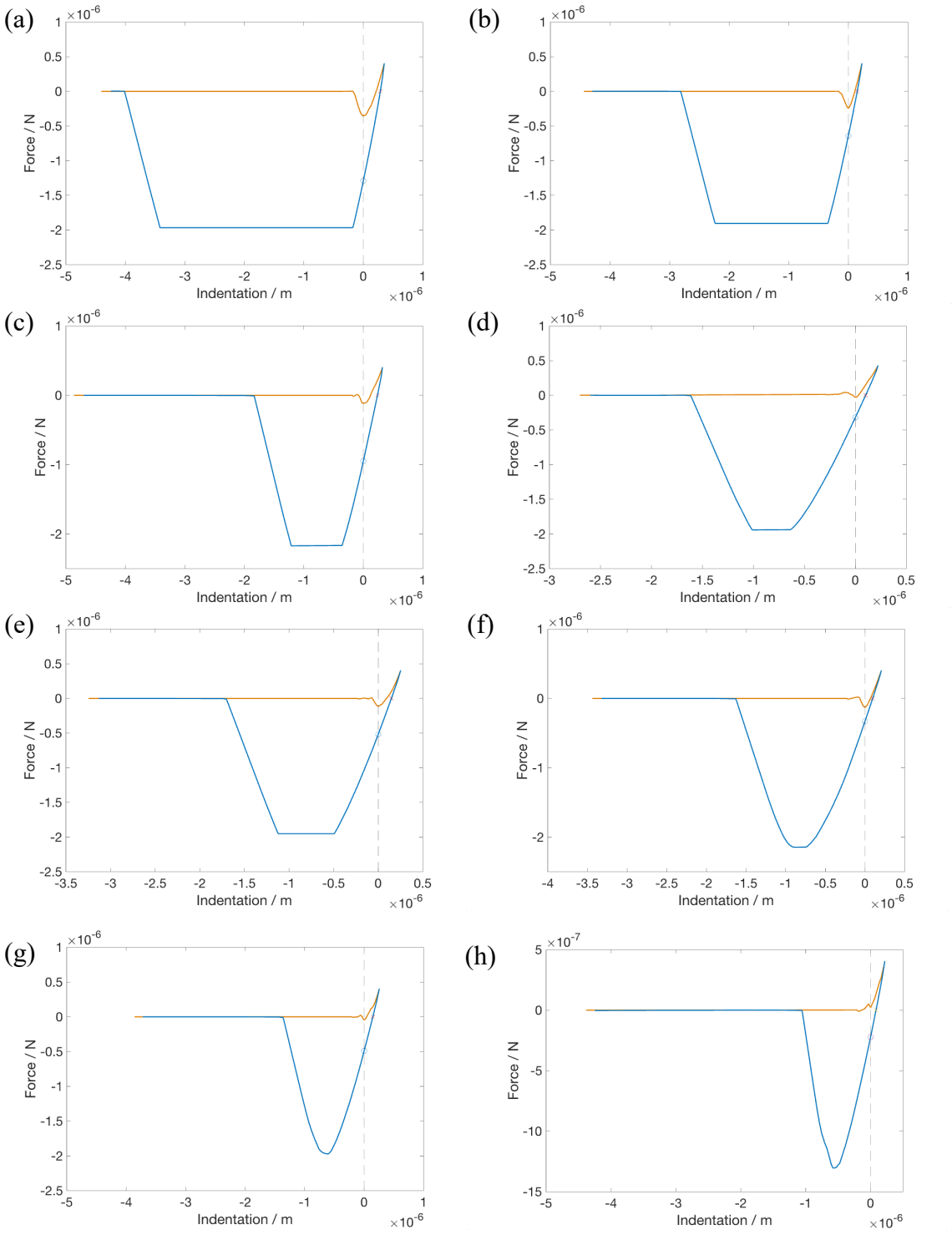

Figure B.2: (a,c,e,g) Force-indentation graphs for A-1D,3D,5D,10D r20 PDMS. **(b,d,f,h)** Force-indentation graphs for W-1D,3D,5D,10D r20 PDMS.

B.3. Representative Dwell-Indentation Graphs for r10 PDMS

A-1D r10

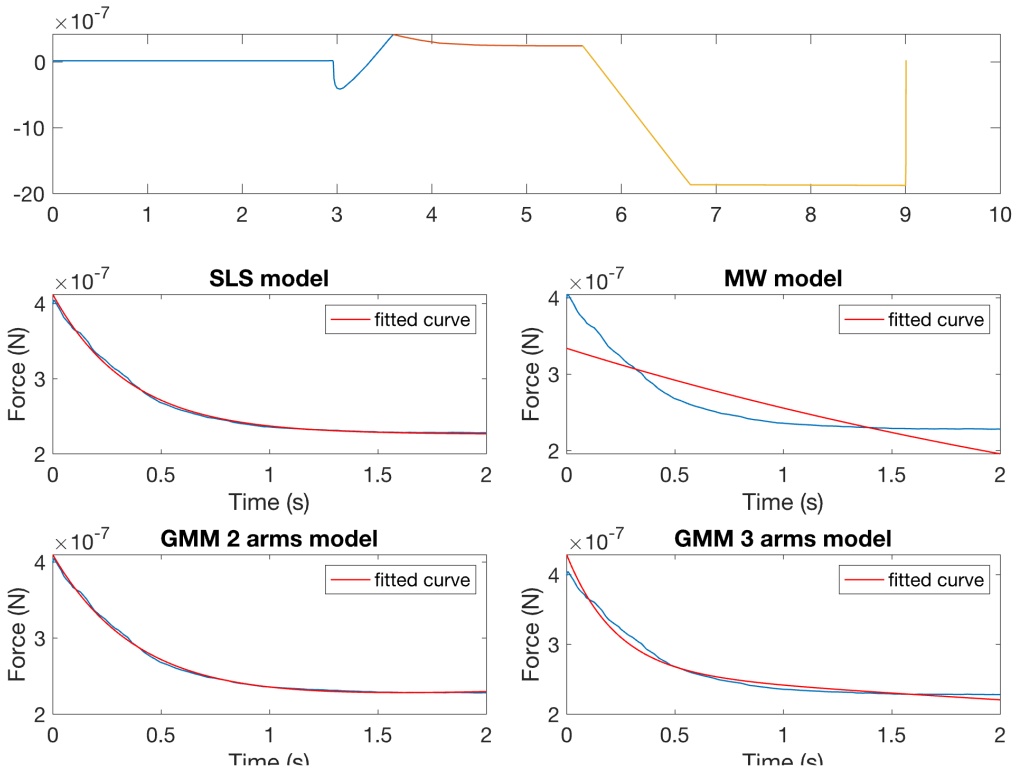

W-1D r10

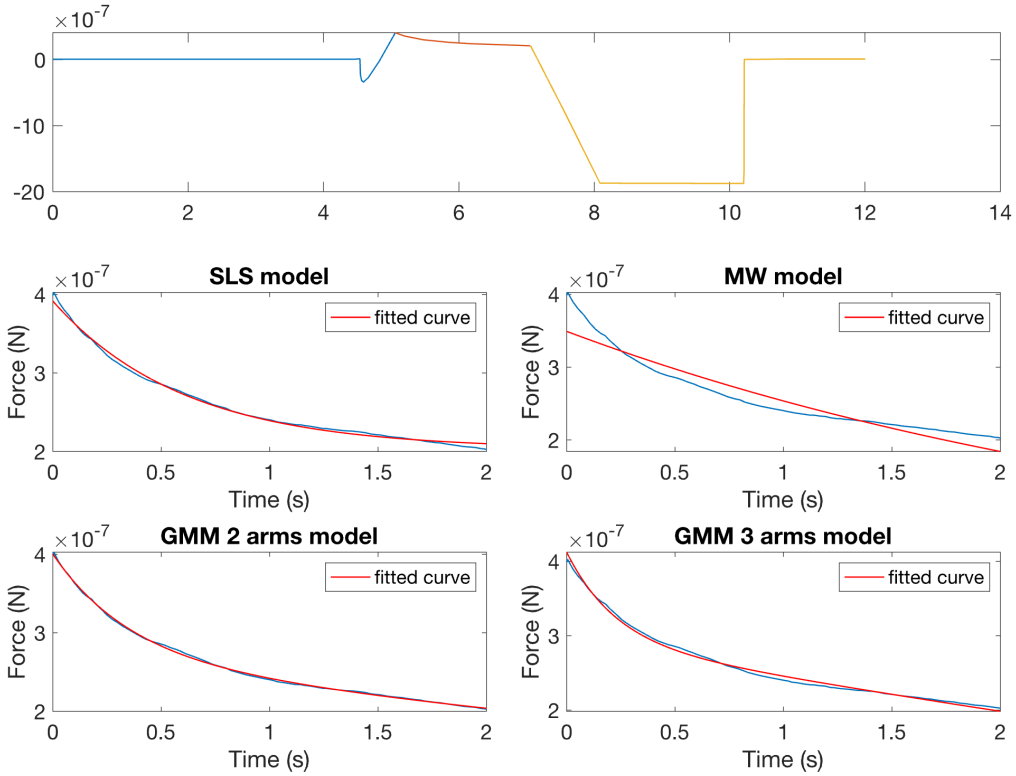

A-3D r10

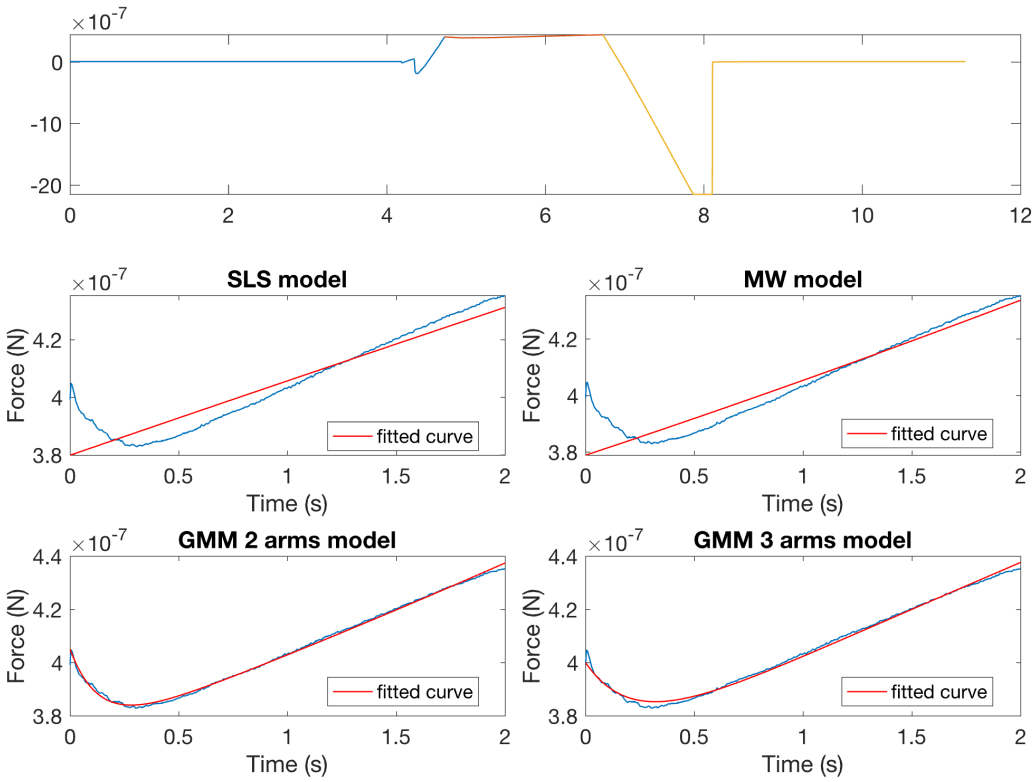

W-3D r10

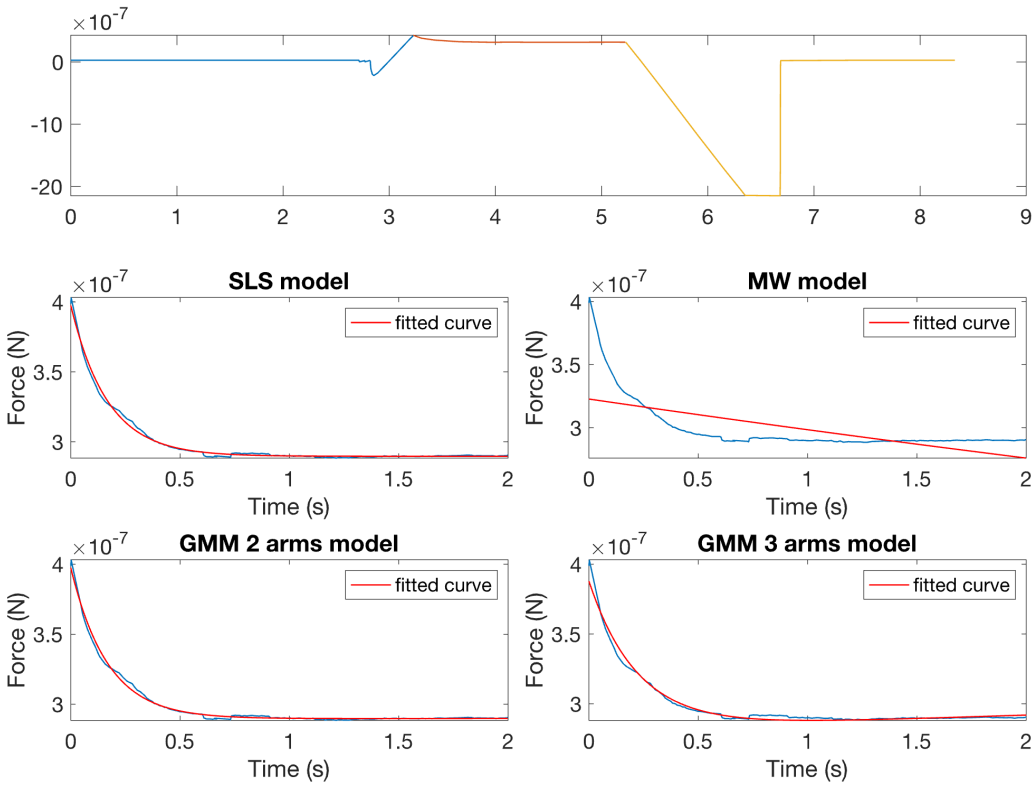

A-5D r10

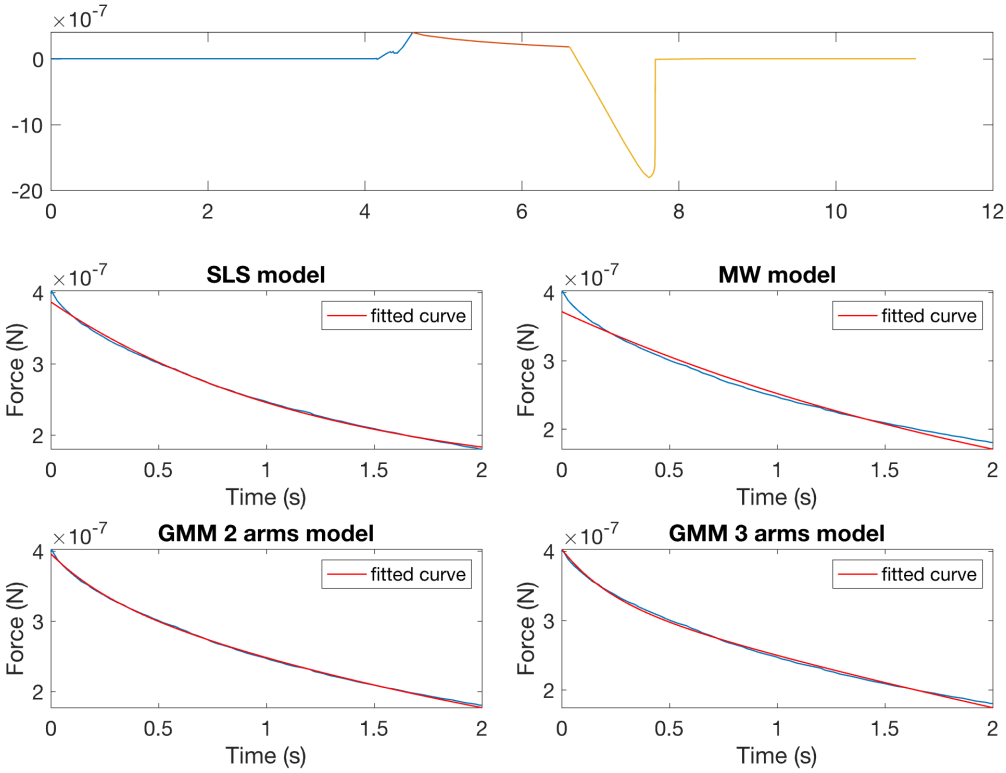

W-5D r10

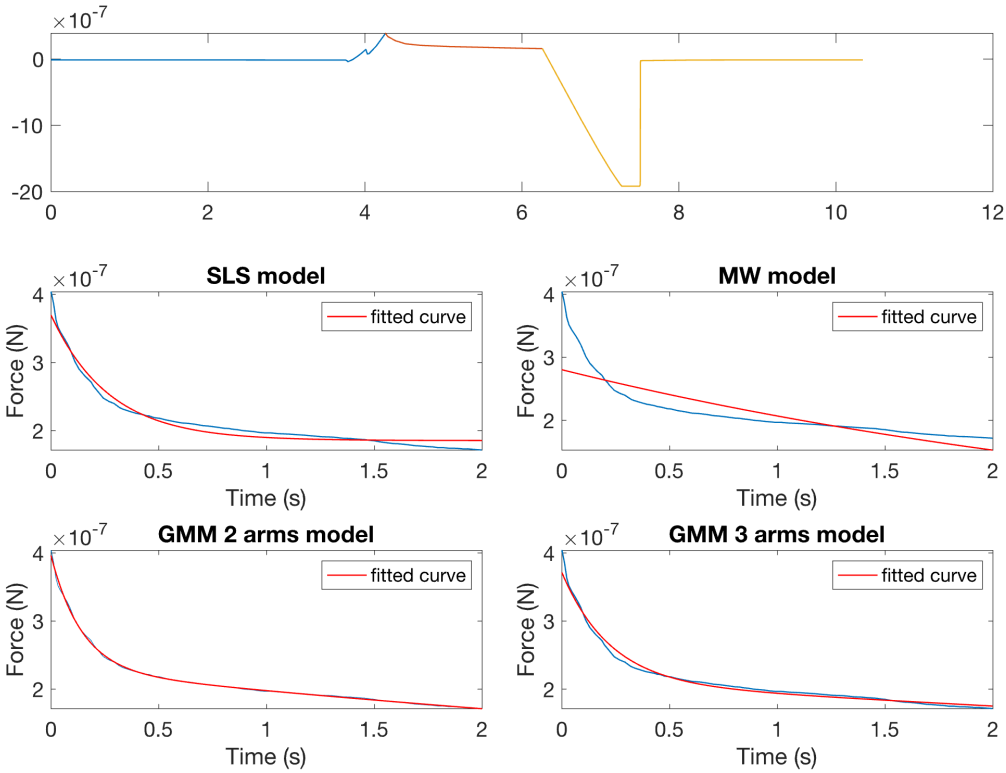

A-10D r10

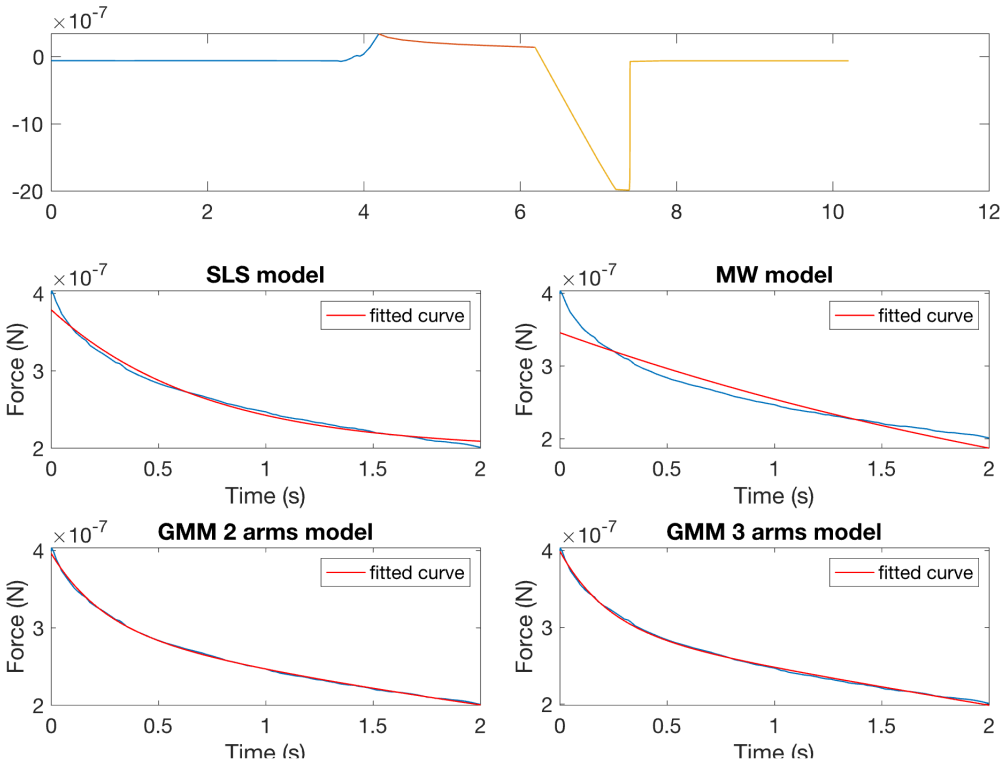

W-10D r10

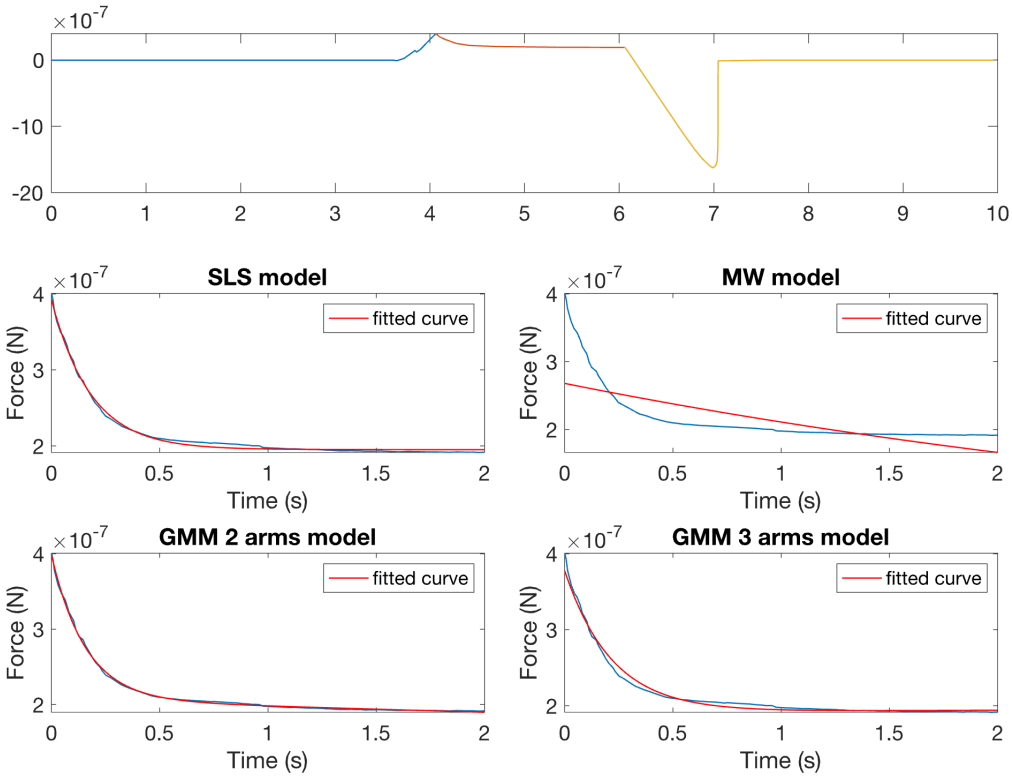

Figure B.3: Dwell indentation graphs for A (Air stored) and W (DI water stored)-1D~10D r10 PDMS. The top graph for each section is the complete force-time (F-t) graph. The bottom four graphs correspond to fitting the dwell region (orange line in the F-t graph) with SLS, MW, GMM-2, and GMM-3 models, respectively.

Table B.1: A summary of mean R-squared value for the r10 sample dwell curve fitting using different models. A represents the air-stored sample, and W represents the DI water-stored sample.

Day		SLS	MW	GMM-2	GMM-3
1D	**A**	0.990 ± 0.009	0.676 ± 0.112	0.994 ± 0.006	0.987 ± 0.010
	W	0.990 ± 0.010	0.864 ± 0.044	0.992 ± 0.019	0.980 ± 0.023
3D	**A**	0.537 ± 0.425	0.684 ± 0.263	0.990 ± 0.011	0.984 ± 0.015
	W	0.982 ± 0.013	0.607 ± 0.091	0.993 ± 0.003	0.988 ± 0.006
5D	**A**	0.993 ± 0.004	0.850 ± 0.137	0.996 ± 0.005	0.995 ± 0.003
	W	0.974 ± 0.088	0.828 ± 0.098	0.994 ± 0.008	0.992 ± 0.008
10D	**A**	0.991 ± 0.003	0.932 ± 0.031	0.998 ± 0.001	0.997 ± 0.001
	W	0.978 ± 0.017	0.600 ± 0.113	0.992 ± 0.005	0.979 ± 0.015

B.4. Representative Dwell-Indentation Graphs for r20 PDMS

A-1D r20

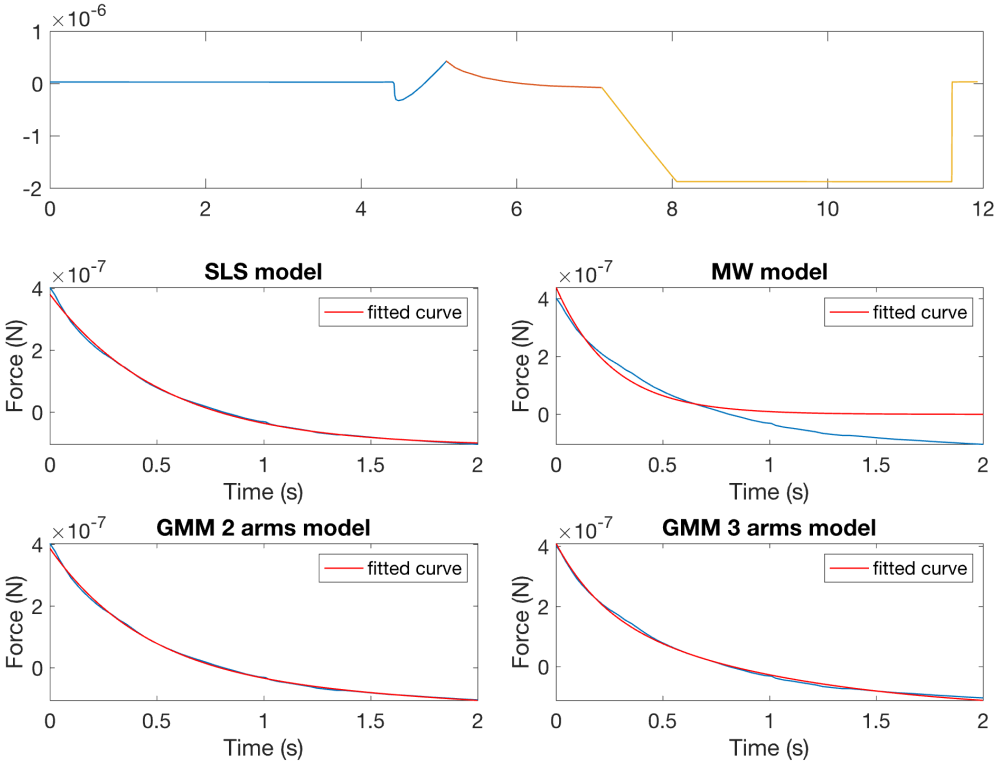

W-1D r20

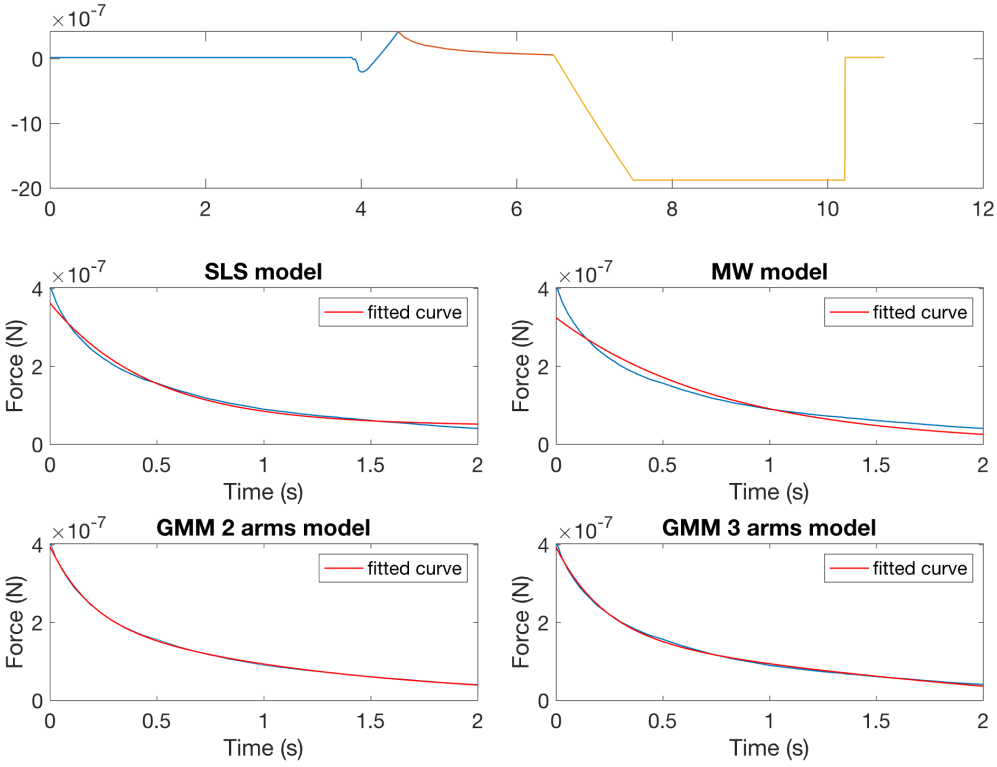

A-3D r20

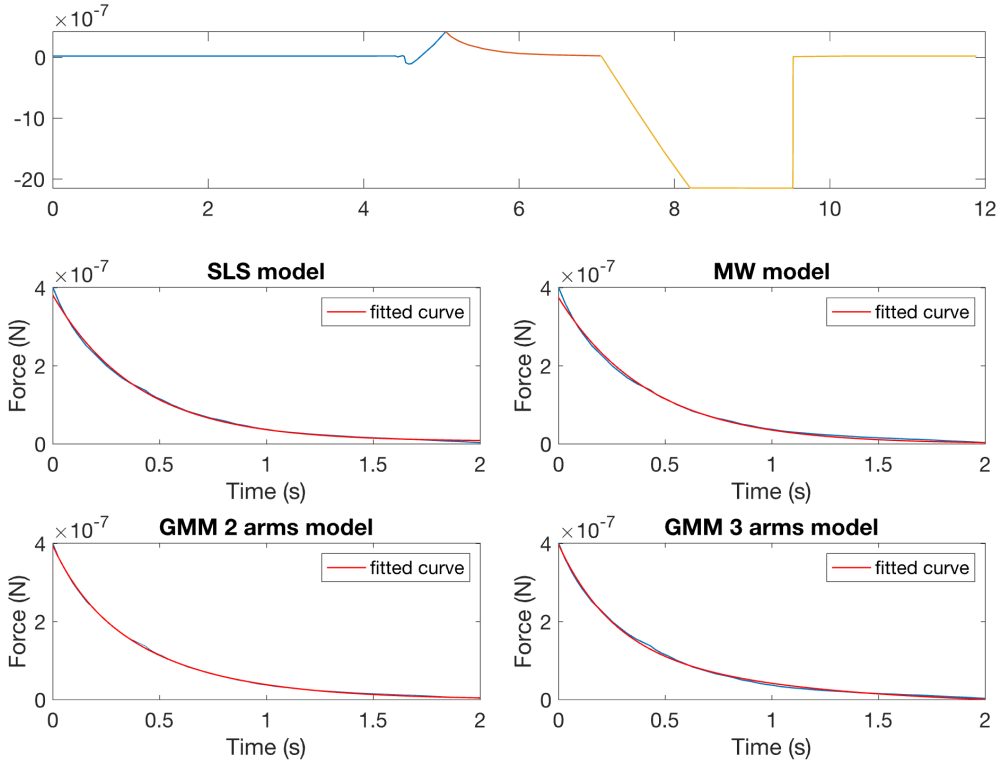

W-3D r20

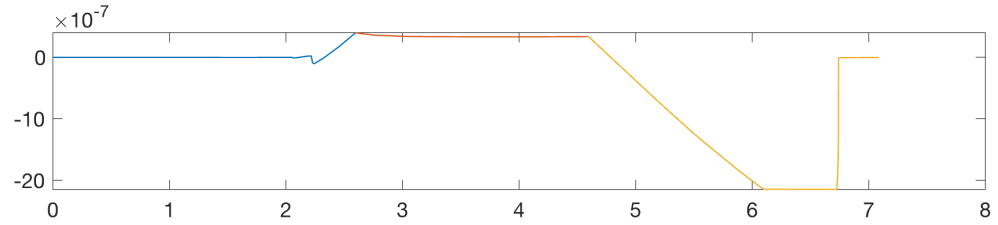

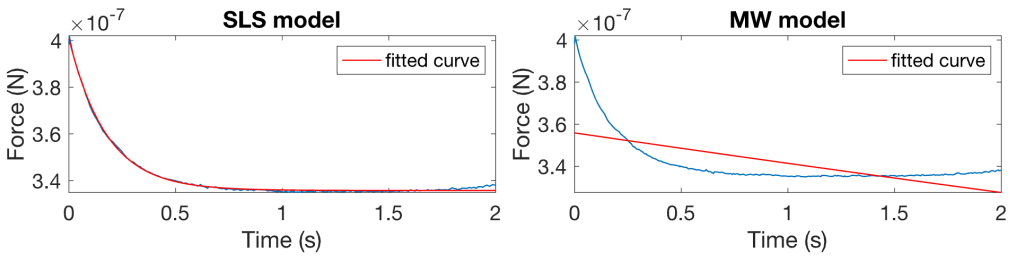

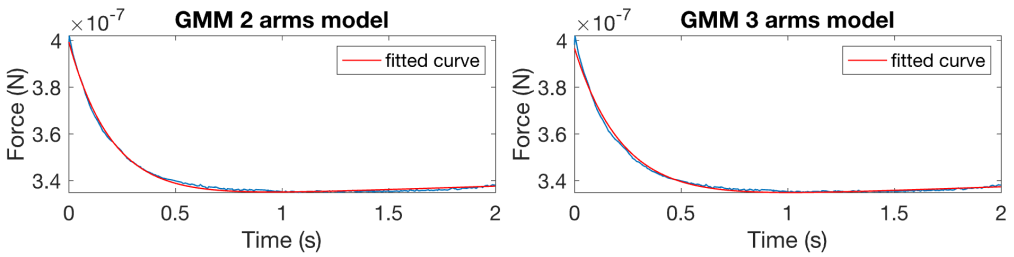

A-5D r20

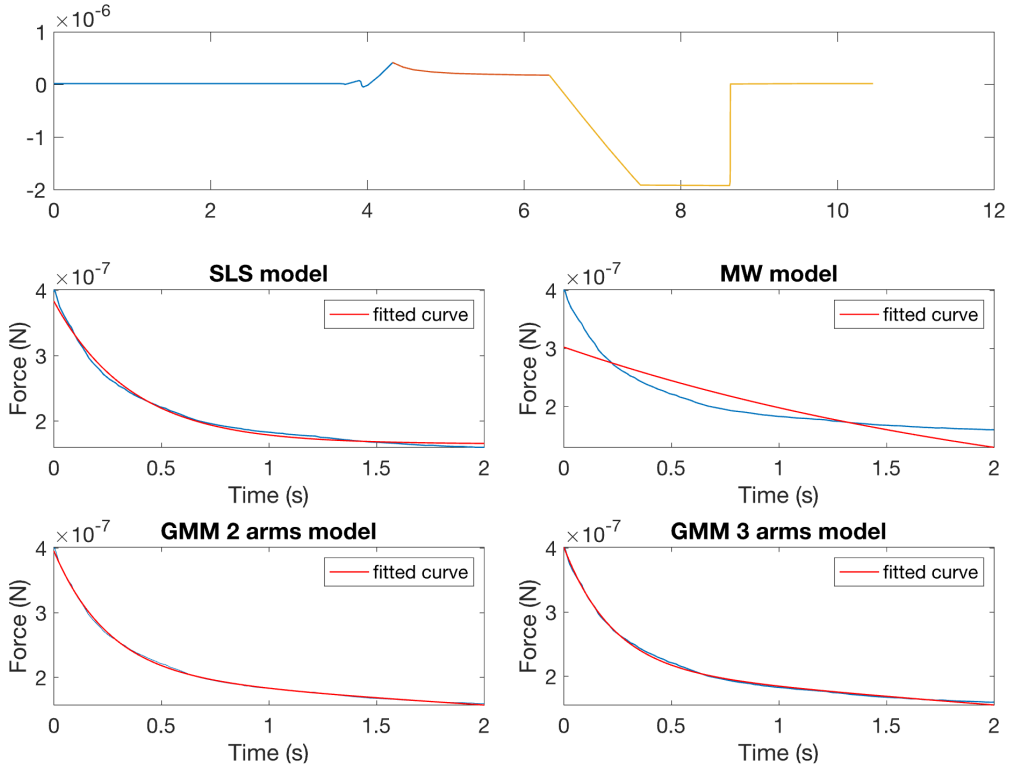

W-5D r20

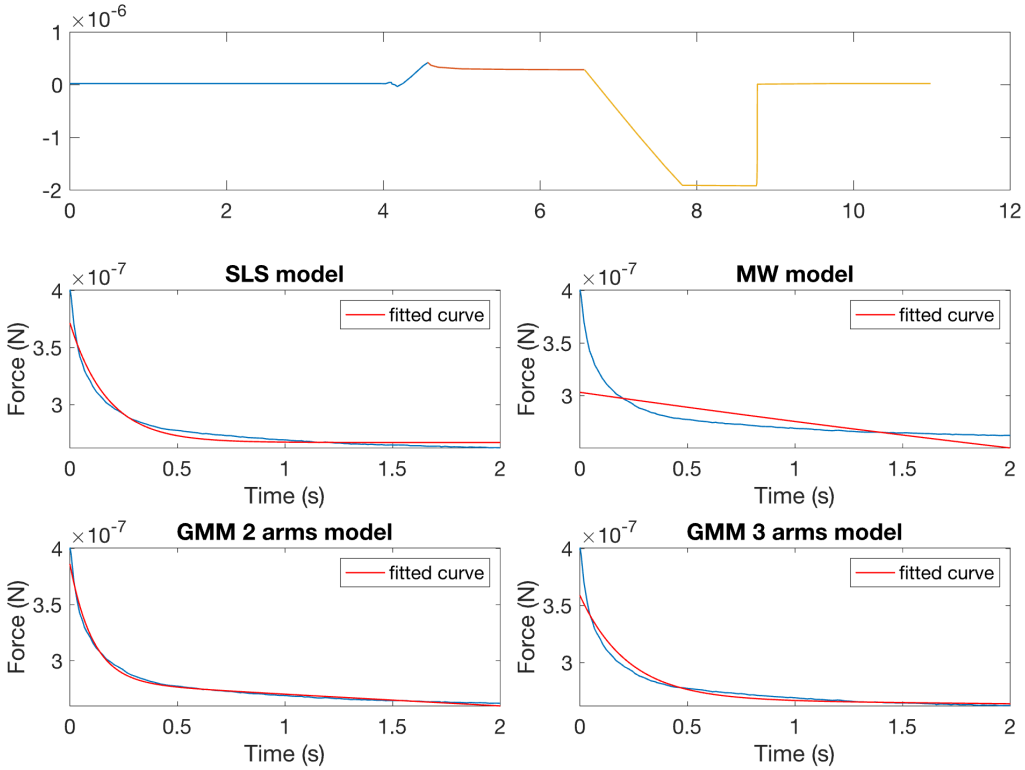

A-10D r20

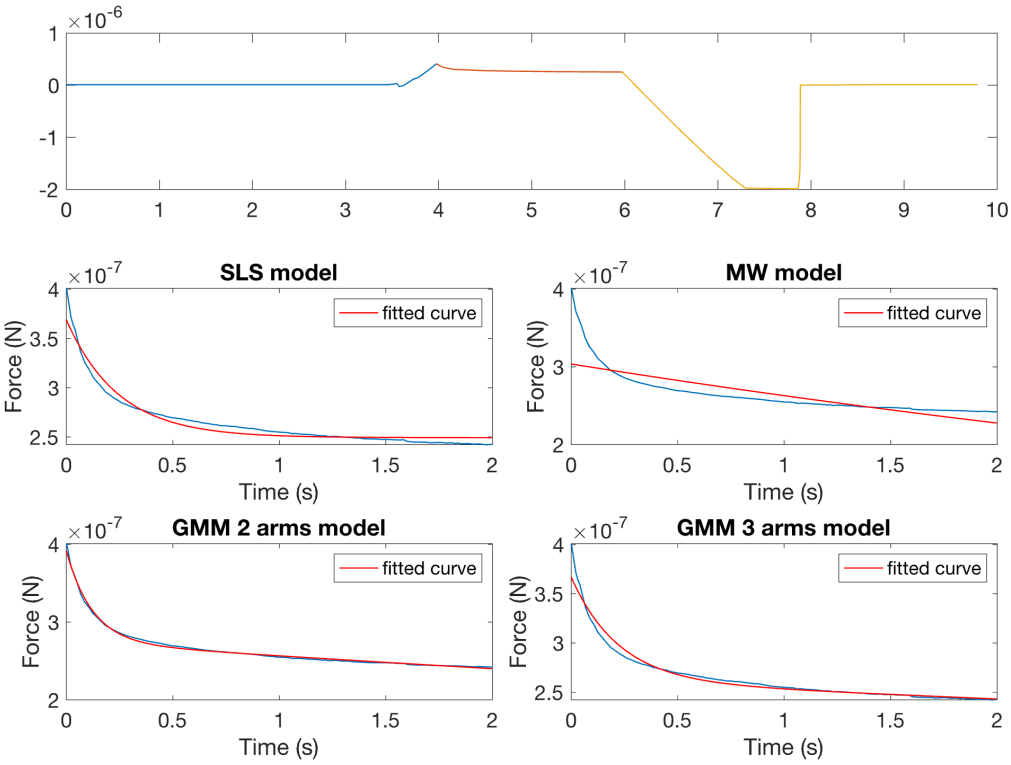

W-10D r20

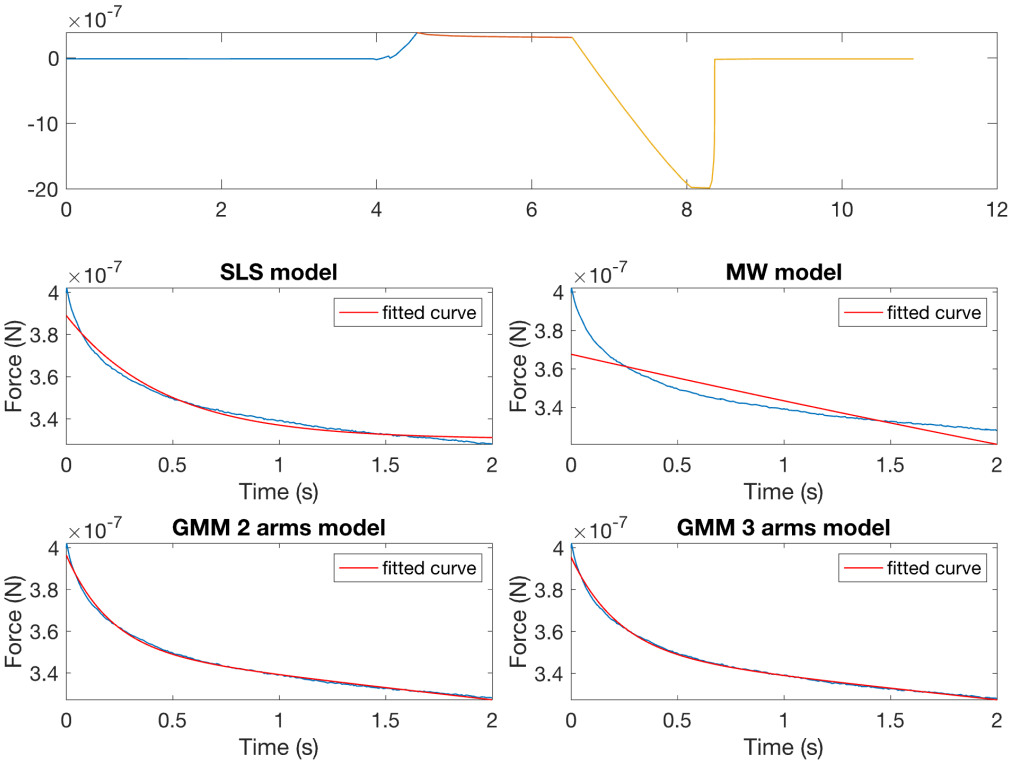

Figure 0.1: Dwell indentation graphs for A and W-1D, 3D, 5D, 10D r20 PDMS. The top graph for each section is the complete force-time (F-t) graph. The bottom four graphs correspond to fitting the dwell region (orange line in the F-t graph) with SLS, MW, GMM-2, and GMM-3 models, respectively.

Table B.2: A summary of mean R-squared value for the r20 sample dwell curve fitting using different models. A represents the air-stored sample, and W represents the DI water-stored sample.

Day		SLS	MW	GMM-2	GMM-3
1D	**A**	0.997 ± 0.003	0.926 ± 0.041	0.997 ± 0.005	0.995 ± 0.003
	W	0.994 ± 0.004	0.884 ± 0.056	0.999 ± 0.001	0.995 ± 0.004
3D	**A**	0.997 ± 0.005	0.881 ± 0.004	0.999 ± 0.001	0.993 ± 0.003
	W	0.981 ± 0.018	0.592 ± 0.184	0.992 ± 0.006	0.991 ± 0.005
5D	**A**	0.982 ± 0.017	0.747 ± 0.076	0.996 ± 0.003	0.991 ± 0.010
	W	0.970 ± 0.019	0.728 ± 0.119	0.988 ± 0.007	0.973 ± 0.016
10D	**A**	0.979 ± 0.015	0.688 ± 0.079	0.991 ± 0.005	0.983 ± 0.014
	W	0.982 ± 0.008	0.850 ± 0.042	0.997 ± 0.001	0.996 ± 0.001

C. Chapter 4 Appendix

Appendix C includes details of AFM images of PEDOT in air, in PBS, and after different pre-drying times before imaging in deionized water; AFM height and phase images data; RMS roughness comparison in deionized water and in PBS; reproducibility of the film RMS roughness after swelling; CV scans of coated and bare Pt electrodes; image of cracked PEDOT thick film.

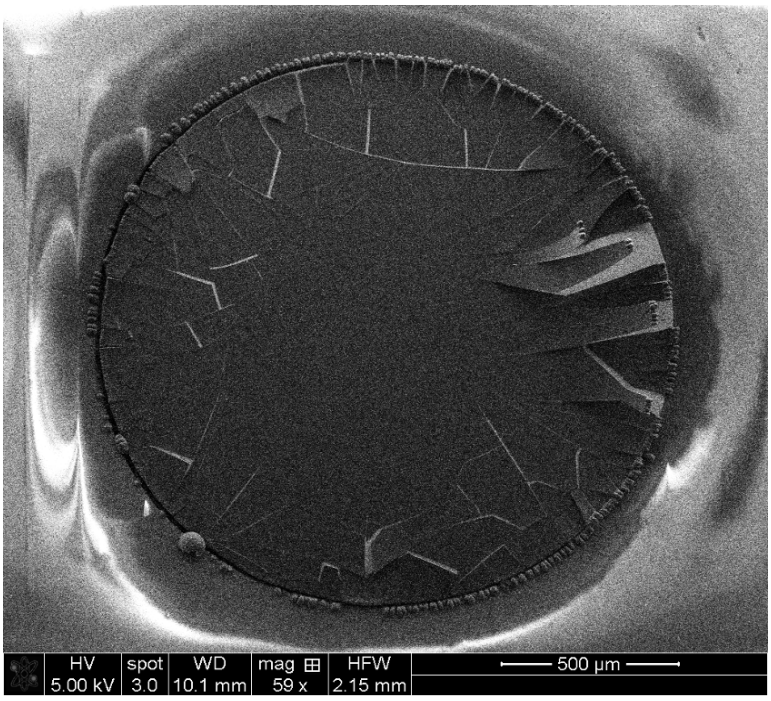

Figure C.1: Scanning electron microscope (SEM) image of a thick PEDOT: PSS film deposited (charge density ca. 1Ccm^{-2}) on the Pt macro disk electrode after blowing with dry nitrogen.

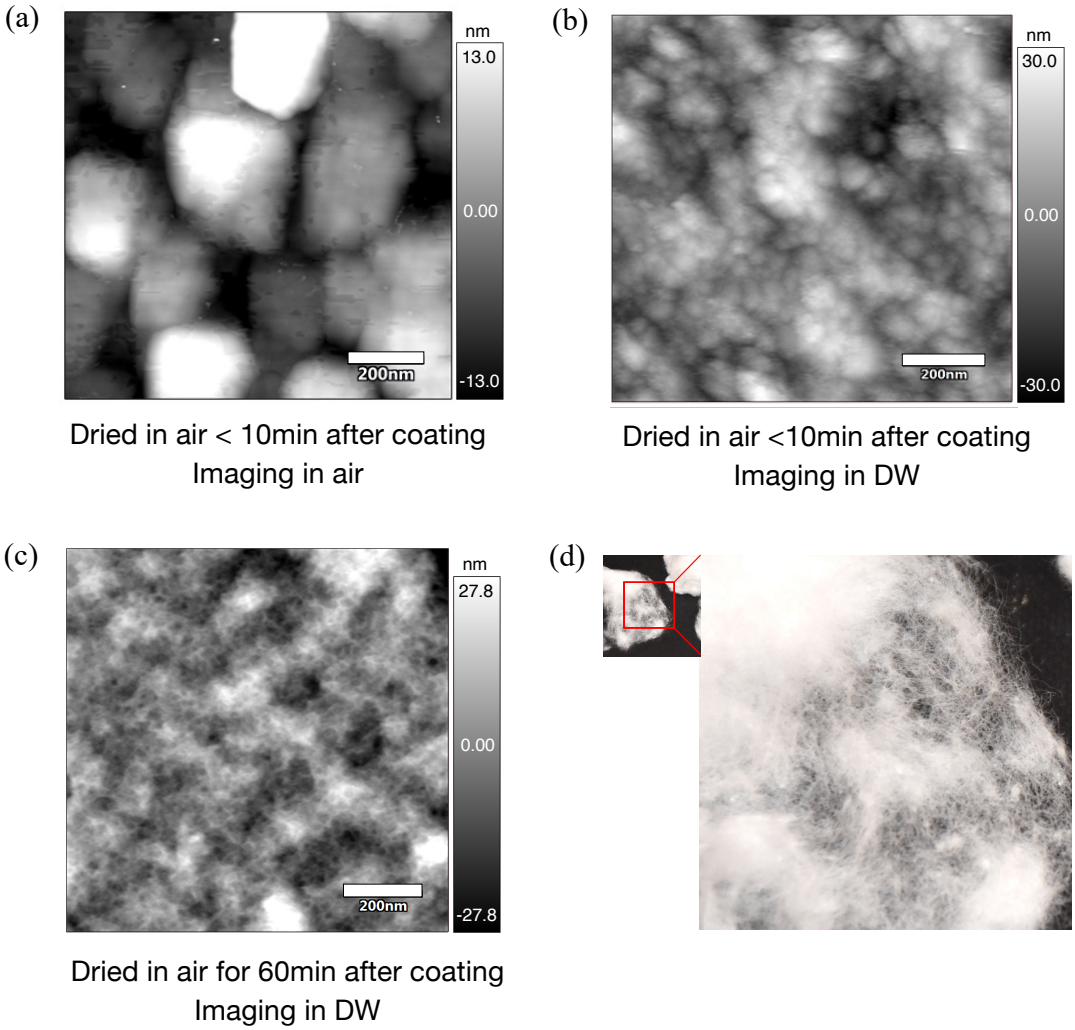

Figure C.2: Surface morphology of 5s coating PEDOT film. The modified electrodes were coated for 5s potentiostatically at 1.0V, dipped in DW, and blown with nitrogen gas to remove excess liquid. All scale bars represent 200nm **(a)** The film was dried in air for less than 10min before being imaged in air. Small structures are visible but not clear. **(b)** The film was dried in air for less than 10min before being imaged in DW. The image has a much better resolution than (a). **(c)** The film was dried in air for 60min before being imaged in DW. The resultant image has not only an improvement in resolution, but also smaller features such as a finely meshed and porous structure can be observed. **(d)** Natural cotton balls and zoom-in features. DW: deionized water.

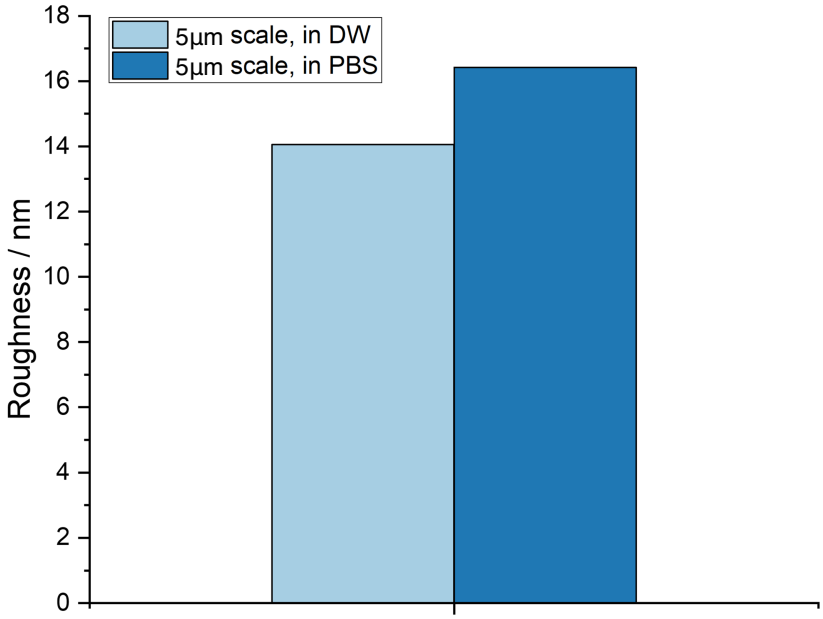

Figure C.3: Comparison of film root-mean-square (RMS) roughness imaged in DW and in PBS. The electrodes were coated with PEDOT: PSS for 60s potentiostatically at 1.0V. The modified electrode was dipped in DW and blown with nitrogen gas to remove excess liquid. Then they were placed at room temperature for 60min before imaging under DW or PBS with AFM tapping mode. DW: deionized water. PBS: Phosphate buffered saline.

Drying Time	<10min	30min	60min
0.5s deposition (scale bar = 400nm)	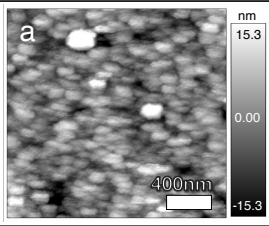	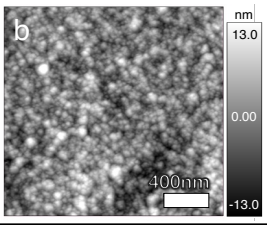	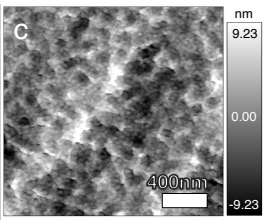
5s deposition (scale bar = 400nm)	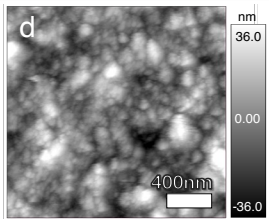	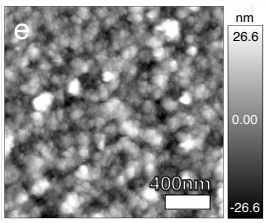	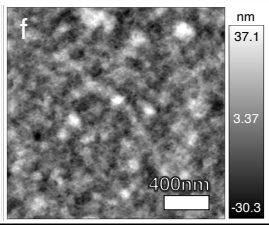
60s deposition (scale bar = 400nm)	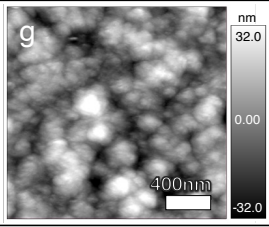	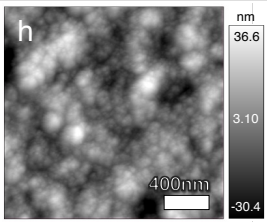	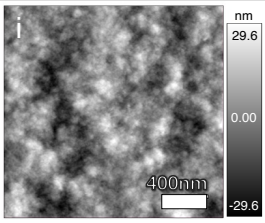

Figure C.4: The morphology of PEDOT: PSS coated Pt electrode surface. The electrode was coated with PEDOT: PSS for 60s potentiostatically at 1.0V. The modified electrodes were dipped in DW and blown with nitrogen gas to remove excess liquid. Then they were placed at room temperature for less than 10min up to 60min before AFM imaging to observe the effect of different extra drying times on the polymer. Images were taken in AFM tapping mode in DW. Deposition times range from 0.5s to 60s. Images were taken with a 2μm scan frame. All scale bars represent 400nm. DW: deionized water.

Soaking time in PBS	<10min	1h	24h
5µm scan frame (Scale bar = 1µm)	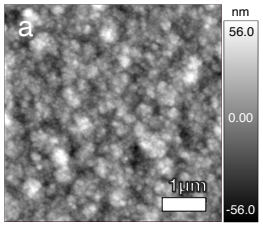	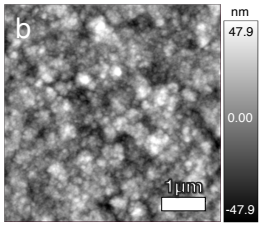	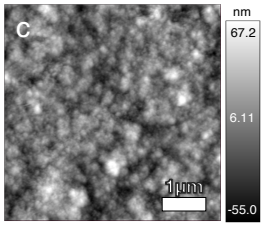
2µm scan frame Scale bar = 400nm	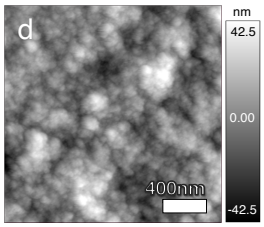	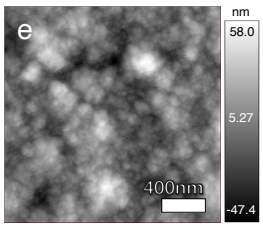	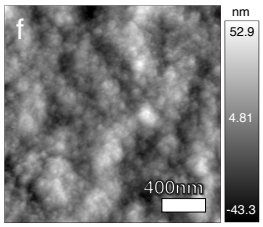
1µm scan frame Scale bar = 200nm	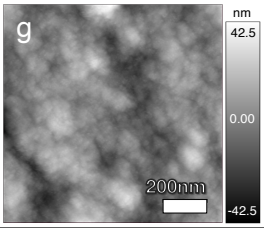	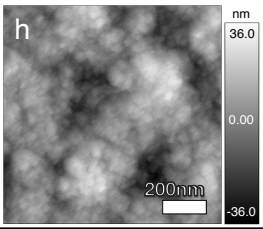	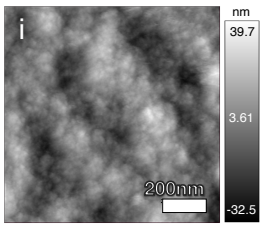

Figure C.5: The morphology of PEDOT: PSS coated Pt electrode surface soaking in 0.01M PBS. The electrode was coated with PEDOT: PSS for 60s potentiostatically at 1.0V. The modified electrode was dipped in DW and blown with nitrogen gas to remove excess liquid. Then they were placed at room temperature for 60min before soaking in 0.01M PBS. Images were taken in AFM tapping mode in 0.01M PBS. The scale bars represent 1µm, 400 nm, and 200 nm from the top to the bottom row respectively. PBS: Phosphate buffered saline.

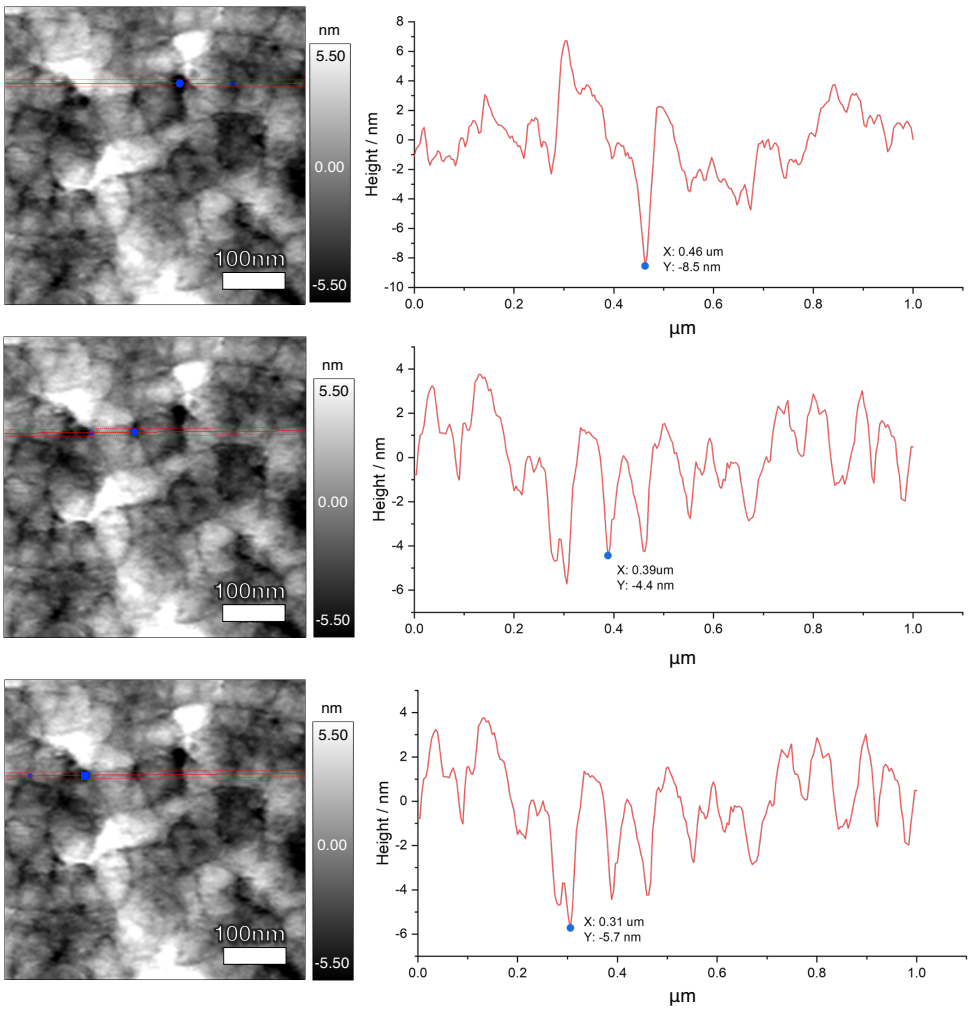

Figure C.6: 0.5s coating imaged in DW with tapping mode AFM. All scale bars represent 100nm. The positions of the pores are labeled on the left images, and their corresponding heights are on the right. DW: deionized water.

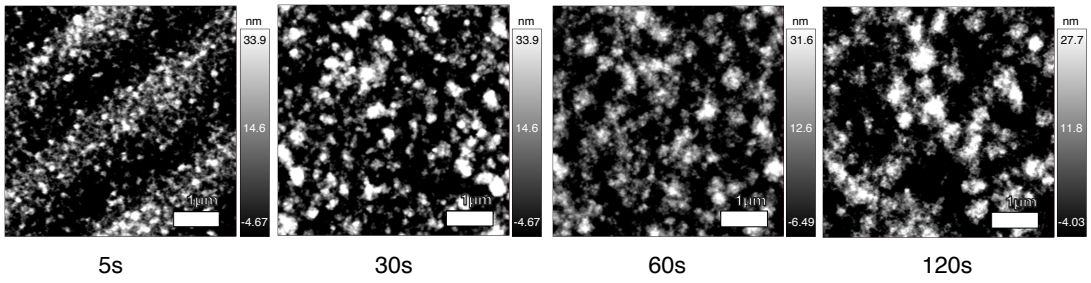

Figure C.7: 5s ~ 120s coating polymer surface. Images were taken in DW with tapping mode AFM. All scale bars represent 1µm. The contrast is adjusted to highlight the formation and growth of nuclei. DW: deionized water.

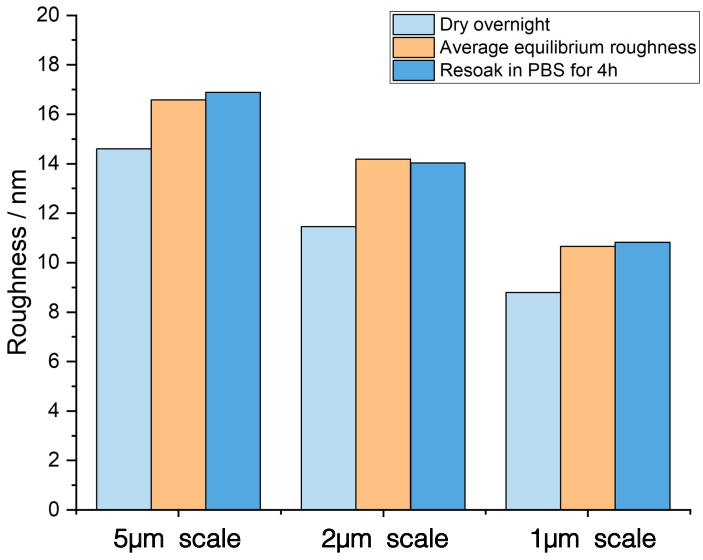

Figure C.8: Test on the reproducibility of the 60s coating RMS roughness after swelling. The film swelled back to its average roughness illustrated in **Figure** 5b (dashed lines) for all scales. PBS: Phosphate buffered saline.

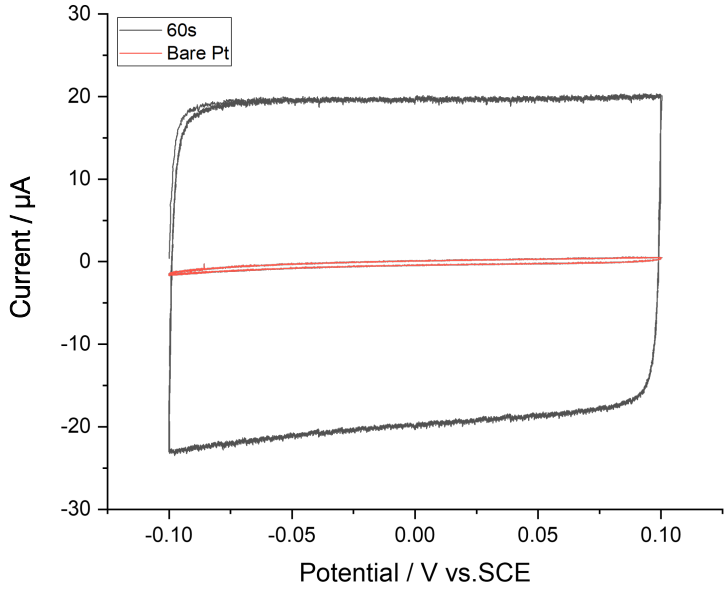

Figure C.9: CV of 60s-coated and bare Pt electrode immersed in 0.01M PBS. The scan started at -0.10V and was swept anodically up to 0.10V and reverse scanned back to -0.01V. The scan continued for 5 cycles. By comparing the area enclosed (A), the capacitance of the 60s-coated electrode is about 80-fold larger than the bare Pt electrode. ($A_{60s} = 38.9\mu AV, A_{bare} = 0.5\mu AV$). PBS: Phosphate buffered saline.

D. Chapter 6 Appendix

This section includes details of the data smoothing, and details of the potential step experiment and analysis.

D.1. PEDOT:Cl Potential Step Experiment Figures

Figure D.1 presents the results of the potential step experiment following **Scheme 6.2**, using a tetrode with WE2 coated with PEDOT:Cl and immersed in 0.01 M PBS.

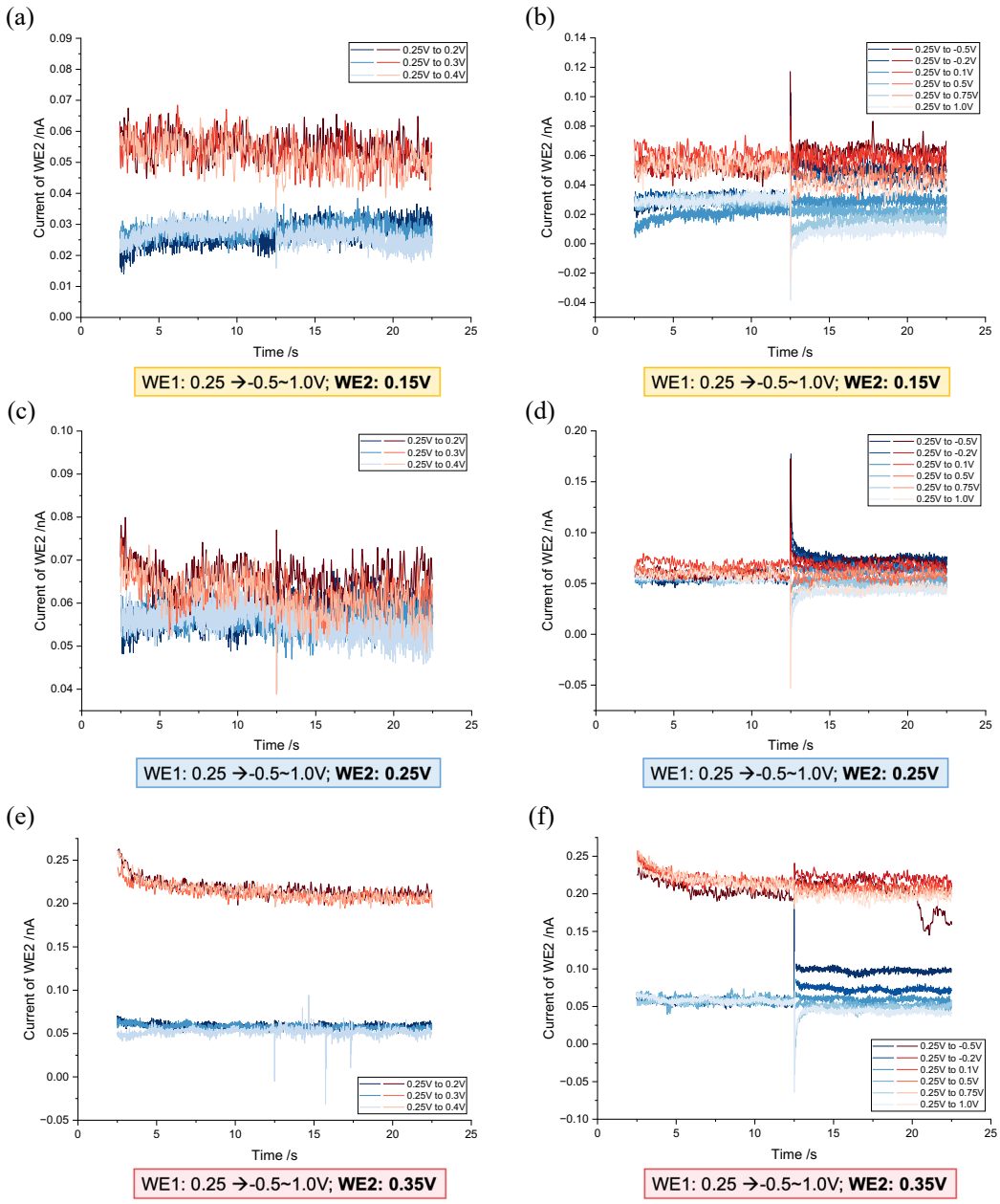

Figure D.1: The currents recorded on WE2, where WE2 was held at 0.25 V/0.15 V/0.35 V, respectively, when the potential on WE1 jumped from 0.25 V to a range of final potentials. The left column graphs (a, c, e) illustrate the situations where the potential step on WE1 triggered little response on WE2. The right column graphs (b, d, f) show the potential steps that led to significant responses on WE2. *Blue lines:* Bare Pt. *Red lines:* PEDOT:Cl coated Pt. All potentials are reported relative to the SCE.

D.2. Potential Step Data Analysis and Preprocessing

This section presents the method of fitting the current transient recorded at WE2 using the equation:

$$I = I_0 + A_1 exp\left(-\frac{t}{t_1}\right) \quad (0.1)$$

I_0 denotes the steady-state current; t_1 is the response time, reflecting how ions around WE2 respond to the sudden potential change at WE1; the sign of A_1 indicates the direction of the resulting current after the potential step, where a positive A_1 suggests a positive current, and vice versa.

Data fitting was carried out using the software Origin 2024. If any smoothing was required, MATLAB was applied. Examples of data preprocessing and fitting for bare Pt WE2 electrodes have been presented in the main text, Chapter 6, Section 6.3.4.1. Examples of the fitting procedures for PEDOT-coated electrodes are presented in the following sections.

D.2.1. PEDOT:PSS Coated Electrodes

In contrast to bare Pt, PEDOT:PSS coated electrodes exhibited a longer response time, hence the full dataset of 10 s was used for fitting. **Figure** D.2 provides a fitting of the current measured at WE2 (held at 0.15 V) after WE1 potential jumped from 0.25 V to -0.1 V. Initially using the same smoothing parameter as in main text Section 6.3.3.2 (p_s = 0.999991, hereafter

referred to as p_i), the fit yielded an R-square of 0.341 (**Figure** D.2(a)). A stronger smoothing on the raw data was therefore performed to check the reliability. The R-square value increased to 0.486 when $p_s = 0.9999$ is set (**Figure** D.2(b)), and the fitting parameters are well within the error range of the ones in **Figure** D.2(a). Care was taken to avoid over-smoothing and associated loss of data integrity.

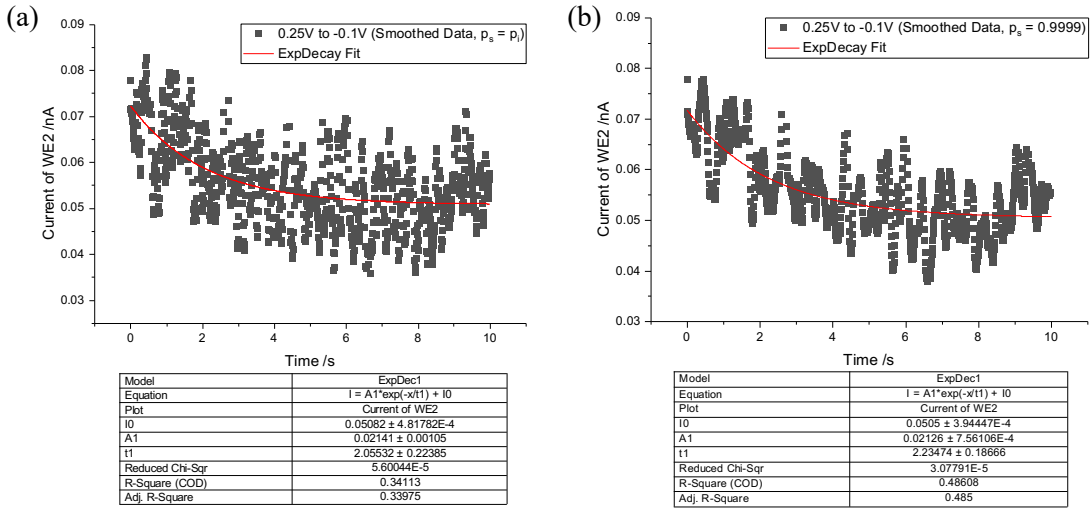

Model	ExpDec1
Equation	I = A1*exp(-x/t1) + I0
Plot	Current of WE2
I0	0.05082 ± 4.81782E-4
A1	0.02141 ± 0.00105
t1	2.05532 ± 0.22385
Reduced Chi-Sqr	5.60044E-5
R-Square (COD)	0.34113
Adj. R-Square	0.33975

Model	ExpDec1
Equation	I = A1*exp(-x/t1) + I0
Plot	Current of WE2
I0	0.0505 ± 3.94447E-4
A1	0.02126 ± 7.56106E-4
t1	2.23474 ± 0.18666
Reduced Chi-Sqr	3.07791E-5
R-Square (COD)	0.48608
Adj. R-Square	0.485

Figure D.2: The current recorded on WE2, when WE2 was held at 0.15 V, respectively, and the potential on WE1 jumped from 0.25 V to -0.1 V. **(a)** The data was preprocessed with a smoothing parameter $p_s = p_i = 0.999991$ **(b)** $p_s = 0.9999$. All potentials are reported relative to the SCE.

D.2.2. PEDOT:Cl Coated Electrodes

In the case of PEDOT:Cl-coated WE2s, the response to potential changes on the adjacent electrode is fast (< 0.1 s). Therefore, the fitting was performed using data from the initial 4 s instead of the entire 10 s recorded (**Figure** D.3).

As the smoothing level was progressively increased, using $p_s = p_i$, 0.9999, and 0.999, the R-Square value improved from 0.105 to 0.242, and lastly to 0.718 (**Figure** D.3). Moreover, the fitting parameters derived from these varying levels of smoothing all fall within the margin of error for the least smoothed data ($p_s = p_i$). Specifically, for p_s = 0.9999 and 0.999, $t_1 = 0.029 \pm 0.005\ s$ and $0.025 \pm 0.002\ s$, respectively. These values are within the error range of $t_1 = 0.023 \pm 0.007\ s$ obtained with the gentlest smoothing $p_s = p_i$.

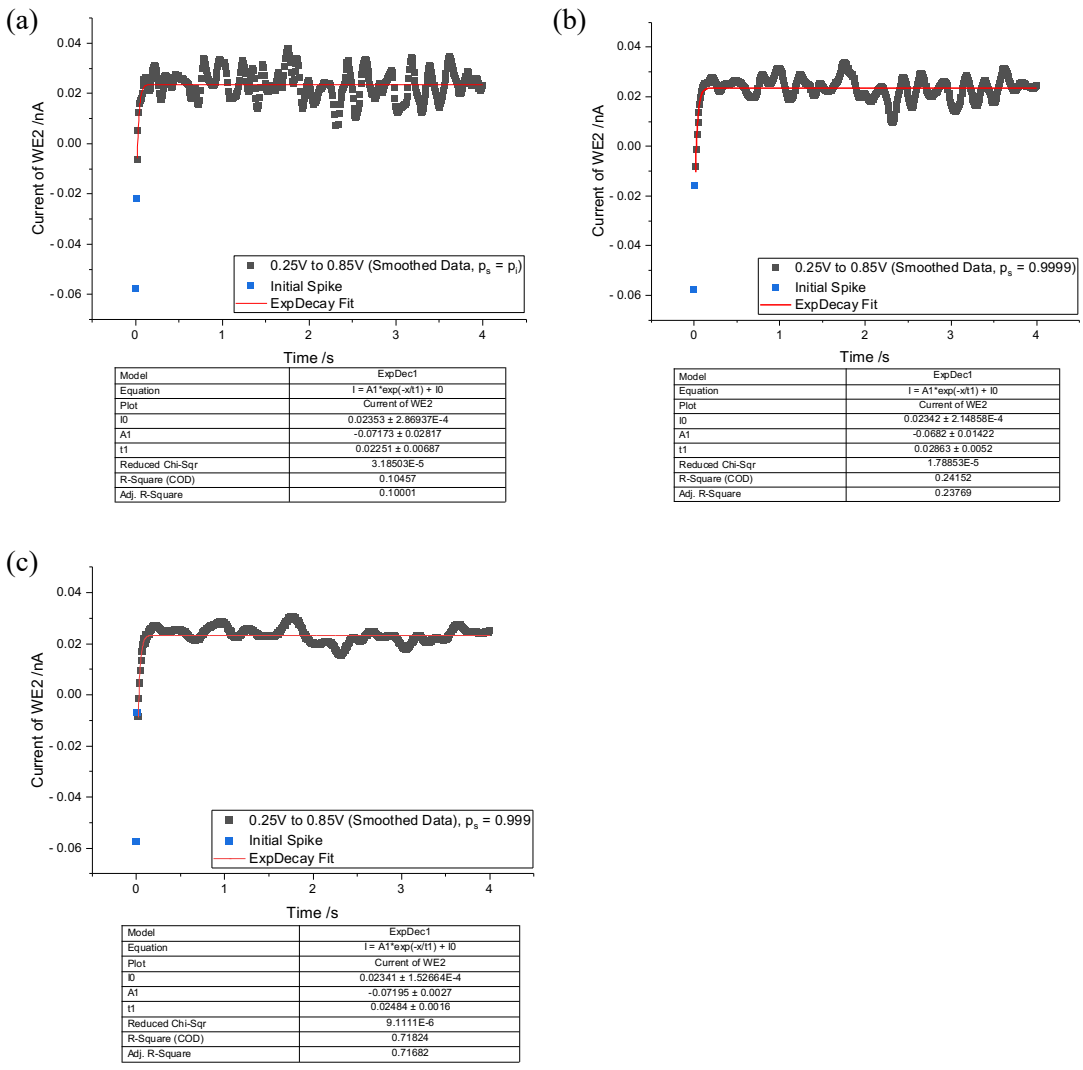

Model	ExpDec1
Equation	I = A1*exp(-x/t1) + I0
Plot	Current of WE2
I0	0.02353 ± 2.86937E-4
A1	-0.07173 ± 0.02817
t1	0.02251 ± 0.00687
Reduced Chi-Sqr	3.18503E-5
R-Square (COD)	0.10457
Adj. R-Square	0.10001

Model	ExpDec1
Equation	I = A1*exp(-x/t1) + I0
Plot	Current of WE2
I0	0.02342 ± 2.14858E-4
A1	-0.0682 ± 0.01422
t1	0.02863 ± 0.0052
Reduced Chi-Sqr	1.78853E-5
R-Square (COD)	0.24152
Adj. R-Square	0.23769

Model	ExpDec1
Equation	I = A1*exp(-x/t1) + I0
Plot	Current of WE2
I0	0.02341 ± 1.52664E-4
A1	-0.07195 ± 0.0027
t1	0.02484 ± 0.0016
Reduced Chi-Sqr	9.1111E-6
R-Square (COD)	0.71824
Adj. R-Square	0.71682

Figure D.3: The current recorded on WE2, where WE2 was held at 0.35 V, respectively, and the potential on WE1 jumped from 0.25 V to 0.85 V. **(a)** The data was preprocessed with a smoothing parameter $p_s = p_i = 0.999991$ **(b)** $p_s = 0.9999$. **(c)** $p_s = 0.999$. All potentials are reported relative to the SCE.

E. Chapter 7 Appendix

A pilot study testing the biocompatibility of the PEDOT-coated tetrode is discussed in Chapter 7 of the main text. This section includes detailed experimental procedures and data collection.

E.1. Surgical Procedure

One adult mouse was involved in the pilot study. Experimental procedures were carried out in strict accordance with the Animals (Scientific Procedures) Act, 1986 (United Kingdom), with a final ethical review by the Animals in Science Regulation Unit of the UK Home Office. All surgical procedures were performed under deep anesthesia using isoflurane (0.5–2%) and oxygen (2 l/min), with analgesia provided before (0.1 mg/kg vetergesic) and after (5 mg/kg metacam) surgery [3, 4]. For the in vivo recording, the mouse was implanted with a single microdrive containing 14 independently vertically adjustable tetrodes (4 W tetrodes, 3 Pt tetrodes, 4 PEDOT:PSS coated Pt tetrodes, 3 PEDOT:Cl coated Pt tetrodes. Tetrode fabrication and polymer deposition procedures are introduced in Chapter 2 and Chapter 6). Each tetrode was loaded into a cannula on the microdrive. Every cannula is connected to a screw (M.10, length = 6mm,) to allow independent control of a tetrode's depth. The target layer was the CA1 region of the hippocampus. After implantation, the exposed parts of the tetrodes were sealed and covered with paraffin wax. Subsequently, the drive was affixed to the skull utilizing dental cement and stainless-steel anchor screws. Two of these anchor screws, both positioned above the cerebellum, were connected to a 50 μm W wire (California Fine Wire) and served to provide a ground potential [3, 4] .For the recordings, each tetrode was carefully adjusted downwards to target the CA1 pyramidale layer of the hippocampus. This adjustment was made by turning a screw connected to each cannula that controls the tetrode's position. The correct placement of tetrode is determined by observing the electrical signals, specifically the electrophysiological

profile of the local field potentials in the hippocampal ripple frequency band, which is characteristic of this brain region [3, 4].

E.2. Recording Procedure and Data Acquisition

Following full recovery from surgery, signal recording started by the end of the fifth week after the surgery. Before starting the recordings on the day, the positions of the tetrodes were finely adjusted to achieve optimal clarity and quantity of spike waveforms, as determined by visual inspection. The extracellular signals from each recording channel were then amplified, combined, and digitized using a single integrated circuit on the head of the animal (RHD2164, Intan Technologies; http://intantech.com/products_RHD2000.html; pass band 0.09 Hz to 7.60 kHz) [3, 4]. These processed signals were digitized at a rate of 20 kHz and subsequently stored on a disk.

E.3. Spike Detection and Unit Isolation

Spike sorting and unit isolation were conducted using an automated clustering pipeline implemented in Kilosort through the SpikeForest framework [3-6]. When processing data acquired from tetrodes, Kilosort confines its templates to channels within a specified tetrode bundle and excludes all other recording channels. The operator then verified the resulting clusters by analyzing cross-channel spike waveforms and examining both auto-correlation and cross-correlation histograms.

References for Appendix

1. R. G. Compton and C. E. Banks, *Understanding voltammetry, 3rd Edition*, World Scientific, 2018.
2. H. Matsuda and Y. Ayabe, *Zeitschrift für Elektrochemie, Berichte der Bunsengesellschaft für physikalische Chemie*, 1955, **59**, 494-503.
3. L.-d.-S. Vítor, B. Demi and D. David, *bioRxiv*, 2023.
4. G. M. Van de Ven, S. Trouche, C. G. McNamara, K. Allen and D. Dupret, *Neuron*, 2016, **92**, 968-974.
5. J. Magland, J. J. Jun, E. Lovero, A. J. Morley, C. L. Hurwitz, A. P. Buccino, S. Garcia and A. H. Barnett, *eLife*, 2020, **9**, e55167.
6. M. Pachitariu, N. A. Steinmetz, S. N. Kadir, M. Carandini and K. D. Harris, *Advances in neural information processing systems*, 2016, **29**.